



Universitat Autònoma de Barcelona

ADVERTIMENT. L'accés als continguts d'aquesta tesi queda condicionat a l'acceptació de les condicions d'ús establertes per la següent llicència Creative Commons:  http://cat.creativecommons.org/?page_id=184

ADVERTENCIA. El acceso a los contenidos de esta tesis queda condicionado a la aceptación de las condiciones de uso establecidas por la siguiente licencia Creative Commons:  <http://es.creativecommons.org/blog/licencias/>

WARNING. The access to the contents of this doctoral thesis it is limited to the acceptance of the use conditions set by the following Creative Commons license:  <https://creativecommons.org/licenses/?lang=en>



**Universitat Autònoma
de Barcelona**

Synchrotron powder diffraction on *operando* batteries at non-ambient temperature

PhD Dissertation
Material Science program

Raphaëlle HOUDEVILLE
Director : Dr. François Fauth
Tutor: Dr. M. Rosa Palacín Peiró

Chemistry Department
Faculty of Sciences

2021



DOC-FAM
DOCTORAL training
programme in
Functional
Advanced Materials
H2020-MSCA-COFUND-2016





Universitat Autònoma
de Barcelona

Difracción de polvo de radiación sincrotrón en baterías *operando* a temperatura no ambiente

Tesis Doctoral
Programa de Doctorado en Ciencia de Materiales

Raphaëlle HOUDEVILLE
Director: Dr. François Fauth
Tutor: Dr. M. Rosa Palacín Peiró

Departamento de Química
Facultad de Ciencias

2021



DOC-FAM
DOctoral training
programme in
Functional
Advanced Materials
H2020-MSCA-COFUND-2016



Jury members

President: Dr. Alois Karl Kuhn, Universidad CEU San Pablo, Madrid

Secretary: Dr. Dino Tonti, Institut de Ciencia de Materials de Barcelona, Barcelona

Vocal: Dr. Jean-Noël Chotard, Laboratoire de Réactivité et Chimie des Solides, Amiens

Substitute: Dr. Flaviano García Alvarado, Universidad CEU San Pablo, Madrid

Substitute: Dr. José Antonio Ayllón Esteve, Universidad Autónoma de Barcelona, Barcelona

After sleeping through a hundred million centuries we have finally opened our eyes on a sumptuous planet, sparkling with color, bountiful with life. Within decades we must close our eyes again. Isn't it a noble, an enlightened way of spending our brief time in the sun, to work at understanding the universe and how we have come to wake up in it? This is how I answer when I am asked—as I am surprisingly often—why I bother to get up in the mornings.

- Richard Dawkins

Acknowledgements

First of all, I would like to express my deepest gratitude for my supervisors Dr. François Fauth and Dr. M. Rosa Palacín for their wholehearted support and guidance throughout this thesis. Thank you for your valuable help, availability and for trusting me during this lifetime adventure. More than everything, your encouragements and positivity helped me overcoming the difficulties I encountered.

This thesis would not have been possible without the invaluable support from ALBA's engineering team who came up with the designs of the thermalized cells and turned their drawings into reality. In particular, thank you to Monserat Prieto Moliné, Joaquín Gonzáles, José Ferrer and BL04-MSPD's technician Francesc Farré for resolving our technical issues. ¡ Muchas gracias por todo!

I also wish to sincerely thank the Laboratoire de Réactivité et Chimie du Solide in Amiens, and more specifically Prof. Christian Masquelier and his group for welcoming me for my secondment. In particular, I would like to thank Dr. Jean-Noël Chotard for guiding me in this new environment and for his mentoring during this month. I learnt a lot about sodium batteries thanks to you and it was a pleasure to work with you. Merci beaucoup pour votre accueil et votre bienveillance !

I am extremely grateful to the European Union for funding this PhD project through the MSCA-DOC-FAM research grant N° 754397. This funding allowed me to participate to various summer schools and seminars to continue learning and disseminate my research. I am also indebted to ALBA synchrotron for providing in-house beamtime which was significantly crucial for collecting the data presented in this thesis.

I would like to acknowledge my colleagues from both BL04-MSPD in ALBA and the Solid State Chemistry group at ICMA-B-CSIC for their helping me overcoming any issue I could encounter. I would like to particularly thank Dr. Ashley P. Black for his help with *operando* experiments, Dr. Roberta Verrelli for sharing her knowledge on calcium batteries and Dr. Alexandre Ponrouch for the many scientific discussions we had. At ALBA, I would like to thank Catalin, Aleksandr, Oriol and Alicia. At ICMA-B-CSIC, thank you to Deyana, Juan, Rafael and Romain. To all of you merci, grazie, mulțumesc, Спасибо, gracias, Благодаря ти.

During this PhD, I had the opportunity to cross paths with many kind people. To that extent, I would like to thank my desk-mates Nithya and Jan. I also would like to mention the other fellows from the DOC-FAM program. It was a pleasure to meet you all and be sure I will cheer for you during your PhD defense.

I would like to thank my family and friends for cheering me and sending me love though we live hundreds of kilometers apart. I would like to send a particular attention to my gaming partners from #PWEG and [YEET] for helping me going through hard times. Muchas gracias a mis amigos de Barcelona, vosotr@s sois como una familia aquí. Last but not least, I would like to thank my companion Damien for all his support and love.

Abstract

The aim of this thesis is to develop and test new thermalized *in situ* cells for X-ray diffraction in *operando* batteries to facilitate studies on electrode materials. The general reason for developing such cells is to study systems with slow kinetics, materials with temperature dependent phase transitions and/or temperature accelerated ageing processes. To assess the cells designed by ALBA's engineering team and LRCS, experiments were carried out with three electrochemical systems.

Solvent cointercalation upon reduction in TiS_2 was studied first in lithium cells, allowing the identification of propylene carbonate as solvent promoting this phenomenon. It was found to be electrochemically driven and to result in the formation of a phase indexed within the $P\bar{3}m1$ space group with parameters $a, b = 3.514(3) \text{ \AA}$ and $c = 17.931(2) \text{ \AA}$ in early stages of reduction. These cell parameters are independent of the electrolyte salt used, but the amount of cointercalated phase formed is determined by the amount of propylene carbonate solvent in the electrolyte. Its formation induces a loss in the cell capacity as it does not evolve upon oxidation.

A study at non-ambient temperature was carried out in calcium cells where development and optimization of the system and protocols was crucial. At 65°C , the reduction of a cell with TiS_2 as positive electrode, an activated carbon negative electrode and $\text{Ca}(\text{TFSI})_2$ in propylene carbonate as electrolyte promoted the formation of a cointercalated phase at early stages of reduction, prior to the observation of another more reduced phase. The cointercalated phase has an expanded c parameter estimated to be $18.41(4) \text{ \AA}$ while the more reduced phase would have a c parameter estimated at $19.23(5) \text{ \AA}$, both phases evolving in the course of reduction and being indexed in the $P\bar{3}m1$ space group. Despite the reaction taking also place at room temperature, the amount of reduced phases is significantly smaller in agreement with the sluggish kinetics of the process which is also consistent with a significant amount of TiS_2 remaining unreacted even at 65°C . Yet, and in contrast to what was observed in lithium cells, these phases are electrochemically active upon oxidation to yield TiS_2 .

Finally, experiments were carried out on both α - and β - polymorphs of $\text{Na}_3\text{V}_2(\text{PO}_4)_3$ (respectively at 2 and 40°C) to check if the thermally driven phase transition could affect the material's redox behavior. During that study, three thermalized systems were used. The intermediary $\text{Na}_2\text{V}_2(\text{PO}_4)_3$ phase was observed clearly and indexed in the $P2/m$ space group with parameters: $a = 14.847(2) \text{ \AA}$, $b = 8.617(7) \text{ \AA}$, $c = 21.554(2) \text{ \AA}$ and $\beta = 90.435(1)^\circ$. Additional measurements proved that the thermalization was necessary to test the α -NVP phase or the material would revert back to the β -NVP if kept at room temperature ($\sim 20^\circ\text{C}$) for too long. Yet, even in the case of thermalized cells, the characteristic peak of the α -NVP phase (-111) was lost upon oxidation and did not reappear upon reduction, which would yield β - $\text{Na}_3\text{V}_2(\text{PO}_4)_3$, although additional experiments would be needed to confirm this aspect.

Resumen

El objetivo de esta tesis ha sido el desarrollo de celdas electroquímicas termalizadas para estudios de materiales de electrodo *in situ* mediante difracción de rayos X en baterías *operando*. La motivación global para la construcción de dichas celdas es la investigación de sistemas con cinética lenta, de materiales con transiciones de fase dependientes de la temperatura y/o procesos de envejecimiento acelerados por la temperatura. Con objeto de evaluar las celdas diseñadas por el equipo de ingeniería de ALBA y el LRCS, se han llevado a cabo experimentos en tres sistemas diferentes.

La cointercalación del disolvente del electrolito durante la reducción de TiS_2 se estudió primero en celdas de litio, lo cual permitió identificar que el fenómeno estaba asociado a la reacción redox en presencia de carbonato de propileno y resultaba en la formación, en los estadios iniciales de la reducción, de una fase que puede indexarse en el grupo espacial $P\bar{3}m1$ con parámetros de celda $a, b = 3.514(3) \text{ \AA}$ y $c = 17.931(2) \text{ \AA}$. Estos parámetros de celda son independientes de la sal utilizada en el electrolito, pero la cantidad de fase cointercalada está relacionada con la cantidad de carbonato de propileno presente. Dicha fase no evoluciona durante la oxidación, y por lo tanto su presencia tiene como consecuencia una pérdida de capacidad electroquímica.

Se realizaron estudios a alta temperatura en celdas de calcio, para los cuales fueron cruciales el desarrollo y optimización de protocolos experimentales. A 65°C , la reducción de una celda con TiS_2 como electrodo positivo, carbón activo como electrodo negativo y $\text{Ca}(\text{TFSI})_2$ en carbonato de propileno como electrolito resultó en la formación de una fase cointercalada al principio del proceso, previa a la aparición de una fase más reducida. La fase cointercalada tiene un parámetro c expandido, de $18.41(4) \text{ \AA}$, mientras que la fase más reducida tiene un parámetro c de $19.23(5) \text{ \AA}$, ambas parecen evolucionar en reducción y pueden indexarse en el grupo espacial $P\bar{3}m1$. A pesar de que la reacción tiene lugar también a temperatura ambiente, la cantidad de fases reducidas es menor, lo cual es consistente con una cinética lenta del proceso, que es también la causa de que una cantidad significativa de TiS_2 permanezca sin reaccionar incluso a 65°C . Sin embargo, y en contraste con los resultados obtenidos en celdas de litio, la formación de dichas fases es reversible y durante la oxidación evolucionan para dar lugar a TiS_2 .

Finalmente se llevaron a cabo experimentos utilizando los dos polimorfos, α - y β - de $\text{Na}_3\text{V}_2(\text{PO}_4)_3$ (a 2 y 40°C respectivamente) con objeto de elucidar si la transición de fase afectaba al comportamiento redox. En el marco de este estudio se utilizaron tres sistemas termalizados diferentes. La presencia de la fase intermedia $\text{Na}_2\text{V}_2(\text{PO}_4)_3$ pudo determinarse claramente. Su difractograma puede indexarse en el grupo espacial $P2/m$ con parámetros de celda: $a = 14.847(2) \text{ \AA}$, $b = 8.617(7) \text{ \AA}$, $c = 21.554(2) \text{ \AA}$ y $\beta = 90.435(1)^\circ$. Medidas complementarias demostraron la necesidad de la termalización para dichos ensayos ya que la fase α -NVP se transforma en β -NVP si se mantiene un cierto tiempo a temperatura ambiente ($\sim 20^\circ\text{C}$). Aun así, el pico característico que indica la presencia de la fase α -NVP (-111) desaparece en oxidación y no reaparece durante la reducción, que parece resultar en la formación de β - $\text{Na}_3\text{V}_2(\text{PO}_4)_3$, aunque serían necesarios experimentos adicionales para confirmarlo totalmente.

List of abbreviations

- AC: activated carbon
- ASS: all solid-state batteries
- CE: counter electrode
- DCM: double crystal monochromator
- DFT: density-functional theory
- DMC: dimethyl carbonate
- DME: dimethoxy ethane
- DSC: differential scanning calorimetry
- EC: ethylene carbonate
- EOD: Earth overshoot day
- FEC: fluoroethylene carbonate
- GCPL: galvanostatic cycling with potential limitation
- GHG: greenhouse gases
- ICMAAB: Institute of Material Science of Barcelona
- LCO: Lithium cobalt oxide, Li_xCoO_2
- LFP: Lithium iron phosphate, Li_xFePO_4
- LIB: lithium-ion battery
- LINAC: Linear Accelerator
- LMO: lithium manganese oxide, $\text{Li}_{1-x}\text{Mn}_2\text{O}_4$
- LP30: commercial solution of LiPF_6 1M in EC:DMC
- LRCS: Laboratoire de Réactivité et Chimie des Solides
- MAD : Multi Analyzer Detector
- MSPD: Material Science and Powder Diffraction
- NASICON: Na Super Ionic Conductors
- NCA: lithium nickel cobalt aluminum, $\text{LiNi}_x\text{Co}_y\text{Al}_z\text{O}_2$
- NGO: non-governmental organization
- NMC: lithium nickel manganese cobalt oxides, $\text{LiNi}_x\text{Mn}_y\text{Co}_{1-x-y}\text{O}_2$
- NVP: sodium vanadium phosphate, $\text{Na}_3\text{V}_2(\text{PO}_4)_3$
- NVPF: sodium vanadium fluorophosphates, $\text{Na}_3\text{V}_2(\text{PO}_4)_2\text{F}_3$
- OCV: open circuit voltage
- PC: propylene carbonate
- PLA: polylactic acid
- POM: polyoximethylene
- PSD: position sensitive detector
- PTFE: polytetrafluoroethylene
- PVDF: polyvinylidene fluoride
- RE: reference electrode
- SEI: solid electrolyte interphase
- SHE: standard hydrogen electrode

- SIB: sodium-ion batteries
- THF: tetrahydrofuran
- WE: working electrode

Table of contents

Acknowledgements	2
Abstract	3
Resumen	4
List of abbreviations	4
I. Introduction.....	16
I.1. General context.....	16
I.2. Batteries	18
I.2.1. Principle.....	18
I.2.2. From Volta's pile to the alkaline battery.....	19
I.2.3. Lithium and lithium-ion batteries.....	21
I.2.4. Improvements in Li-ion technologies.....	24
I.2.5. Other lithium based concepts	25
I.2.6. Next generation batteries	26
I.2.6.1. Sodium-ion batteries	26
I.2.6.2. Calcium based batteries	28
I.3. Aim and context of the thesis	29
II. Experimental techniques.....	32
II. 1. Chemical and electrochemical characterization	32
II. 1. 1. Electrolyte preparation.....	32
II. 1. 2. Karl-Fisher titration.....	33
II. 1. 3. Electrode preparation.....	34
II. 1. 4. Electrochemical cells	35
II. 1. 5. Chronopotentiometry and (de-)intercalation redox mechanism.....	36
II. 2. Crystallography and X-ray diffraction.....	38
II. 2. 1. Principle	38
II. 2. 2. X-rays in a laboratory.....	41
II. 2. 3. X-rays in ALBA-CELLS synchrotron.....	43
II. 2. 3. 1. Functioning principle	43
II. 2. 3. 2. Insertion devices.....	45
II. 2. 4. BL04- MSPD	46
II. 3. <i>In situ</i> X-ray diffraction on battery	49
II. 3. 1. Choice of <i>in situ</i> cells element.....	51

II. 3. 1. 1. Additional contributions from the other battery parts	51
II. 3. 1. 2. Electrode preparation for <i>in situ</i> experiment.....	52
II. 3. 1. 3. Advantages of <i>in situ</i> experiments in synchrotron.....	52
II. 3. 2. Cell thermalization.....	54
III. Lithium insertion in TiS_2 and cointercalation	62
III. 1. Pristine sample characterisation.....	62
III. 2. Choice of electrolyte	65
III. 3. Operando experiments	65
III. 4. <i>Ex situ</i> complementary tests	76
III. 5. Conclusion	78
IV. Calcium intercalation in TiS_2	80
IV. 1. Experiments carried out above ambient temperature	82
IV. 1. 1. Ca// TiS_2 cells at 100°C	82
IV. 1. 2. AC// TiS_2 cells at 65°C.....	85
IV. 1. 2. 1. <i>Ex situ</i> preparatory work	85
IV. 1. 2. 2. <i>Operando</i> experiments.....	87
IV. 2. Experiment at room temperature	92
IV. 3. Conclusion	95
V. Temperature dependent studies on $\text{Na}_3\text{V}_2(\text{PO}_4)_3$	98
V. 1. Investigation of pristine $\text{Na}_3\text{V}_2(\text{PO}_4)_3$	100
V. 2. Investigation of the redox mechanism for $\text{Na}_3\text{V}_2(\text{PO}_4)_3$ at room temperature.....	103
V. 2. 1. Preliminary <i>operando</i> experiments with synchrotron radiation.....	103
V. 2. 2. <i>Operando</i> experiment using a laboratory X-ray diffractometer (secondment at LRCS)	106
V. 3. Temperature dependent synchrotron experiments	108
V. 2. 3. Hexagonal cell.....	109
V. 2. 3. 1. Test at room temperature.....	109
V. 2. 3. 2. The α -NVP phase (2°C)	112
V. 2. 4. Experiments carried out using the coin cell oven	113
V. 2. 4. 1. The β -NVP phase (45°C)	113
V. 2. 4. 2. The α -NVP phase (2°C)	114
V. 2. 5. Experiments using the Leriche cell.....	115
V. 2. 5. 1. Room temperature	115
V. 2. 5. 2. The α -NVP phase (2°C)	116

V. 4. Conclusion	118
General conclusion	124
Bibliography.....	127

List of figures

Figure I.1 - Earth Overshoot Days (EOD) between 1970-2020, reprinted from overshootday.org ¹	16
Figure I.2 - a) Greenhouse gases emission per region and per year ⁴ ; b) Global primary energy per source in 2019 ³	17
Figure I.3 - Schematic representation of a battery during charge and discharge.....	18
Figure I.4 – a) Schematic representation of a Li/TiS ₂ battery (reprinted from ref 8), b)An Exxon LiTiS ₂ rechargeable lithium battery exhibited at the Chicago electric vehicle show in 1977(reprinted from ref ²⁵ , and c) solar clock with rechargeable Li/TiS ₂ battery built by Exxon (reprinted from ref 26).....	22
Figure I.5 - Schematic representation of a Li/CoO ₂ battery (reprinted from ref 8).....	22
Figure I.6 - Schematic representation of a Li-ion battery, using petroleum coke vs LiCoO ₂ (reprinted from ref 8)	23
Figure I.7 – a) Structure of a NASICON compound and its lantern-like unit cell, b) structure of Na ₃ V ₂ (PO ₄) ₂ F ₃ , both reprinted from 55	27
Figure I.8 –Standard reduction potential and theoretical gravimetric and volumetric capacities for different metal electrodes. Values for graphite used in Li-ion cells are given for comparison (reprinted from ref 62)	28
Figure II.1– a) Schematic representation of the Karl Fischer apparatus, b) photography of the Metrohm 899 Coulometer used.....	34
Figure III.2 – Pattern number (10min increment in time) vs voltage and associated X-ray surface plots of cells cycled with a) LP30, b) LiPF ₆ 1 M in EC:DMC:PC 2:1:2 and c) LiTFSI 1 M in EC:PC 1:1.	67
Figure III.3 - Reduction and oxidation curve of TiS ₂ cells cycled with LP30 (blue) and 0.67M LiPF ₆ in EC:PC:DMC 33:33:33 (red).....	75
Figure IV.1 – <i>Ex-situ</i> X-ray diffraction patterns collected at different stages of TiS ₂ reduction in Ca cells at 100°C using calcium metal CE and 0.45 M Ca(BF ₄) ₂ in EC:PC as electrolyte, with structural models proposed for the different phases observed of Ca//TiS ₂ cells collected at different stage of electrochemistry, reprinted from 70.....	81
Figure IV.2 - a) Capacity vs. potential curves at 100 °C and C/100 rate for AC//TiS ₂ cells, using 0.3M Ca(BF ₄) ₂ in EC:PC (pink curve) and 0.3M Ca(TFSI) ₂ in PC (blue curve) as electrolytes and (b) corresponding <i>ex situ</i> X-ray diffraction patterns. The characteristic XRD pattern of TiS ₂ pristine electrode is also displayed for comparison. (reprinted from 71)	82
Figure V.1 –Capacity vs. potential profile of carbon coated NVP vs. Na cells at C/5, using different amounts of carbon used during the synthesis: 1g, 1.5g and 2g for samples denoted C-1, C-2 and C-3 for ~6.8 g of NVP respectively. Reprinted from 144.	99

Figure V.2 - a) DSC profile of NVP, reprinted from 75, b) comparison of X-ray diffraction patterns of α -NVP and β -NVP, and c) structures of α -NVP, β -NVP and γ -NVP.	100
Figure V.3 – a) Evolution of the characteristic peak (-111) of the α -NVP phase as a function of temperature and b) evolution of the patterns as a function of temperature while cooling (blue) and heating (red).....	102
Figure V.4 - a) Pattern number (10min increment in time) vs cell potential and b) associated X-ray surface plots ($\lambda = 0.826 \text{ \AA}$) of a Leriche cell cycled with NVP using NP30+FEC electrolyte at C/10 at room temperature at MSPD. Grey ticks represent the calculated x values in $\text{Na}_x\text{V}_2(\text{PO}_4)_3$. White, orange and purple bands represent the patterns on which the Na_3 , Na_2 and Na_1 phases are visible, respectively.	104
Figure V.5 – LeBail refinement of pattern N° 132 containing two phases: $\text{Na}_1\text{V}_2(\text{PO}_4)_3$ and $\text{Na}_2\text{V}_2(\text{PO}_4)_3$, the red dots correspond to the measured pattern, the black line the calculated pattern, the blue line the difference between the calculated and measured pattern. The pink ticks correspond to the $\text{Na}_2\text{V}_2(\text{PO}_4)_3$ phase while the green ones corresponds to the $\text{Na}_1\text{V}_2(\text{PO}_4)_3$ phase	105
Figure V.6 – a) Hexagonal cell mounted on the D8 Discover diffractometer and b) exploded view of the cell configuration used in that study	106
Figure V.7 – a) Pattern number (1h increment in time) vs cell potential, every red dot represents a pattern and b) associated X-ray surface plots ($\lambda = 0.709 \text{ \AA}$) taken while cycling a hexagonal cell loaded with NVP using NP30+FEC electrolyte at C/10 on a D8 discover diffractometer. Data is presented in Q (\AA^{-1}) and a conversion to degrees at $\lambda = 0.826 \text{ \AA}$ is provided on the upper axis. Grey ticks represent the calculated x values in $\text{Na}_x\text{V}_2(\text{PO}_4)_3$. White, orange and Purple bands represent the patterns on which the Na_3 , Na_2 and Na_1 phases are visible, respectively.....	107
Figure V.8 - X-ray diffraction patterns n°1, 17 and 20 of the cycling presented above. Black, red and blue ticks represent the positions of peaks corresponding to $\text{Na}_3\text{V}_2(\text{PO}_4)_3$, $\text{Na}_2\text{V}_2(\text{PO}_4)_3$, and $\text{Na}_1\text{V}_2(\text{PO}_4)_3$ respectively.	108
Figure V.9 – a) Pattern number (10min increment in time) vs cell potential and b) associated X-ray surface plots ($\lambda = 0.826 \text{ \AA}$) taken in an hexagonal cell cycled with NVP using NP30+FEC electrolyte at C/5 at room temperature at MSPD. Grey ticks represent the calculated x values in $\text{Na}_x\text{V}_2(\text{PO}_4)_3$. White, orange and purple bands represent the patterns on which the Na_3 , Na_2 and Na_1 phases are visible, respectively.	110
Figure V.10 - Patterns of NVP taken in cells stored at Low and High temperature, right out of the freezer/oven and after 2 hours, the asterisk represents the characteristic peak of the α -phase.....	112
Figure V.11 – a) Pattern number (5 min increment in time) vs cell potential and b) associated X-ray surface plots ($\lambda = 0.826 \text{ \AA}$) of a hexagonal cell cycled with NVP using NP30+FEC electrolyte at C/5 at 2°C. Grey ticks represent the calculated x values in $\text{Na}_x\text{V}_2(\text{PO}_4)_3$. White, orange and purple bands represent the patterns on which the Na_3 , Na_2 and Na_1 phases are visible, respectively.	113

Figure V.12 – a) Pattern number (5 min increment in time) vs cell potential and b) associated X-ray surface plots ($\lambda = 0.826 \text{ \AA}$) of a coin cell cycled with NVP using NP30+FEC electrolyte at C/10 at 45°C. Grey ticks represent the calculated x values $\text{Na}_x\text{V}_2(\text{PO}_4)_3$. White, orange and purple bands represent the patterns on which the Na_3 , Na_2 and Na_1 phases are visible, respectively. 114

Figure V.13 – a) Pattern number (5 min increment in time) vs cell potential and b) associated X-ray surface plots ($\lambda = 0.826 \text{ \AA}$) of a coin-cell cycled with NVP using NP30+FEC electrolyte at C/10 at 2°C. Grey ticks represent the calculated x values in $\text{Na}_x\text{V}_2(\text{PO}_4)_3$. White, orange, purple and red bands represent the patterns on which the Na_3 , Na_2 , Na_1 and unknown phases are visible, respectively. ... 115

Figure V.14 — a) Pattern number (10min increment in time) vs cell potential and b) associated X-ray surface plots ($\lambda = 0.826 \text{ \AA}$) of a Leriche cell cycled with NVP using NP30+FEC electrolyte at C/7 at room temperature at MSPD Grey ticks represent the calculated x values in $\text{Na}_x\text{V}_2(\text{PO}_4)_3$. White and orange bands represent the patterns on which the Na_3 and Na_2 phases are visible, respectively. 116

Figure V.15 – a) Pattern number (10 min increment in time) vs cell potential and b) associated X-ray surface plots ($\lambda = 0.826 \text{ \AA}$) of a Leriche cell cycled with NVP using NP30+FEC electrolyte at C/7 (15 min OCV every hour) at 2°C. Grey ticks represent the calculated x values in $\text{Na}_x\text{V}_2(\text{PO}_4)_3$. White, orange and purple bands represent the patterns on which the Na_3 , Na_2 and Na_1 phases are visible, respectively. 117

Figure V.16 - Patterns collected in oxidation of a hexagonal, coin and Leriche cell at 2°C, one pattern every hour and last pattern collected in reduction, if any, (blue) 118

Figure V.17 - Summary of electrochemical behavior of all cells discussed in this chapter, cell potential vs the calculated x value in $\text{Na}_x\text{V}_2(\text{PO}_4)_3$ 121

Figure V.18 - Summary of all surface plots presented in this chapter corresponding to the electrochemical curves presented before. Most pattern are measured at $\lambda = 0.826 \text{ \AA}$ except for the first one that was measured at $\lambda = 0.709 \text{ \AA}$. White, orange and purple stripes typically represent the domains of existence of the Na_3 , Na_2 and Na_1 phases respectively. 122

List of tables

Table I.1 - Main breakthroughs in battery research; inventors, chemistries and voltages of batteries through history.....	20
Table I.2 - Properties of various cathode materials used in commercial lithium ion batteries at the present time and the advantages, disadvantages. Reprinted from ref 38	25
Table IV.1 - Summary of the lattice parameters for the phases studied in this chapter	82
Table IV.2 - Summary of the values at which the 001 peaks of Phases 1 and 3 appear during the cycling of an AC//TiS ₂ Leriche cell using 0.3 M Ca(TFSI) ₂ in PC as electrolyte at C/75 rate and 60°C ...	89
Table V.1 – Unit cell parameters of α-NVP (as reported in ref 75) and β-NVP in monoclinic and rhombohedral structure (as reported in 145).....	101
Table V.2 – Lattice parameters and main peaks corresponding to the different phases observed ...	105
Table V.3 - Results of the refinements for the different phases found in the cycling of NVP	110
Table 4 - Summary of all cells made during this chapter and of the observations made	119

I. Introduction

I.1. General context

The depletion of fossil fuels has become a topic of common interest for our modern society. Non-governmental organization (NGO) such as Global Footprint Network established the Earth Overshoot Day (EOD), that is: the calendar date on which humanity’s consumption for the year exceeds Earth’s capacity to regenerate those resources.¹ Although the calculation method is debated², the (EOD) is regarded by the general public as a powerful environmental index. Besides 2020, that day was gradually reached earlier in the past few years as shown in [figure 1](#) — 8 months separate the 90’s and 2020’s.

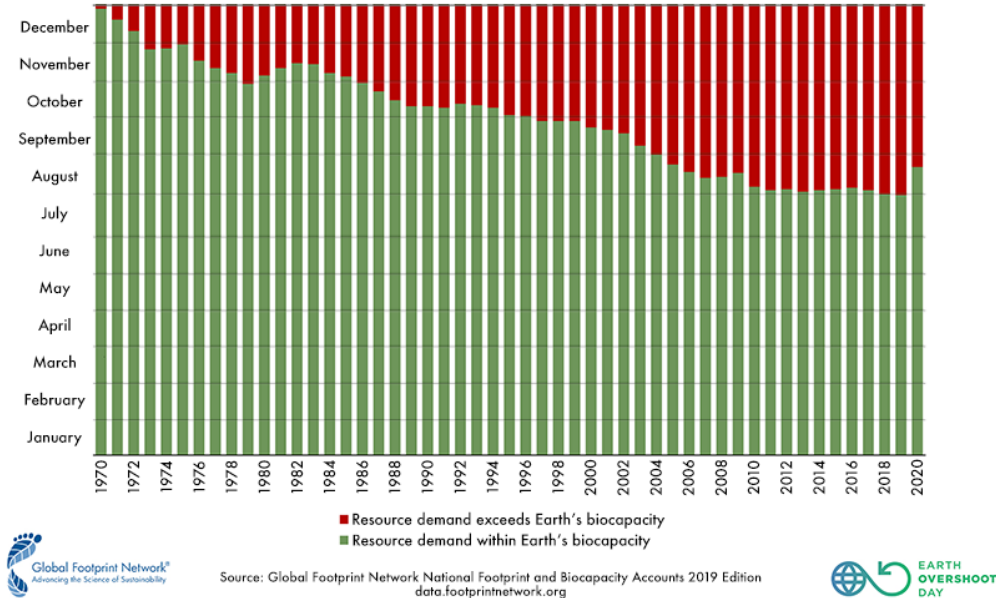


Figure I.1 - Earth Overshoot Days (EOD) between 1970-2020, reprinted from overshootday.org¹

Indeed, the world population, and both resource and energy consumption increased exponentially since the 1950’s and the latter eventually reached 158 839 TWh in 2019.³ As a side effect, harmful production of greenhouse gases (GHG) increased in the last decades ([fig I.2a](#))⁴ impacting negatively the environment. To cope with this issue, several climate agreements were held in Copenhagen, Nagoya, and Paris (resp. 2009, 2010, and 2015) to attempt minimizing these climate changes. In 2018, the energy sector was responsible of nearly half of GHG emissions,⁵ while 87% of the energy production results from the exploitation of polluting fossil fuels — coal, oil, natural gases,³ ([fig I.2b](#)). On another side, nuclear power also relies on non-renewable resources and generates hardly-disposable wastes. It suffers a popular movement against it, especially after Chernobyl and Fukushima incidents, which led some countries in Europe to plan a phase out nuclear power. Because of the pollution generated and the limited availability of the raw materials, these energy sources are meant to be replaced by greener ones.

While hydroelectric (dam, tidal power station) power is a green alternative, their infrastructures damage the ecosystem and lands. Instead, solar and wind energy seem the most promising renewable energy sources, while being economically viable. Solar panel's energy payback time being comprised between 1 and 1.5 year,⁶ and wind turbines have one of the lowest global warming potential per unit of electrical energy generated.⁷ However, wind and solar energies are intermittent and need external storages during production peaks to be able to release energy when needed. For this grid storage application, lithium-ion (LIB) battery is nowadays a technology of choice for its high energy capacity and efficiency.

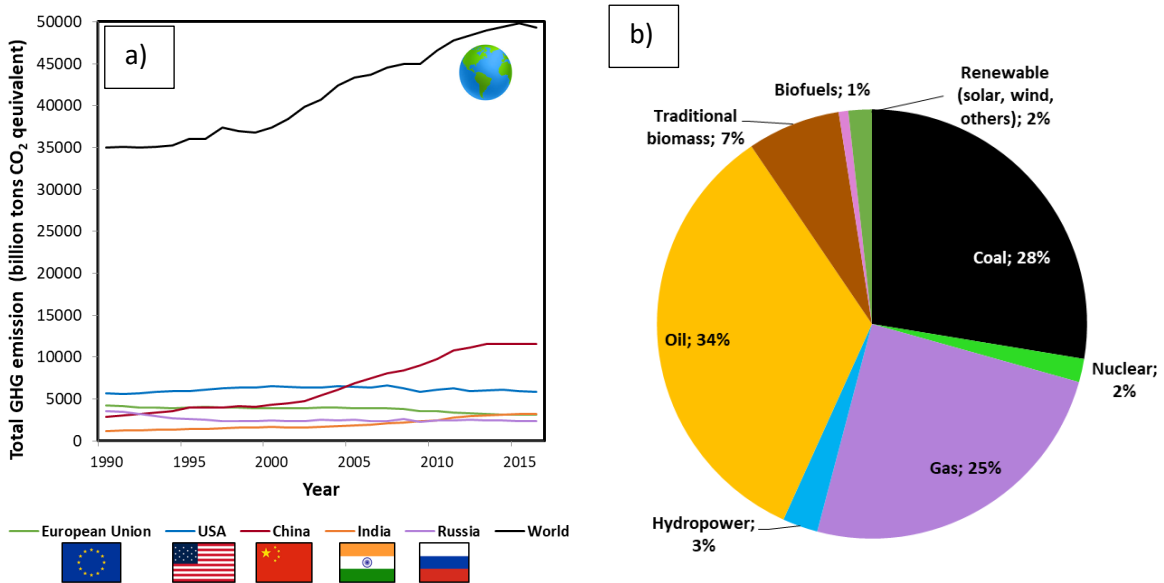


Figure I.2 - a) Greenhouse gases emission per region and per year⁴; b) Global primary energy per source in 2019³

First commercialized by Sony Energytech in the early 90's, Li-ion battery quickly became the technology of choice to power electronic devices such as phones, laptops or video game consoles, and even the Mars rover *Perseverance* or, since 2015, the ISS space-station. Due to its light weight and electrochemical performance, it outperformed well-established technologies such as nickel-cadmium or nickel metal hydride batteries. More recently, Li-ion batteries came to be the technology of choice to power hybrid or electric vehicles because of these advantages. In 2019, the Nobel Prize was awarded to Stan Whittingham, John B. Goodenough and Akira Yoshino for their contribution in the development of LIB, opening a door to "a fossil fuel-free world".⁸ Global Li-ion battery market size represented 44.2 billion USD in 2019 and is expected to grow up to 94.4 billion USD by 2025.⁹

A 70kWh Tesla Model S battery contains 10kg of lithium¹⁰ (corresponding to 53 kg of raw lithium carbonate) while the global lithium production in 2019 was approximated to 77,000 tons.¹¹ The latter would result in less than 6.5 million electric cars a year, which is far from the 74.9 million gas cars sold worldwide in 2019.¹² Moreover, this rough estimation does not take into account that a part of the lithium is needed for electronic devices, grid storage or applications in other industries. If the market of electric vehicles continues to grow, the limited availability of raw materials (lithium, cobalt used in some common positive electrode materials) will quickly become an issue. In 2016, the World Economic Forum of Davos ranked *Next generation batteries* as the #2 game-changing technologies, being a cornerstone in the fourth industrial revolution.¹³ To that extent, new materials need to be

designed and tested to get these new generation batteries to their full potential. New battery chemistries based on more abundant elements such as sodium and calcium for instance are being developed, these elements being respectively the sixth and fifth most abundant ones on the Earth's crust.¹⁴

I.2. Batteries

I.2.1. Principle

A battery is a device that converts chemical energy into electrical energy and *vice-versa*. It is composed of one or several electrochemical cells that can be assembled together – in series or in parallel - to obtain a desired voltage and intensity. An electrochemical cell is typically composed of two electrodes that undergo reduction/oxidation (redox) reactions which are separated by an ion conducting but electronically insulating medium, the electrolyte. The latter is typically a liquid (salt dissolved in solvent), but solid (polymers, ceramics), or gel concepts do also exist. Gel electrolytes are more practical for commercialization since the risk of leaking is inferior to liquid electrolytes, while All Solid State batteries are not commercialized yet but the research is particularly active on that field. (see [section I.2.5.](#))

The potential difference between the electrodes determines the theoretical cell voltage E_{cell} , which is related to the Gibbs free energy:

$$\Delta G_0 = n \cdot F \cdot E_{cell}$$

Where n is the number of electrons involved in the reaction, F the Faraday constant and E_{cell} the potential of the cell at open circuit given by $E_{cell} = E_{Positive\ electrode} - E_{Negative\ electrode}$.

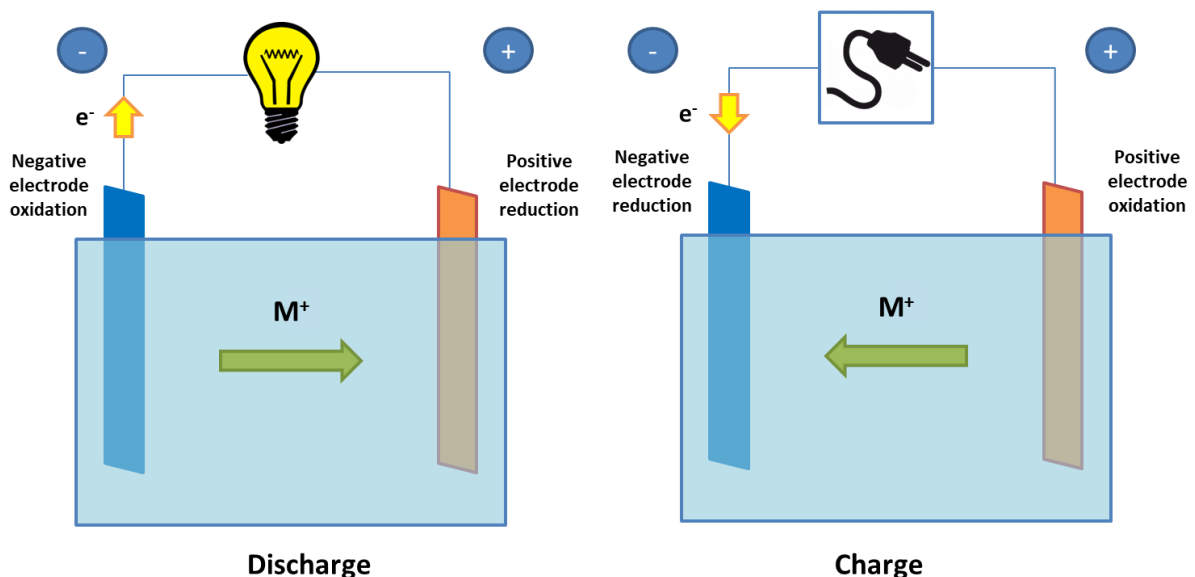


Figure I.3 - Schematic representation of a battery during charge and discharge

During battery discharge (thermodynamically spontaneous reaction), the negative electrode gives electrons to the external circuit and is oxidized (anode) while the positive electrode accepts electrons

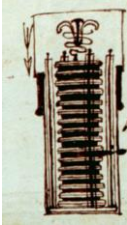
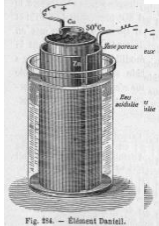


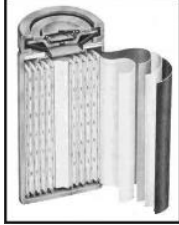
from the external circuit and is reduced (cathode). The reverse processes take place upon battery recharge.

I.2.2. From Volta's pile to the alkaline battery

When Galvani discovered in 1786 what he called "*animal electricity*", Alessandro Volta had the intuition that the effect observed did not have an animal origin but rather had something to do with the metals used by Galvani in the experiments. To prove his theory, he assembled a pile of metallic disks, alternating zinc and copper, separated by felt soaked in brine and was able to generate an electric current. By doing so, Volta created the first battery in 1800, exploiting the oxidation of zinc and the reduction of brine, which potential was 0.76 V.¹⁵ However, the felt tended to dry and prevent the battery's good functioning. Therefore, the design was improved, especially by William Cruickshank with the Trough battery. Later in 1836, John Frederic Daniell created a cell composed of two compartments containing two different solutions: CuSO_4 and ZnSO_4 able to deliver 1.10V. In 1854, Wilhelm Josef Sinsteden¹⁶ created the first lead-acid battery, which was not rechargeable yet but was able to achieve 2.5 V. Gaston Planté took over Sinsteden's work and managed to recharge the lead-acid battery in 1859, which was a cornerstone in battery development. In 1880, Faure invented a method of coating lead plates, increasing the "active mass" and significantly improving the battery capacity. Its "pasted electrode" allowed an easier use and the commercialization of the accumulator.

In 1866, Georges Leclanché designed a primary (*i.e.* non rechargeable) battery with a zinc negative electrode, a positive electrode consisting of manganese dioxide mixed with carbon and an aqueous electrolyte consisting of a mixture of zinc chloride and ammonium chloride. The substitution of this electrolyte by an alkaline one, exhibiting higher ionic conductivity, was a turning point in the development. Indeed, using this electrolyte, new battery rechargeable technologies were developed, such as Ni/Cd and Ni/Fe, developed by Waldemar Jungner in 1899 and Thomas Edison in 1901, both using nickel hydroxide as positive electrodes. These technologies were the precursors of the nickel metal hydride (NiMH) technology, commercialized from 1989, which avoided the use of toxic cadmium. Although it is still widely used in non-plug-in electric vehicles, its market share has been decreasing in the last 20 years because of the emergence of LIB which took over the application in portable electronics.¹⁷ [Table I.1](#) summarizes the main advances in battery research described above.

Table I.1 - Main breakthroughs in battery research; inventors, chemistries and voltages of batteries through history

Inventor	Year	Chemistry	Voltage (V)	
Volta	1800	Zn-O ₂	0,76	
Daniell	1836	Cu-Zn	1,1	 <small>Fig. 214. — Element Daniell.</small>
Planté	1859	Lead-Acid	2,5	
Leclanché	1866	Zn-MnO ₂	1,4	
Jungner/Edison	1899/1901	Ni-Cd	1,2	

I.2.3. Lithium and lithium-ion batteries

Lithium was early identified as an interesting negative electrode material due to its low density and its low reduction potential (-3.05 V vs standard hydrogen electrode (SHE)),¹⁸ determined by G.N. Lewis in 1913.¹⁹ However, its high reactivity to oxygen and water made its handling tedious and impossible the use of aqueous electrolytes. Thus, its electrochemistry could not be well developed until the 1960-70's when organic solvents were already widely available. William S. Harris in 1958²⁰ in his PhD thesis was the first to study lithium electrodeposition using several lithium salts (LiCl, LiBr) and cyclic esters as electrolyte solvents, including ethylene and propylene carbonate (EC and PC respectively), which are still commonly used in batteries today. The first lithium batteries developed were primary. The lithium-iodine battery, first commercialized in 1972 by the Catalyst Research Corporation^{21,22} used a solid electrolyte and was commercialized to replace zinc-mercury oxides batteries in pacemakers which suffered from their short lifetime and unreliability, and other concepts using liquid electrolytes were developed also at this time.

In parallel, efforts to develop rechargeable lithium based battery focused in finding an adequate positive electrode. Intercalation chemistry, which had been intensively developed by that time, offered a very suitable playground. Lithium intercalation in titanium disulfide (TiS₂) by Walter Rüdorff in 1965²³ and further studied by Rouxel in 1973²⁴ was particularly interesting and inspired further studies by Stan Whittingham²⁵ working at Exxon and led to the fabrication of a solar clock demonstrator powered by this battery and even a 45Wh cell size prototyped by Exxon in 1977. [Figure I.4](#) shows a representation of this battery and the commercial battery in use. These cells were using either lithium metal or a lithium aluminium alloy as negative electrode, dioxolane as electrolyte solvent and LiClO₄ as electrolyte salt, being later replaced by LiB(CH₃)₄ for safety reasons.

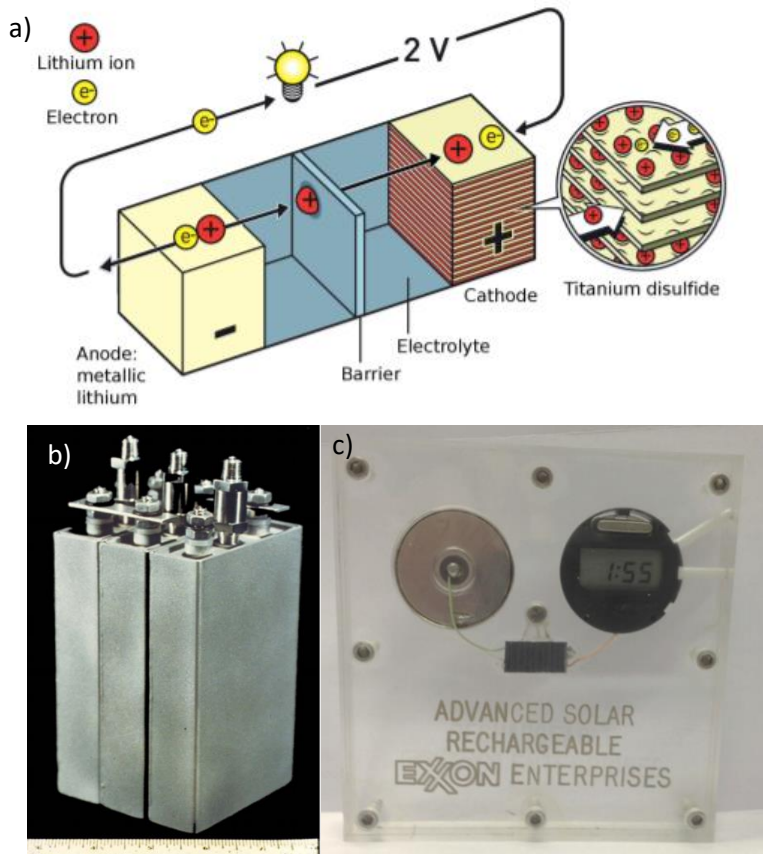


Figure I.4 – a) Schematic representation of a Li/TiS₂ battery (reprinted from ref 8), b) An Exxon LiTiS₂ rechargeable lithium battery exhibited at the Chicago electric vehicle show in 1977 (reprinted from ref 26, and c) solar clock with rechargeable Li/TiS₂ battery built by Exxon (reprinted from ref 27)

Another breakthrough came in 1979 when John B. Goodenough synthesized LiCoO₂ (LCO)^{28,29} which adopts an analogous crystal structure as TiS₂ but already contains lithium in its structure, which will become relevant later on. Moreover, this material has the advantage of exhibiting a much higher potential (4V) as a result of the higher electronegativity of oxygen when compared to sulfur (fig. I.5) Goodenough assembled a battery with this new material using LiBF₄ in propylene carbonate as electrolyte.

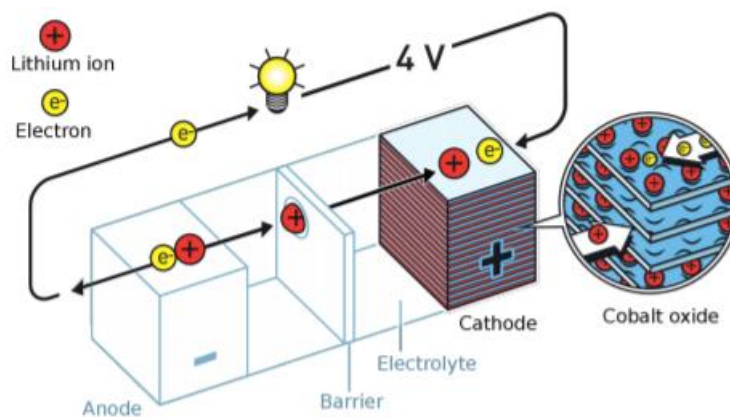


Figure I.5 - Schematic representation of a Li/CoO₂ battery (reprinted from ref 8)

On the negative electrode side, lithium electrodeposits upon battery recharge were shown to have a tendency to dendritic growth. Dendrites may pierce through the separator and contact both electrodes, creating a short circuit and eventually a thermal runaway and explosion. Two approaches were investigated to solve this issue: choosing an electrolyte allowing a smoother lithium deposition on the anode, or replacing metallic lithium by another material. Following the former approach, Michel Armand and his coworkers developed in 1978 a solvent-free polymer battery using lithium triflate and polyethyleneoxide.³⁰ Alternatively the originally so-called *lithium rocking chair battery* and currently termed Li-ion technology was developed, which avoids the use of lithium metal at the negative electrode. Already in 1938, Rüdorff demonstrated that hydrogen sulfate ion could migrate electrochemically between two graphite electrodes.³¹ Graphite was an attractive material that, despite a higher potential than lithium (thus giving a lower cell voltage) could accommodate up to six lithium ions per carbon atoms. Yet, solvent cointercalation led ultimately to graphite exfoliation. Akira Yoshino and his group, working for Asahi Kasei, identified heat-treated petroleum coke as a stable electrode that reversibly intercalate lithium ion electrochemically. Using Goodenough's LCO and a lithium salt in propylene carbonate electrolyte,^{32,33} as presented in figure I.6, he demonstrated that petroleum coke could be used as an anode for batteries. That battery had a 4.1V voltage and an energy density of ~80 Wh/kg. In parallel new research on electrolytes proved that adjusting their composition to include the presence of ethylene carbonate led to the formation of a passivating layer formed from insoluble solvent reduction products (solid electrolyte interphase (SEI) enabling lithium transport) and avoid cointercalation of the solvent in graphite.³⁴ Using graphite resulted in a slightly higher voltage (4.2V). Thus, LIB as we know it was born and began to be commercialized in the 90's by Sony.³⁵

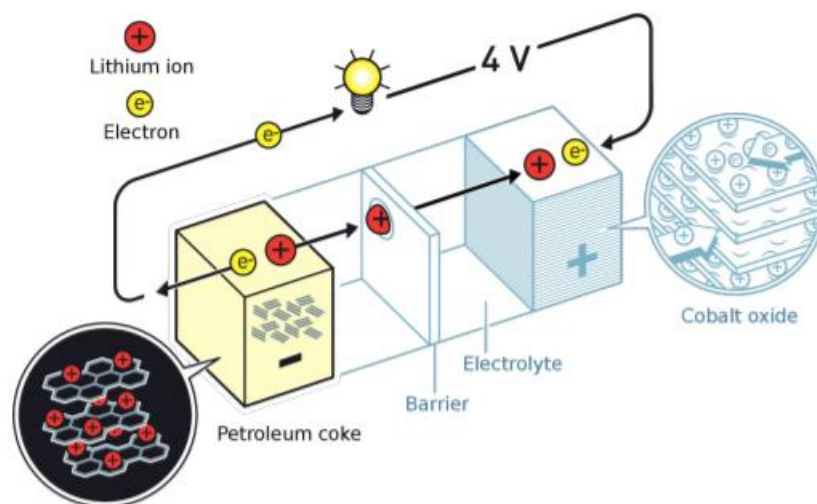


Figure I.6 - Schematic representation of a Li-ion battery, using petroleum coke vs LiCoO_2 (reprinted from ref 8)

I.2.4. Improvements in Li-ion technologies

After the above discussed breakthroughs, other new positive electrode materials were intensively studied, with a strong contribution by Goodenough's group, involving for instance LiMn_2O_4 ³⁶ (LMO) or LiFePO_4 (LFP)³⁷ which have both reached practical application in commercial cells. An alternative research pathway focused on substituting the cobalt in LCO for sustainability and cost reasons, while at the same time enhancing the electrochemical capacity. This led to the development of lithium nickel manganese cobalt oxides (NMC)³⁸ with the general chemical formula $\text{LiNi}_x\text{Mn}_y\text{Co}_{1-x-y}\text{O}_2$ (where $x+y+z=1$). The subscripts denoting the atomic ratios are used to abbreviate the formula: 532, 442 or 811 (except for the initially investigated $x = y = 1/3$ which is commonly referred as either 111 or 333). Currently, both 111 and 532 are commonly used in commercial cells.³⁹ Alternatively, lithium nickel cobalt aluminum oxides (NCA) with the general chemical formula $\text{LiNi}_x\text{Co}_y\text{Al}_z\text{O}_2$ (where $x+y+z=1$)³⁹ were also developed, with improved thermal stability, $\text{LiNi}_{0.8}\text{Co}_{0.15}\text{Al}_{0.05}$ being the most optimized composition used commercially. These materials widely apply in batteries for electric vehicles. For example Tesla uses NCA containing batteries in its model X, while the BMW i3 are equipped with NMC batteries. The properties of the different positive electrodes currently used in commercial batteries are summarized in [Table I.2](#).

Table I.2 - Properties of various cathode materials used in commercial lithium ion batteries at the present time and the advantages, disadvantages. Reprinted from ref 39

Cathode material	Midpoint voltage vs Li (C/20)	Specific Capacity (Ah/kg)	Advantages	Disadvantages	Applications
LCO	3.9	155	In common use, good cycle life, good energy	Moderate charged state thermal stability,	Mainly smaller portable electronics (3C)
LMO	4.0	100-120	Very good thermal stability, inexpensive, very good power capability	Moderate cycle life, lower energy	Higher power applications such as power tools and electric motive power
NCA	3.7	180	Very good energy, good power capability, good cycle life	Moderate charged state thermal stability, sensitive to moisture even in discharged state	Excellent for motive power and premium electronic applications
NMC	3.8	160	Very good combination of properties (energy, power, cycle life and thermal stability)	Patent issues	Both portable and high power applications including power tools and electric vehicles
LFP	3.4	160	Very good thermal stability and cycle life, good power capability	Lower energy, special preparation conditions	Mainly used in high power such as power tools and energy storage applications, patent issues

I.2.5. Other lithium based concepts

The discovery of new types of highly lithium-ion conducting solid electrolytes sparked interest for All Solid-State batteries (ASS) which would present significant advantages in terms of safety, since avoiding organic solvents eliminates the risks of electrolyte leakage and thermal runaway. Oxide-, polymer-, sulfur- and phosphate-based electrolytes have been developed such as LLZO ($\text{Li}_7\text{La}_3\text{Zr}_2\text{O}_{12}$),³⁸ LGPS ($\text{Li}_{10}\text{GeP}_2\text{S}_{12}$) or Argyrodite (Ag_8GeS_6).⁴⁰ In terms of performance, this concept makes possible the use of lithium metal as negative electrode, which would enable very high energy densities. Still, dendritic growth is not yet fully solved and the concept still not commercialized despite several press release announcements.^{40,41}

Other battery concepts involving metallic Li which have been the focus of intensive research are lithium-sulfur (Li-S) and lithium-air batteries (Li-O₂).⁴² The former was investigated since the 1940's while the concept for the latter was proposed in the late 1990's.⁴³ The Li-S battery relies on the reduction of sulfur at the positive electrode to finally yield Li₂S. Yet, this reaction involves the formation of soluble lithium polysulfides (Li_2S_x , $6 \leq x \leq 8$) as intermediates, which can then migrate and react at the negative electrode ("shuttle effect"). This results in low coulombic efficiency, self-

discharge⁴⁴ and short cycle life.⁴⁵ Diverse strategies have been used to attempt solving this issue⁴² and some start-up companies such as Sion Power (US — sionpower.com) or OXIS Energy (Great Britain — oxisenergy.com) started to fabricate them. On the other hand, Li-O₂ relies on the catalytic reduction of O₂ at the positive electrode. The products formed depend on the nature of the electrolyte. In the case of aqueous electrolytes, LiOH is formed and the lithium surface should be properly protected with an ion conductive layer.⁴⁶ In organic electrolytes, despite Li₂O could ultimately be achieved, Li₂O₂ is most commonly formed. The main challenges for the latter are related to the strong reactivity of the electrolyte with the species formed during the catalytic reduction of O₂. Although the stability of the ethers is higher than that of alkyl carbonate solvents, studies showed that only 60% of the O₂ can be reversibly converted.⁴² Despite the recent progresses achieved, these batteries are still far from commercialization.

I.2.6. Next generation batteries

To address the concerns related of a future limited supply in raw materials (*i.e.* Li, Co, natural graphite), new chemistries using different electroactive ions than lithium are developed. The research aims to use more abundant elements such as sodium, calcium, magnesium or aluminum for example. Because of its similarities with lithium, sodium seems to be the easiest alternative to implement. However, since the other ions (Ca²⁺, Mg²⁺ and Al³⁺) carry multiple charges, taming them for the purpose of electrochemical storage would require a major breakthrough. Next generation batteries aim to provide high energy density, longer service life, low cost and versatility. Their level of technological development is only high for the case of sodium, with multivalent concepts still needing to overcome bottlenecks at a fundamental scale.⁴⁷ The state of the art for sodium-ion and calcium based batteries is described in more detail below, as they are more relevant to the research carried out in the framework of this PhD.

I.2.6.1. Sodium-ion batteries

Development of sodium intercalation compounds was carried out side-by-side with that of their lithium counterparts. Commercialization of Li-ion-batteries eclipsed the prospects of developing analogous sodium-ion batteries (SIBs) in the 90's despite proof of concept was already achieved.^{48,49} The booming demand in energy storage renewed interest in SIB. Indeed, sodium is the sixth most abundant element on Earth crust,¹⁴ and has an inexpensive and non-energy-intensive extraction process.⁵⁰ For both SIBs and LIBs, capacity and voltage is determined by electrode materials and there is no reason why comparable performance cannot be *a priori* expected. Indeed, the main difference is related to the slightly lower standard redox potential of lithium when compared to sodium, which sets the lowest potential operation limit on the negative side. A relevant advantage for SIBs is that, contrary to lithium, sodium does not electrochemically form alloys with aluminum. Hence aluminum current collectors can be used on the negative side, cheaper and lighter than copper used in Li-ion batteries. Beyond the obvious chemical similarities between Li and Na which could grant fast progress for SIB, relevant differences must be taken into account as well. The larger radius of the sodium ion and hence the different coordination topology needs to be taken into account when considering intercalation compounds as electrode materials. Layered compounds such as Na_xCoO₂ and Na_xMnO₂, similar to those used in Li, were already studied back in the 1970's^{51,52} and

still heavily investigated today. A turning point of sodium intercalation compounds was the study of Na Super Ionic Conductors (NASICON) polyanionic compounds, with a structure consisting of a combination of XO_4 tetrahedra ($X = P, S$) and MO_6 octahedra ($M =$ transition metal). These polyhedra are arranged in so-called lantern unit cells (Fig. I.7) and allow the formation of frameworks with low-energy Na^+ migration pathways. Amongst the phosphate NASICONs, $Na_3V_2(PO_4)_3$ (NVP) exhibits high energy density, ~ 400 Wh/kg, and thermal stability in the oxidized state.⁵³ The synthesis of alternative polyanionic fluorine-containing electrode materials enabled to increase the operating voltage of the Na cells, $Na_3V_2(PO_4)_2F_3$ (NVPF) being the current state-of-the-art for positive electrode compound. It is important to note that for both NVP and NVPF, two sodium ions are reversibly (de-)inserted during the oxidation/reduction process, resulting in $NaV_2(PO_4)_3$ ⁵⁴ and $NaV_2(PO_4)_2F_3$ ⁵⁵ at the end of the oxidation.

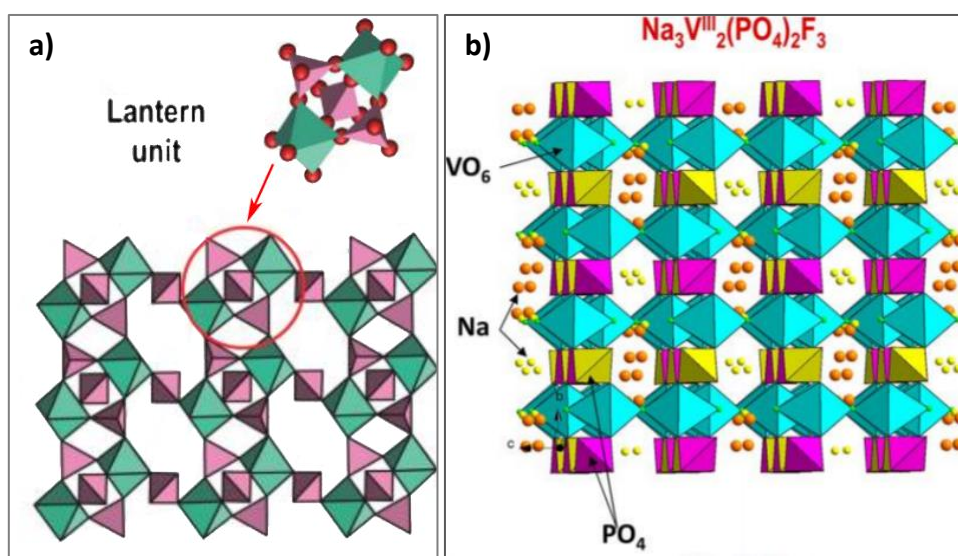


Figure I.7 – a) Structure of a NASICON compound and its lantern-like unit cell, b) structure of $Na_3V_2(PO_4)_2F_3$, both reprinted from 56

On the negative electrode side, the growth of dendrites during repeated sodium metal plating/stripping prevents its safe use as negative electrode, similarly to what happens for the case of lithium metal. However, and in contrast to lithium, graphite does not allow reversible sodium intercalation^{57,58} (unless solvated to form ternary intercalation compounds),⁵⁹ and hence is not a suitable negative electrode. Other types of non-graphitic carbonaceous materials can be used instead, in which amorphous areas embedding and partially crosslinking more graphitic segments (graphene layers), such as hard carbons⁶⁰ which can exhibit capacities higher than 300 mA.h/g⁶¹ at a low redox potential⁵⁸ making it suitable for a negative electrode.

Alternatively, metal alloys or oxides have also been studied, $Na_2Ti_3O_7$ being remarkable by its low operation potential (*ca.* 0.3 V vs. Na^+/Na). Electrolytes for SIBs are usually similar to those of LIBs, and consist of sodium salts ($NaClO_4$, $NaPF_6$, $NaCF_3SO_3$, NaFSI, NaTFSI, or $NaBF_4$) dissolved in organic solvents (EC, PC, dimethyl carbonate (DMC)) which can exhibit a wide potential operation window.⁶² Today, Tiamat (France – tiamat-energy.com) and Faradion (Great-Britain – faradion.co.uk) fabricate SIBs in Europe using hard carbon negative electrodes and polyanionic and layered positive electrode materials respectively.

I.2.6.2. Calcium based batteries

Metallic negative electrodes enable high energy density batteries (Fig. I.8) but, as discussed above, both lithium and sodium come with issues related to dendritic growth. Moreover, sodium has a low melting point (98°C) which could also be of concern in terms of safety. Batteries based on alternative metals such as calcium (Ca) and magnesium (Mg) are appealing for their low cost and abundance of raw materials (calcium and magnesium are respectively the fifth and eighth most abundant elements on Earth's crust).¹⁴ Moreover, Ca and Mg would also benefit from their low standard reduction potential (-2.87 V and -2.37 V vs. SHE respectively) and their divalent character. Indeed, for each mol of ion (de-)inserted, two mol of electrons are exchanged which gives them a theoretical advantage in terms of specific capacity.

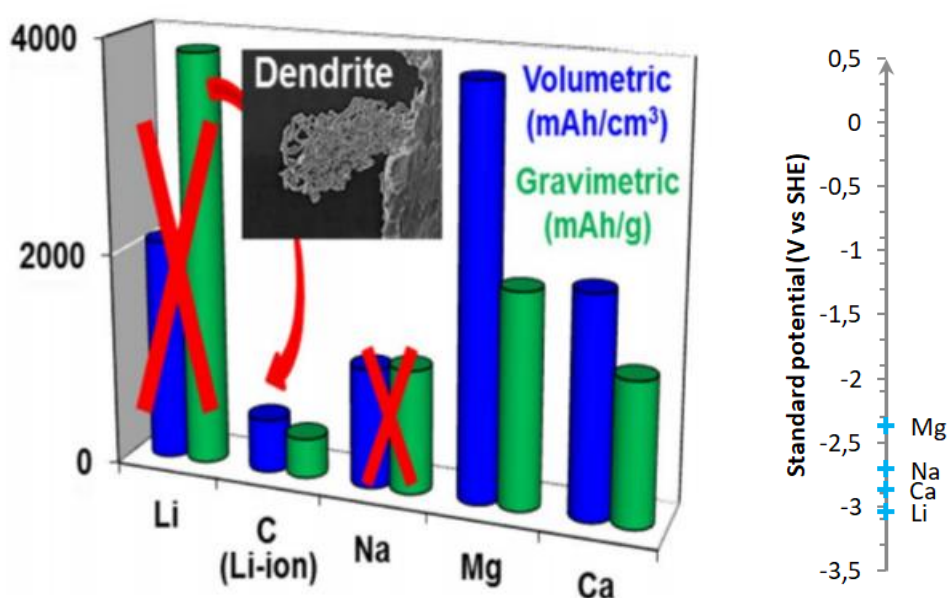


Figure I.8 – Standard reduction potential and theoretical gravimetric and volumetric capacities for different metal electrodes. Values for graphite used in Li-ion cells are given for comparison (reprinted from ref 63)

The key to the practical use of such metals as negative electrodes is finding adequate electrolytes that allow their reversible plating/stripping. In the case of calcium, a preliminary study by Aurbach⁶⁴ proved that electrodeposition was not possible when using the conventional organic solvents commonly used in the battery field. This hindered further research on the topic, at the exception of the study of Amatucci on inorganic compounds as host material for polyvalent cation in 2001⁶⁵ which used activated carbon as the negative electrode instead. It is only recently that studies reporting electrolytes enabling reversible plating/stripping on metallic calcium have appeared. In 2016, Ponrouch *et al.* used $\text{Ca}(\text{BF}_4)_2$ in EC:PC at 100°C⁶⁶ while Bruce and co-workers in 2017 managed to reversibly plate/stripe calcium at room temperature using $\text{Ca}(\text{BH}_4)_2$ in tetrahydrofuran (THF). The latter enabled higher coulombic efficiency despite narrower stability at high potentials.⁶⁷ In 2019, two papers issued independently by Nazar⁶⁸ and Fichtner⁶⁹ reported the use of $\text{Ca}[\text{B}(\text{hfp})_4]_2$ in DME (dimethoxy ethane) at room temperature. It is also worth noting that pretreatment of the calcium electrode could allow reversible plating/stripping with other electrolytes.⁷⁰

Research aiming at finding suitable positive electrodes has also been blooming in recent years. Yet, this is far from being an easy task as reversible intercalation of multivalent ions in inorganic hosts is hampered by coulombic interactions hindering migration within the electrode. In addition to that, ion pairing in the electrolyte, also enhanced for divalent ions, induces larger desolvation energies which further penalize calcium intercalation. Computational studies (e.g. density-functional theory – DFT) are a key tool to explore several possible cathode materials, from structures of already reported compounds to virtual materials that could be stable but have yet to be synthesized. The experimental elucidation of real reactivity is complex, as side reactions involving the electrolyte may interfere and thus, complementary characterization techniques coupled to electrochemistry are compulsory. Reversible intercalation and de-intercalation of calcium has been proved for instance in TiS_2 ,^{71,72} despite calcium is cointercalated with solvent molecules. Further operando X-ray diffraction studies on this system have been carried out in the framework of this PhD.

I.3. Aim and context of the thesis

This thesis is the result of the collaboration between CELLS-ALBA synchrotron and the Institute of Material Science of Barcelona (ICMAB-CSIC) which aim is to develop and test solutions for *in situ* and *operando* diffraction at non-ambient temperature conditions. Indeed, *in situ* and *operando* diffraction studies on batteries were very early identified as a precious tool to get a mechanistic understanding of the ion intercalation in the host structure. Using *in situ* cells avoid the drawbacks imposed by *ex situ* studies related to the preparation of samples in different redox stages, which also involves some risk of the electroactive phase being altered during handling (evolution of metastable phases, contamination by air or humidity, etc.). Moreover, *operando* experiments enable an extension of studies to grasp the influence of the testing protocol (rate, temperature, etc.). After the first study performed by Chianelli in 1978,⁷³ several types of *in situ* cells were developed with different geometries and windows, and to adapt the experimental conditions. While they can be used in laboratory diffraction setups, they reveal their best potential in synchrotrons, where time and angle resolution allow better quality snapshots. To the best of our knowledge, and despite being relevant for studying systems with slow kinetics or for ageing studies, no *operando in situ* cells for data collection in non-ambient temperature conditions were available commercially at the beginning of this thesis.

Within this scenario, CELLS-ALBA's engineering team worked on the development of solutions based on both a modification of Leriche cell⁷⁴ and a thermalized holder for coin cell.⁷⁵ Moreover, a new prototype was designed in Laboratoire de Réactivité et Chimie des Solides (LRCS – Amiens, France) to fit better the needs of laboratory diffractometer. An example of use of the cells developed consisted in the study of Ca insertion in TiS_2 at high temperature. As preparatory work, room temperature studies using Li//TiS_2 cells were performed, using different electrolytes salts and solvents, which gave a better comprehension of the cointercalation phenomenon. Ultimately, Ca//TiS_2 cells were thermalized using the modified Leriche prototype and charged/discharged. Because the reaction kinetics related to plating/stripping on the metallic Ca is slow, additional data were collected at room temperature using activated carbon as the negative electrode.

Another study using all the thermalized setup was carried out on a sodium positive electrode material. Thanks to the mobility period included in the DOC-FAM COFUND program funding this PhD, The opportunity to spend one month at LRCS arose to test such cells on a laboratory setup as well. A study of NVP was hence performed at ambient temperature using both synchrotron and laboratory X-rays, and at non-ambient temperature (from -2°C to 40°C) in synchrotron. NVP crystallizes in different phases depending on the temperature⁷⁶ and because one of the phase transitions is close to room temperature, the thermalization allowed isolating each phase. This study also allowed the observation of the intermediary phase $\text{Na}_2\text{V}_2(\text{PO}_4)_3$ ⁷⁷ during the charge/discharge cycles.

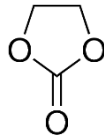
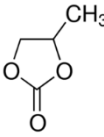
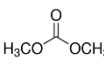
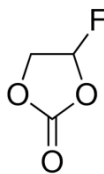
II. Experimental techniques

II.1. Chemical and electrochemical characterization

II.1.1. Electrolyte preparation

Different electrolytes were used in the course of this PhD. These were prepared inside an argon-filled glove box by dissolving the corresponding salts in the chosen organic solvents (see Table II.1).

Table II.1 – Electrolytes salts and solvents used in the thesis

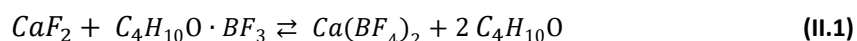
	Compound	Chemical formula	Supplier	Purity
Salts	Lithium hexafluorophosphate	LiPF_6	Alfa Aesar	98%
	Lithium tetrafluoroborate	LiBF_4	Alfa Aesar	99.87%
	Lithium bis-oxalatoborate	LiBOB	Chemetall	99,99%
	Lithium bis(trifluoromethanesulfonyl)imide	LiTFSI	Sigma-Aldrich	$\geq 99\%$
	Sodium hexafluorophosphate	NaPF_6	Strem Chemicals	99%
	Calcium bis(trifluoromethanesulfonyl)imide	$\text{Ca}(\text{TFSI})_2$	Solvionic	99.5%
	Solvents	Ethylene carbonate (EC)		Sigma-Aldrich
Propylene carbonate (PC)			Sigma-Aldrich	Anhydrous, 99.7%
Dimethyl carbonate (DMC)			Sigma-Aldrich	Anhydrous, $\geq 99\%$
Fluoroethylene carbonate (FEC)			Sigma-Aldrich	99%

In addition to those, a commercial 1M solution of lithium hexafluorophosphate (LiPF_6) in ethylene carbonate (EC):dimethyl carbonate (DMC) (1:1, battery grade) supplied by Sigma-Aldrich, commonly named LP30, was also used. 0.67M LiPF_6 in EC:DMC: propylene carbonate (PC) at a volumetric ratio of 33:33:33 was prepared by adding PC to the commercial LP30.

Electrolytes containing $\text{Ca}(\text{BF}_4)_2$ were either prepared with commercial $\text{Ca}(\text{BF}_4)_2 \cdot x\text{H}_2\text{O}$ salt (Alfa Aesar) or with synthesized $\text{Ca}(\text{BF}_4)_2$. In the former case, it is necessary to dry the salt using a Buchi vacuum oven for 3 days following a specific temperature ramp. In parallel, the EC:PC solvent mixture

is dried with molecular sieves before dissolving the dry salt. The electrolyte still contains water and is stirred over a heating plate for several days in the glove box to remove the remaining water. The water content was periodically controlled by Karl Fischer titration (see below) until the electrolyte contains less than 80 ppm of water.

Alternatively $\text{Ca}(\text{BF}_4)_2$ was prepared, as described by Forero-Saboya⁷⁸ by mixing 1.47g (18.8 mmol) CaF_2 (ultra-dry, 99.99% metals basis, Alfa Aesar) with an excess (6g – 42.2 mmol) of boron trifluoride diethyletherate in an Ar-filled glove box. The reactive mixture was sealed in a PTFE-lined stainless steel autoclave and heated up to 150°C for 72h. After cooling down at room temperature, the autoclave was reopened in the glove box and the solid product was recovered, washed several time with THF and dried under vacuum. The reaction proceeds as follows:

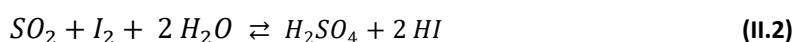


From the X-ray diffraction pattern of the reaction product it can be inferred that it contains two phases: $\text{Ca}(\text{BF}_4)_2$ and CaF_2 , which indicates that the reaction is not complete. Quantification by Rietveld refinement indicates that ~30% of CaF_2 remains at the end of the reaction. Since CaF_2 does not dissolve in EC or PC, nor is electrochemically active, the powder was used without further purification and the CaF_2 was simply allowed to sediment at the bottom of the electrolyte containing flask.

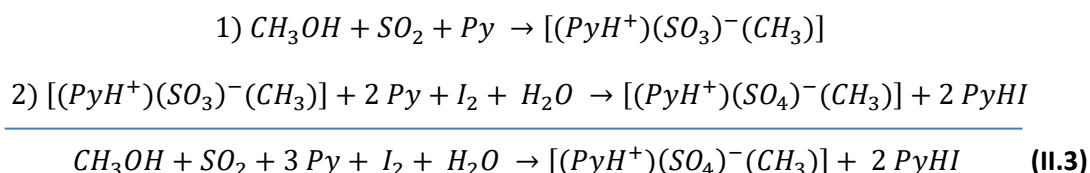
II.1.2. Karl-Fischer titration

Quantifying the water content in electrolytes is crucial since traces of water could lead to parasitic side-reaction. To do so, the coulometric Karl Fischer titration is commonly used,

The Karl Fischer titration is called after the German chemist who invented it in 1935.⁷⁹ The principle of the titration relies on the sulfur dioxide reduction in presence of water, discovered decades earlier by Bunsen which can be summarized by:



This reaction is not complete, which means some water remains in the reactive media. To shift the equilibrium toward a complete water consumption, pyridine, an organic base, is used to eliminate the sulfuric acid produced. Moreover, the reaction solvent is methanol which will also react and change the stoichiometry of the reaction as shown in the equations below:⁸⁰



where *Py* is the pyridine base and CH_3OH the methanol solvent.

The reaction takes place in two steps: 1) the formation of a methyl sulfite intermediary and, 2) the oxidation of this intermediary which consumes one molecule of water for one molecule of iodine. Not only the pyridine allows a complete reaction, but the methanol also change the ratio $\text{H}_2\text{O}:\text{I}_2$ from

2:1 to 1:1 which makes end point determination easier. It is important to note that for safety reasons, methanol and pyridine are less used nowadays and tend to be replaced by metoxymethanol and imidazole, respectively.

Two methods can be used to determine the titration end point: a volumetric and a coulometric method. The latter enables detection of lower amounts of water in the sample (from a few ppms to 5% of water) and is commonly used to analyze the amount of water in battery electrolytes. In the course of this thesis, a 899 Coulometer from Metrohm was used. It is composed of a vessel containing the reactive media and two pairs of electrodes: the indicator and the generator electrode (Fig. II.1. a and b). When water is inserted in the vessel, the generator electrode produces iodine through electrolysis that reacts with water. Once the water is consumed by the reaction (II.3), the production of iodine stops and the water content is retrieved as a function of the time needed to complete the reaction.

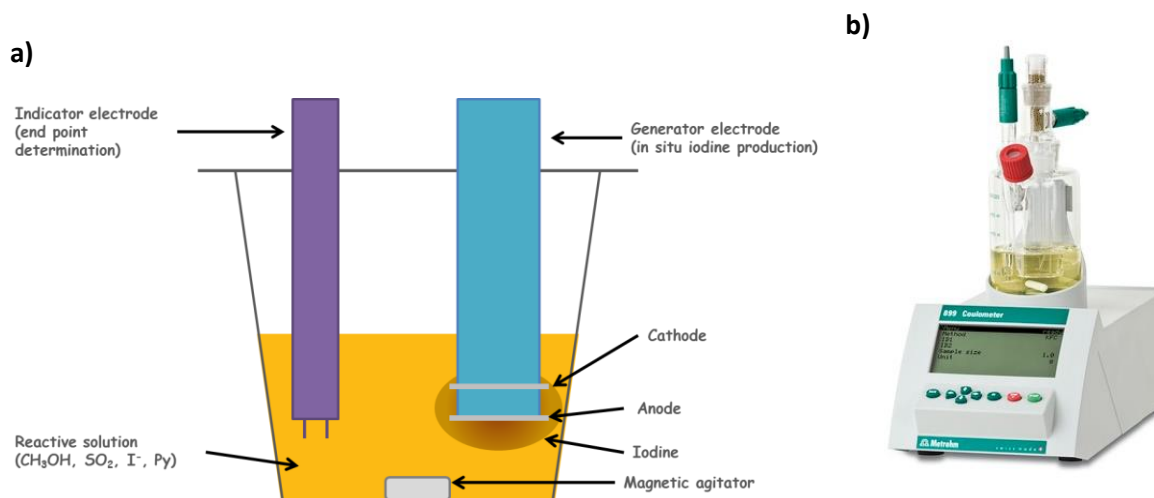


Figure II.1– a) Schematic representation of the Karl Fischer apparatus, b) photograph of the Metrohm 899 Coulometer used

II.1.3. Electrode preparation

All the positive electrodes made during this PhD consisted of a mixture of the active material with carbon black. In some cases, polyvinylidene fluoride (PVDF) was also used as a binder. Loose powder TiS₂ electrodes were prepared in an Ar-filled glove box by mixing TiS₂ (Sigma-Aldrich, 99.995 %), black carbon (Super P, Timcal, Switzerland) and PVDF (Arkema) in 84:10:6 ratios and grinding thoroughly the powder with mortar and pestle. In the case of carbon coated Na₃V₂(PO₄)₃ (NVP), which was synthesized⁵³ at LRCS (Amiens, France), a 80:20 mixture of NVP:black carbon was prepared by ball-milling for 10 min with a SPEX-8000 and dried before use.

In both cases, tape casted electrodes were prepared by dispersing 80:10:10 mixture of active material, black carbon and PVDF in N-methyl-2-pyrrolidone (Aldrich, ≥99.9%). The slurry was mixed for 1h in a planetary ball-miller and doctor blade casted on 18 μm thick aluminum foil (Goodfellow, 99%). The resulting tape was dried at 120°C for 3h, and 11 mm diameter disks electrodes were punched and pressed at 8 tons before use.

Either metals or activated carbon were used as counter electrodes in electrochemical experiments. Lithium ribbon (Chemetall) or chips (0.6 mm thick, MTI, 99.9%) were scratched to remove the oxides surface layer and used as negative electrodes in lithium electrolyte containing cells. Sodium electrodes were sliced from sodium cubes (Sigma Aldrich, 99.9%). Calcium electrode pellets were prepared by scratching and pressing calcium granules (Alfa Aesar, 99.5%) up to 8 tons. The pellets were then scratched before mounting the cells. Commercial activated carbon cloth (Kynol, ACC-509220) disk electrodes were punched and dried under vacuum before use.⁷²

II.1.4. Electrochemical cells

For experiments not being conducted *operando*, Swagelok cells were typically used. These are build using gas tubing fittings, as first reported in 1992 by Guyomard and Tarascon.⁸¹ Their airtightness makes them ideal for isolating the battery components from the air and moisture and the setup is versatile as components are available in various sizes, shapes (for 2 or 3 electrodes – see Figure II. a) and materials (most commonly stainless steel but also PTFE, titanium, nylon) and are complemented with *ad hoc* designed plungers for electrode connection. In this thesis, the plungers were either made of stainless steel 316 or aluminum. Stainless steel plunger and current collectors are commonly used in the negative side as it does not form alloys with the different metals used (contrary to aluminum which can form Li-Al alloys). However, if used on the positive side stainless steel can oxidize at voltages as low as 3.1 V⁸² (vs Li⁺/Li – that value may vary depending on the electrolyte). When working at such voltages, aluminum can be used up to 3.9 V in oxidation, except with a TFSI-based electrolyte where it tends to be corroded.⁸³ One can still use the aluminum plunger if some additive salt such as LiPF₆ is added to the electrolyte.^{84,85} The plungers are covered by a Teflon ribbon to keep them isolated from the Swagelok body. Swagelok cells can be inserted in an oven to perform *ex situ* electrochemical tests at non-ambient temperature.

In electrochemical analysis, we refer to the material of interest as working electrode (WE) while the other electrode is called counter electrode (CE). In the case of two electrode cells, the potential difference is measured between the WE and the CE, and hence may be affected by redox processes at the CE. The use of a separate reference electrode (RE) is advisable, especially in the case of new battery chemistries for which no standard components exist yet, to be able to independently control and monitor the behavior of the working/counter electrode within the cell. The three-electrode setup works by applying a voltage between RE and WE while no current flows between the two electrodes. Therefore, electric current only flows between the CE and the WE. (Figure II.2 b)

The electrodes are isolated from each other thanks to separators. Their purpose is to avoid any shorts-circuits while acting as an electrolyte reservoir to allow ionic conductivity. They can be made from a large range of material such as nonwoven fibers (cotton, nylon, polyester), polymer films (polyethylene, polypropylene) or ceramics. In our case Wattman glass fiber separators (GE Healthcare, 420 μm thick) were used. In some tests involving sodium anode, Celgard 2500 microporous polypropylene carbonate separators (25 μm thick) were added for their mechanical resistance. Typically, we used two Wattman separators between each electrode in Swagelok-cells (4 separators in 3-electrode cells), while we used only one separator in the *in situ* cells, though the number of separators has little to no influence on the diffraction data (see section II. 3. 1).

To achieve reliable results, the RE should have a constant potential over time, with great reproducibility. To avoid blocking the ionic conduction between the WE and CE, the RE is placed in the side compartment of the Swagelok body. It usually consists of a stainless steel onto which the desired metal is pressed. However, because the RE is away from the WE-CE stack, some voltage discrepancy may be observed.⁸⁶ In specific cases, a lithium RE was inserted in the cell using a copper grid and a tailored plunger as shown in figure II.2 c). The RE is therefore placed between the two Wattman glass fiber separators to isolate it from the other electrodes.

All electrochemical cells have to be assembled in Ar-filled glovebox in order to prevent any air contamination.

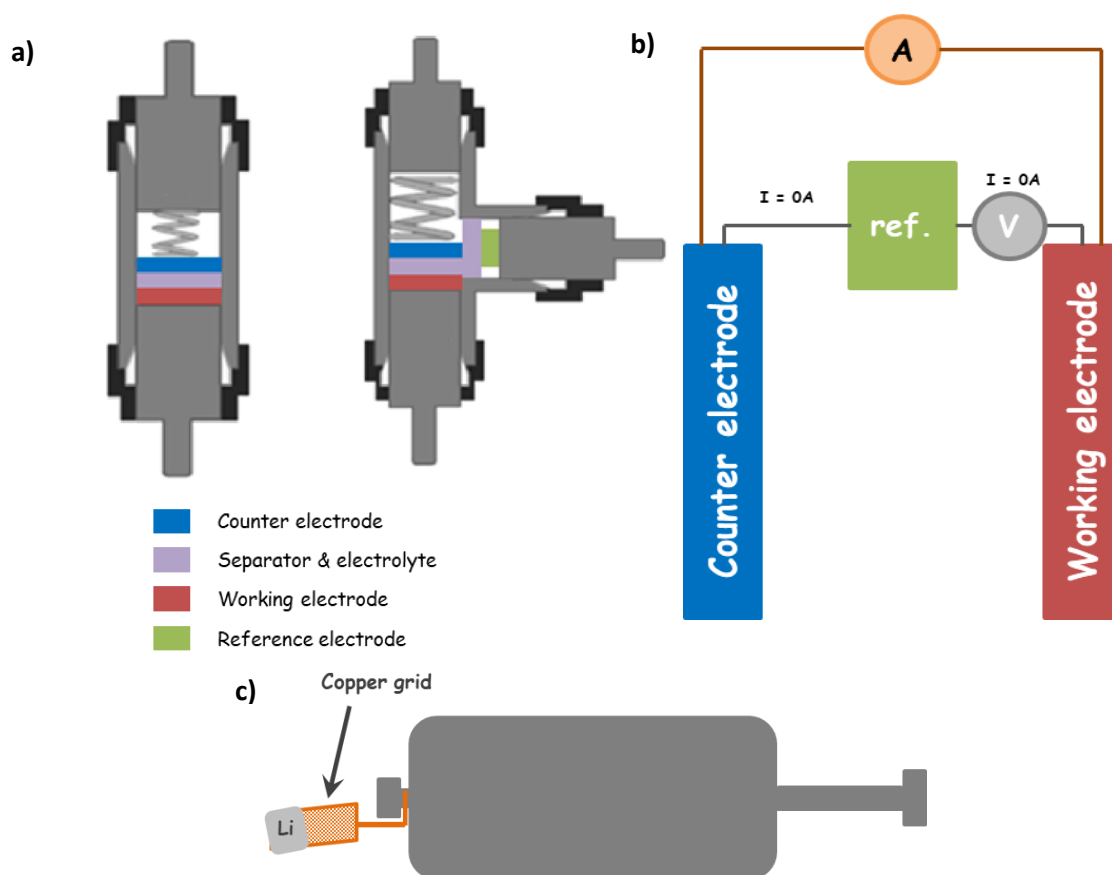


Figure II.2 – a) Schematic representation of two and three electrodes Swagelok cells, b) how voltage and intensity are controlled in a three-electrode setup, c) lithium reference mounted on a tailored plunger.

II.1.5. Chronopotentiometry and (de-)intercalation redox mechanism

Chronopotentiometry consists in applying a constant current (I) to the WE and measuring the potential as a function of time. By doing so, the electrode material is reduced ($I < 0$ A) or oxidized ($I > 0$ A) at a constant rate up to potential cutoffs fixed by the user. In battery research, where multiple redox cycles are carried out, chronopotentiometry experiments are often denoted

galvanostatic cycling with potential limitation (GCPL). In this thesis, the GCPL is monitored thanks to a VSP potentiostat and the EC-Lab software from Bio-Logic. The voltage profile can either be plotted as a function of time, or capacity (in mAh/g), which, for the case of intercalation reactions, can be translated into mol of ion intercalated or de-intercalated assuming no other redox processes take place. Before GCPL, the voltage of the cell with no intensity applied (open circuit voltage (OCV)) is usually monitored for periods ranging from 1 to 5 hours in order to assess stability. The intensity applied in chronopotentiometry is often denoted as C-rate. Two alternative definitions for this concept are commonly used: the amount of time needed to react with 1 mol of electrons (typically applied for fundamental studies on intercalation compounds) or the amount of time needed to completely charge or discharge a cell (applied to commercial cells). In this thesis, the former will be used with C/n denoting reaction with one mole of electrons (and hence one mole of Li⁺ or 0.5 moles of Ca²⁺ for instance) in n hours. Changing the C-rate allows grasping information about the kinetics of the different redox processes taking place and hence the power performance of the cells.

The shape of the GCPL curve is linked with the ion (de-)intercalation redox mechanism. In the case of a monophasic transformation, the ion (de-)intercalates homogeneously in the material. In X-ray diffraction, this manifests as a gradual shift of the reflections due to the change in composition (Fig. II.3 a). Vegard's law states that in a solid solution or an alloy, there is a linear relation between the material's lattice parameters and the concentration of its components, at constant temperature. This can be mathematically expressed as:

$$\alpha_{A_{1-x}B_x} = (1 - x)\alpha_A + x \alpha_B \quad (\text{II.4})$$

where α_A , α_B and $\alpha_{A_{1-x}B_x}$ are the lattice parameters of the phase A, B and the $A_{x-1}B_x$ alloy / solid solution, respectively and x the concentration of B in the solid solution. This is, for example, the case for Li_xTiS_2 , $0 \leq x \leq 1$ mol. Alternatively, if a two-phase process takes place, the (de-)intercalated phase has to nucleate, overcoming an energy barrier to create the interface and the new phase front propagates from the nucleation site to the whole material. During this biphasic mechanism, the lattice parameters of both the initial and the final phase remain constant, and only their relative amounts change. Therefore, on the X-ray diffraction patterns the initial phase gradually disappears while peaks corresponding to the new phase appear at the same time (Fig. II.3 b). An example of such mechanism would be Li_xFePO_4 with $0 \leq x \leq 1$.

The evolution of the voltage profile throughout the redox process depends on the mechanism. This can be explained through the Gibb's phase rule, expressed as:

$$F = C - P + 2 \quad (\text{II.5})$$

where C is the numbers of components, P the number of phases and F the degree of freedom of the system, *i.e.* the number of independent physical parameters used to describe the system. In the case of electrochemical (de-)intercalation, the system is composed of two components, the initial and the final material, therefore C=2. During a monophasic transformation, P=1 thus F=3. Two degrees of freedom are occupied by temperature and pressure, which are supposed to be constant. Therefore, one degree of freedom remains for the potential which would gradually decrease (or increase) as the ion is (de-)intercalated (Fig. II.3 a) following the relation given by Armand:⁸⁷

$$E = E^\circ - \frac{nRT}{F} \times \ln\left(\frac{x}{1-x}\right) \quad (\text{II.6})$$

where E° is the standard potential of the electrode, R the gas constant ($R= 8.314 \text{ J}\cdot\text{K}^{-1}\cdot\text{mol}^{-1}$), F the Faraday constant ($96\,485 \text{ C}\cdot\text{mol}^{-1}$), T the temperature, x the mol of intercalated ion and n a constant either equal to 1 or 2. On the contrary, during a biphasic transformation, $P=2$ and $F=2$, which are taken by temperature and pressure. Therefore, the voltage has to remain constant during the transformation (Fig. II.3 b).

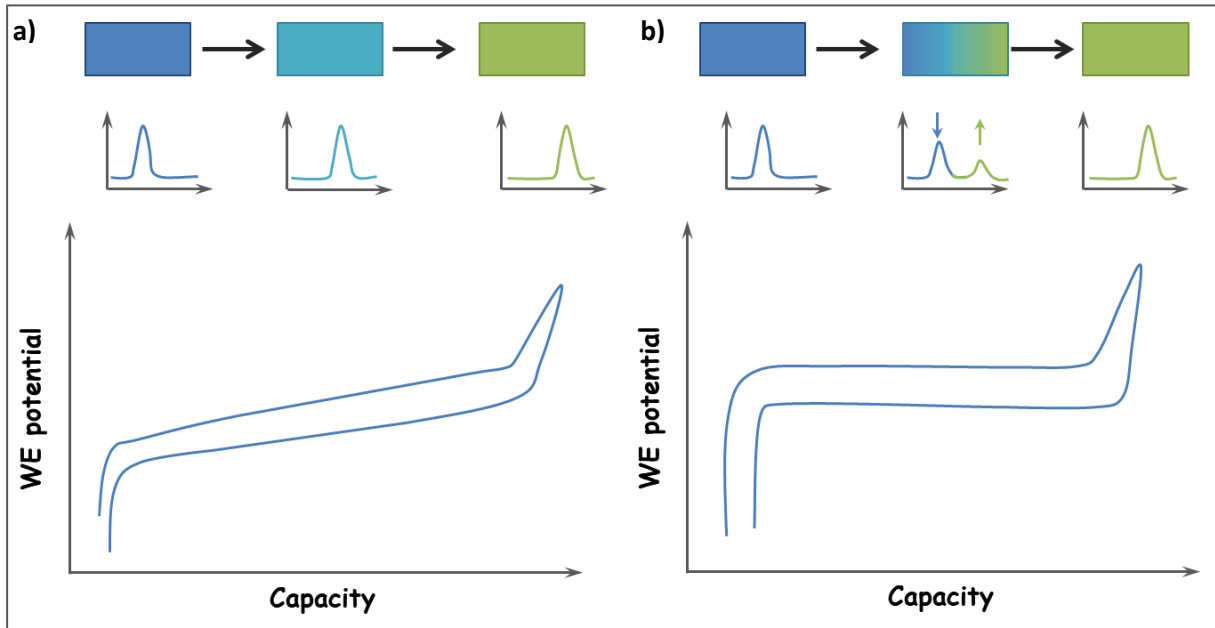


Figure II.3 – Schematic representation, X-ray diffraction patterns and voltage versus capacity profiles corresponding to a) monophasic process, and b) biphasic process

II.2. Crystallography and X-ray diffraction

II.2.1. Principle

Electrodes in batteries often contain crystalline materials, *i.e.* solids whose components (atoms, ions or molecules) are organized within a pattern, a unit cell, replicated in the three dimensions of space to form a lattice. The components forms (hkl) planes where h, k and l are called the Miller indices; two (hkl) planes of the same family are separated by the distance d_{hkl} . Crystal structures are defined by the symmetry properties of the unit cell and described using 14 Bravais lattice and 230 space groups. To probe the crystal structure and lattice parameters, advanced techniques such as X-ray crystallography, neutron diffraction and electron diffraction are used. In battery research, X-ray diffraction allows the study of ion (de-)intercalation mechanism in electrodes.

X-rays are penetrating electromagnetic waves with wavelengths ranging between 10 pm to 10 nm, between ultraviolet and gamma rays (see figure II.4a). Their discovery in 1895 by Wilhelm Röntgen

allowed scientific breakthrough, especially in medical science (radiology – see figure II.4b), but also in crystallography. Because of its wavelength being the same order of magnitude as the inter-atomic distance in a crystal, X-rays can interact with the atoms' electron cloud and are diffracted through elastic scattering (figure II.4 c), following the Bragg's law:

$$2d_{hkl} \sin(\theta) = n\lambda \quad (II.7)$$

where d_{hkl} is the distance between two crystallographic planes, ϑ the beam's angle of incidence, n the order of the diffraction and λ the wavelength.

The intensity of the Bragg peaks is proportional to the structure factor F_{hkl} which depends on the components position in the lattice and the nature of the components. It can be calculated by the formula:

$$F_{hkl} = \sum_{j=1}^N f_j e^{[-2\pi i(hx_j + ky_j + lk_j)]} \quad (II.8)$$

where f_j is the scattering factor, depending of the number of electrons in the electronic cloud of the j^{th} atom, h, k and l the Miller indices and x_j, y_j and z_j are the coordinates of the components of the unit cell (with $0 \leq x_j, y_j, z_j \leq 1$).

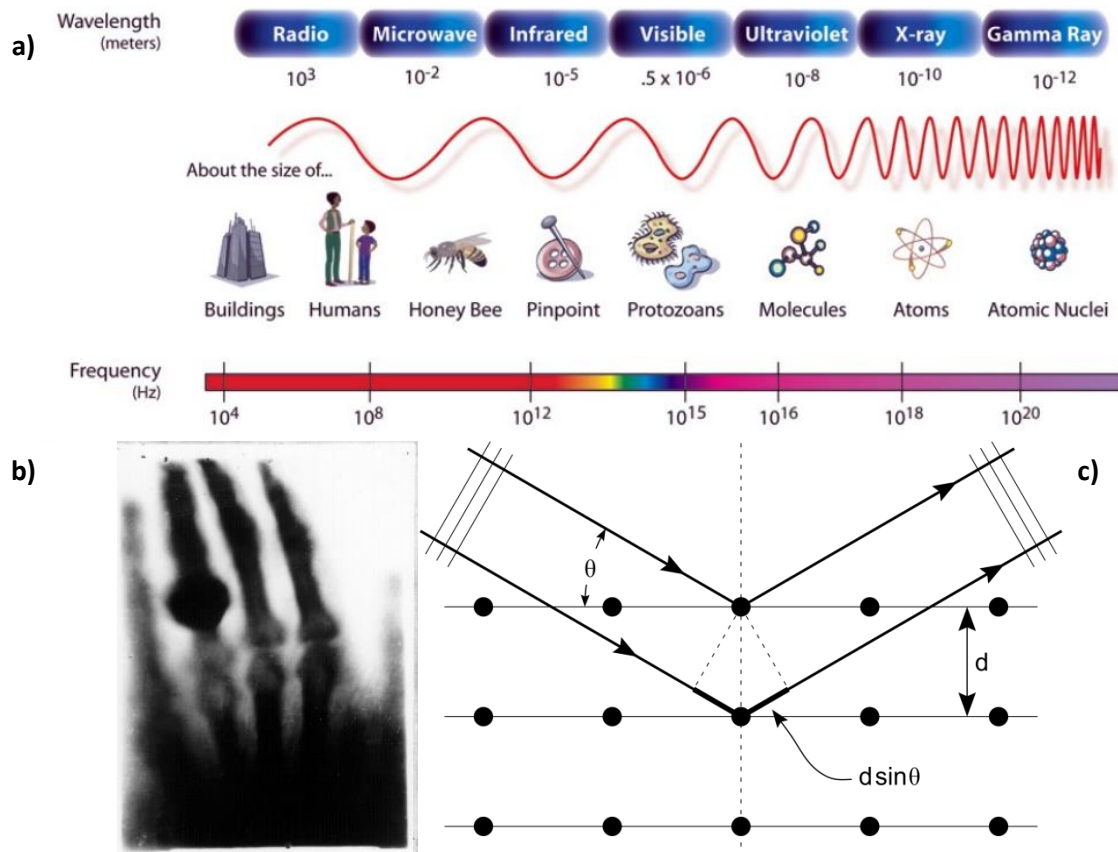


Figure II.4 – a) Electromagnetic spectrum, b) first radiography taken and c) schematic representation of X-rays diffracted by a crystal

In 1912, Max von Laue already found a relation between crystal structures and diffraction patterns but it is only on 1969 that Hugo Rietveld created a whole pattern refinement method. Rietveld method allows the extraction of crystal lattice properties⁸⁸ by comparing a calculated whole pattern profile to experimental data. To do so, the X-ray diffraction pattern is decomposed into three peak properties: position, intensity and shape. Each of these three components is affected by the crystal

structure, the specimen properties and the instrumental parameters; a non-exhaustive list of these parameters is given in [table II.2](#).

Table II.2 - Parameters influencing the profile of a X-ray diffraction pattern. Reprinted from ref. 89

Pattern component	Crystal structure	Specimen property	Instrumental parameter
Peak position	Unit cell parameter (a,b,c,α,β,γ)	Absorption Porosity	Radiation (wavelength)
Peak intensity	Atomic parameters (x,y,z,B,etc.)	Preferred orientation Absorbtion Porosity	Geometry and configuration Radiation (Lorentz, polarization)
Peak shape	Crystallinity Disorder Defects	Grain size Strain Stress	Radiation (spectral purity) Geometry Beam conditioning

To obtain the calculated profile, the user must enter an approximation of the parameters in the program which generates a pattern thanks to several functions. The peak position is given by the Bragg's law while the peak intensity is given by the formula:

$$I_{hkl} = K \times p_{hkl} \times L_{\theta} \times P_{\theta} \times A_{\theta} \times T_{hkl} \times E_{hkl} \times |F_{hkl}|^2 \quad (\text{II.9})$$

where:

- K is the scale factor, used to normalize the experimental intensities with the calculated intensities. It corresponds to the amount of material probed by radiation
- p_{hkl} is the multiplicity factor, which express the number of equivalent atoms obtained by symmetry operation in the lattice. It reduces the number of redundant calculations
- L_{θ} is the Lorentzian multiplier, defined by the geometry of diffraction.
- P_{θ} is a polarization factor, which express a partial polarization of the diffracted beam (neglected in mots cases of 3rd generation synchrotron radiation)
- A_{θ} is the absorption multiplier, which express absorption of both the incident and diffracted beams. At synchrotron, proper selection of the radiation energy can make it negligible
- T_{hkl} is the preferred orientation factor, which express a possible deviation from a complete randomness in the distribution of crystallites' orientations.
- E_{hkl} is the extinction multiplier, which express deviations from the kinematical diffraction model.
- F_{hkl} is the structure factor (or the structure amplitude), which is defined by the type and position of the atoms in the crystal structure of the material.

Finally the peak shape is a mathematical function, which must be ideally described by an analytical formula for computational gain purpose, and which essentially reflects the instrumental contribution. Pure Gaussian or Lorentzian functions are definitely too simple for the effective description of the peak shape, hence standardly used peak shape functions are a combination of both: the Pseudo-Voigt (linear combination of Gaussian and Lorentzian function) or the Pearson-VII (modified Gaussian) function. Then, a background (either calculated or entered manually by the user) is subtracted and the functions are summed. A graphical

representation of each step is presented in figure II.5. Once the model is calculated, the program compares it to the experimental data thanks to the method of the least squares. In order to minimize the discrepancy between the model and the data, the program refines parameters selected by the user. It is important to note that the method requires a reasonable estimate of the parameters to obtain a good fit, otherwise no reliable calculated mode can be obtained. Moreover different starting models or refinement strategies are necessary to test the robustness of the final calculated solution.

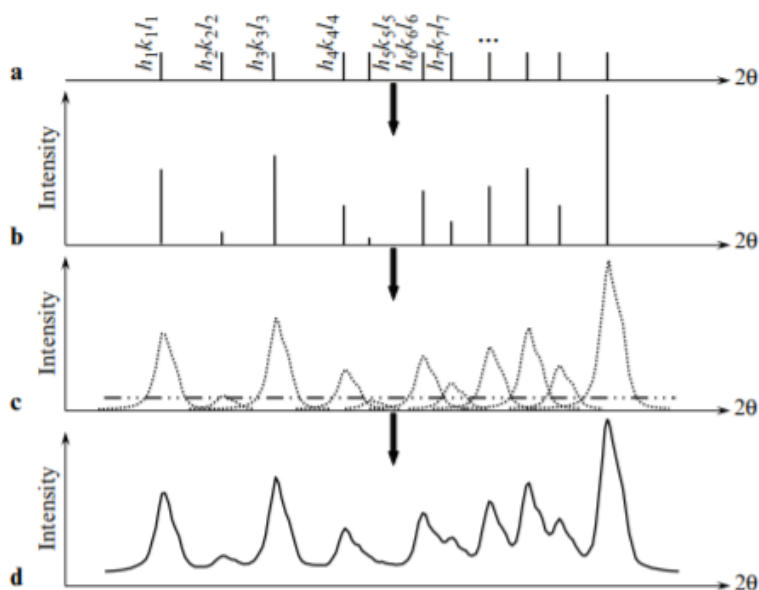


Figure II.5 - Graphical representation of the successive steps of the Rietveld refinement: determination of a) peak position, b) peak intensity, c) peak shape, d) background subtraction and slight peak overlapping. Reprinted from ref. 89

The functions mentioned above are sometimes not sufficient to describe the patterns for they do not take into account some experimental contribution (i.e. peak asymmetry, sample position in the diffractometer). Additional correction functions are implemented to the Rietveld method to improve the refinement and quantify those parameters.

Sometimes, the crystal structure is not sufficiently known to perform Rietveld analysis and Le Bail method (also called profile matching) is used instead. This method focuses on simulating the peaks intensities with a least squares analysis to refine the unit cell, without the requirement of structural model.

II.2.2. X-rays in a laboratory

Most X-ray diffractometers (i.e. Bruker D8 advance) are in the Bragg-Brentano geometry which was historically imposed by the low energy of Cu based-tube not allowing high penetration through materials. Hence, Bragg-Brentano geometry is typical of data collection in reflection mode. In the Bragg-Brentano geometry, the distance source-sample is constant and the diffracted beam is collected at their convergence point.⁹⁰ On the contrary, transmission mode in Debye-Scherrer geometry is the geometry of choice for synchrotrons, seldom used in laboratory diffractometers.

However, some laboratory setups using molybdenum or silver sources, or rotating anodes can achieve transmission mode (*i.e.* Bruker D8 discover).

X-rays are produced in a source composed of a vessel under vacuum where a tungsten cathode produces electrons that are accelerated thanks to an anode. X-rays can have different wavelengths depending on the anode material, the most common anode being copper giving a $\lambda = 1.5406 \text{ \AA}$, but molybdenum, cobalt and silver anodes can also be used to get wavelengths of 0.7107 \AA , 1.7903 \AA and 0.5638 \AA , respectively, for the K_{α} radiation. The K_{α} radiation is typically the most intense spectral line released by an element which electrons were excited. Depending on the orbital where the electron was located, the released energy is different and will emit $K_{\alpha 1}$ and $K_{\alpha 2}$ radiation, and in some cases a third radiation with higher energy: K_{β} . Therefore the X-ray source is not monochromatic which needs to be taken into account when analyzing the resulting X-ray pattern.

Some X-ray diffractometers use a rotating anode as a source. Originally, rotating anodes were designed to address the problem of overheating anodes which reduces their efficiency. By rotating the anode several hundred revolutions per minute the heat is dispersed throughout the whole disk and cooling down the piece is easier. This rotation also gives an advantage in terms of signal: with a given electron beam size, the surface hit on the anode is larger on a rotating anode than in a conventional one, producing therefore more X-rays. X-ray diffractometers using a rotating anode are recommended for higher X-ray flux and longer scans.

Once the X-rays are emitted, they go through the primary optics where a monochromator eliminates the K_{β} radiation (and even the $K_{\alpha 2}$ radiation for some high resolution diffractometer) and slits reduce the beam divergence, allowing better peak resolution. Then, the beam illuminates the sample, which can be in multiple forms such as capillary, monocrystal or specimen holder. The sample can be rotated to increase powder averaging and obtain better statistics during data collection. When encountering the sample, X-rays are diffracted and the diffracted beam goes, optionally, through the secondary optics which purpose is to reduce the noise and to improve the pattern resolution, and where a second monochromator suppresses white, fluorescence and K_{β} radiations before the detector. To be noted that this signal quality improvement through the secondary optics is at high intensity cost. The detector converts the received X-ray beam into an electric signal. It consists most commonly in a punctual scintillation detector but position sensitive detectors, similar to those used in synchrotrons, are nowadays used offering higher throughput. [Figure II.6](#) schematize the description of the machine.

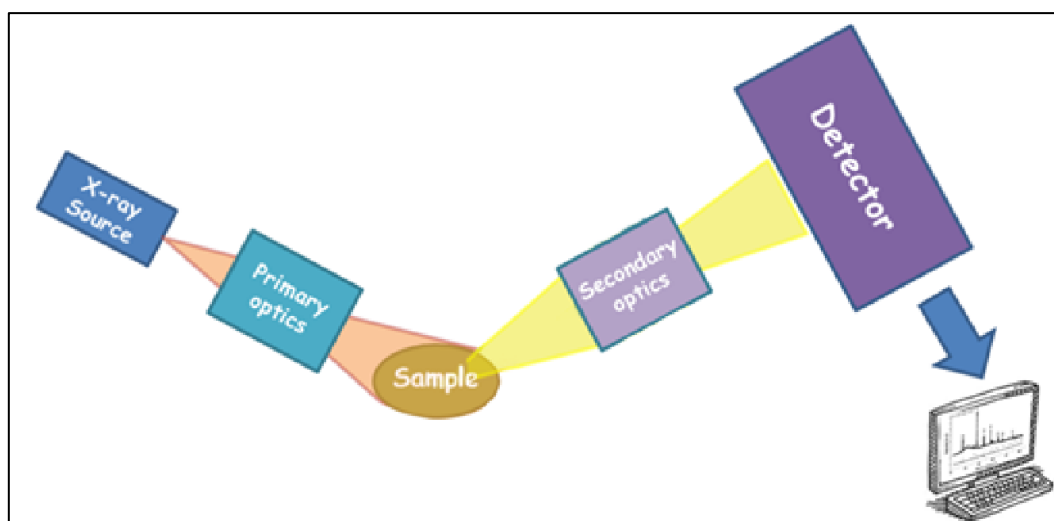


Figure II.6 - Schematic representation of a laboratory diffractometer

II.2.3. X-rays in ALBA-CELLS synchrotron

Although laboratory X-ray diffractometers can be tweaked to improve their performances, they are outperformed by synchrotron facilities. The main advantage of a synchrotron is its brilliance, four orders of magnitude higher than a laboratory diffractometer. Indeed, synchrotron light has high flux over a small beam (2*0.5 mm), which coupled with an adequate detector allows the collection of a full pattern in seconds. Besides, synchrotrons offer large energy tunability over the different beamlines, from UV to X-rays, and a single beamline can operate at various energies. Adapting the beam energy can be crucial in some experiments to avoid some Bragg peaks overlap,⁹¹ or in the case of *in situ* studies to overcome the absorption of the *in situ* cell's elements.

II.2.3.1. Functioning principle

A synchrotron is a cyclic particle accelerator in which the magnetic field bending charged particles (generally electrons) beam is increasing to be synchronized with the increasing speed of electrons, allowing higher energies to be reached. In the case of the synchrotron, the electron source is a Linear Accelerator (LINAC), where a tungsten filament, impregnated with barium oxide, is heated up to 1200°C under vacuum. Next, the emitted electrons go through a bunching region in order to increase their energy and to decrease their bunch length. Then, they pass through an accelerating structure where the beam energy is increased up to 100 MeV. Since higher energies are required, a booster is used to increase the electron speed to reach the 3 GeV beam energy at ALBA. The booster is like a “mini synchrotron” as the magnetic field is synchronized with the incoming electron flow. The electrons are then inserted in the storage ring where an assembly of bending magnets and quadrupoles are repeated throughout the structure. It is important to note that the whole process described above takes place under ultra-high vacuum (10^{-10} mbar order). Figure II.7 shows the different parts of the synchrotron.

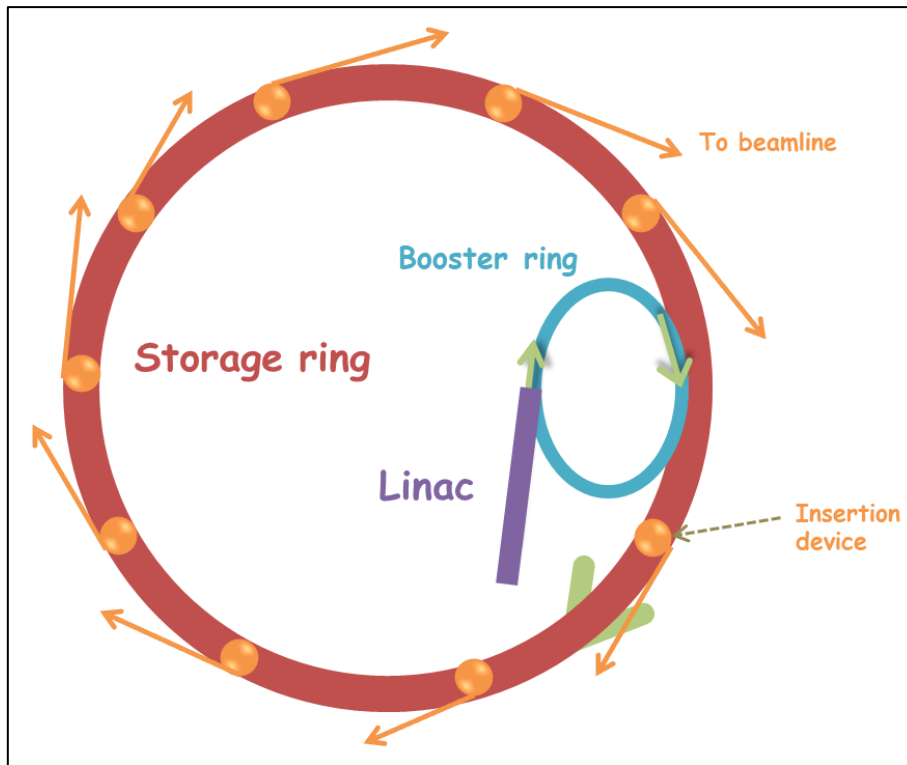


Figure II.7 - Schematic representation of a synchrotron

In a third generation synchrotron such as ALBA, the storage “ring” is in fact a succession of straights sections which offer the possibility to insert optimized synchrotron X-ray sources, so called insertion devices. Dipole bending magnets guide the electrons through the different sections. At each trajectory steering, either at bending magnets or in insertion devices, electrons produce synchrotron radiation that can be extracted to a beamline. Because the electron speed v is close to light speed c , the radiation is emitted in a conic shape instead of a sphere (fig. II.8). The natural opening angle, also called natural divergence, of the radiation cone is $\theta \approx \gamma^{-1}$, γ being the Lorentz factor given by the relation:

$$\gamma = \frac{E}{mc^2} \quad (II.10)$$

where E is the energy of the electrons in the storage ring and mc^2 the electron rest mass equal to 511keV; the Lorentz factor can be hence expressed as:

$$\gamma = 1957E \text{ (with } E \text{ expressed in GeV)} \quad (II.11)$$

At ALBA, the beam energy is 3GeV which results in a natural vertical divergence γ^{-1} of 0.17 mrad (0.0098°).

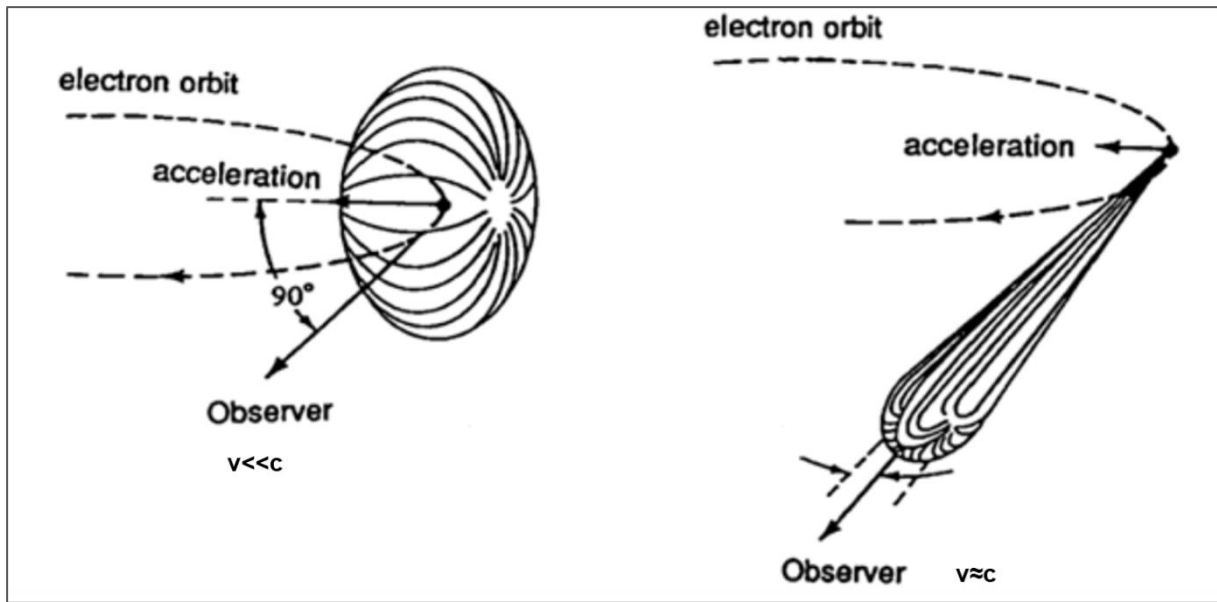


Figure II.8 - Radiation emission by an electron as a function of the electron speed v , reprinted from ref 92

II.2.3.2. Insertion devices

The first element of the beamline is the insertion device, placed in a storage ring's straight sections. It is composed of a series of magnets that deflects the incoming electron beam several times, and synchrotron radiation is emitted at each wiggle. The insertion device strength parameter is given by the formula:

$$K = \frac{eB\lambda_u}{2\pi m_e c} \quad (II.12)$$

where

- e is the electron charge,
- B the magnetic field,
- λ_u is the spatial period of the magnets
- c is the light celerity.

If $K \ll 1$, each wiggle builds constructive interference, producing a very focused and brilliant beam, collimated on the electrons' orbit plane, the device created is called an undulator. The resulting photon-energy spectrum is composed of harmonic peaks which are used to tune the beam energy and for which intensity is proportional to the square of wiggles numbers. However the beam intensity decrease with the number of the harmonic, which means the undulator is most efficient at lower energies, as shown in figure II. 9. On the contrary, if $K \gg 1$ the insertion device is a wiggler, where each wiggle produces incoherent radiation of intensity proportional to the number of wiggles. The X-ray beam is broader, hence less brilliant than with an undulator, but the photon-energy spectrum is continuous and high over a large range of energies (fig. II.9), which makes the wiggler more advantageous at higher energies.

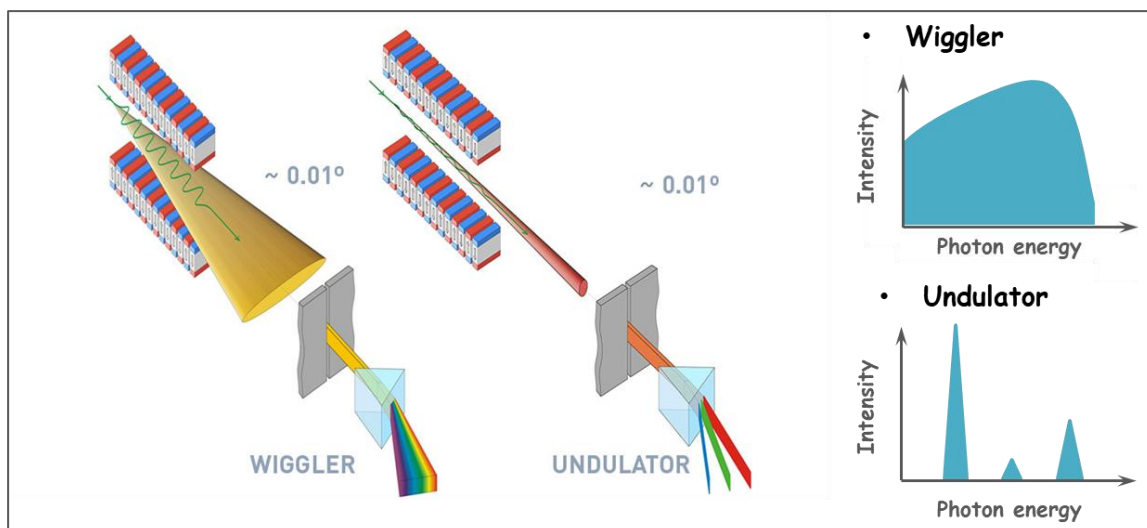


Figure II.9 - Schematic representations of a wiggler and an undulator, and their respective photon-energy spectrum

II.2.4. BL04- MSPD

At ALBA-CELLS, the BL04 beamline is dedicated to Material Science and Powder Diffraction (MSPD). Experiments such as high angular resolution powder diffraction, high pressure powder diffraction using diamond anvil cells and micro-powder diffraction at high energy can be performed. The following description of optics is specific to MSPD beamline, and a global schematic representation of the beamline is given in figure II.10.

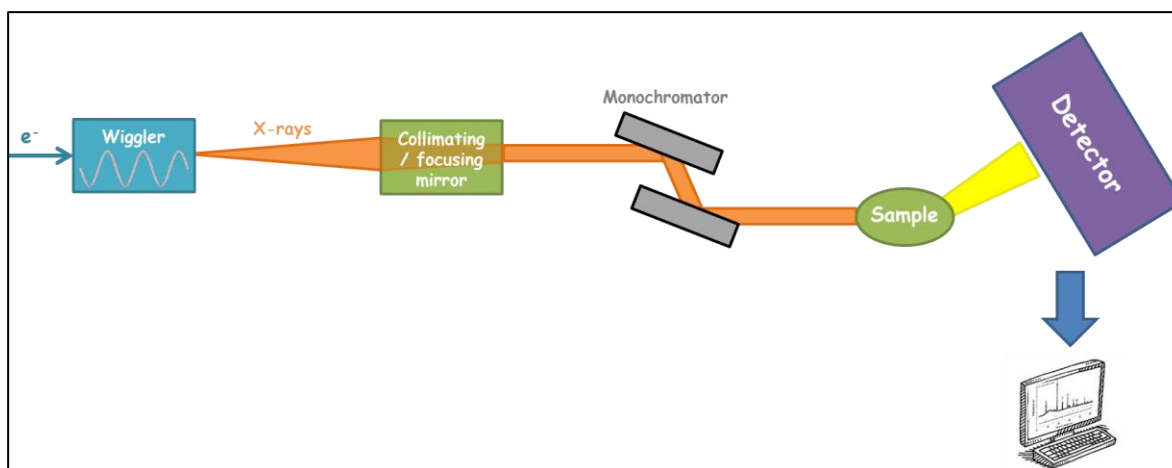


Figure II.10 - Schematic representation of optics on MSPD beamline

In order to perform such experiments, the insertion device is a $\sim 30\text{mm}$ period length and 60.5 periods multipole superconductive wiggler (from Budker Institute, Novosibirsk) with magnetic field as high as 2.1 Tesla. After the wiggler, the synchrotron beam goes through the front end. The first purpose of the front end is to condition the beam for the experiment, thanks to slits to regulate the light intensity, a mask to remove the Bremsstrahlung radiation (radiation emitted by an electron losing kinetic energy), a photon shutter to control the sample illumination, and a mask to constraint the non-negligible horizontal divergence (and reduce the heat load downstream). Its second purpose is to act as a safety element with a radiation shutter that is interlocked with the experimental hutch

to prevent radiation exposure, and a vacuum trigger unit to preserve the vacuum in the storage ring in case there would be a leak on the beamline side. Finally, the front end also possesses an X-ray beam position monitor to ease the beamline alignment with the accelerator.

The beam departing from the wiggler – and thus the front end – is polychromatic. To tune the beam into a monochromatic wavelength, a fixed exit double crystal monochromator (DCM) delivered by Bruker is used. The DCM exploits the (111) Bragg reflection of two silicon (Si) crystals separated by a variable distance of ~10 mm. This distance is slightly tuned when changing the energy so to ensure the beam exit with fixed 20 mm offset.^{93,94} The whole double crystal assembly is rotated to select the experiment energy following the Bragg law (equation II.7). On BL04-MSPD, the DCM allows operating in the 8 to 50 keV energy range. The outgoing energy resolution is intrinsic to the crystal materials, the Bragg reflection used and to the divergence of the incoming beam; for BL04-MSPD it results in $\Delta E/E \sim 1.5 \cdot 10^{-4}$. As a result, the accurate wavelength value is recalculated from the Bragg reflections of silicon SRM640d NIST standard since a discrepancy between the setup and the real value may occur. Because the DCM selects a tiny part of the overall spectrum, the “unwanted” radiation is hence absorbed, heat is accumulated by the first crystal essentially and has to be evacuated. Moreover, heat might deform the crystals and degrade the energy resolution. For this reason both crystals are cooled cryogenically.

A mirror is inserted between the front end and the DCM, working at 2 mrad grazing incidence. Its purpose is to reduce the vertical divergence of the source (close to the synchrotron natural divergence) and eliminate the high energy harmonics that cannot be discriminated by the DCM. On BL04-MSPD, the mirror is positioned upstream the DCM to reduce the heat load on the DCM first crystal. It consists of a 1.2m long water cooled Si block mounted on a so called bending mechanism allowing the application of a curvature in radius range from 5 to 50 km. The mirror mechanism and mirror block itself were delivered by CINEL and WINLIGHT, respectively. When operating with MYTHEN position sensitive detector (PSD), the mirror is bent down to ~9 km resulting in focusing the vertical beam at the powder station (35 m from the source, 14 m from the mirror). Lowest vertical divergence (~20 μ rad) is achieved in so called collimating mode by applying a 21 km radius curvature. The latter mode, together with MAD detection setup, offers the best instrumental angular resolution.⁹³ On the other hand, the focusing mode as used with MYTHEN PSD offers a higher flux on the sample.

The mirror supports the highest heat load induced by the synchrotron beam, so the silicon block has to be efficiently cooled. To keep a thermal contact between the coolant (water) and the silicon block, the mirror is partially immersed in liquid “Galinstan”, a eutectic alloy of gallium, indium and tin. In addition to the raw Si, the mirror is also coated with two layers of rhodium (Rh) and platinum (Pt) (~ 600 Å thick). Each of these three materials has different reflectivity curves with energy cutoffs at ~15keV, 33keV and 41 keV for Si, Rh and Pt, respectively (fig II.11). This energy cut off distribution is used to select the optimum surface layer in order to eliminate the higher harmonics that can propagate after the monochromator.

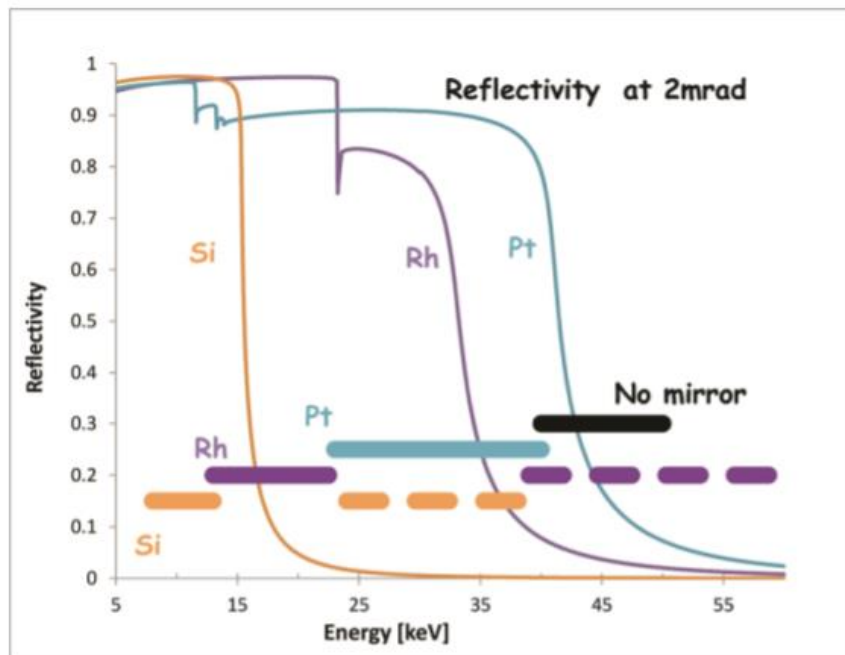


Figure II.11 - Calculated reflectivity of mirror coatings at 2 mrad incidence angle. The plain wide lines show the operating energy ranges of each coating, the dotted wide line the energy range which is suppressed by the mirror. Reprinted from ref. 94

Throughout the whole optics system, beam defining slit systems, intensity monitors and beam imaging devices allow better control and diagnosis of the beam. After going through the DCM the beam illuminates the sample, usually – but not necessarily – enclosed in a capillary. The sample diffracts the X-ray beam and the resulting signal is captured by a detector.

One of the detector used on the powder diffraction station is a 6 modules MYTHEN (Microstrip sYstem for Time-rEsolved experimeNt),⁶ a technology developed by the Swiss Light Source and now commercialized by DECTRIS Ltd (www.dectris.com). It is a PSD, spanning a $\sim 40^\circ$ angular range in effective step of 0.006° . It is hence efficient for high throughput and/or time-resolved powder diffraction experiments, especially *in situ* experiments. Since the photons diffracted by the sample are no charged particles, they need to be converted into an electrical signal. To do so, the semi-conductive properties of silicon are used. The detector is composed of 1280 current collectors bonded to silicon sensors with an *ad-hoc* n-doped and p-doped distribution (fig. II.12). When the sensor is hit by a photon, electron-hole pairs are created by photoelectric effect. Those electrons are pulled toward the aluminum current collector at the back of the sensor by an electric field. An indium solder connects each sensor to an electric circuit that transforms the electric signal into a readable data. Each photon of energy E_0 produces a charge Q which is of the order of a few thousands of electrons ($Q = E_0 / 3.6 \text{ eV}$ for Si) which allows an accurate and individual counting of the photons (hence the single photon counter appellation).⁹⁷ BL04-MSPD is as well equipped with a scanning based Multi Analyzer Detector (MAD) offering highest possible angular resolution but requiring longer acquisition time for covering a significant angular range; typically 1 hour with MAD against minutes for MYTHEN PSD.

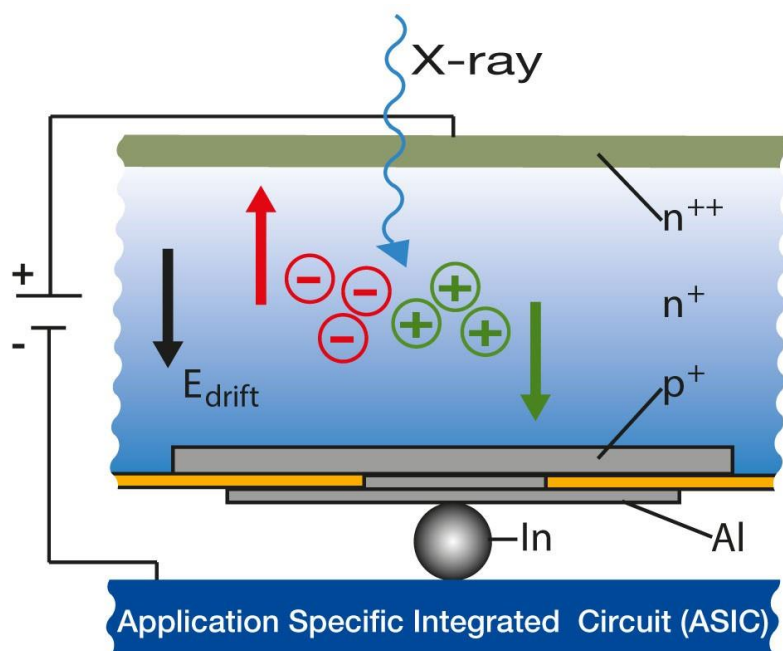


Figure II.12 - Schematic representation of a Si X-ray sensor, reprinted from 96

II.3. *In situ* X-ray diffraction on battery

After Whittingham proved possible electrochemical intercalation of lithium ions in TiS_2 , the electrochemistry of the system was studied intensively but the insertion mechanism had yet to be understood. In 1978, Chianelli working for Exxon performed the first *in situ operando* data collection on a battery. In the first model used, the cell components were sealed inside a polyethylene bag which diffraction peaks occulted some of the TiS_2 peaks. Therefore Chianelli switched to beryllium windows. Indeed, beryllium has a low X-rays scattering factor which makes it ideal despite its toxicity, and although some diffraction peaks are visible, they were not overlapping TiS_2 peaks. Other *in situ* cells were designed through the years as shown in figure II.13. In particular the cell proposed by Morcrette,⁹⁸ based on Amatucci's cell,⁹⁹ is similar to the commonly used Swagelok cells.⁸¹ This design was later improved by Leriche.⁷⁴ Another approach was the development of *in situ* coin cells, more compact and which geometry is closer to the commercialized batteries.⁷⁵ Using *in situ* cells avoid the drawbacks imposed by *ex situ* studies related to the preparation of samples in different redox stages, which also involves some risk of the electroactive phase being altered (evolution of metastable phases, contamination by air or humidity, etc.) during handling. Moreover, *operando* experiments enable an extension of studies to grasp the influence of the testing protocol (rate, temperature, etc.). For those reasons, *in situ* cells allowing *operando* studies are becoming a widely spread tool.

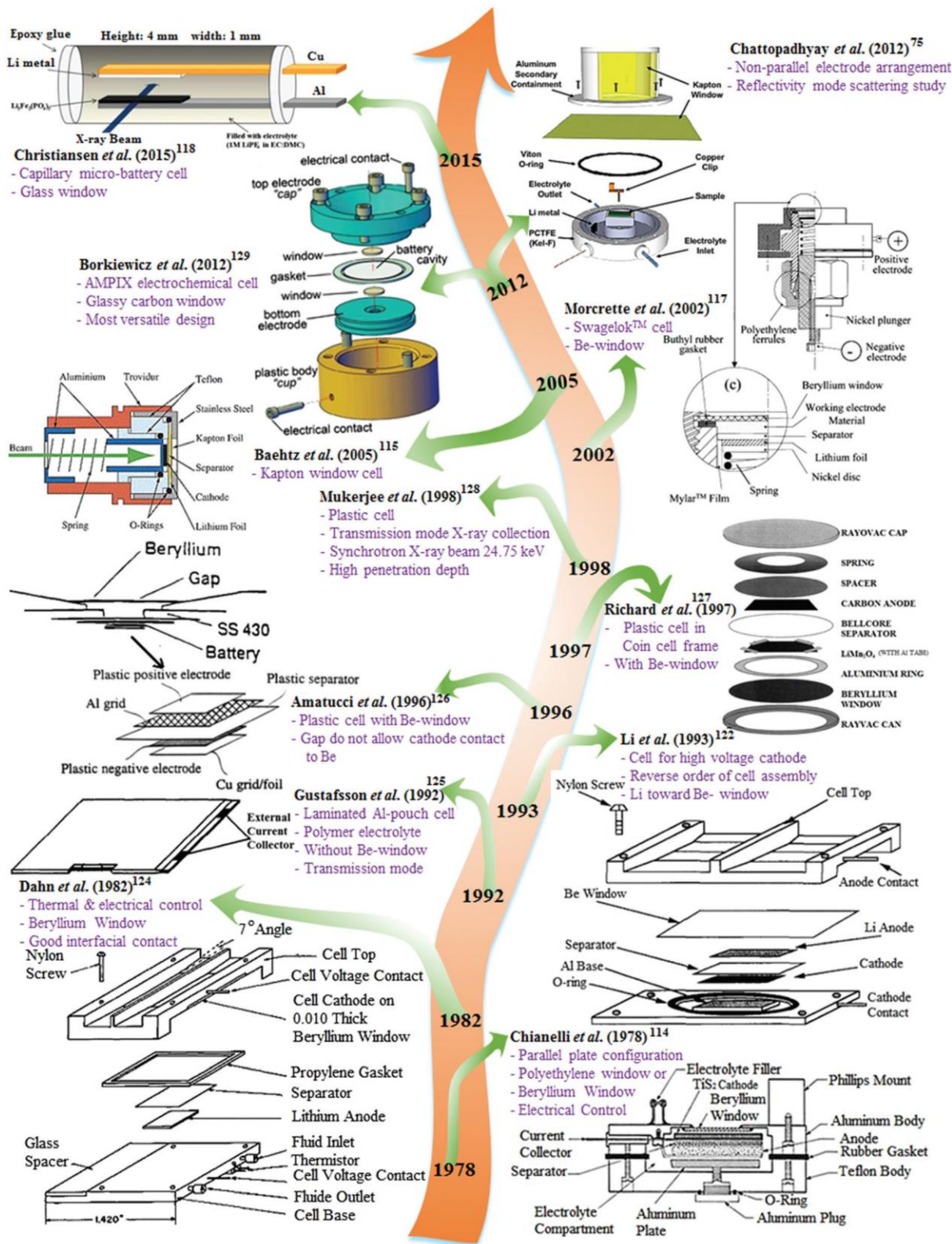


Figure II.13 - Different *in situ* cell geometry through the years, reprinted from ref 100

II.3.1. Choice of *in situ* cells element

II.3.1.1. Additional contributions from the other battery parts

Some practical considerations need to be taken into account when performing *in situ* X-ray diffraction. X-rays may interact (by absorption or diffraction) with all the cell components crossed by the beam, and it is important to carefully choose them.

Figure II.14 represent patterns collected in a Li vs TiS_2 *in situ* cell with different windows. The windows are usually made of beryllium (300 μm thick - fig II.14 a and b) which is a light element and thus has a low X-ray absorption and scattering factor. But because of beryllium toxicity or a risk of corrosion, other window materials are considered, especially to work at high temperature. To be used as windows, a material must meet the following properties: airtightness, electrical conductivity, rigidity as well as allowing X-ray penetration. Amorphous glassy carbon (300 to 500 μm thick) is an appealing alternative to beryllium since it is compatible with high temperatures and does not diffract nor absorb much X-rays but generates some characteristic background augmentation at low angles (fig II.14 c). Furthermore, these windows need to be handled carefully for their fragility – they are likely to break under too much stress and to compromise the cell airtightness. Aluminum (300 μm thick) can be used but its absorption is higher than beryllium and the active material will have low intensity in comparison (fig II.14 d). Note that on figure II.14, there might be some discrepancy between the theoretical value and the measured pattern: the cell was placed in such a way that the active material is in the center of the diffractometer, hence the windows are not centered and their diffracted peaks shifted. In the coin cells, the windows are made of glass (130 μm thick).

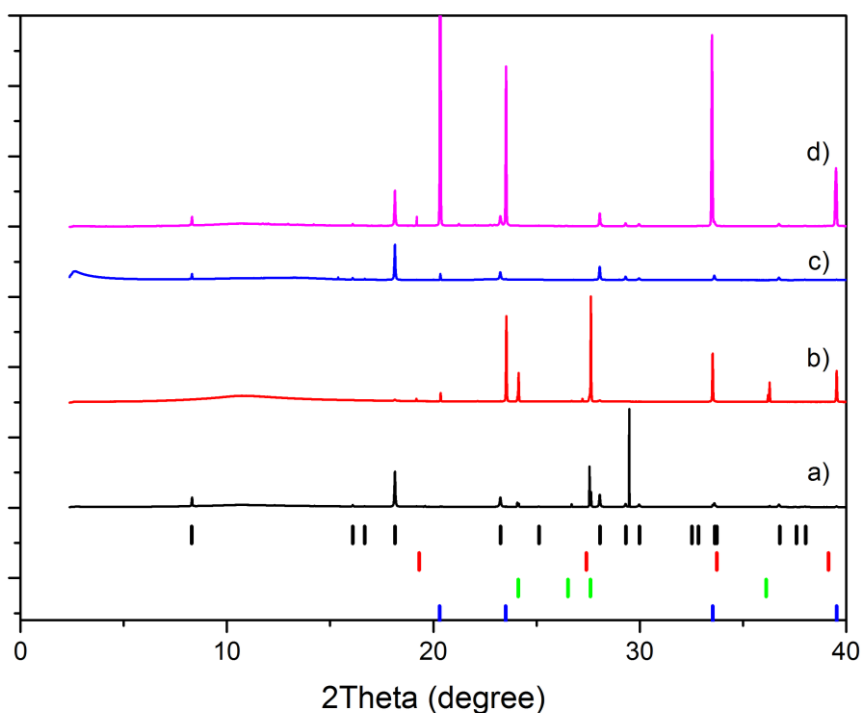


Figure II.14 - X-ray diffraction patterns of Li// TiS_2 cells with Al foil and a) Be window, b) Be window and tape, c) Glassy carbon window and d) Al window. Black ticks represent the position of TiS_2 peaks, red tick Li, green Be and blue Al.

In addition to the windows, thin metallic – aluminum (10 μm), copper (12.5 μm) or stainless steel (12.5 μm) – foil is added to protect the window from corrosion – and in the case of coin cell with non-conductive glass as windows, to ensure a uniform electrical conductivity. The experimental conditions determine which foil is best to use: for example it is better to avoid aluminum in cells used at high potential or containing an electrolyte with the TFSI anion. Calcium may also be incompatible with copper, therefore stainless steel is privileged when using $\text{Ca}(\text{TFSI})_2$ electrolyte.

When using a metallic negative electrode (lithium, sodium or calcium) additional intense peak may appear on the patterns. Punching a hole in this electrode could help avoiding those peaks, but there is a risk to alter the electrochemistry at the exact spot probed by X-rays hence possibly exhibiting a different electrochemical reaction than the rest of the electrode.

All the components mentioned above will contribute to the X-ray diffraction pattern (Fig II.14), sometimes with textured peaks (some of its reflections may appear more intense), and the peaks of the active material will appear with poor intensity. Although those additional peaks are intense, they do not saturate the detector thanks to the MYTHEN PSD dynamic range and longer acquisition time can be used to enhance the peaks of the active material. To minimize the absorption and diffracted peaks of these elements, it is possible to decrease their thickness to a certain extent, but preparing adequately the electrode is more critical to maximize the active material signal.

II.3.1.2. Electrode preparation for *in situ* experiment

For *in situ* experiments, it is generally recommended to use loose powder electrodes instead of casting on a tape for two reasons: casting the material on a tape (400 μm of composite + 18 μm Al) may induce severe preferred orientation with layered materials (see fig II.14 b), which may prevent the observation of some reflections, and the amount of material may not be enough to get pattern with high enough intensity values. By placing a thick pile of loose powder in the center of the beam, the amount of material probed – and therefore the signal – is higher and the risk of severe preferred orientation is minimized. Electrochemistry may not be as smooth as if the electrode was casted but it ensures that most of the material reacting is probed by the beam. When preparing the electrode, it is important to select additives that will not diffract X-rays. For example, one would rather choose amorphous polyvinylidene difluoride (PVDF) rather than polytetrafluoroethylene (PTFE) which exhibits diffraction peaks¹⁰¹ that may overlap with the studied material's peaks.

II.3.1.3. Advantages of *in situ* experiments in synchrotron

While *in situ* X-ray diffraction cell can be used in laboratory set up for routine test, they are used to their fullest potential in synchrotrons. The energy can be selected in order to maximize the active material's signal with respect to the other components. With such brilliant X-ray source, it is less problematic to use more absorbing materials (aluminum window, copper or stainless steel foil). Another advantage of the synchrotron is its high photon flux allowing the collection of good angular resolution pattern in a short amount of time: a 40° pattern can be measured in 30s while it would take several minutes (~15-20 min) with a laboratory diffractometer with rotating anode. This time resolution allows working at higher C-rate since the changes in the electrode material's composition will be negligible during the data collection, which is not the case for a pattern collected with longer

integration time. Monitoring extra-fast cycling (up to 25C!)¹⁰² is possible, although to better appreciate the ion (de-)intercalation, C-rates closer to real operating conditions (*ca.* C/10 - C/20) are preferred. In those cases, up to eight cells can be cycled at the same time.¹⁰³ However, experiments involving low C-rates (slower than C/50) are seldom taking place in synchrotron as the beamtime granted hardly exceeds 3 days, and better suit a laboratory setup.

X-ray diffraction data collection and electrochemical cycling are performed at the same time. The cell, mounted in the center of the diffractometer, is periodically illuminated by X-rays while a potentiostat is continuously connected to the cell to control the electrochemistry (see figure II.15). Then, the X-ray diffraction and electrochemical data are synchronized thanks to tailored programs. In figure II.15 c, the correlation between the GCPL and patterns measured with a Li//TiS₂ cell containing LIBOB 1M in EC:PC is presented as an example.

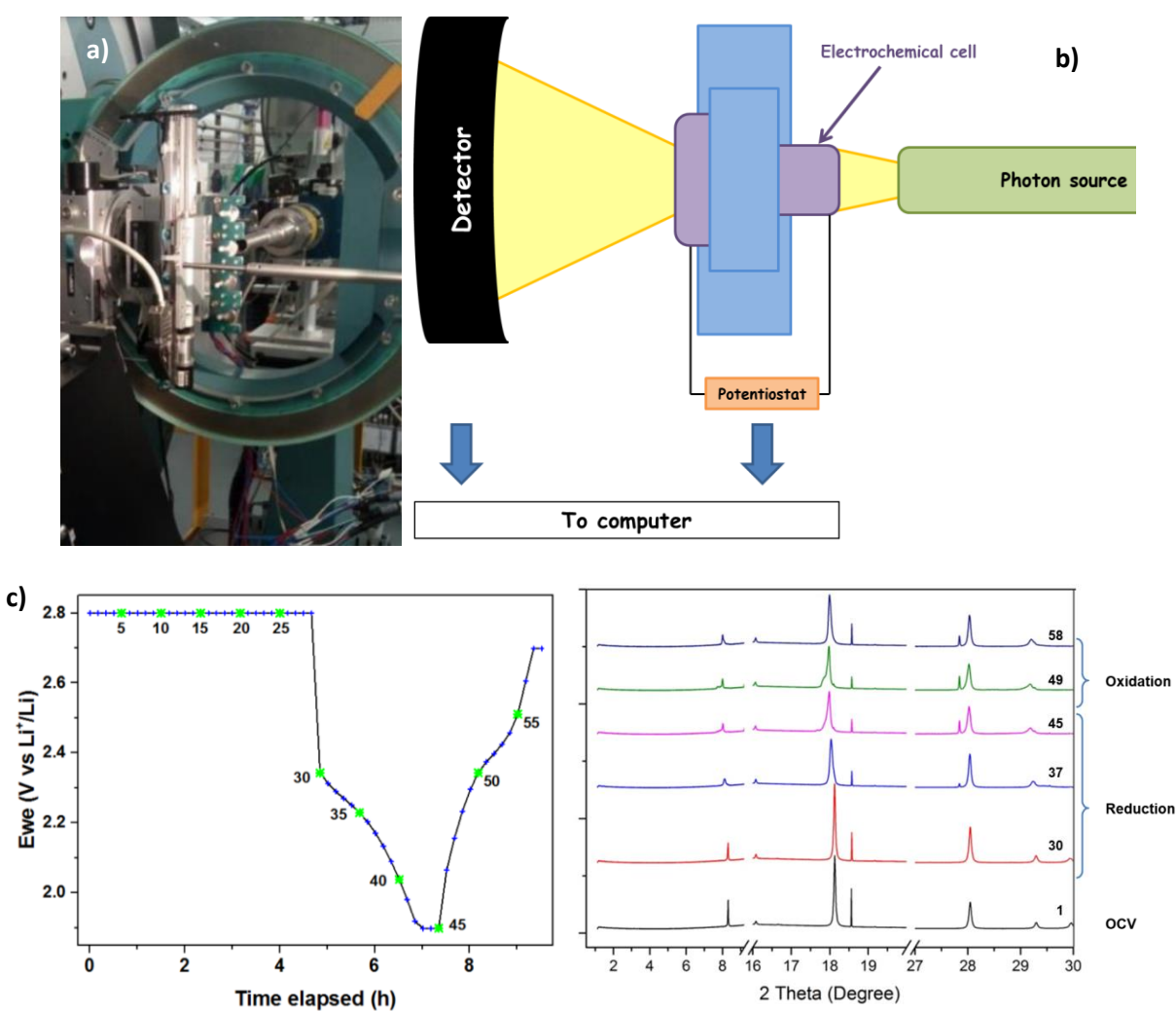


Figure II.15 - Cell mounting on the MSPD-beamline, a) picture of coin cells, b) schematic representation, c) example of electrochemical data and X-ray diffraction patterns collected at the same time

II.3.2. Cell thermalization

II.3.2.1. Types of cell used

In this thesis three types of *in situ* cells were used: the cell described by Morcrette in 2002 (Swagelok-like) and modified by Leriche (later referred as Leriche cell),⁷⁴ coin cells and a new prototype designed at Laboratoire de Réactivité et Chimie des Solides (LRCS – Amiens, France). The former cell was created with the idea of being used in laboratory setups, in both transmission and reflection mode, with different window apertures and plungers. It is composed of four parts: the main body, the lid, the plunger and the screw (see fig II.16). The main body and the lid are screwed together to enclose the window and the protective foil (labeled as part C); in that case, beryllium protected by aluminum. The cell's components (electrodes, separator, and electrolyte) are assembled in a standard way. A boPET (Mylar) or Kapton foil is used to prevent any contact between the plunger and the main body, and the cell is closed by the plunger and the screw. The plunger has a piston-like design, composed of two cylinders (Parts A and B) that can translate along each other thanks to a spring to ensure a good contact between the elements. At the top of the piston, a detachable cap allows the mounting of the second window. Thank to this plunger design, X-ray diffraction by transmission is possible, but can be replaced by a full plunger associated with a spring and current collector for reflection mode. Airtightness is ensured by three o-rings: one between the plunger's cylinders and one in contact with each window. A PTFE ferrule is also placed around the plunger between the main body and the screw: its objective is to keep the cell airtight while insulating the plunger from the main body. The electric contacts are placed on the plunger and on the screw corresponding to the CE and the WE, respectively. A Nylon 6,6 support was 3D printed by ALBA's engineering team to mount the cells on the beamline's motorized translation stage so that each cell crosses the beam in turn (fig II.16 c). In fact, the stage's range and the cells' width determine how much cells can be mounted at the same time: in that case, up to three cells.

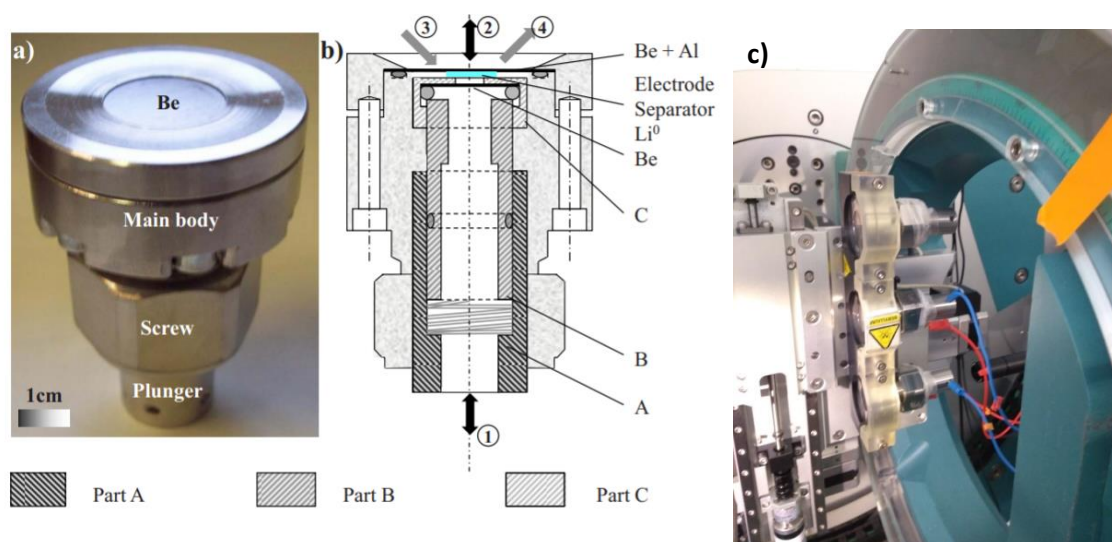


Figure II. 16 - Leriche cell a) photography and b) drawing. Reprinted from 74. c) Three cells mounted on the MSPD beamline

In situ coin cells differ from the regular design by holes in the casing and current collector. These holes are drilled by electroerosion of the stainless steel parts, making the surface smoother than a

mechanical drilling. A glass (130 μm thick) or a Kapton (75 μm) window is glued to the casing to seal the hole (in this thesis, only glass windows coin cells were used).¹⁰³ The cell is built by superposing the different parts (lower casing, protective foil, WE separator, CE, current collector, spring, seal and top casing) and sealed thanks to a MTI hydraulic crimping tool (fig. II.17 a, b). The voltage is measured between the upper (CE) and lower (WE) part of the casing. A 3D-printed support in tough resin (filament2print.com) for this kind of cells can hold up to four cells, but a carrousel-like setup can support up to eight cells.¹⁰³

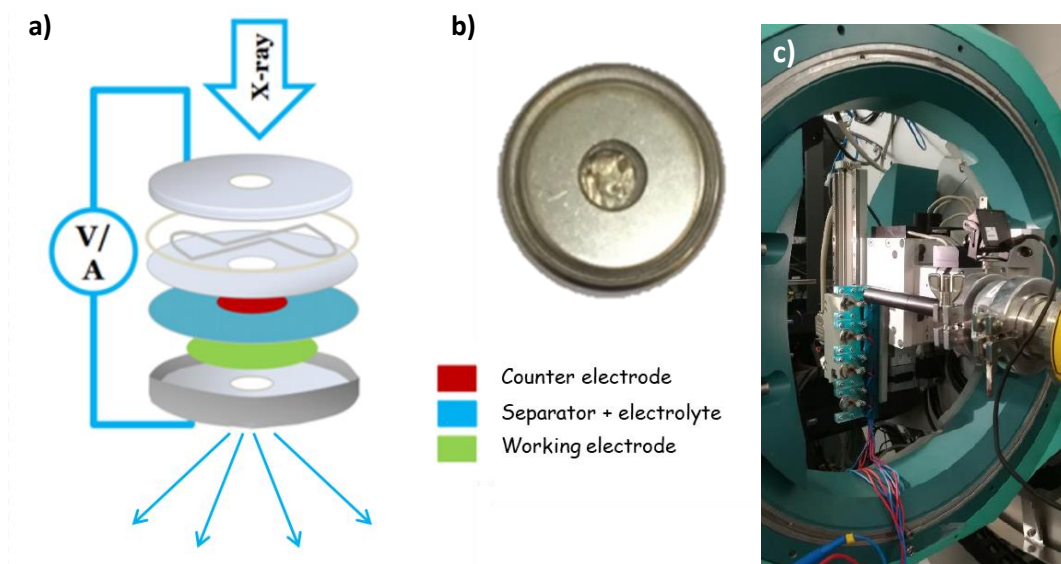


Figure II.17 - In situ coin cell a) representation, b) photography and c) mounting on the beamline

The last cell was used during the secondment at LRCs and called the “hexagonal cell”. Its design is similar to the Leriche cell but more compact. In the same way as described above, the window is inserted between the lid and the main body of the cell, where an o-ring keeps the cell airtight. The electrochemical components are put in place and the cell can be closed. This time, instead of a piston, the plunger is screwed in the cell, ensuring a sufficient, constant and reproducible pressure and a good contact between the parts. A second o-ring is located above the thread to ensure airtightness (fig. II.18 a). In that case, the voltage is measured between the plunger (CE) and one of the screws holding the lid and the main body together (WE). A full plunger is used for *in situ* data collection in reflection mode, but a hollow plunger can be used for transition mode. In that case, another o-ring is placed at the base of the plunger and a second window is inserted before closing the cell. The window can be made of beryllium or glassy carbon or fabricated by piercing a hole in a stainless steel current collector and polishing the surface before sticking a kapton tape on both sides to keep the cell airtight, as shown in figure II.18 b). A support in polylactic acid (PLA) was designed to mount the cell on a D8 discover X-ray diffractometer from Bruker with rotating anode (figure II.18 c).

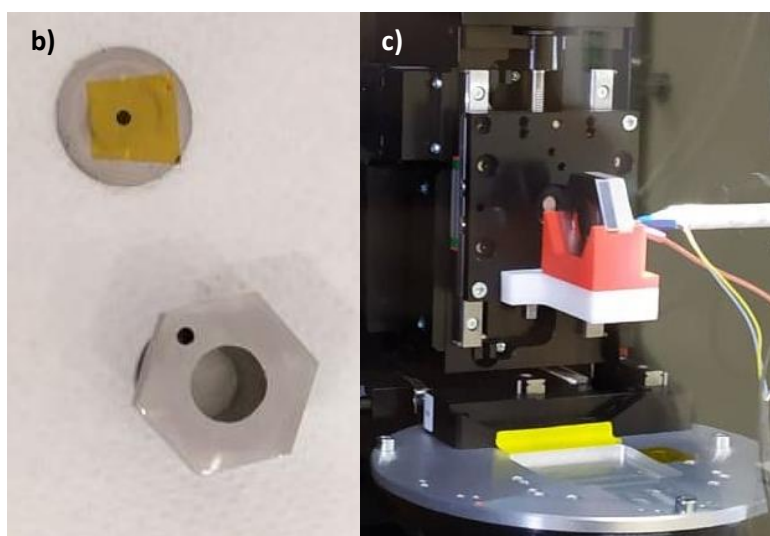
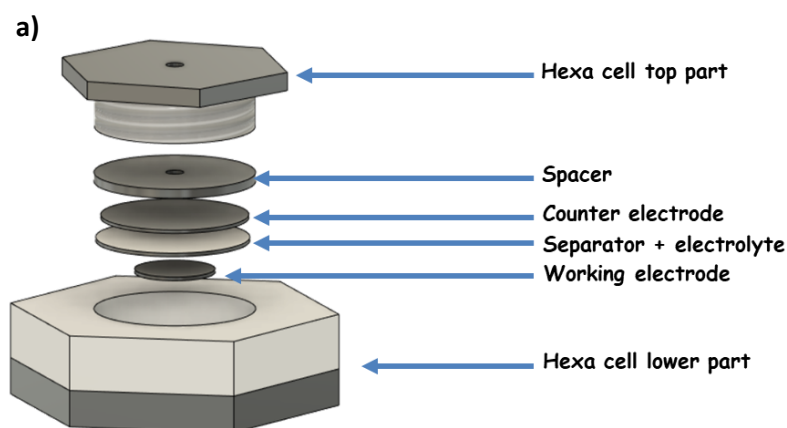


Figure II.18 - a) Exploded view of the hexagonal cell, b) plunger and stainless steel "window" used for transmission mode, c) cell mounted on the D8 discover diffractometer

II.3.2.2. Thermalization and calibration

With the three cells, thermalization is achieved by oil circulation as it allows both heating and cooling the cell and is unlikely to interfere with electrochemistry. Fluid circulation was ensured at ALBA by a Julabo CF31 chiller that can be remote controlled, used with the commercial silicon oil called "Thermal H10" (temperature range from -20°C to 180°C). The bath is connected to the electrochemical setup thanks to insulated PTFE pipes. Indeed, this material was chosen to avoid any electrical contact with the bath that could create parasitic electrical signal. The pipes are covered with foam to minimize the heat dissipation between the bath and the electrochemical setup.

On the Leriche setup, the former idea was to create a larger and thicker lid in which oil circulation is used to thermalize the cell (fig II.19 a). However, it increases the size of the already-large cell and more importantly, the lid's angle is too narrow to allow X-ray diffraction in reflection mode. A second prototype was designed (fig II.19 b), this time keeping the original lid but by modifying the main body to allow fluid circulation, the cell size being smaller than the first prototype. It is important to note that with this design, the cell is thermalized at the closest of the battery material. Again, a Nylon 6,6 support was used to mount two cells on the beamline.

The temperature calibration of the cell was made by collecting X-ray diffraction pattern of a SRM 640d NIST silicon standard enclosed in the cell. Set temperature of the oil bath was augmented by steps of 5°C and circulated in the cell thanks to the Julabo chiller and stabilized for 5 minutes, after which the pattern was collected and the temperature re-increased. By applying Rietveld refinement to the pattern, the silicon cell parameter were retrieved and compared to data collected in a Si capillary and thermalized using OXFORD 700 cryostream. The resulting calibration curve is presented in figure II.19 c). Two cells containing Si were prepared: one with aluminum and the other with a glassy carbon window to assess the dependence of the window material on the thermalization, but the results were the same. The calibration curve of the thermalized cell is similar to the data obtained by heating the capillary, although some discrepancy is visible at the lowest and highest temperature tested, proving the thermalization is efficient in our range of interest.

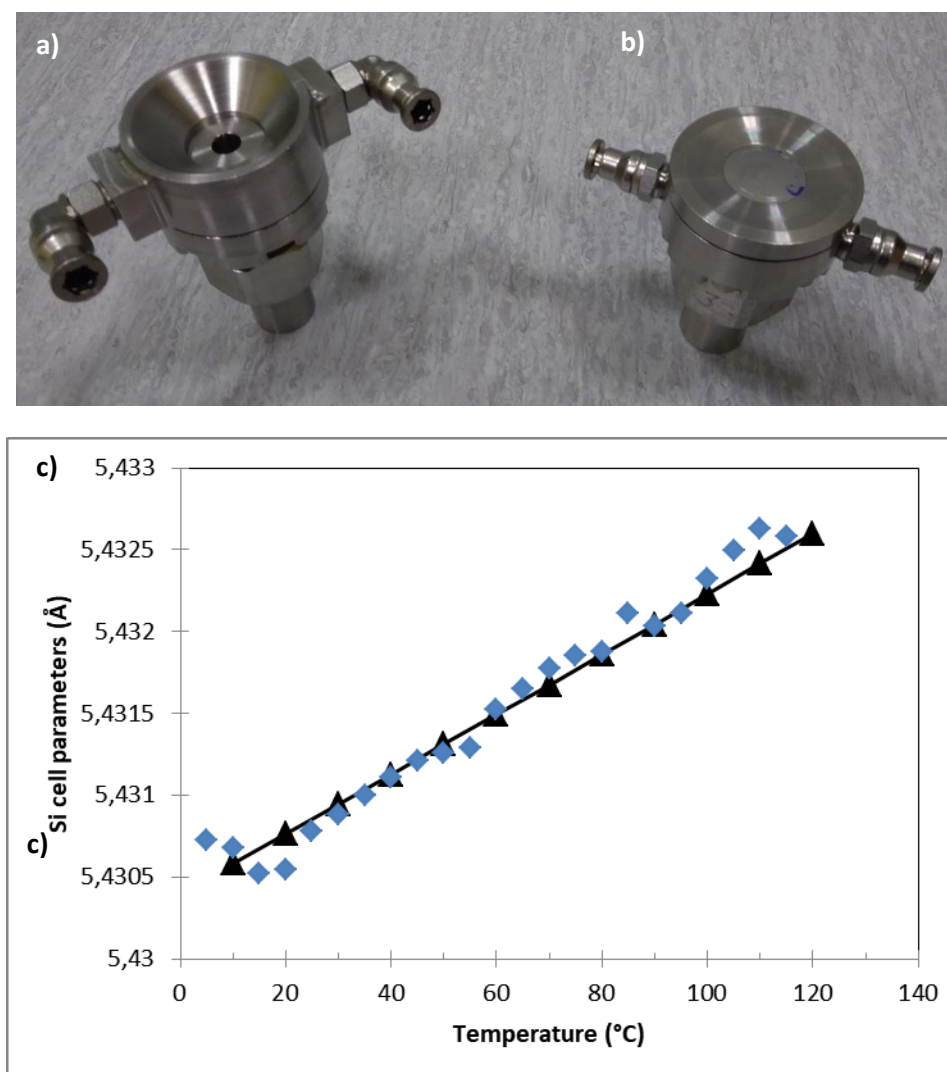


Figure II.19 - The two prototypes of modified Leriche cell, with oil circulating through a) the lid, and b) the main body part. c) Calibration curve of the second prototype: black line represents the data collected in capillary, blue dots the points collected with the second cell.

The two other cells being more compact than the Leriche cell, circulating fluid in their structure was impossible. The new approach was therefore to create a thermalized support. In the case of the coin cell, an oven was created, originally by circulating oil in two plates of polyoximethylene (POM) holding the coin cell. POM was chosen for its electrical insulating properties which are unfortunately coupled

with poor thermic conductivity. For that reason, the calibration performed with the same settings as above was not conclusive. Another prototype was conceived by replacing one of the sides by an aluminum plate and by placing insulating foam around the holder (fig. II.20 a and b), and a new calibration was done (Fig. II.20 c). This time, temperature steps of 2°C were applied but only a few points were selected for refinement in order to create the calibration curve. It seems that, although temperature can be monitored thanks to this setup, the thermalization is not as efficient as the modified Leriche – which may partly be imputed to the fast temperature steps.

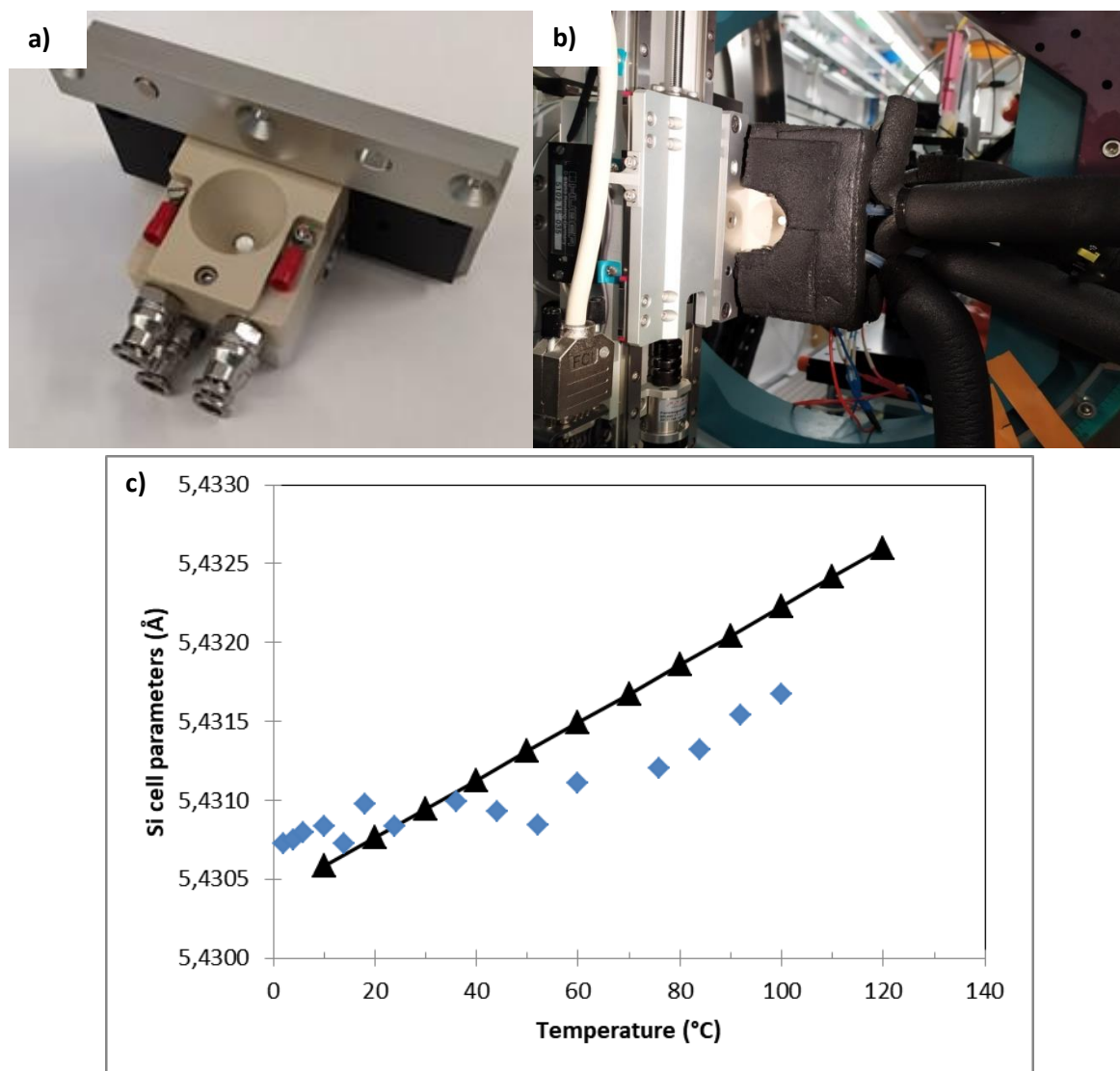


Figure II.20 –a) Cell mounting on the beamline and b) calibration curve of the first coin cell oven: black line represents the data collected in capillary, blue dots the points collected with the cell

For the hexagonal cell, LRCS designed a copper ring to encircle the cell. Before mounting the cell in the copper ring, it is important to stick Kapton tape around the cell to avoid any electrical contact between the cell and the ring. A polylactic acid (PLA) support allows the mounting of the cell in the diffractometer as shown in figure II.21 a) and b). Temperature calibration was performed at LRCS by placing a thermocouple on the window in contact with the WE and recording the temperature while the chiller applied temperature by steps of 10°C every 30 min (fig. II.21 c).

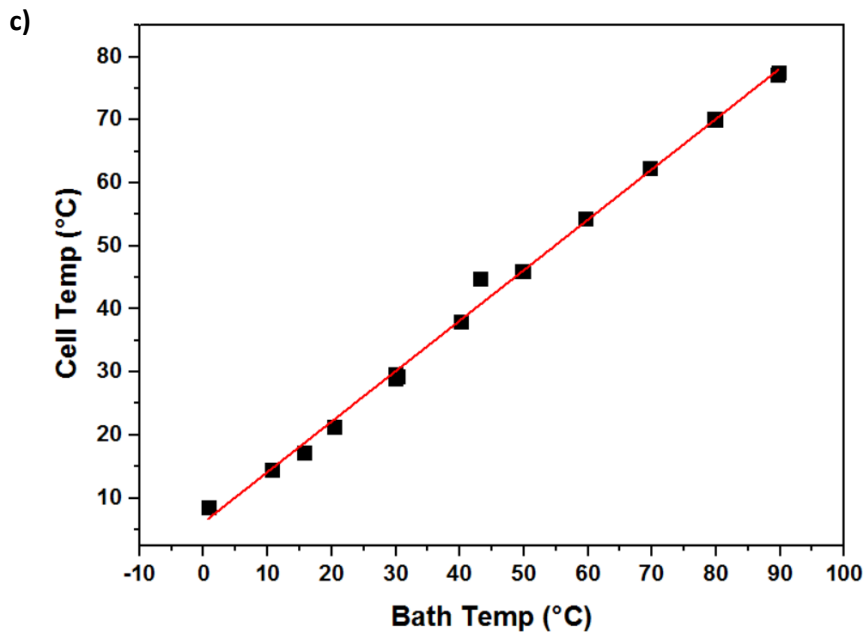
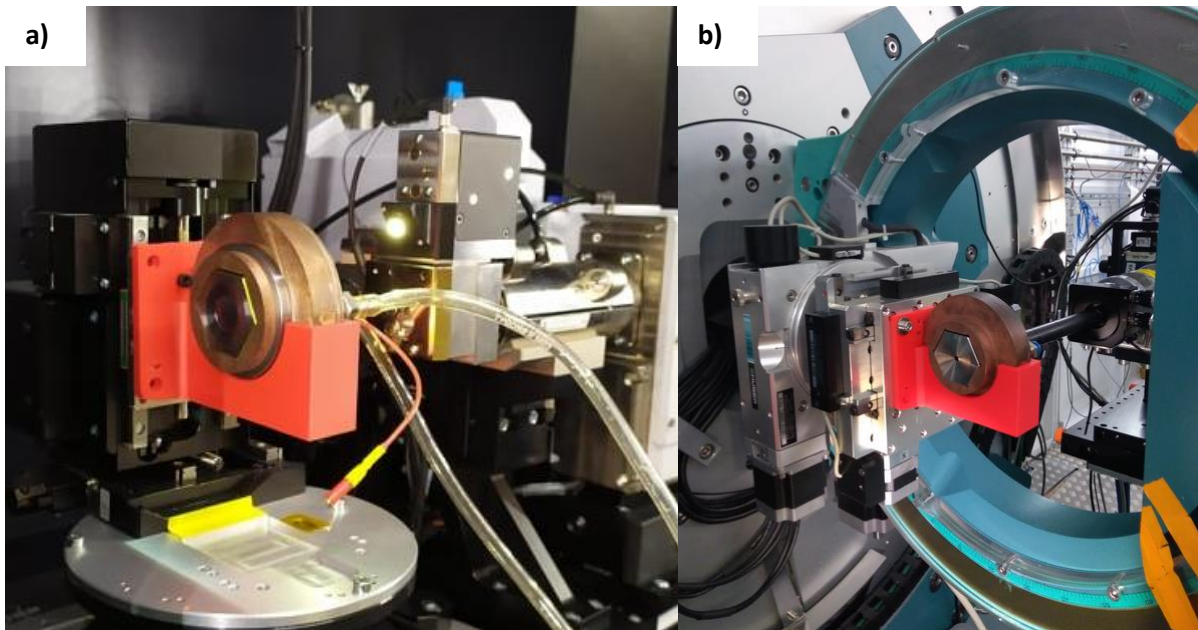


Figure II.21 - Hexagonal cell and its thermalized setup mounted a) on the D8 discovery and b) on the MSPD beamline, c) temperature calibration of the setup, courtesy of LRCS

To conclude this part, it is important to note that some problems arise when thermalizing the cells. Those issues were noticed when performing beamtime experiment and one goal of the thesis was to propose solutions to overcome them.

Heat dissipation at the surface of the pipes and the support is compensated by putting insulating foam around the different elements as mentioned above. Because the foam makes the manipulation harder and the pipes may be hot, it is sometimes difficult to properly make the connections between the pipes and the cells. In some cases, the fluid may leak which is not always noticed immediately since the setup is inside the closed hutch during the experiment. Thus, the heating bath will slowly loose liquid and the fluid circulation will be stopped, cancelling the thermalization. When working below room temperature, the pipes become harder and difficult to handle, and some condensation

appears on the setup, which can transform into ice if the temperature is below 0°C. This leads to a background augmentation or the apparition of ice peaks if water is condensed / frozen on the passage of the beam. The only possibility to get rid of this would be to operate in dry atmosphere, but by blowing a stream of dry nitrogen in front of the larger window (and not directly on it as it may affect the thermalization), one can reduce the amount of water condensing (fig. II.22). It was suspected that the water could also create parasitic electrical noise / short circuits, so the contacts were insulated by sticking Kapton tape before the start of the experiment.

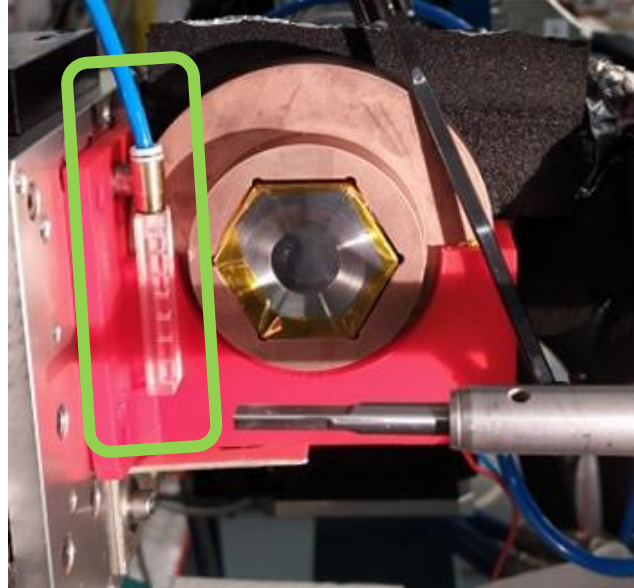


Figure II.22 - Placing a dry nitrogen blower (framed in green) to create a "screen" before the window helps avoiding too most of water condensation

III. Lithium insertion in TiS_2 and cointercalation

One of the scientific aims targeted within this PhD was to get further insights in the process of calcium intercalation in TiS_2 reported by Tchitchekova *et al.*⁷¹ in 2018, as stated in [section I.2.6.2](#). In that study, calcium intercalation took place at high temperature (100 °C) and involved the formation of a phase with large interlayer distance which was supposed to be due to electrolyte solvent cointercalation. To get a better understanding over the formation of cointercalated TiS_2 a comparative study was carried out on lithium systems which do exhibit faster kinetics and hence can also be studied at room temperature. These experiments were also useful to assess our room temperature setups. Early *in situ* and *operando* studies on this system aimed at elucidating the redox mechanism of TiS_2 from a structural point of view (typically single phase vs. two phase).^{73,104} The first *operando* study was performed by Chianelli *et al.*⁷³ and allowed to prove that the insertion mechanism was single phase with formation of a solid solution and, using complementary techniques, information on nucleation and diffusion was gathered throughout the cycle. Later on, Dahn and co-workers reinvestigated this mechanism with a different cell design.¹⁰⁴ The electrolyte used was at that time seldom considered as an essential parameter affecting the nature of the Li insertion process. Chianelli *et al.* used 2M LiClO_4 in dioxolane whereas Dahn and co-workers used 1 M LiAsF_6 in propylene carbonate (PC) and mentioned cointercalation of PC at high voltages, despite being deemed to be a minor feature and not further investigated. The same applies to electrochemical conditions. Chianelli *et al.* operated in standard galvanostatic mode (*ca.* C/16 to C/32), while Dahn *et al.* used similar rates but a much slower pulsed protocol enabling equilibration of electrode, which is assessed by comparing two patterns taken in open circuit with 10 h difference.

In this thesis, further *operando* studies on the intercalation of lithium in TiS_2 were carried out using synchrotron radiation with the aim of shedding further light on the influence of the electrochemical protocol and electrolyte used in the phases formed. In particular, LiPF_6 , LiBF_4 , lithium bis(trifluoromethanesulfonyl)imide (LiTFSI) and lithium bis-oxalatoborate (LiBOB) salts in different alkylcarbonates (including PC) were investigated. C-rates of either C/5 or C/15 were used and data were collected during the electrochemical cycling (*i.e.* without pausing the cell during data collection). This study unveiled some properties of the cointercalation and its correlation with the electrochemical response, enabling to get a more comprehensive picture of the process. The results presented are part of the paper entitled: "*Operando* Synchrotron X-ray Diffraction Studies on TiS_2 : The Effect of Propylene Carbonate on Reduction Mechanism".¹⁰⁵

III.1. Pristine sample characterisation

Titanium disulfide crystalizes in the hexagonal system, space group $P3m1$. Its structure is characterized by the presence of titanium atoms within sulfur octahedra which are sharing edges and form layers exhibiting a hexagonal stacking along the *c*-axis as represented in [figure III.1 a](#)). Those layers are stacked together, leaving a Van der Waals gap in which intercalation of neutral or charged species can take place ([Fig.III.1 b](#)). In batteries, the electroactive ion intercalation is concomitant with

the reduction of the titanium, going from a +4 oxidation state to a +3. Because of this lamellar structure, preferred orientation was expected for patterns corresponding to *in situ* cells but surprisingly occurred as well for samples sealed inside capillaries. Figure III.2 depicts the patterns and refinement corresponding to the electrode powder mix measured in a rotating capillary a) and a pattern collected in a coin-cell after its assembly b). In that case, the electrolyte used was LP30. All parasitic peaks, related to the aluminum current collectors or lithium foil, were excluded for the refinement. The patterns exhibit significant differences in the relative intensities of the 001 and 110 peaks. The 001 peak is the second most intense peak in the pattern corresponding to the capillary while its intensity is decreased by about half in the pattern corresponding to the cell. The peak ratio is also different when focusing on the 102 and 110 reflections. In the capillary, the 102 peak is more intense than the 110 while it is the opposite in the *in situ* cell. Patterns were refined using the Rietveld method taking the structure reported by Bear and McTaggart (ICSD card N° 651178).¹⁰⁶ For preferred orientation correction, the March function as implemented in the Fullprof suite was applied assuming orientation along the Z-axis. For the pattern corresponding to the capillary, the parameter translating the preferred orientation was found to be $Pref1 = 0.749$ while for the one corresponding to the *in situ* cells, in that case a coin cell, $Pref1 = 1.379$. The strong preferred orientation associated to the platelet-like TiS_2 crystallites was not totally suppressed by rotating the capillary. Indeed, the strong intensities measured on the 00l reflections indicate that the crystallites were stacked horizontally inside the 0.7 mm capillary, exposing the 00l planes parallel to diffraction plane and therefore over estimating the 00l reflections in transmission geometry. The same horizontal stacking of platelet-like crystallites takes place in the *in situ* cells but these are now allocated perpendicular to the beam minimizing the 00l and increasing the $hk0$ reflections collected at the detector in a transmission mode, but would remain visible in a laboratory diffractometer in reflection mode. In extreme cases, the 00l reflections completely disappear in synchrotron as shown in the previous chapter (see fig II.14).

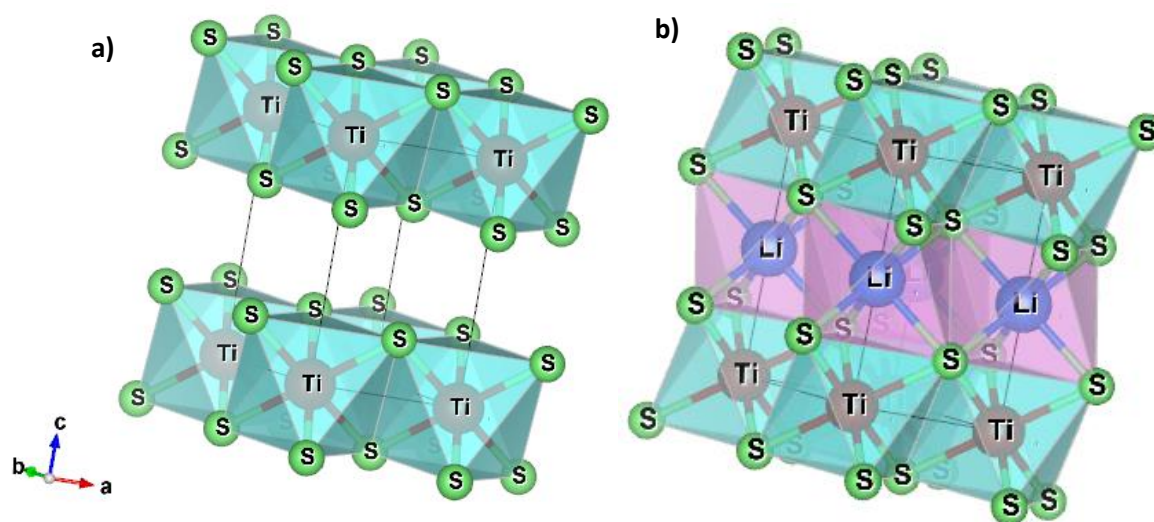


Figure III.1 - Representation of the structure of a) TiS_2 and b) $LiTiS_2$

Another feature clearly visible on both patterns resides in the background increase at angles lower than $2\theta \leq 20^\circ$ in the pattern corresponding to the capillary and a bump centered at $2\theta \sim 12^\circ$ in the one corresponding to *in situ* cells (see figures 1.a and 1.b respectively). The former effect arises from the amorphous carbon exhibiting scattering in the small angle regime.¹⁰⁷ The bump in background occurs only in *in situ* cells loaded with liquid electrolyte, and its intensity is higher than the carbon contribution. This background bump position is solvent dependent centered at 3.9 Å *d*-spacing for LP30 and gradually moving towards higher *d*-spacing when increasing the PC content, reaching 4.3 Å when the electrolyte only contains PC as a solvent, as depicted in figure III.2.c).

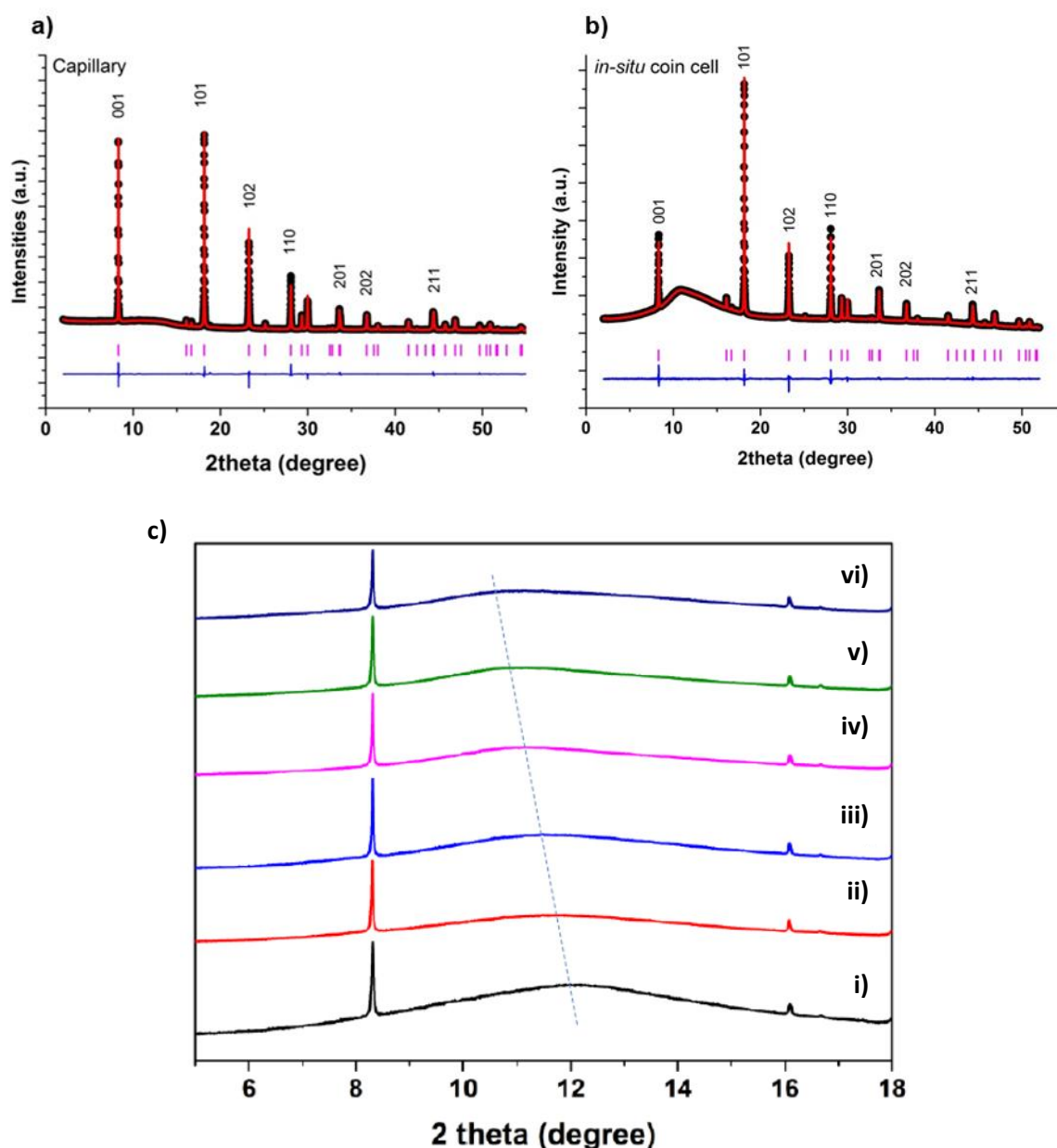


Figure III.2 -- Observed and calculated synchrotron X-ray powder diffraction patterns for TiS₂ electrodes measured a) in capillary and b) in an *in situ* cell assembled with LP30. C) X-ray diffraction patterns of a *in situ* cell loaded with TiS₂ and LiPF₆-based electrolytes i) 1M in EC:DMC (1:1), ii) LiPF₆ 0.67M in EC:PC:DMC (33:33:33), iii) 1M in EC:DMC:PC (2:1:2), iv) 1M in EC:PC (2:3), v) EC:PC (3:7) and vi) LiPF₆ 1 M in PC, close-up on the bump caused by the electrolyte. A dashline was added to show the bump center's position evolution.

III.2. Choice of electrolyte

In this study, four salts and three solvents were chosen to prepare the different electrolyte mixes. LP30 was used since it is the electrolyte used in commercial Li-ion batteries and LiPF₆-based electrolytes were thus prepared. LiBF₄- and LiTFSI-based electrolytes were chosen since they are the lithium equivalent to the calcium electrolytes that we anticipated to use in the Ca//TiS₂ study. During preliminary testing, we observed noisy oxidation when using LiBF₄ 1M in EC:PC electrolyte in a Li//TiS₂ cell cycled at 100°C (Fig. III.3), likely due to electrolyte decomposition, and was excluded from high temperature tests. Therefore, LiBOB-based electrolytes were added to the study in anticipation for thermalized tests. LiBOB decomposes at voltages below 1.8V¹⁰⁸ and it was used with a higher threshold voltage.

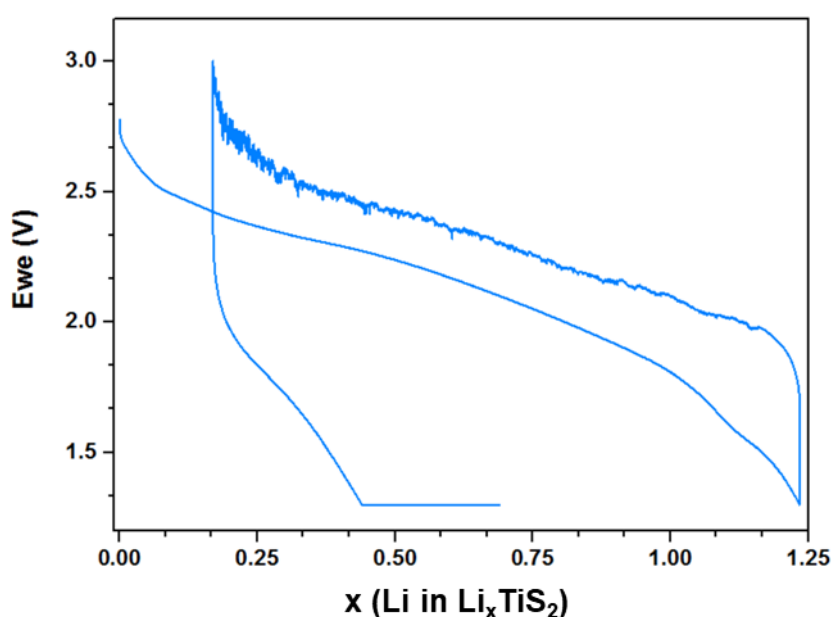


Figure III.3 – Potential vs capacity for a Li//TiS₂ cell at C/15 at 100°C with LiBF₄ in EC:PC electrolyte

III.3. Operando experiments

In situ cells were prepared using loose powder composite electrode as WE and lithium foil as CE. After an OCV period, the cells were cycled in GCPL at either C/5 or C/15 (*i.e.* inserting 1 mol of Li per mol of TiS₂ in 5 or 15 hours, respectively), starting with a reduction. The potential thresholds were fixed at 1.5V in reduction and 3V in oxidation, except when using LiBOB where the potential was limited to 1.8V upon reduction to avoid its degradation.¹⁰⁸ This prevented the complete Li insertion as was demonstrated by collecting data in the same voltage window but with LiBF₄ in EC:PC. To ensure that the phase is stable at the end of each oxidation or reduction cycle, the potential was fixed for 1h and several patterns were collected.

For this study, *in situ* coin cell and Leriche cell were used. The type of cell did not seem to have any impact on the results apart from the additional peaks from the beryllium windows used in Leriche cell. The *operando* measurements were conducted at ALBA synchrotron on the powder diffraction

station of the BL04-MSPD beamline,^{93,94} using the position sensitive detector MYTHEN⁹⁵ at 15 keV ($\lambda=0.826\text{\AA}$) beam energy. The XRD patterns were collected in the $\approx 2.3 \leq 2\theta \leq 48^\circ$ range, with 72 s effective integration time, ensuring 10 minutes frequency between successive patterns. Pristine electrode material was measured in a spinning 0.7 mm capillary to get better statistics. Cells were centered on the diffractometer by comparing the patterns with previously measured TiS_2 in capillary. This alignment procedure consisted in adjusting the position of the cell along the incoming beam. The lattice parameters were extracted from the patterns using the Le Bail refinement method as implemented in the FullProf suite software.¹⁰⁹

All data collection begins by, at least, a 1h OCV and no spontaneous reaction was observed, and the patterns were refined to find a lattice where $a = 3.409 \text{\AA}$ and $c = 5.700 \text{\AA}$. Such dimensions are in good accordance with data presented in literature.¹⁰⁶ Figure III.4 a, c and e displays the characteristic galvanostatic profiles of TiS_2 electrodes subjected to 1h OCV followed by GCPL tests at C/15 in coin cells. The electrolytes used were LP30, LiPF_6 in EC:DMC:PC (2:1:2) and LiTFSI in EC:PC (1:1), respectively. The corresponding *operando* XRD patterns collected with the routine described above are shown in figure III.4 b, d, and f. On the X-ray diffraction patterns b and f, the beam was lost for a short period, causing the loss of 5 patterns at the end of the reduction (from pattern 91 to 95 incl., represented by a horizontal blue line).

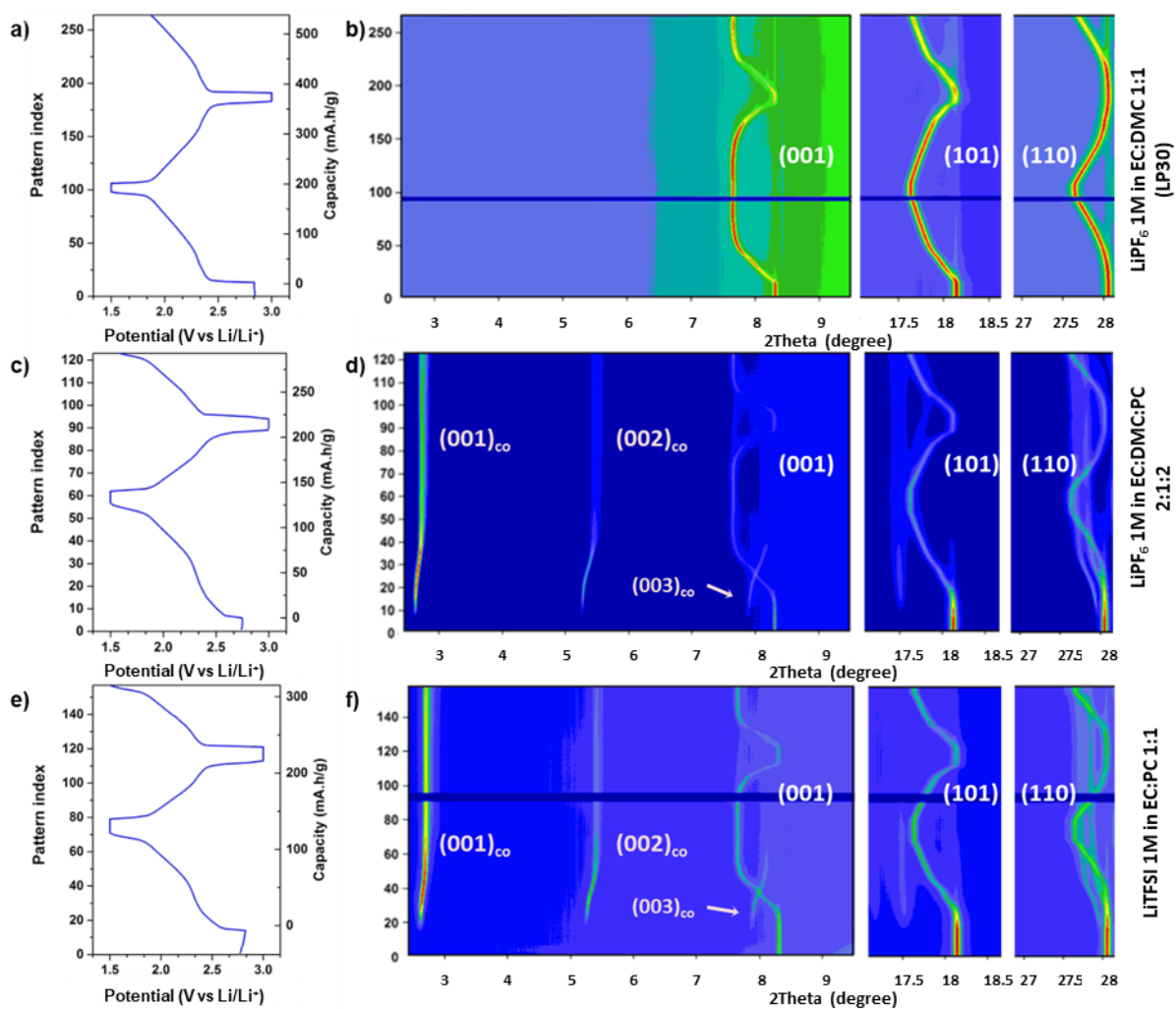


Figure III.4 – Pattern number (10min increment in time) vs voltage and associated X-ray surface plots of cells cycled with a) LP30, b) LiPF₆ 1 M in EC:DMC:PC 2:1:2 and c) LiTFSI 1 M in EC:PC 1:1.

The patterns corresponding to the cell cycled with LP30 are consistent with the typical lithium insertion process expected in TiS₂. During the reduction, the Li_xTiS₂ solid solution starts to form, as well documented previously^{73,104,110} and TiS₂ reflections shifting towards lower angles which indicate that the lattice is expanding, first along the *c*-axis, and later along the *a*- and *b*-axis. At the end of the reduction the lattice parameters were refined to find $a = 3.458 \text{ \AA}$ and $c = 6.187 \text{ \AA}$, in good accordance with values reported in literature for the LiTiS₂ phase.^{73,111,112} Upon re-oxidation, the reverse process takes place. A second reduction step was carried out highlighting the reversibility of the process.

To assess the coherence of our data, a comparison was made with the data published by Thompson¹¹¹ derived from blending TiS₂ and LiTiS₂ powders in different proportions and annealing them to achieve Li_xTiS₂ with different values of *x*. Figure III.5 a) presents the lattice parameters *a* and *c* corresponding to Li_xTiS₂ at different lithium contents obtained from Le Bail refinement of synchrotron diffraction data collected while cycling in two different PC-free electrolytes, in comparison with the values obtained by Thompson. While Thompson's data is presented with respect to the *x* calculated following the mixtures he prepared, our data was plotted directly using the *x* value deduced from the electrochemical experiments considering that lithium intercalation is

the only redox process taking place. The comparison was done for two experiments made with different electrolytes: LP30 cycled at C/5, and 1 M LiTFSI in EC:DMC (1:1)(v:v), cycled at C/15. In the early stages of reduction ($0 \leq x \leq 0.35$), the c -parameter increases rapidly with a sharp slope while the a -parameter grows moderately. Above $x > 0.35$, the c -parameter saturates at 6.19 Å while the slope of the a -parameter increases progressively until reaching 3.458 Å for one inserted lithium.¹¹¹

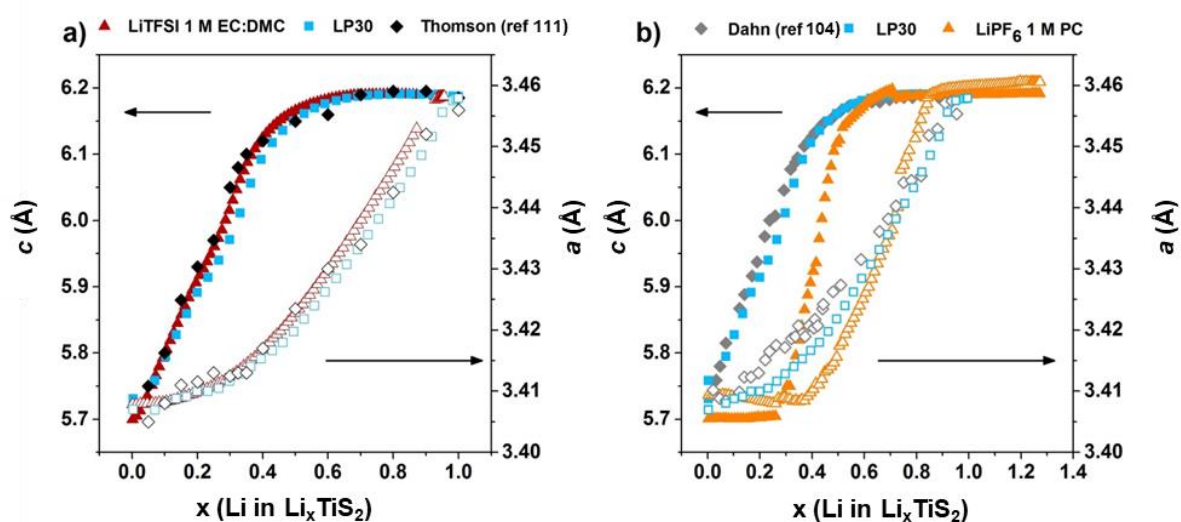


Figure III.5 -- Comparison of the Li_xTiS_2 phase lattice parameters upon reduction for experiments carried out with different electrolytes. Full symbols represent the c -axis parameter (left), empty symbol the a -axis (right). a) Black diamonds are the data retrieved from ref 111, blue squares correspond to data resulting from the experiment carried out with LP30 electrolyte at C/5 and red triangles to those derived from 1 M LiTFSI in EC:DMC (1:1) at C/15. b) Grey diamonds represent data taken from ref 104, blue squares correspond to data resulting from the experiment carried out with LP30, and orange triangles to 1 M LiPF₆ in PC.

In the case of PC-containing electrolytes (figure III.4 d, f and III.6) the X-ray diffraction patterns exhibit intense peaks at $2\theta \approx 2.7^\circ$, 5.4° and 8.1° appearing at the very early stage of reduction together with the peaks corresponding to Li_xTiS_2 . These values correspond to significantly large real space d -spacing (17.52, 8.76 and 5.85 Å at the end of the reduction, respectively for the 3 first reflections), which is approximately three times larger than the pristine lattice along the c -axis. Some low angle peaks with similar d -spacing were also mentioned by Dahn and $(17.8 \text{ Å})^{104}$ and Whittingham $(18.4 \text{ Å})^{110}$ and related to propylene carbonate cointercalation but not further investigated. This new phase exhibiting an expanded c -parameter will later be mentioned as cointercalated phase. To study in depth this phenomenon a series of *operando* experiments with different salts and PC containing solvents have been conducted.

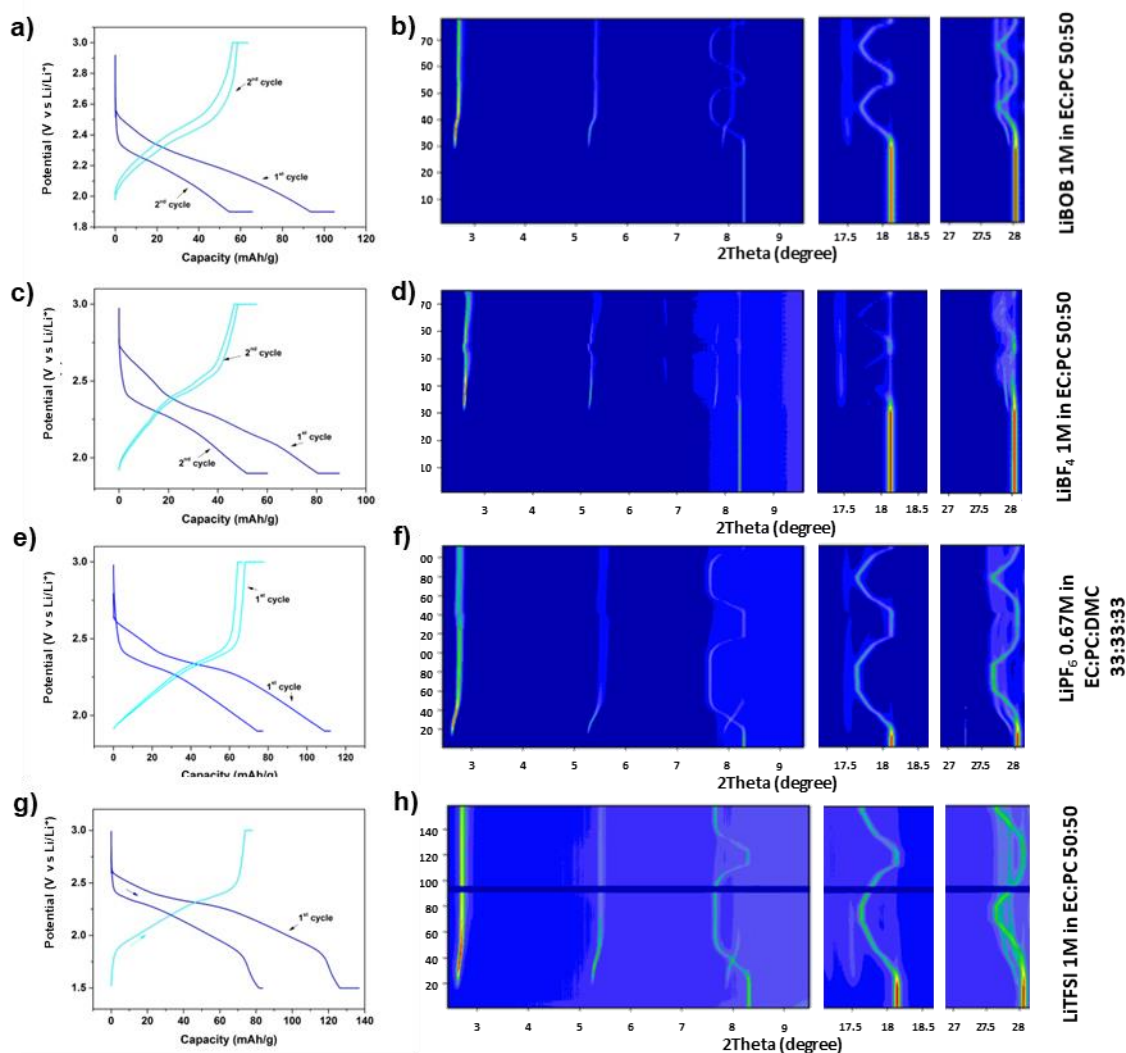


Figure III.6 - - In operando X-ray surface plots of cells cycled twice in a-b) 1M LiBOB in EC:PC (50:50), c-d) 1M LiBF₄ in EC:PC (50:50), e-f) 0.67M LiPF₆ in EC:PC:DMC (33:33:33) and g-h) 1M LiTFSI in EC:PC (50:50). The two former were cycled at C/5 and the two latter at C/15

Concomitant to the formation of the cointercalated phase, the intensity of the Bragg reflections of the TiS₂ phase drops by 70-80% as depicted in figure III.7. Interestingly, in the early stages of lithium insertion, while the reflections of the Li_xTiS₂ phase drift towards lower angles, the reflections of the cointercalated phase shift toward higher angles, indicating a contraction of the lattice from 17.96 Å to 17.52 Å in average (from 2θ = 2.63° to 2.70°). Though no explanation was found, this phenomenon is reproducible. Upon reoxidation, the cell parameters of Li_xTiS₂ phase decrease as lithium is deinserted, but the peaks corresponding to the cointercalated phase remain unchanged, which was already documented by Dahn.¹⁰⁴ However, this phenomenon is not irreversible in all systems as described by Tchitchekova⁷¹ and Verrelli in the case of calcium.⁷² Tchitchekova *et al.* were using Ca(BF₄)₂ 0.45 M in EC:PC at 100°C and Verrelli *et al.* were using either Ca(BF₄)₂ or Ca(TFSI)₂ 0.3 M in PC, at either room temperature, 60°C or 100°C. In all these cases, a phase similar to ours was observed, with larger cell parameters, which disappears upon reoxidation, indicating a reversibility of cointercalation in those cases. We tentatively ascribed this difference of reversibility for the cointercalated phases in Li and Ca cells to the fact that Li and Ca cation complexes present different

coulombic interactions with the host structure. Note also that Tchitchekova⁷¹ mentioned a cointercalated phase appearing upon reduction with $\text{Mg}(\text{TFSI})_2$ 0.3 M in EC:PC but no re-oxidation was performed on that paper, therefore we cannot conclude on the reversibility of the cointercalation in this system. Though the cointercalation is irreversible with lithium, it is still possible to perform further reduction/oxidation cycles, with the only changes observed being related to the Li_xTiS_2 phase, as proven by the second reduction performed on these two cells. Other experiments carried out using both types of *in situ* cells, faster C-rates, other solvent mixtures and salts are coherent with the data presented (see figure III.6 and III.8).

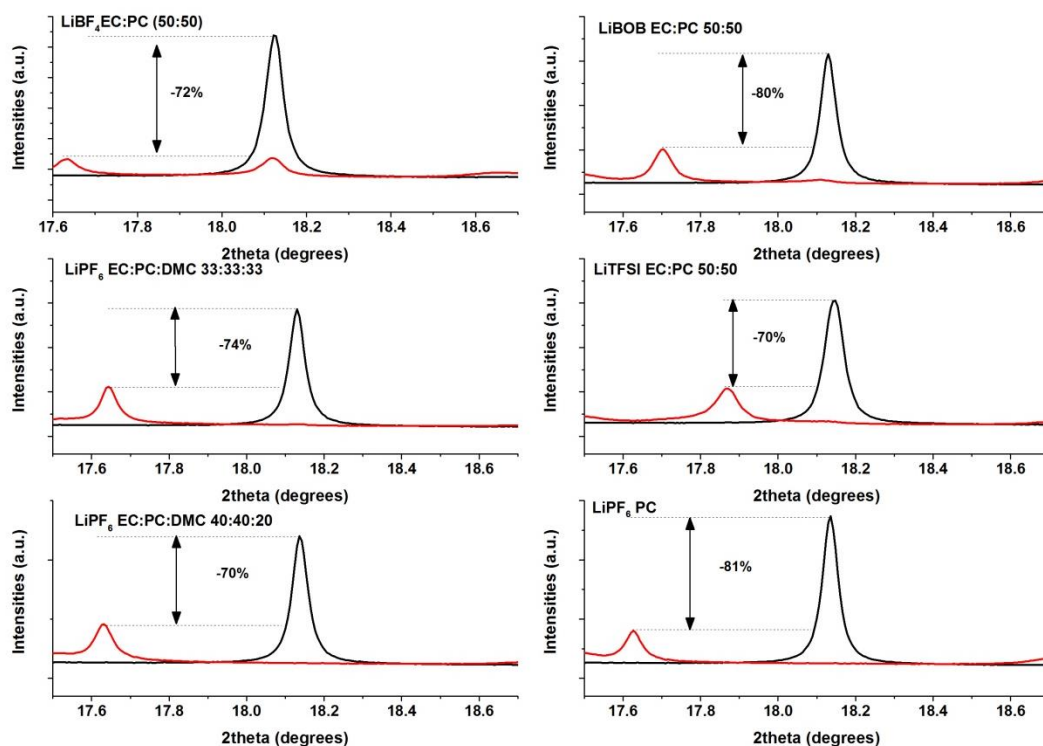


Figure III.7 - Comparison of the 101 reflection's integrated intensity on the pristine material and on the material at the end of the reduction

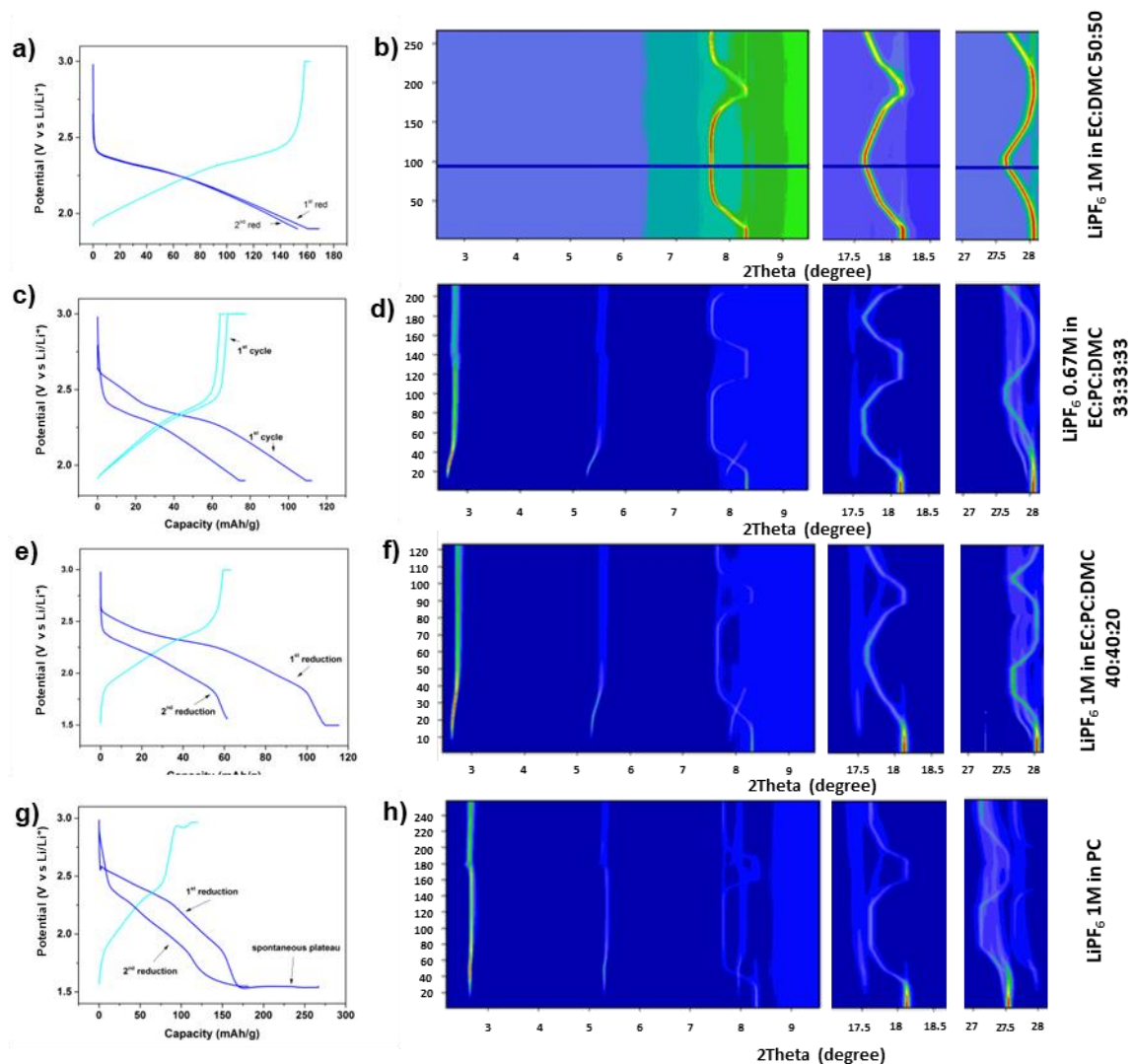


Figure III.8 – Capacity vs potential of TiS_2 positive electrodes and corresponding SXRD surface plots in LPF_6 electrolytes, 1M in EC:DMC 50:50 (a-b), 0.67M in EC:PC:DMC 33:33:33 (c-d), 1M in EC:PC:DMC 40:40:20 (e-f) and 1M in PC (g-h), all at C/15.

The a and c parameters of the Li_xTiS_2 phase as function of the lithium inserted using LP30 and 1 M LiPF_6 in PC at C/5 rate are shown in figure 3 b, The results are compared with those reported by Dahn and co-workers in an *in situ* cell using 1 M LiAsF_6 in PC as electrolyte.¹⁰⁴ Although Dahn's and Thompson's¹¹¹ curves are similar, we observe a discrepancy with our data at early stages of reduction ($0 \leq x \leq 0.28$) resulting in a smaller hysteresis. Knowing from figure III.4 d and f that PC is cointercalated at early stage of reduction, the range $0 \leq x \leq 0.28$ shown in figure III.5. b does not correspond to the real amount of lithium in Li_xTiS_2 . A method to calculate the experimental capacity related to the formation of Li_xTiS_2 will be developed later in this chapter.

In order to get further insights into the structure evolution of the cointercalated phase trough the reduction process a Le Bail refinement was carried out for the XRD patterns corresponding to early stages and at the end of the first reduction of TiS_2 electrodes cycled in 1 M LiPF_6 in EC:DMC:PC 2:1:2 electrolyte shown in figure II.4 b), pattern 15 and 60, respectively. The results are displayed in figure III.9 The patterns were refined considering two phases, the Li_xTiS_2 that follows lattice parameter evolution related to the formation of the solid solution through the reduction process and

a cointercalated phase that appears at early stages of reduction characterized by its low angle reflections at $2\theta \approx 2.7^\circ$, 5.4° and 8.1° . Both phases were fitted in the hexagonal space group $P\bar{3}m1$. In [figure III.9 a](#), in addition to these two phases, aluminum and lithium from the current collector and CE, respectively, are considered in the fitting while for [figure III.9 b](#) they were considered as excluded regions for aim of clarity. The lattice parameters of the cointercalated phase were found to be $a = 3.514 \text{ \AA}$ and $c = 17.931 \text{ \AA}$ at early stages of reduction (pattern 15) and $a = 3.5835 \text{ \AA}$ and $c = 17.155 \text{ \AA}$ at the end of first reduction (pattern 60). Attempts to probe the configuration of the cointercalated PC molecule by IR were hindered by the low resolution of the spectra in the carbonyl stretching region.²⁶

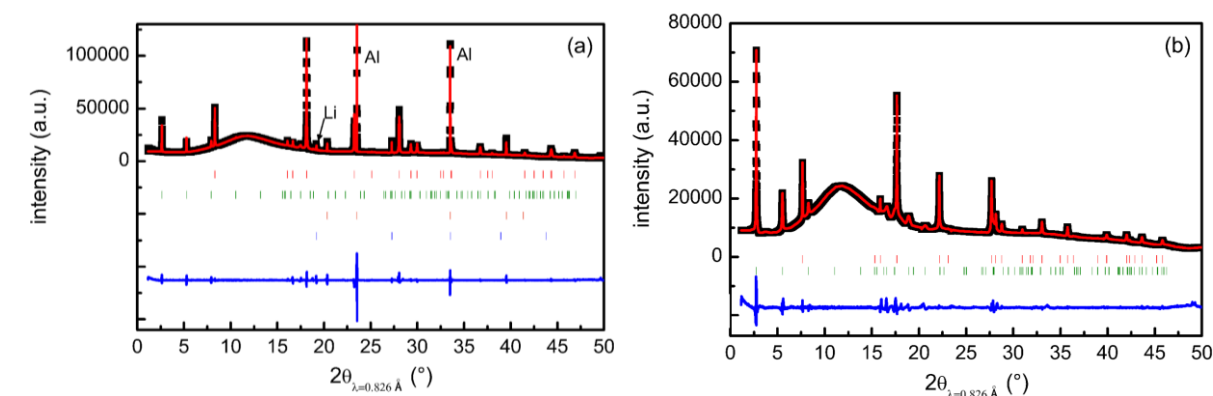


Figure III.9 - Le Bail profile fitting corresponding to the beginning of cointercalation (pattern 15) (a) and the end of the reduction (pattern 60) (b) of TiS_2 electrodes cycled in 1M LiPF_6 in EC:PC:DMC 40:40:20 electrolyte, upper ticks correspond to calculated reflection of Li_xTiS_2 (red), upper middle for cointercalated, lower middle for Al (orange) and lower ticks are for Li metal (blue). Black dots represent the observed intensity, red line the calculated one and the blue line the difference between the experimental and calculated pattern.

To assess the independence of the cointercalation from the salt and to make sure the presence of PC in the electrolyte is the only key factor triggering the cointercalation process, reduction was performed using the four salts tested in a solvent mix that contained PC, using the same configuration and program as before, except for the cell containing LiBF_4 where a Leriche cell was used instead of coin cell. The electrolytes tested were 1 M of either LiBOB (i), LiBF_4 (ii) or LiTFSI (iv) in EC:PC (1:1) and PC added to LP30 resulting in a 0.67 M LiPF_6 in EC:DMC:PC (33:33:33) electrolyte (iii). The voltage vs. capacity plots for the first reduction are presented in [figure III.10 a](#)). Patterns have been collected *operando* through the whole reduction and reoxidation, (see [figure III.6](#)) but only the last pattern of the reduction is presented in [figure III.10 b](#)) to compare eventual structural changes. The reduction curves are similar with no significant impact of the salt. A little bump is visible at low capacity around 2.5 V on the reduction curve of the cell containing LiBOB , but this feature is not salt dependent and will be discussed later. Regarding the diffraction pattern, in addition to the Li_xTiS_2 reflections, new peaks can be observed, principally at low angles ($2\theta \approx 2.7^\circ$, 5.4° and 8.1°) as it was hinted in [figure III.4](#). Patterns were normalized with respect to the LiTiS_2 001 reflection (7.64°). Peak intensities are comparable in all cases, indicating that the nature of the anions present in the electrolyte does not have a significant influence in the formation the cointercalated phase. Patterns corresponding to reduction of TiS_2 in cells using the same electrolyte salts but either EC or EC:DMC (1:1) as solvents do not show any cointercalation peaks, indicating that these are triggered by the presence of PC.

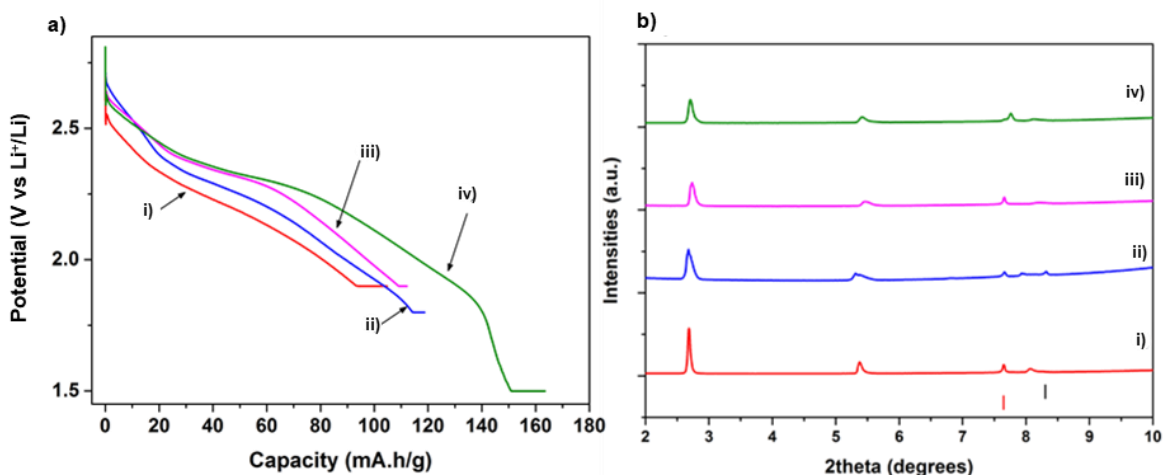


Figure III.10 – Electrochemical reduction curve (a) and last reduction SXR patterns (b) of cells cycled with i) 1 M LiBOB in EC:PC (1:1), ii) 1 M LiBF₄ in EC:PC (1:1), iii) 0.67 M LiPF₆ in EC:DMC:PC (33:33:33) and iv) 1 M LiTFSI in EC:PC (1:1). Black and red ticks represent the 001 reflection of pristine TiS₂ and LiTiS₂ respectively.

Figure III.11 a) depicts synchrotron X-ray diffraction patterns of titanium disulfide electrodes at the end of reduction for cells cycled with LiPF₆-based electrolytes but different PC content. The electrolytes tested were 1 M LiPF₆ in EC:DMC (1:1), 0.67 M LiPF₆ in EC:DMC:PC (33:33:33), 1 M LiPF₆ in EC:DMC:PC (2:1:2), 1 M LiPF₆ in EC:PC 2:3, 1 M LiPF₆ in EC:PC 3:7 and 1 M LiPF₆ in PC. Patterns were normalized with respect to the LiTiS₂ 001 reflection (7.64°). The electrochemical curves and the X-ray diffraction data collected throughout the full experiment (two cycles) are presented in figure III.8. A pseudo plateau is visible on the cell cycled with the electrolyte containing 100% PC (figure III.8.g) at ca. 1.55V after inserting ≈ 0.8mol of lithium. In all electrolytes, the reflections of both Li_xTiS₂ and cointercalated phases are found at the same position, meaning that the cell parameters of the cointercalated phase are not dependent on the electrolyte composition. However, the intensity of the peaks related to the cointercalated phase increases with the PC content, while the intensity of the peaks related to Li_xTiS₂ phase decrease. In an attempt to quantify the amount of cointercalated phase formed, the ratio between the intensity of the 001 peak of the cointercalated phase at the end of the reduction and the 001 peak of the pristine TiS₂ was calculated for each electrolyte. The resulting values are plotted as a function of the PC content in the electrolytes in figure III.11 b). As the amount of PC in the electrolyte increases, the ratio between the two phases increases, confirming the observation that more cointercalated phase is formed, the maximum of intensity being observed with the LiPF₆ in 100% PC electrolyte.

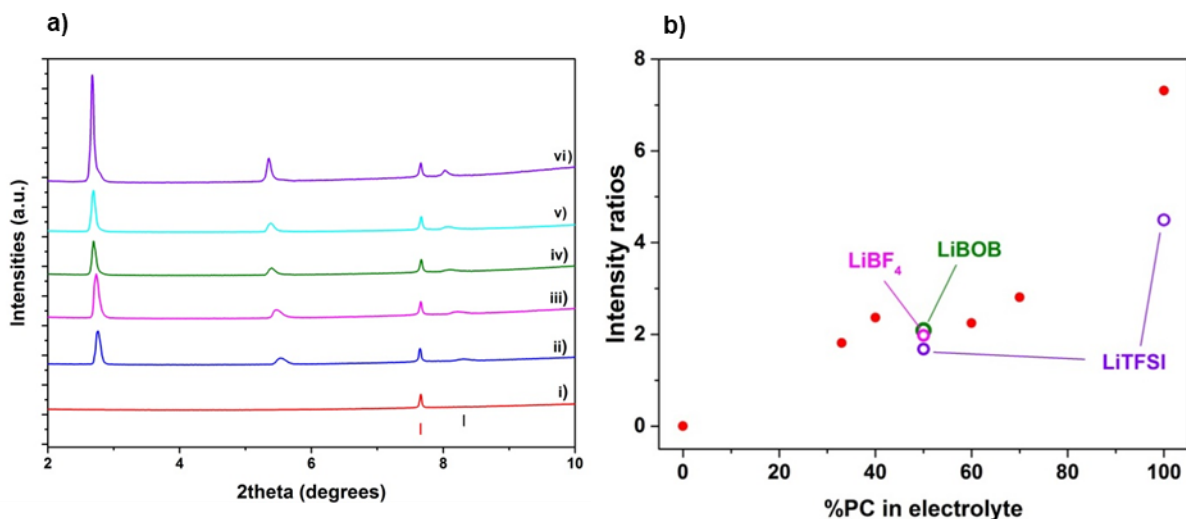


Figure III.11 – a) Last reduction SXRD pattern of cells cycled with LiPF₆ based electrolytes, i) 1 M in EC:DMC (1:1), ii) 0.67 M in EC:PC:DMC(3:3:3), iii) 1 M in EC:PC:DMC (2:2:1), iv) 1 M in EC:PC 2:3, v) 1 M in EC:PC 3:7 and vi) 1 M in PC. Black and red ticks represent the 001 reflection of pristine TiS₂ and LiTiS₂, respectively; ii) intensity ratio between the 001 cointercalation peak and 001 pristine TiS₂ peak as a function of the proportion of PC in the electrolyte. Red dots correspond to LiPF₆-based electrolytes, pink circle to LiBF₄, green circle to LiBOB and purple circles to LiTFSI

In an attempt to link the capacity loss with the phases present in the electrode, figure III.12 a) was built similarly to figure III.5. Figure III.12 a and b presents the lattice parameters a and c of Li _{x} TiS₂ at different lithium contents obtained from Le Bail refinement of synchrotron operando diffraction data collected in either LP30 or 0.67M LiPF₆ in EC:DMC:PC (33:33:33), in comparison with the data from ref 104. The corresponding electrochemical curves are presented in figure III.13. In this case, the plot seems to be compressed along the x -axis, the data not matching Dahn's trend. Indeed, the x is calculated considering that the only electrochemical process taking place is lithium insertion into TiS₂ to form Li _{x} TiS₂, without taking into account the charge related to formation of the cointercalated phase. Thompson¹¹¹ described three pseudo-linear zones of the curves: between $x = 0$ and $x = 0.35$ for both a and c parameter, and between $x = 0.35$ and $x = 1$ for the a -parameter only. Linear regression was applied to these zones on the curve corresponding to LP30 to obtain formulas linking the lattice parameters and x . Thanks to these formulas the x was recalculated and fits better the curve from Dahn and LP30, which is representative of the amount of lithium inserted. This confirms that the formation of the cointercalated phase does not affect the formation of Li _{x} TiS₂. Moreover, as seen in figure III.4, the cointercalation is irreversible. This seems to indicate that the TiS₂ particles that reacted to form the cointercalated phase are unable to de-intercalate lithium afterwards, creating an electrochemically dead mass with respect to the Li intercalation which is coherent with the reversible capacity loss observed (see figure III.13).

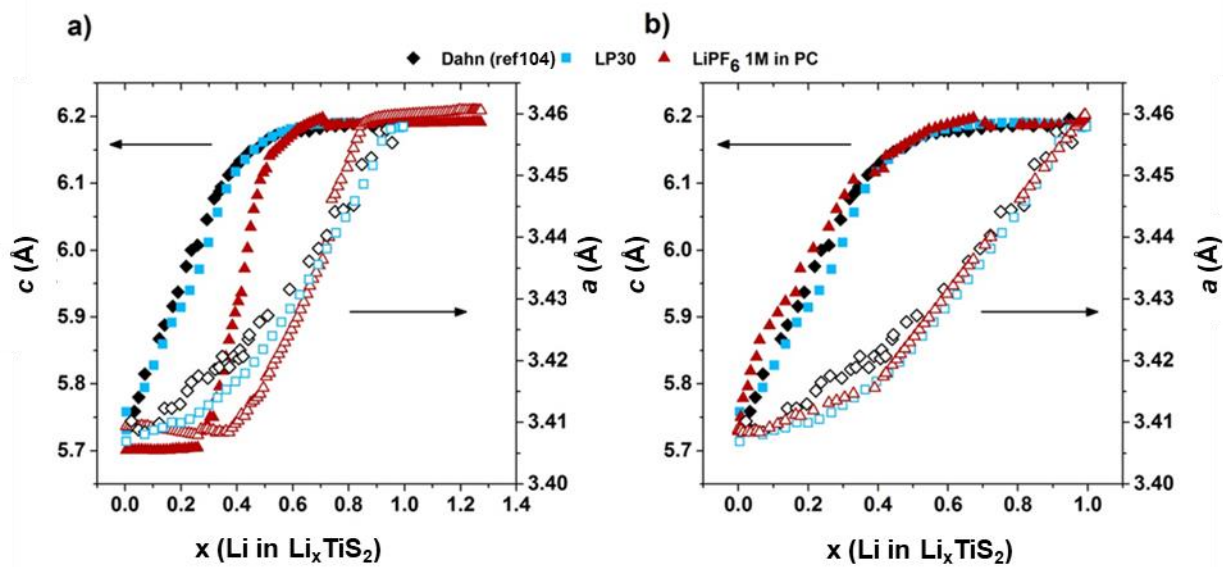


Figure III.12 - Comparison of the Li_xTiS_2 phase lattice parameters upon *operando* reduction of TiS_2 in several cells using different electrolytes. Left plot depicts the data without correction, right plot depicts the same points but where x is corrected using the method described. Full symbols represent the values along the c -axis (left), empty symbol along the a -axis (right). Diamonds are the data retrieved from ref 5, blue squares were obtained from the experiment using LP30 electrolyte and red triangles with 0.67 M LiPF_6 in EC:PC:DMC (33:33:33)

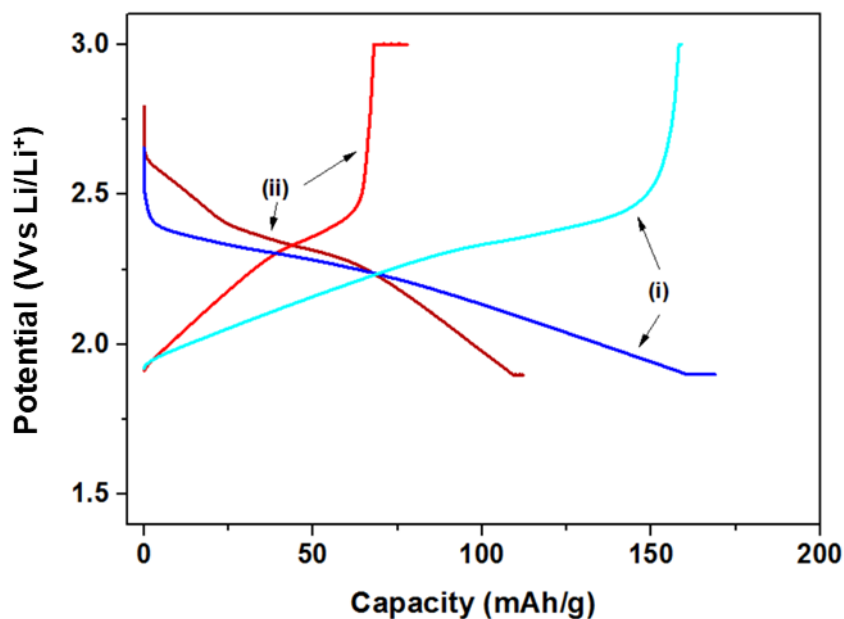


Figure III.2 - Reduction and oxidation curve of TiS_2 cells cycled with LP30 (blue) and 0.67M LiPF_6 in EC:PC:DMC 33:33:33 (red).

III.4. *Ex situ* complementary tests

To point out how the cointercalation affects the reversible capacity, a series of tests was carried out *ex situ* in three-electrodes Swagelok cells using a TiS_2 casted electrode. Electrolytes tested were 1 M LiPF_6 in either EC:DMC (1:1), EC:DMC:PC (33:33:33), EC:DMC:PC (2:1:2), EC:PC (3:7) or PC. Electrochemical curves for the first reduction are presented in [figure III.14 a](#)) while the capacity at the end of the reduction and the reversibility of the first cycle are plotted versus the amount of PC in [figure III.14 c\) and d](#)), respectively. The reversibility is the ratio between the reoxidation capacity and the reduction capacity. It appears clearly that the more the electrolyte contains PC, the more the capacity and the reversibility of the first cycle are decreasing. Here again, it seems that the capacity and reversibility loss are proportional to the amount of PC in the electrolyte, which implies that the capacity loss may be linked to the amount of cointercalated phase formed.

Another interesting electrochemical feature, solely observed for PC containing electrolytes, appears at the beginning of the first reduction (at *ca.* 2.5 V and can be appreciated in [figure III.14 b](#)). After the initial potential drop, the voltage re-increases before decreasing again, creating some bump in the curve. The more the electrolyte contains PC and the more pronounced is the bump. This feature was observed with good reproducibility in several *in situ* cells (two-electrodes) and three-electrodes Swagelok cells and coincides with the appearance of cointercalation peaks. A similar signature was observed when inserting calcium with a $\text{Ca}(\text{TFSI})_2$ 0.3 M in PC electrolyte.⁷² Since occurring in PC containing electrolytes exclusively and at the onset of the cointercalation phase as demonstrated by XRD experiments, it is believed this effect to reflect the nucleation of the cointercalated phase.

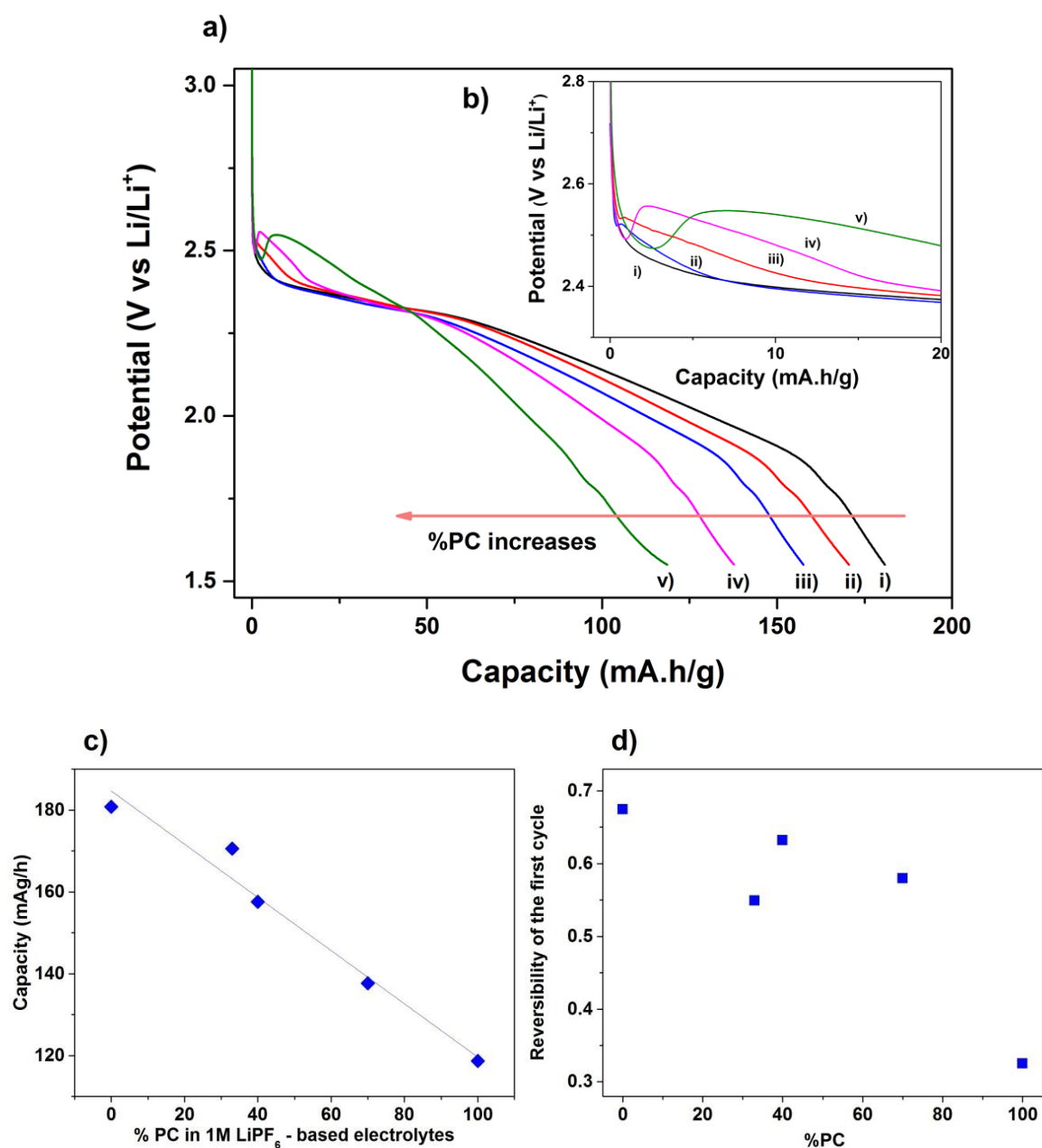


Figure III.14 - a) Reduction curve at C/15 of cells cycled with 1 M LiPF₆ in i) EC:DMC (1:1), ii) EC:DMC:PC (33:33:33), iii) EC:DMC:PC (2:1:2), iv) EC:PC (3:7) and v) PC ; b) close-up of the early stage of discharge ; c) Resulting capacity versus the amount of PC contained in the electrolyte ; d) Reversibility of the first cycle with respect of the amount of PC contained in the electrolyte

Although solvent cointercalation in TiS₂ was documented in cells using PC containing lithium,^{104,110} calcium or magnesium based electrolytes,^{71,72} no similar studies have been reported for sodium or potassium containing cells. The different behavior of the cointercalated phase with respect to reversibility of its formation is most likely related to the strength of the cation interaction with the solvent. Moreover, the nature of the cation itself may also have some influence, as nicely shown by DFT studies considering the intercalation of different cations on TiS₂.^{113,114}

III.5. Conclusion

The main conclusion of this chapter is the observation of solvent cointercalation when reducing TiS_2 in lithium cells containing PC in the electrolyte, with the formation of a phase with a c -parameter equal to 17.5 Å. Cointercalation is found to be electrochemically driven and happening at the very early stages of reduction. By performing analogous experiments in different electrolytes containing different salts and with different cycling conditions (C-rate, potential window), we were able to conclude that neither the nature of the salt nor the cycling conditions have any influence in the formation of the cointercalated phase. However, the content of PC in the electrolyte plays a major role in the amount of cointercalated phase formed, capacity loss and irreversibility. Cointercalation was found to be irreversible, as this phase does not revert back to TiS_2 after reoxidation, and hence it is a source of irreversible capacity upon the first cycle. Yet, this phase does not evolve upon cycling and the formation of Li_xTiS_2 with $x = 1$ is observed in all cells.

Interestingly, and as mentioned above, the formation of a cointercalated phase was found to be reversible in Ca cells.⁷¹ In that case, the cointercalated phase appears to be larger than what we found with Li ($a = 3.514$ Å and $c = 17.931$ Å for Li, and $a = 3.417$ Å and $c = 28.040$ Å for Ca). Further investigation is needed in order to better understand the different interactions between the host structure and Li or Ca cation complexes. In this sense, a complementary study performed in calcium cells is presented in [chapter IV](#).

IV. Calcium intercalation in TiS_2

The development of high energy density battery technologies, based on divalent metals as the negative electrode is very appealing. Ca is an especially interesting choice due to the combination of low standard reduction potential, close to that of lithium and sodium, and natural abundance¹¹⁵ (fifth most abundant element on the Earth's crust). While the topic had deserved little attention in the past due mainly to the absence of suitable electrolytes for operation of calcium electrodes, research efforts have intensified since Ponrouch *et al.* reported reversible plating/stripping of calcium at 100°C in 2016 using $\text{Ca}(\text{BF}_4)_2$ in EC:PC as electrolyte.⁶⁶ Since then, new electrolyte formulations were developed enabling operation at room temperature^{67–69} despite none of them being optimum in terms of electrochemical stability window and ability to sustain prolonged cycling.

The advent of viable electrolytes prompted screening of positive electrode materials to achieve proof-of-concept of the technology. Inorganic positive electrode materials, such as those used in LIBs, were obviously interesting candidates to explore. They commonly react through a redox mechanism involving reversible topotactic insertion of ions into a host without any major structural changes. Such materials are required to exhibit a structural framework with interconnected sites wherein the intercalated ion can diffuse and an electronic band structure able to reversibly accept/donate electrons. Yet, success has been rather limited, as *a priori* interesting compounds in terms of theoretical capacity and expected operation potential, such as CaMoO_3 or CaMn_2O_4 , were not found to exhibit redox activity in calcium cells, which was attributed to too large energy barriers for migration of calcium ions in the crystal structure, as deduced from DFT calculations.^{116,117} In other cases, such as $\text{Ca}_3\text{Co}_2\text{O}_6$,¹¹⁸ electrochemical oxidation in 0.45 M $\text{Ca}(\text{BF}_4)_2$ in EC:PC as electrolyte enabled extraction of ca. 0.7 moles of calcium from the crystal structure, despite no reinsertion was possible. Classical intercalation hosts with crystal structures exhibiting a van der Waals gap, such as TiS_2 , in which intercalation of a wide range of neutral or charged species has been achieved,^{23,24,119–121} represented an interesting alternative. Indeed, calcium intercalation in TiS_2 to yield $\text{Ca}_{0.5}\text{TiS}_2$ was already long ago reported by Rouxel and coworkers¹¹⁹ through chemical reaction with calcium metal in liquid ammonia and heating to eliminate cointercalated NH_3 molecules.

Reversible electrochemical intercalation of calcium in TiS_2 was achieved by Tchitchekova *et al.*⁷¹ at 100°C using calcium metal as negative electrode and 0.45 M $\text{Ca}(\text{BF}_4)_2$ in EC:PC as electrolyte. *Ex situ* diffraction experiments enabled to detect four different phases at the end of the reduction, as shown in figure IV.1: the unreacted TiS_2 , a phase with a very large interlayer space (*c*-parameter 28.040 Å) which was attributed to solvent cointercalation and denoted phase 1, the $\text{Ca}_{0.5}\text{TiS}_2$ phase reported by Le Blanc-Sorreau (denoted as phase 2), and third one (denoted phase 3), for which the observed peaks would be consistent with a second stage calcium intercalated structure. The relative amount of each phase depends on the capacity achieved, with phase 1 being formed in the early stages of reduction and peaks corresponding to $\text{Ca}_{0.5}\text{TiS}_2$ being intense only after reduction to much lower potential. The results achieved did not enable to infer the formation of any Ca_xTiS_2 solid solution, as happens in the case of lithium intercalation. The significant amount of TiS_2 remaining at the end of reduction is likely related to sluggish reaction kinetics. From diffraction data, it was impossible to refine the calcium occupancy using Rietveld methods in these phases, inputted to a lack of theoretical model, however calcium intercalation was confirmed by differential absorption

tomography at the Ca L2 edge using the BL09-MISTRAL beamline at ALBA. Upon reoxidation the peaks corresponding to the three reduced phases were found to disappear, with the diffraction patterns exhibiting only the peaks corresponding to TiS_2 . Interestingly, this is in contrast with what we have observed for the solvent cointercalated phase in lithium cells (see [Chapter III](#)).

Using a calcium metal as negative electrode severely restricts the viable electrolyte choices, as these are constrained to the few formulations reported to date involving numerous technical issues such as need to work at high temperature, limited stability upon oxidation, complex synthesis of the salts etc. The simplest choice to avoid these issues is to use activated carbon (AC) as negative electrodes, as already done by Amatucci and co-workers in 2005⁶⁵ to study the feasibility of calcium intercalation in V_2O_5 . AC does not operate through a faradaic but through a capacitive redox mechanism, with charge being stored electrostatically through ions adsorption on the carbon's wide specific surface area (no charge transfer involved).⁸⁶ The advantages of using it include high reversibility, operation window matching the stability of most electrolytes and versatility in terms of ions that can be adsorbed. Yet, its relatively low specific capacity requires careful cell balancing to make sure the counterelectrode (CE) is significantly oversized with respect to the expected capacity of the working electrode. Using AC CE, enabled in the course of this PhD, proved the feasibility of calcium intercalation in TiS_2 at moderate (65°C) and even room temperature using $\text{Ca}(\text{TFSI})_2$ in PC as electrolyte.⁷² In this case, phase 2 ($\text{Ca}_{0.5}\text{TiS}_2$) was not observed ([figure IV.2](#)) and only peaks corresponding to phase 1 and phase 3 are visible on the patterns at the end of the reduction. A summary of the lattice parameters reported for the calcium intercalated phases, all indexed within the $R\bar{3}m$ space group, is given in [table IV.1](#).

Since all these observations were made *ex situ*, this raises the question on whether the $\text{Ca}_{0.5}\text{TiS}_2$ phase is still actually formed at some point using $\text{Ca}(\text{TFSI})_2$ in PC as electrolyte at room temperature and also whether there is any significant degree of solid solution formed for the phases observed, as some differences exist in the reported cell parameters.

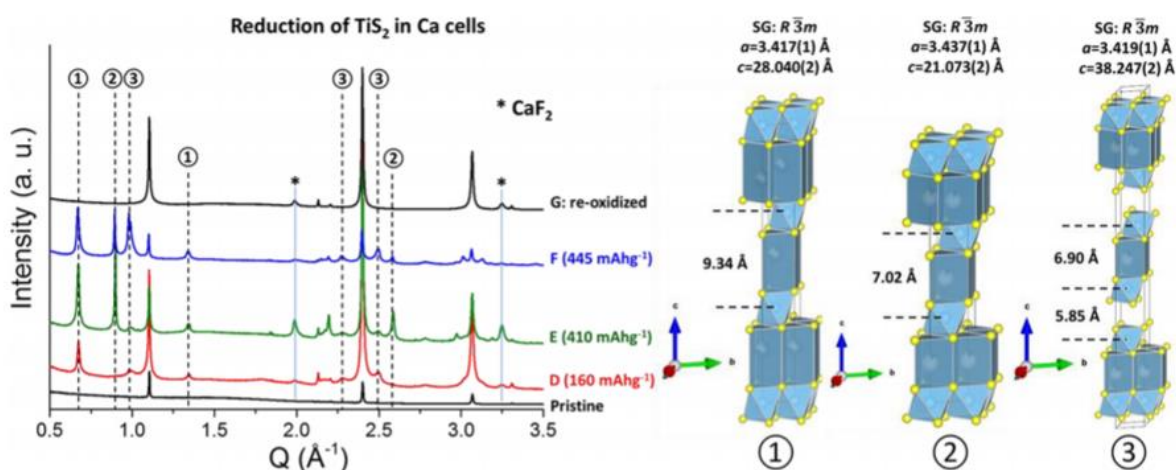


Figure IV.3 – *Ex-situ* X-ray diffraction patterns collected at different stages of TiS_2 reduction in Ca cells at 100°C using calcium metal CE and 0.45 M $\text{Ca}(\text{BF}_4)_2$ in EC:PC as electrolyte, with structural models proposed for the different phases observed of Ca// TiS_2 cells collected at different stage of electrochemistry, reprinted from 71

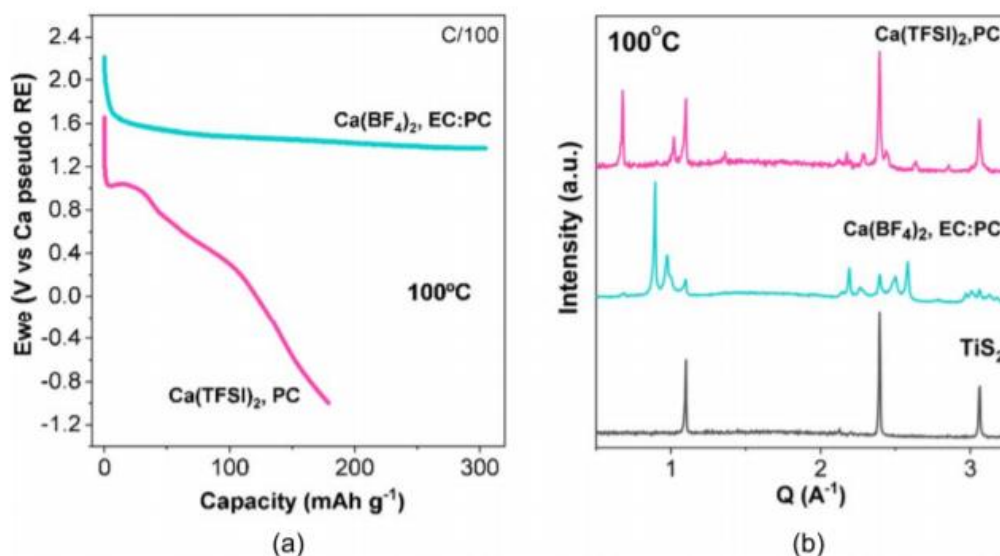


Figure IV.4 - a) Capacity vs. potential curves at 100 °C and C/100 rate for AC//TiS₂ cells, using 0.3M Ca(BF₄)₂ in EC:PC (pink curve) and 0.3M Ca(TFSI)₂ in PC (blue curve) as electrolytes and (b) corresponding *ex situ* X-ray diffraction patterns. The characteristic XRD pattern of TiS₂ pristine electrode is also displayed for comparison. (reprinted from 72)

Table IV.3 - Summary of the lattice parameters for the phases reported to form upon reduction of TiS₂ in calcium cells

		Ca(BF ₄) ₂ in EC:PC (Ca metal, from 71)	Ca(TFSI) ₂ in PC at 60°C (AC, from 72)	Ca(TFSI) ₂ in PC at room temp. (AC, from 72)
Pristine TiS ₂	a (Å)		3.4018(2)	
	c (Å)		5.6941(7)	
Cointercalated PC (Phase 1)	a (Å)	3.417(1)	3.4070(4)	3.40914(27)
	c (Å)	28.040(2)	27.75(6)	28.321(5)
Ca _x TiS ₂ (x ≈ 0.5) ¹¹⁹ (Phase 2)	a (Å)	3.437(1)		
	c (Å)	21.073(2)		
Second-stage (Phase 3)	a (Å)	3.419(1)	3.3535(4)	37.730(6)
	c (Å)	38.247(2)	36.986(4)	37.730

Within this scenario, *operando* experiments were undertaken as part of this PhD aimed at getting further information about the phases formed during reduction of TiS₂ in calcium cells in different conditions.

IV.1. Experiments carried out above ambient temperature

IV.1.1. Ca//TiS₂ cells at 100°C

The first experiment was simply targeting an *operando* reproduction of Tchitchekova's experiment⁷¹ using the modified *in situ* Leriche cell with 0.45M Ca(BF₄)₂ in EC:PC as electrolyte and calcium metal as CE. Yet, some conditions had to be adapted, the first being the use of loose powder mixtures of TiS₂ and carbon black (see section II.1.3.) instead of tape casted electrodes on aluminum in order to avoid preferential orientation preventing the observation of 00*l* reflections (see section III.1), and the second the acceleration of the testing rate from C/100 to C/25 (per moles of electrons exchanged, corresponding to C/200 to C/50 per moles of ion exchanged) to shorten the overall duration of each cycle, which would otherwise be too beamtime consuming. The benefits of punching a hole in the

calcium disk to avoid the presence of very intense Ca peaks in the patterns were assessed, but it was finally deemed unnecessary. The first attempts were done using a glassy carbon cell window without metallic foil since their electrical and thermal conductivity was thought to be sufficient. These windows are safer to use than beryllium, especially at elevated temperatures, and allow avoiding the additional peaks appearing when using aluminum windows, at the cost however of a significant background at low angles.

Two cells prepared as described above were connected to the Julabo chiller with the bath set at 105°C to ensure the temperature enabled calcium plating/stripping. The open circuit voltage of the cells was close to 2.5 V and 2 V (vs Ca^{2+}/Ca), similar to Tchitchekova *et al.* observations. After launching reduction at C/25 (50 h to insert 1 mol of ions) the potential either dropped to the threshold limit or started to re-increase (see figure IV.3). This was attributed to the rate being too fast to allow reversible plating/stripping at the CE, especially considering that the cell setup might be less efficient than the conventional Swagelok cells. Thus, the C-rate was decreased to favor the Ca plating/stripping reaction at the CE, first to C/50 (100 h to insert 1 mol of ions) and afterwards to C/100 (200 h to insert 1 mol of ions, see figure IV.4), with the behavior of different cells not being reproducible either, the potential cut off for reduction was set at 0.6 V vs Ca^{2+}/Ca and most of the cells ended their reduction at $x = 0.15$ in Ca_xTiS_2 , assuming that all the electrochemical capacity was related to calcium intercalation in TiS_2 with no side reactions, despite in some cases larger values were achieved up to $x = 0.25$ at C/100. Upon reoxidation the potential quickly reached the upper limit, and that step gave low capacity in comparison of the previous one (figure IV.3). These results can be attributed to the fact that the setup is optimized for crystallographic data acquisition rather than electrochemical performance (high polarization, two electrodes only, used with loose powder). Another issue is the electrolyte decomposition reaction being favored by high temperature and slower rates. As a consequence, it is likely that the only phenomenon taking place is the formation of CaF_2 due to the decomposition of $\text{Ca}(\text{BF}_4)_2$ to the point that it is the only phenomenon taking place as shown in figure IV.4 and IV.5.

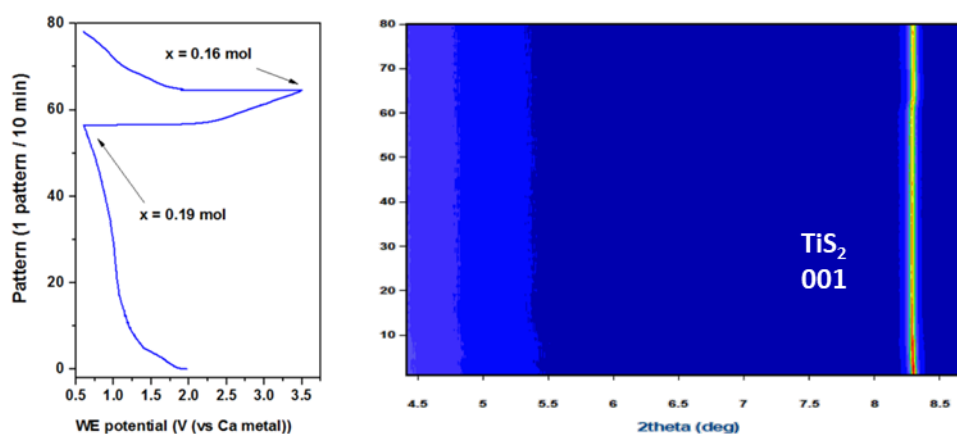


Figure IV.3 - Electrochemical curve and patterns collected during the cycling of a with a Ca/TiS_2 Leriche cell at 100°C at C/25 using 0.45 M $\text{Ca}(\text{BF}_4)_2$ in EC:PC as electrolyte. No changes are visible in the patterns throughout the cycle.

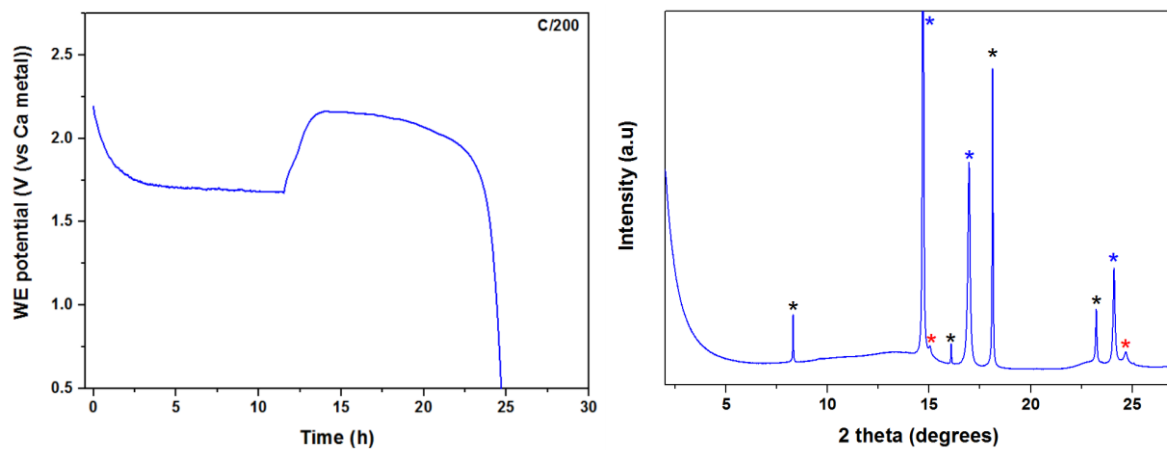


Figure IV.4 – a) Electrochemical reduction of Ca//TiS₂ in an *in situ* Leriche cell at C/100, at 100°C using 0.45 M Ca(BF₄)₂ in EC:PC electrolyte. No software inputs were modified during that reduction. b) X-ray diffraction pattern taken at the end of the reduction ($x = 0.18$) at $\lambda = 0.826 \text{ \AA}$. The black stars show the peaks of TiS₂, the blue ones calcium and red ones CaF₂.

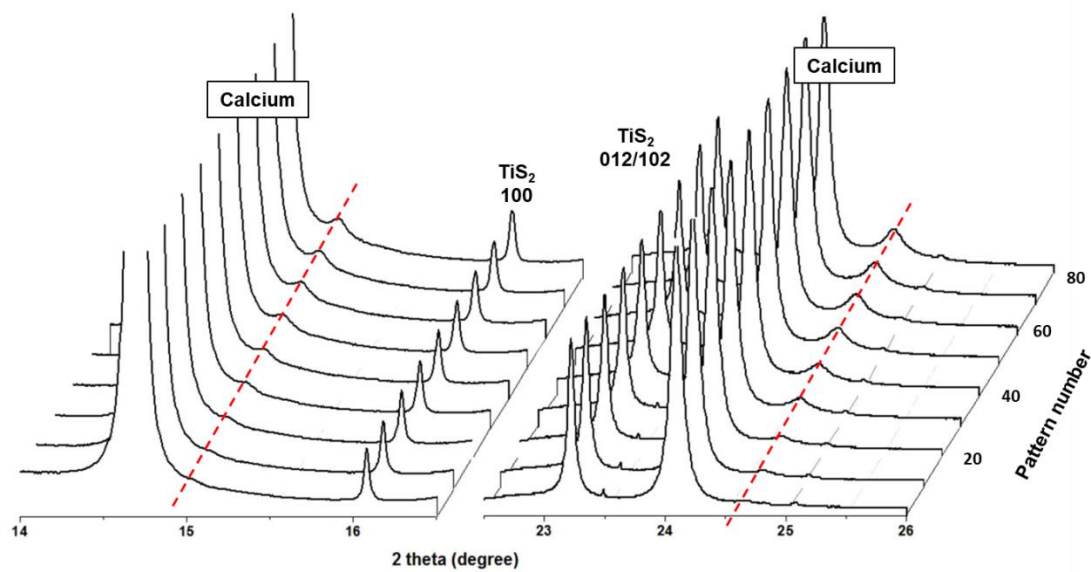


Figure IV.5 - Patterns collected during the cycling of a Ca//TiS₂ Leriche cell at C/25 and at 100°C using 0.3M Ca(TFSI)₂ at $\lambda = 0.826 \text{ \AA}$. The red dotted lines represent the position of the peaks of CaF

IV.1.2. AC//TiS₂ cells at 65°C

To overcome the issues related with electrolyte decomposition, the operating temperature was reduced. Since this hinders the plating/stripping of calcium metal on the negative electrode, AC (Kynol) was used instead.⁷² As the specific capacity of AC is much lower (35 mAh/g)⁷² than that expected on the positive side, equilibration of the cell was ensured by placing 3 disks (16 mm diameter with a specific mass of 1.800 m²/g) of AC at the CE for ~ 5mg of TiS₂ electrode mix on the working electrode side. Since no calcium plating/stripping was expected on the negative side, a different electrolyte can be used. Changing the electrolyte avoids the difficulties in drying commercial or on-site synthesizing the Ca(BF₄)₂ salt.⁷⁸ Hence 0.3M Ca(TFSI)₂ in PC, which does not require further drying was used.

IV.1.2.1. *Ex situ* preparatory work

In order to optimize the cell configuration, several thermalized Leriche cells were prepared with aluminum windows, copper foils and AC CE disks of different diameters. Given the fragility and lower electronic conductivity of glassy carbon windows, aluminum windows were selected for the preliminary tests since no *in situ* data collection was performed. To preserve the window material from corrosion due to direct contact with the TFSI anion⁸³ and to ensure both good electrical and thermal conduction, a copper foil was added. A first cell was prepared using electrode mixture (10% of carbon black, 6% of PVDF) and 3 disks of AC (18 mm diameter). The cell was thermalized at 65°C using the Julabo chiller (hence in the same conditions than for diffraction experiment) and launched upon reduction at C/50 (100h to insert 1 mol of ions), with a potential threshold set to -4V vs. the AC CE. Unfortunately it showed a very noisy evolution of the potential with time (figure IV.6 a), which was attributed to internal short circuits which could be induced by accidental deposition of positive electrode powder on the cell's walls or a too large size of the AC disks. Indeed, although the disks were smaller than the inner diameter of the cell (19 mm) and well centered, their diameter tends to expand as they are pressed while closing the cell, and may enter in contact with the metallic parts of the cell if the Kapton foil covering the the cell wall slips slightly during the cell assembly.

The positive electrode material was retrieved at the end of reduction (after 66.7h and $x = 0.63$ assuming that all the electrochemical capacity was related to calcium intercalation in TiS₂ to form Ca_xTiS₂, with no side reactions) and a pattern was collected at $\lambda = 0.4124 \text{ \AA}$ (see figure IV.6 b). Despite the noisy behavior of the cell, the pattern is consistent with the results of Tchitchekova *et al.*⁷¹ and Verrelli *et al.*⁷² and exhibits three intense peaks at $2\vartheta = 1.24^\circ$, 2.46° and 3.69° (respectively, $d = 19.05$, 9.60 and 6.40 \AA) which are attributed to the cointercalated phase (Phase 1).^{71,72} A small peak at $2\vartheta = 3.93^\circ$ ($d = 6.01 \text{ \AA}$) can be observed, which could be attributed to Phase 3. Surprisingly, a third phase with a broad peak at $2\vartheta = 1.64^\circ$ ($d = 14.40 \text{ \AA}$), and additional peaks at $2\vartheta = 3.33^\circ$ and 4.06° (respectively $d = 7.09$ and 5.82 \AA) are observed, which were not reported previously.⁷² This new phase could be formed by the decomposition of the electrolyte due to the hectic reduction.

Taking into account the results described above, a new cell was assembled with the same windows and foil, but taking special care to wipe the walls with a tissue before inserting the negative electrode, using this time smaller diameter AC disks (16 mm) and adding a second separator. When launching the cell upon reduction at C/50 (100h to insert 1 mol of ions), the potential decreased in a

much smoother way, and after 57 h of cycling ($x = 0.55$ assuming that all the electrochemical capacity was related to calcium intercalation in TiS_2 to form Ca_xTiS_2 , with no side reactions) the potential started to increase. The cell was stopped and the positive electrode material was retrieved and sealed in a capillary, the corresponding diffraction pattern indicates only the presence of the Phase 1 (see figure IV.6 b).

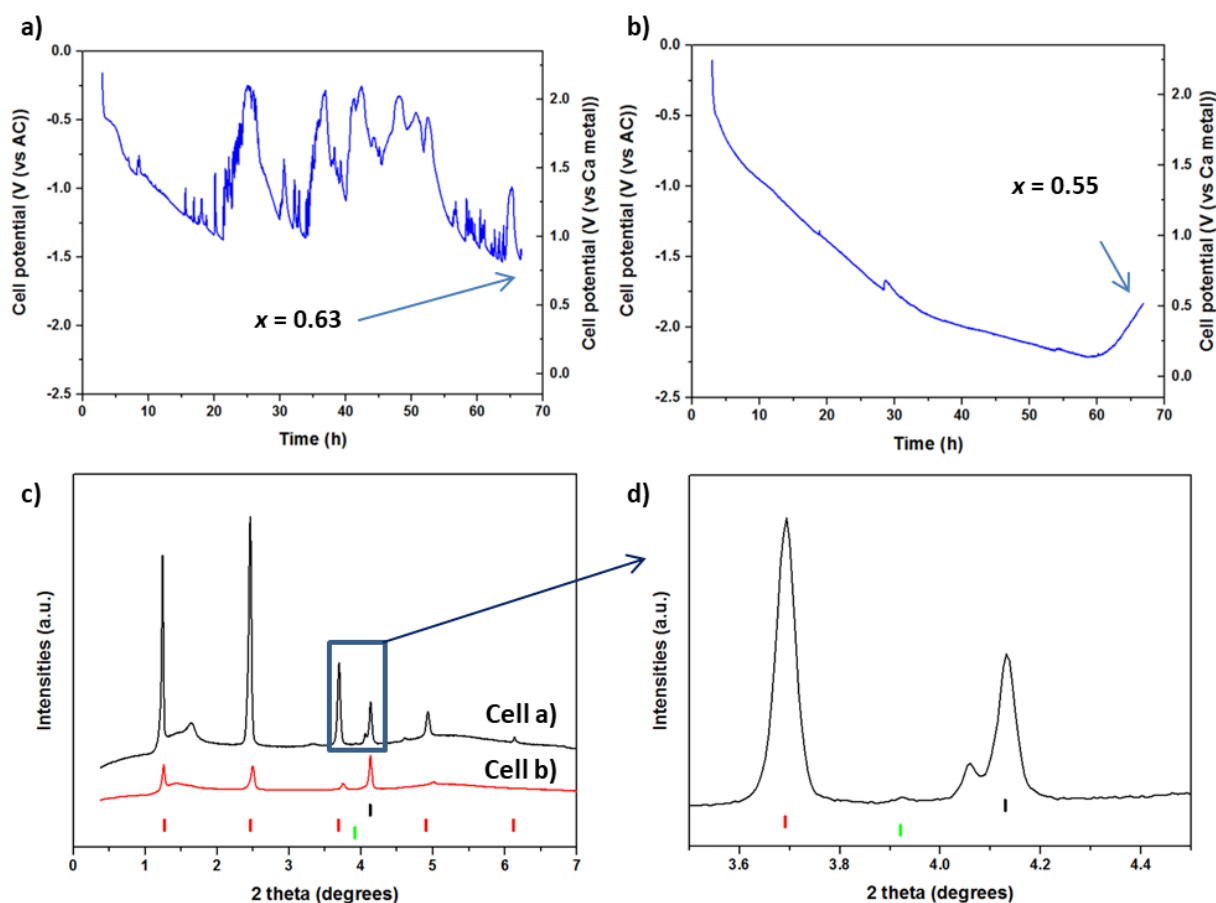


Figure IV.6 – Potential vs time profile for AC/TiS₂ Leriche cells tested at C/50 rate and 65°C with 0.3 M Ca(TFSI)₂ as electrolytes and AC disk CE, a) 18 mm diameter, b) 16 mm diameter; c) X-ray diffraction patterns collected at the end of the reduction of both cells ($\lambda = 0.4124 \text{ \AA}$), normalized with respect to the 001 TiS₂ peak ($2\theta = 4.13^\circ$), d) close up near the TiS₂ 001 peak. The black ticks represent TiS₂, the red ones the Phase 1 and the green one the Phase 3.

These experiments enabled us to conclude that the bad results from the experiment carried out at 100°C with Ca metal as CE were mostly related to the slow kinetics of the Ca plating/stripping reaction at the CE and the enhanced electrolyte decomposition at high temperatures and low current. Since results compatible with those achieved previously in standard Swagelok cells could be achieved, further *operando* experiments were undertaken.

IV.1.2.2. Operando experiments

Lerliche cells were assembled with glassy carbon windows and a stainless steel 316 foil on the working electrode side, and loaded with the electrode material (in ratios 84:10:6 active material:black carbon:PVDF) and three disks of AC (16 mm diameter). In that case, the glassy carbon windows were chosen for their transparency to X-ray in comparison with aluminum. For the current collector, stainless steel was used to avoid any reaction between calcium and copper, although it is unlikely to occur. Since the cells tested at C/50 exhibited successful behavior, C/37 (75 h to insert 1 mol of ion) rate and 65° temperature was used for the *operando* test, expecting to keep the good electrochemical response while decreasing the beamtime needed. The cells were tested between -2 V and 1.5V vs AC (0.35 V and 3.85 V vs Ca²⁺/Ca) on the MSPD powder diffraction station and patterns were collected at $\lambda = 0.826 \text{ \AA}$. A special measuring routine was made to ensure the material's transformation was uniform: patterns were collected in three areas of the cell, one pattern was collected every 5 minutes and hence each area was measured every 15 min.

Figure IV.6 depicts the electrochemical profile achieved and the corresponding diffraction patterns. The potential is gradually seen to decrease upon reduction with no pseudo-plateau observed, as in the case of the three-electrode experiments carried out by Verrelli *et al.*⁷² In the X-ray diffraction patterns, new peaks appear at early stages of discharge ($x = 0.07$ assuming that all the electrochemical capacity was related to calcium intercalation in TiS₂ to form Ca_xTiS₂, with no side reactions), at $2\theta = 2.57^\circ$, 5.16° and 7.75° (corresponding to $d = 18.41 \text{ \AA}$, 9.17 \AA and 6.11 \AA , respectively), which are likely the *001*, *002* and *003* reflections of the cointercalated phase (Phase 1). Note that the angular domain investigated by Tchitchekova and Verrelli^{71,72} did not cover angles low enough to be able to observe the *001* peak, which prompted at the assignment of the *R3m* space group which does not seem to be correct as this reflection is not a systematic extinction. Instead, the *P3m1* space group (same as pristine TiS₂ and Li_xTiS₂), seems the most appropriate choice.

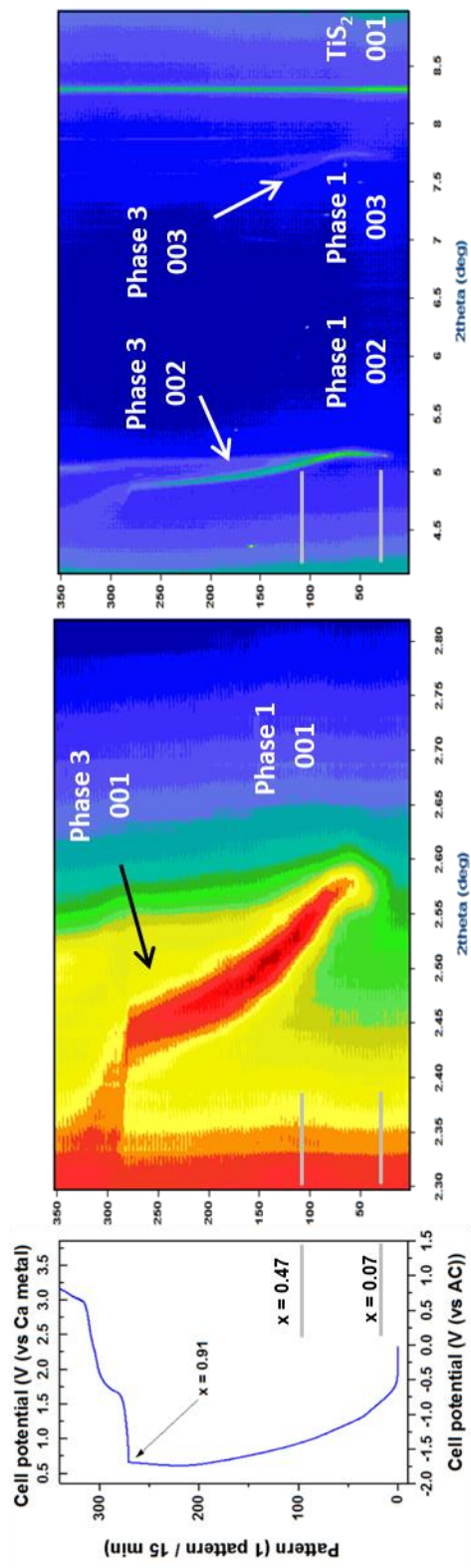


Figure IV.6 – Potential vs time profile and patterns collected with AC//TIS₂ Leriche cell using 0.3 M Ca(TFSI)₂ in PC as electrolyte at C/37 at 65°C

Later, at $x = 0.47$ (~ 38 h of reduction), new peaks emerged at $2\theta = 2.46^\circ$, 4.93° and 7.38° (corresponding to 19.23 \AA , 9.60 \AA and 6.42 \AA) which seem to grow at the expense of Phase 1 related peaks. Again, despite the first peak not being observed in the previous works on the topic^{71,72} due to data acquisition starting at lower angular values, those reflections are coherent with the Phase 3 previously reported. The position of these peaks shifts towards lower angles (to $2\theta = 2.41^\circ$ and 5.00° at $x = 0.81$) upon reduction proceeds, which is likely related to an increase in the amount of intercalated calcium ions. However, this hypothesis cannot be confirmed by X-ray diffraction data alone since the crystallographic model of the phase is still unknown and the amount of Ca cannot be refined. Table IV.2 summarizes the angles and d -spacing at which the peaks of both phase 1 and 3 appear. These *operando* experiments were crucial to evidence such shifts, which could be considered to be within experimental error or related to sample misalignments for *ex situ* experiments. Given the low signal to noise ratio for the peaks related to TiS_2 and intercalated phases (figure IV.7), partially related to the use of the glassy carbon window, a background correction was applied for a more clear evaluation of the patterns evolution.

Table IV.4 - Summary of the x values at which the 001 peaks of Phases 1 and 3 appear during the cycling of an AC// TiS_2 Leriche cell using 0.3 M Ca(TFSI)_2 in PC as electrolyte at C/75 rate and 60°C

Pattern number	x	Phase 1		Phase 3	
		2θ of 001 peak (degree)	c -parameter (\AA)	2θ of 001 peak (degree)	c -parameter (\AA)
1	0	N.A.	N.A.	N.A.	N.A.
50	0.14	2.56	18.49	N.A.	N.A.
100	0.31	2.54	18.63	N.A.	N.A.
150	0.48	2.50	18.93	2.49	19.01
200	0.65	2.53	18.71	2.45	19.32
250	0.84	2.53	18.71	2.41	19.64
300	0.81	2.52	18.78	N.A.	N.A.
350	0.67	2.51	18.86	N.A.	N.A.

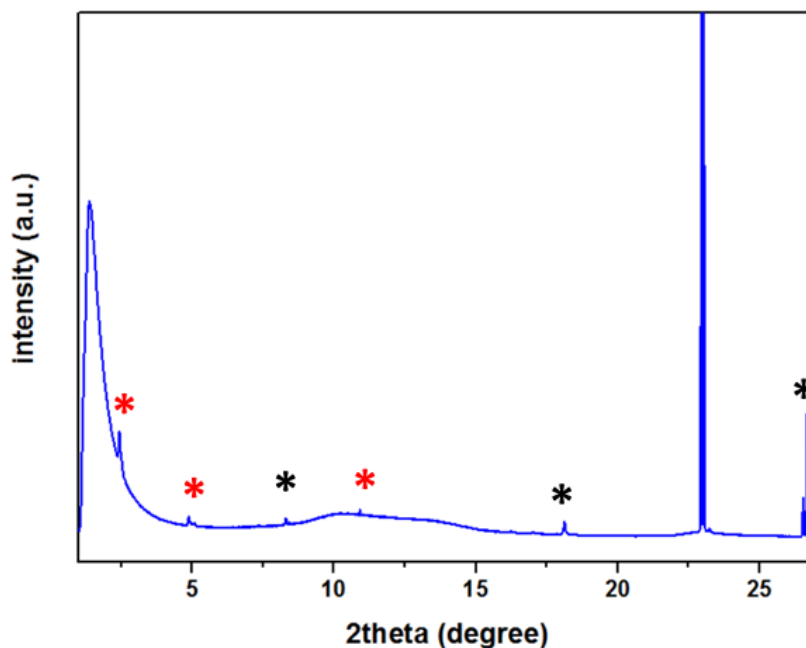


Figure IV.7 – X-ray diffraction pattern collected at the end of the reduction of a AC//TiS₂ Leriche cell, using 0.3 M Ca(TFSI)₂ in PC as electrolyte at 65°C at C/75 rate and 65°C. Black stars represent peaks of TiS₂, red stars represent the peaks of phase 1 and 3

Figure IV.8 shows selected corrected patterns at different stages of reduction/oxidation highlighting the presence of unreacted TiS₂ even at the end of reduction, in agreement with a sluggish kinetics scenario. In addition to the starting material, the peaks from phase 1 appear at $2\theta = 2.57^\circ$, 5.16° and 7.75° on the red pattern ($x = 0.14$), and later the peaks of phase 3 emerging at $x = 0.48$ (pink pattern) and shifting to $2\theta = 2.41^\circ$ and 5.00° at the end of the reduction. The change in position of the peaks is likely related to the amount of species intercalated in the structure of TiS₂ (calcium and/or cointercalated solvent). The presence of more intermediate phases can be inferred from these data, with likely some biphasic regions. Yet, further experiments would be needed to confirm all these speculations. The most significant differences with the lithium case are the amount of unreacted TiS₂ related to the sluggish kinetics and the evolution of the cointercalated phases.

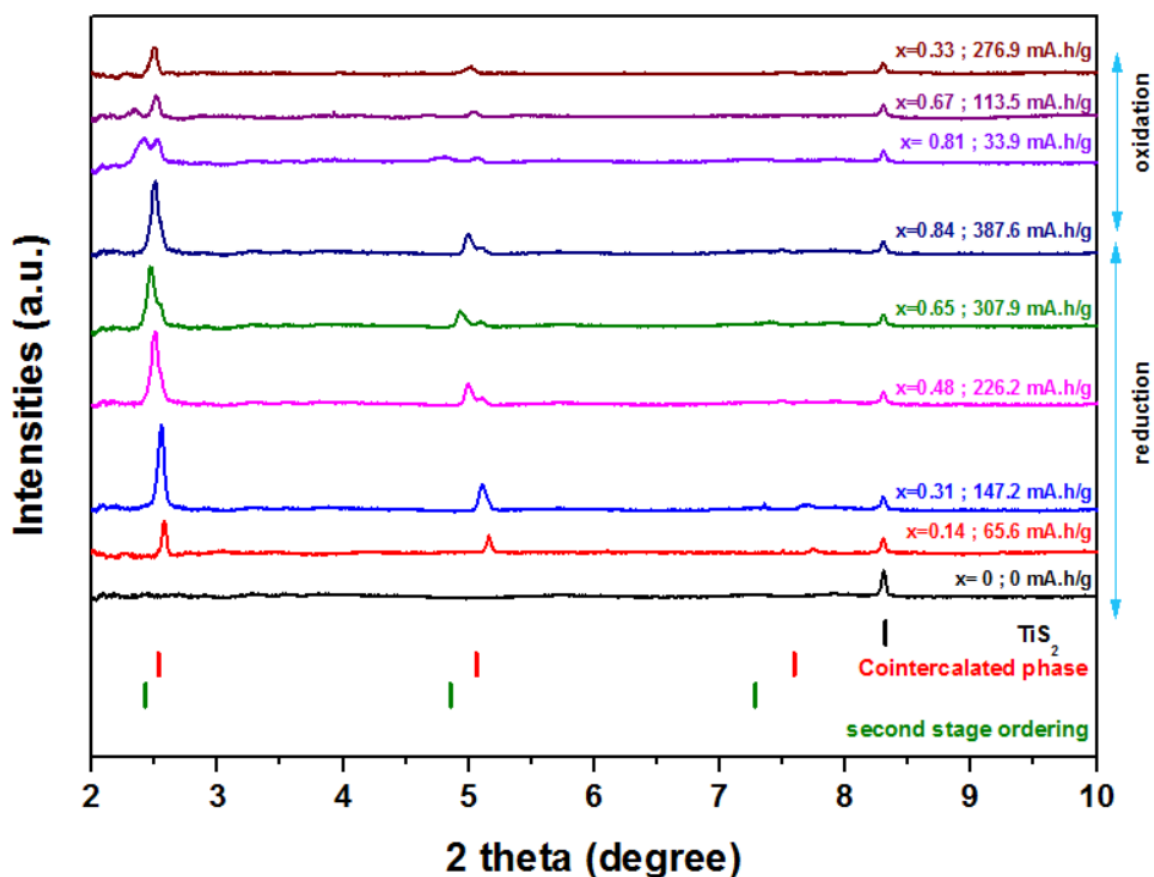


Figure IV.8 – Patterns collected during the cycling with 8h interval (every 50 patterns). Black ticks represent the reflection of TiS_2 , red ticks the Phase 1 and blue ticks the Phase 3

Because only the peaks related to the $00l$ plans are visible, only an estimation of the c -parameter can be given. This problem was also met during the refinement of the cointercalated phase in lithium systems, where the $h00$ and $0k0$ reflections had much lower intensities than those of $00l$. Because the unit cell cannot be defined and no theoretical model is available to describe this phase, no refinement can be performed, event by Le Bail fitting. However, since the cell was aligned on the powder diffraction station, the d spacing should give a reasonable estimate for the c -parameter of each phase. For the cointercalated phase (Phase 1), the c parameter was found to be 18.41 \AA , which is a bit higher than the value found for the cointercalated phase in lithium systems (17.5 \AA).¹⁰⁵ The discrepancy with the lithium value can be explained by the difference in size of the lithium and of the calcium ion (0.9 \AA and 1.14 \AA , respectively),¹²² or, most likely, to a different amount of cointercalated solvent molecules as can be expected from the different coordination numbers exhibited by lithium and calcium ions in the electrolyte. Furthermore, it is also important that the operating temperature (room temperature with lithium, 65°C here) could also play a role. In contrast, this c value is significantly different from the one suggested by Tchitchekova⁷¹ and Verrelli⁷² ($\sim 28 \text{ \AA}$)^{71,72}, which was simply a result of the wrong indexation using the $R\bar{3}m$ space group, considering the peak at $Q = 0.668 \text{ \AA}^{-1}$ ($d = 9.40 \text{ \AA}$) as the 003 reflection. Using the $P\bar{3}m1$ space group and by indexing the peaks at $2\theta = 2.57^\circ$ and 5.16° as the 001 and 002 peaks respectively, the c -parameter is evaluated to be 18.41 \AA .

For Phase 3, and again due to a wrong indexation resulting from the experiments not covering low angular domains, the calculated c parameter is 19.23 Å, instead of (~ 38 Å) reported in previous work.^{71,72}

Upon reoxidation, the potential stabilized at 1.1 V (vs AC, 3.45 V vs Ca^{2+}/Ca) and Phase 3 disappeared. Unfortunately, we could not continue to measure patterns because the beam was stopped for maintenance, but the oxidation continued until stopped manually at $x = 0.02$. A pattern was collected when the beam restarted at $x = 0.29$, and the Phase 3 had completely disappeared but the cointercalated phase remained. The oxidized electrode powder was tentatively retrieved for *ex situ* data collection, unfortunately the capillary broke before the measurement was made.

IV.2. Experiment at room temperature

Following Verrelli's work, demonstrating feasibility of calcium intercalation in TiS_2 , even at room temperature, using AC CE and 0.3M $\text{Ca}(\text{TFSI})_2$ in PC as electrolyte⁷² it was tempting to study the process *operando* as well.

In this case, since no thermalization was needed, *in situ* coin cells with glass windows were used, and in order to enhance the efficiency of the full experiment, a setup enabling the alternative sequential measurement of four cells was applied using the sample changer described in ref.¹⁰³ (see [section II.3.2.1](#)) which enabled running this experiment concomitant to other *operando* tests not related to this PhD.¹²³ The AC and positive electrode mix was loaded and equilibrated as mentioned above with three disk of 16 mm of AC and ~ 5 mg of electrode material (in ratios 84:10:6), as these values were found to be satisfactory in the previous experiments. Contrary to Leriche cell, coin cells have limited thickness (3.2 mm for CR2032 type used in this case) preventing loading large amount of electrode active materials, as glass windows might break during the crimping process if the components of the cell are too thick. A 316 stainless steel foil was placed on the positive side to ensure uniform electrical contact between the casing and the electrode.

The C-rate was C/25 (50 h to insert 1 mol of ions) to ensure that at least one cycle could be completed with the available beamtime and voltage threshold upon reduction was initially set to -2.5 V (vs AC, -0.15 V vs Ca^{2+}/Ca) but was later set at -5 V upon the second cycle to promote further reduction, of unreacted TiS_2 . The patterns collected are presented in [figure IV.9](#). Since the beam was lost several times during the experiment, the periods during which no patterns were collected are represented by blue horizontal bands on the surface plots. The potential was found to decrease rapidly during the first reduction, reaching the -2.5 V threshold voltage in 6h ($x = 0.10$ in Ca_xTiS_2 assuming that all the electrochemical capacity was related to calcium intercalation in TiS_2 to form Ca_xTiS_2 , with no side reactions). Upon reoxidation, the potential rose quickly then exhibited a more moderate slope to finally form a pseudo-plateau centered around 1.28 V vs AC (3.63 V vs Ca^{2+}/Ca). During that reduction, a small peak appeared at $2\theta = 2.13^\circ$ (corresponding to $d = 21,9$ Å). Although it disappeared upon reoxidation, it is unlikely to be an electrochemically formed phase but rather a disturbance from a misplaced grain in the material. Apart from this grain, no other modification was observed.

Once a capacity upon oxidation was reached slightly in excess to the one achieved upon reduction ($x = -0.05$) the intensity was manually switched upon reduction, to prevent any material degradation. At the end of that reoxidation, no other phase than the pristine TiS_2 is present.

During the second reduction down to, -5 V vs AC (-2.65 vs Ca^{2+}/Ca , $x = 0.4$), peaks at $2\theta = 2.57^\circ$ and 5.11° ($d = 18.41 \text{ \AA}$ and 9.26 \AA respectively), started to appear for $x = 0.02$, and, as observed previously at 65°C and seemed to broaden at the end of the reduction. Upon reoxidation, these peaks gradually disappeared. The oxidation ended at 1.65 V vs AC (4 V vs Ca^{2+}/Ca). Selected patterns are presented in [figure IV.10](#) with a background correction to enhance the visibility. During that second oxidation, the peaks related to phase 1 appeared at similar position to those reported in [section IV.1.2.2](#) ($2\theta = 2.54$ and 5.16° (respectively $d = 18.63$ and 9.17 \AA)) and shifted in the same way as mentioned above. It is important to note that the intensities of the peaks from these new phases are lower at room temperature than at 65°C , reflection that the difference in temperature was enough to promote faster kinetics in that case. The c -parameter found for Phase 1 was found to be the same than at 65°C (18.41 \AA) and therefore does not seem to be dependent on the temperature. However, no peaks related to phase 3 were visible, which sounds logical since the reduction was stopped at $x = 0.4$, *i.e.* at a stage where that phase was not formed yet in the previous experiment. Upon reoxidation, the peaks of phase 1 gradually disappear and are completely absent from the patterns at $x = -0.06$. That negative value comes from the fact that the assuming that x is calculated as if the calcium insertion is the only phenomenon taking place, while it is not the case in this experiment. This evidenced the full reversibility of the cointercalation process in the case of calcium, even at room temperature, which is in stark contrast with the behavior of the lithium cointercalated phase that did not evolve upon further oxidation.

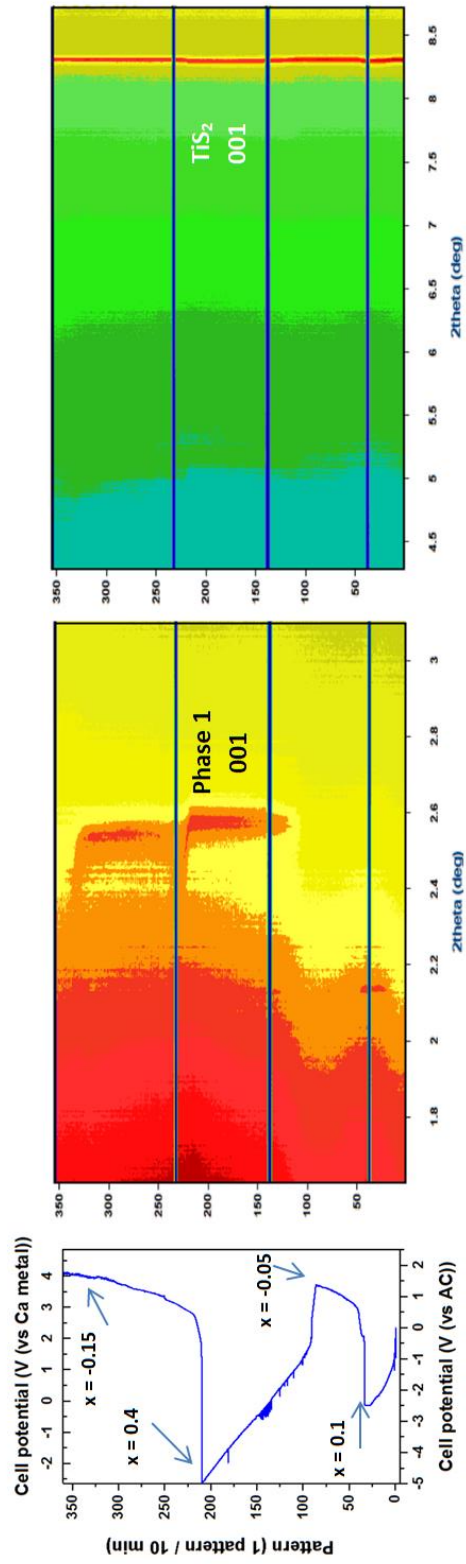


Figure IV.9 – Potential vs time profile and patterns collected with a AC//TiS₂ coin cell at room temperature at C/25 using 0.3 M Ca(TFSI)₂ in PC electrolyte

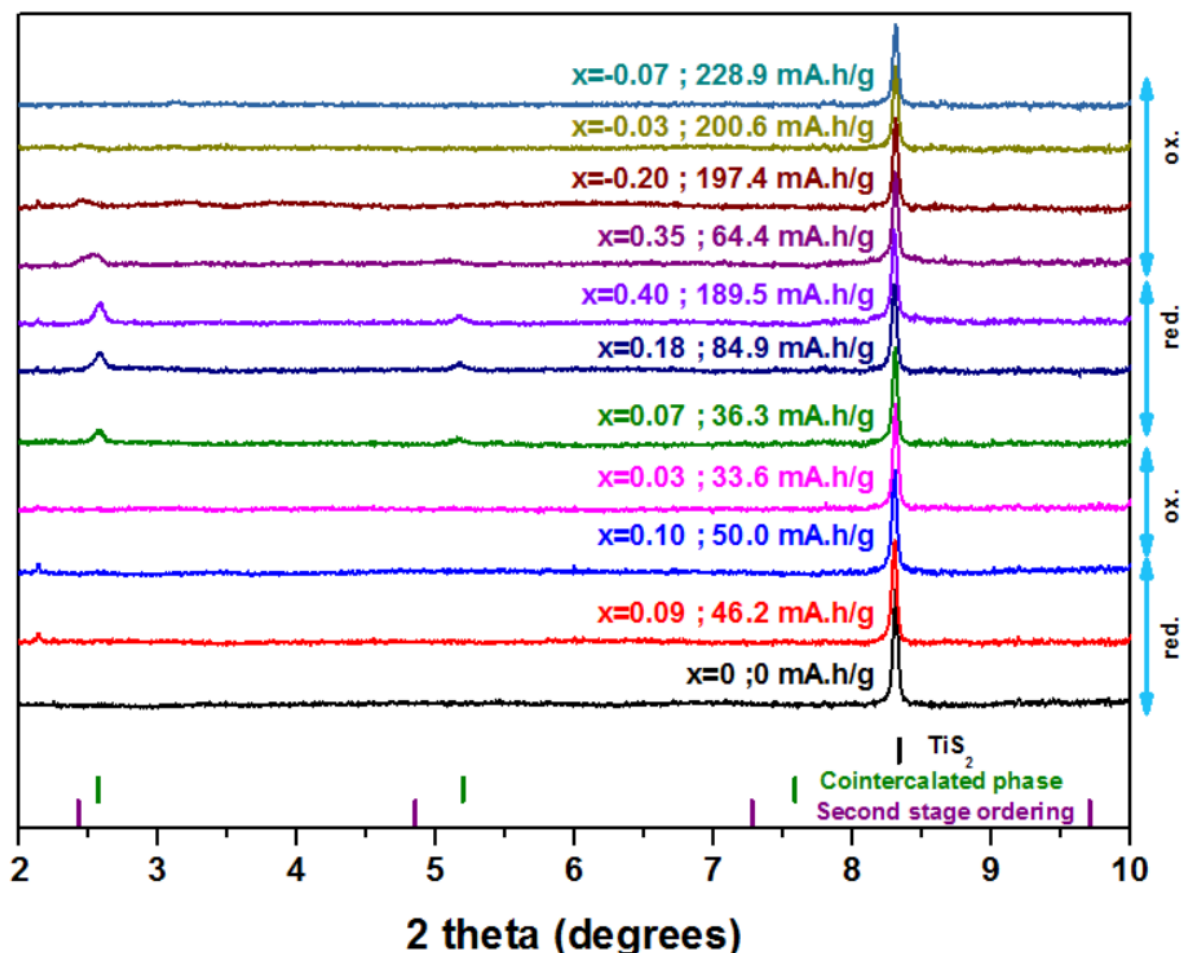


Figure IV.10 – a) Patterns collected during the cycling of a AC//TiS₂ coin cell at C/25 rate and room temperature

IV.3. Conclusion

Experiments performed at 100°C using calcium metal as CE were tricky most likely due to issues related to the plating/stripping of calcium at the CE which resulted in a high cell polarization, with only electrolyte decomposition being observed. Yet, decrease of the temperature to 65°C coupled to the use of AC CE and Ca(TFSI)₂ in PC as electrolyte enabled following the reduction of TiS₂ operando, with initially the formation of the cointercalated phase (Phase 1) previously reported and the appearance of new phase (Phase 3) which might correspond to a second stage intercalate.^{71,72} Given that the X-ray data acquisition started at lower values than in previous experiments, low angle peaks could be observed which allowed to correct the previous indexation provided for such phases. The *c*-parameter for the calcium containing solvent cointercalated phase is 18.41 Å, therefore similar to the one observed for the lithium containing cointercalated phase (see chapter III, *c* = 17.5 Å);¹⁰⁵ and the *c*-parameter for phase 3 was calculated to be 19.23 Å. Moreover, the operando experiment enabled to grasp a much more complex mechanism, with possibly the composition of these phases evolving upon reduction and the potential existence of other intermediates, as deduced from the evolution of the peaks observed at low angles.

It is puzzling that the lithium containing solvent cointercalated phase does not seem to evolve upon cycling, and hence results in capacity loss while the formation of the calcium containing solvent cointercalated phase seems to be reversible, which is undoubtedly related to stronger interactions of Ca^{2+} ions with the solvent molecules with respect to Li^+ . However, to ensure the comparison is correct, one would need to test cointercalation in lithium cells at C/50 or slower for a meaningful comparison of the reversibility of formation of the cointercalated phase. Another interesting feature is the second stage structure (phase 3) that seemed to be formed at the expense of the cointercalated phase, which certainly deserves further attention. Overall, it was found that temperature was not a key factor with respect to the nature of the phases formed but had an influence on the intensities of the peaks, hence on the kinetics. Indeed, the peaks of phase 1 and 3 are more intense at 65°C indicating that temperature enhances faster kinetics, which can also be inputted to the different C-rates between both experiments.

In conclusion and despite the experimental hurdles associated not to the experimental setup but to the system under study, *operando* experiments were useful to confirm previous results obtained *ex situ* and provide more insights on the complexity of the mechanism, with the protocols used paving the way for the study of other positive electrode materials.¹²³ However, since reactions with calcium have very slow kinetics, it may be difficult to obtain enough beamtime to perform such experiment in synchrotron (experiment time > 4 days) and thermalized cells compatible with laboratory diffractometer may constitute a better alternative, especially if high resolution is not needed.

V. Temperature dependent studies on $\text{Na}_3\text{V}_2(\text{PO}_4)_3$

As stated in the introduction (section 1.2.6.1), the synthesis of NASICON compounds was a cornerstone in the development of positive electrodes for sodium batteries. Among them, the Vanadium containing compound $\text{Na}_3\text{V}_2(\text{PO}_4)_3$ (NVP), which structure was reported by Delmas in 1978¹²⁴ and first electrochemical desodiation by Gopalakrishnan¹²⁵ in 1992, exhibits interesting properties, especially in terms of high ionic conductivity, capacity (116 mAh/g)⁵³ and operating voltage (3.4V vs Na^+/Na) despite a low electronic conductivity and consequently poor cycle and rate performance.¹²⁶ This problem was later overcome with the synthesis of carbon-coated NVP.^{53,127,128} Recent studies showed cycling of a Na/NVP battery as fast as C/200 and over 30000 cycles.⁵³ To improve the energy density of the positive electrode, especially by enabling the insertion of a 4th sodium in the NASICON structure, substitutions of the vanadium towards another transition metal are studied. Thanks to the tunability of the NASICON structure, several composite mixes involving different elements (e.g. Ni,^{129,130} Al,^{131,132} Mn,^{77,130,133} Fe^{130,134}) were synthesized and tested recently.

While most studies report NVP's structure as rhombohedral (space group $R\bar{3}c$), the presence of a monoclinic distortion and superstructure was mentioned in several reports.^{135–138} A study published in 2015,⁷⁶ combining the results of synchrotron powder and single crystal X-ray diffraction, evidenced the presence of satellite peaks, indicating the presence of a superstructure which was compatible with a monoclinic unit cell with the $C121$ space group.⁷⁶ That same paper indicated the possible existence of three structural transitions when investigated using differential scanning calorimetry (DSC). Above 178°C, the high temperature γ -NVP phase adopts a rhombohedral $R\bar{3}c$ space group while the low temperature α -NVP phase, obtained below 12.2°C crystallizes in the $C2/c$ space group, and is characterized by a peak at $d = 7.13$ Å. Two incommensurate monoclinic phases, β -NVP and β' -NVP were observed between those temperatures (transition at 118°C). The β -NVP phase is usually the one observed at room temperature, and can be indexed within the $C121$ space group. It is important to highlight the presence of a severe temperature hysteresis for the transition between α - and β -NVP: based on that DSC measurement (10°C/min rate), the transformation occurs at 12.2°C when cooling but up to 25.8°C when heating. Note the hysteresis depends on the warming/cooling rate, hence a sample measured at a temperature below 28.5°C (\pm room temperature, depending on the season and the geographical location) can therefore exhibit features of the α -phase depending on its "thermal history". A 2017 study by Zhang *et al.*¹³⁹ investigated the material at low temperature carrying out a DSC experiment upon heating at a the same rate of 10°C /min and found that both NVP and the partially desodiated $\text{NaV}_2(\text{PO}_4)_3$ undergo a phase transition at 283K (\sim 10°C).¹³⁹ However, the DSC was not performed while cooling the sample, and the occurrence of an eventual temperature hysteresis with $\text{NaV}_2(\text{PO}_4)_3$ could not be assessed. The low temperature desodiated $\text{NaV}_2(\text{PO}_4)_3$ has lower symmetry, going from the $R\bar{3}c$ space group to $C2/c$ with lattice parameters $a = 14.757$, $b = 8.472$ Å, $c = 21.212$ Å, and $\beta = 90.248^\circ$. The low temperature phase differs from the high temperature phase by the relative intensities of the 300 and 018 peaks ($d = 2.43$ and 2.5 Å respectively), which were observed after 6h of data collection. However, Zhang *et al.* do not see the existence of the peak at $d = 7.13$ Å highlighted by the 2015 study as the angular domain used in their experiment was not low enough.⁷⁶

Full understanding of the redox mechanism of this compound has been complex and there is still some controversy regarding the charge compensation process during oxidation and Na^+ deintercalation, the two hypothesis being that either one single vanadium atom is oxidized and hence involves $\text{V}^{4+}/\text{V}^{3+}$ and $\text{V}^{3+}/\text{V}^{2+}$ redox couples or both vanadium atoms are oxidized and only the couple $\text{V}^{4+}/\text{V}^{3+}$ is involved. Yet, two recent studies using *operando* magnetometry¹⁴⁰ and X-ray absorption spectroscopy¹⁴¹ tend to prove the latter, in line with what has been observed for $\text{Na}_3\text{V}_2(\text{PO}_4)_2\text{F}_3$.¹⁴² Typically, NVP exhibits a potential plateau at 3.4 V during the oxidation and 3.35 V during the reduction. Those voltages may be slightly affected by overpotentials due to cell polarization or the amount/thickness of carbon coating on the NVP particles. A potential jump of a few mV is also commonly observed at half the reduction capacity as depicted in figure V.1 usually attributed to an intermediary phase at $x = 2$. This phase can be observed through X-ray diffraction while oxidizing/reducing NVP, likely $\text{Na}_2\text{V}_2(\text{PO}_4)_3$ at C-rates such as C/5 or C/10.^{77,139,143} However, this phase was only observed in a few patterns around $x = 2$ in $\text{Na}_x\text{V}_2(\text{PO}_4)_3$ and was not isolated *ex situ* to the best of our knowledge. When performing cyclic voltammetry with scan rates ranging from 0.5 to 5.0 mV/s (from 3 to 5 C) using α -NVP (at 273K ; 0°C), Zhang reports a gradual transition in oxidation (one-phase mechanism) from $\text{Na}_3\text{V}_2(\text{PO}_4)_3$ to $\text{NaV}_2(\text{PO}_4)_3$ while the reverse process is biphasic during the reduction.¹³⁹ These observations on the X-ray diffraction patterns were confirmed by Pawley refinements to extrapolate the lattice parameters as a function of the reaction time.

The goal of this chapter is to get further insights in the redox mechanism of NVP. The three cell setups described in section II.3.2.2. have been used to electrochemically oxidize/reduce NVP at different temperatures to see if the temperature affects the intermediary phase's stability.

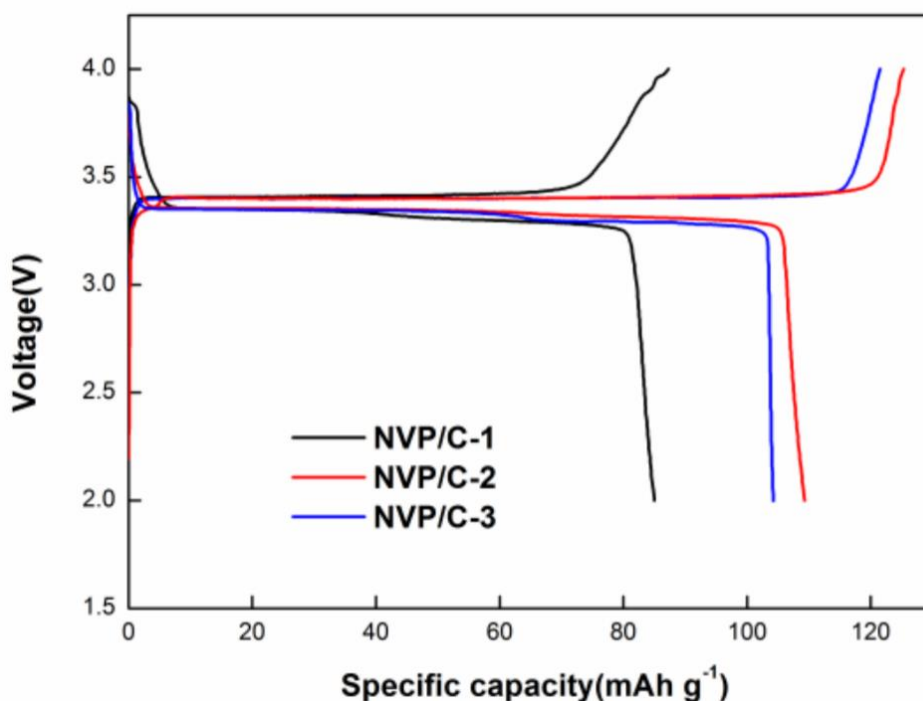


Figure V.1 – Capacity vs. potential profile of carbon coated NVP vs. Na cells at C/5, using different amounts of carbon used during the synthesis: 1g, 1.5g and 2g for samples denoted C-1, C-2 and C-3 for ~6.8 g of NVP respectively. Reprinted from ¹⁴⁴.

V.1. Investigation of pristine $\text{Na}_3\text{V}_2(\text{PO}_4)_3$

As mentioned above, a DSC study on NVP evidenced the existence of phase transitions in this compound as a function of temperature: α -, β - β' - and γ -phases are successively observed as the temperature increases.⁷⁶ As shown by the DSC profile (fig V.2 a), the transition between β -NVP and α -NVP occurs near room temperature, hence samples will have a different composition depending on the effective ambient conditions during data collection and/or history of sample (preparation/storage). The α -NVP phase is characterized by a small reflection, indexed as -111 at $d = 7.13 \text{ \AA}$ ($2\theta = 6.63^\circ$ at $\lambda = 0.826 \text{ \AA}$) (fig V.2 b) and a splitting of the 116 reflection ($d = 2.79 \text{ \AA}$),⁷⁶ undergoing a monoclinic distortion, yet keeping the NASICON structure as shown in figure V.2c). In that case, the lantern unit of the NASICON is distorted by the creation of vacancies of the sodium's coordination sphere. Although the space group is different, the cell size remains similar in the two phases. Table V.1 summarizes the lattice parameters of both phases, and also that of the high temperature γ -phase, retrieved by Rietveld and refinement of the modulation vectors from data collected on a single crystal.

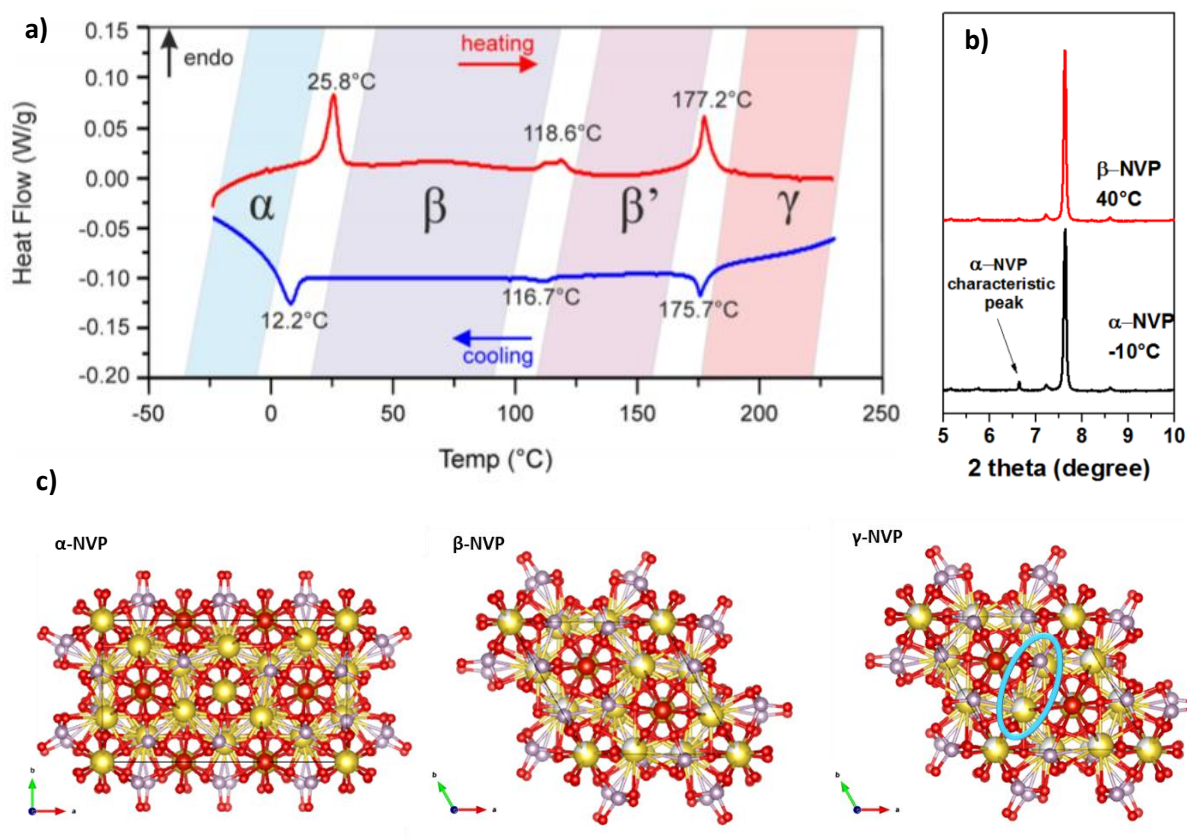


Figure V.2 - a) DSC profile of NVP, reprinted from 76, b) comparison of X-ray diffraction patterns of α -NVP and β -NVP, and c) structures of α -NVP, β -NVP and γ -NVP.

Table V.1 – Unit cell parameters of α -NVP (as reported in ref 76) and β -NVP in monoclinic and rhombohedral structure (as reported in ¹⁴⁵)

	α -NVP ⁷⁶	β -NVP (monoclinic)	β -NVP (rhombohedral) ¹⁴⁵	γ -NVP ⁷⁶
Space group	<i>C2/c</i>	<i>C121</i>	<i>R3c</i>	<i>R3c</i>
a (Å)	15.1244(6)	15.1089(4)	8.7288(2)	8.73382(4)
b (Å)	8.7287(3)	8.71848(2)	8.7288(2)	8.73382(4)
c (Å)	21.6143(8)	21.7898(5)	21.8042(7)	21.91438(17)
β (°)	90.163(2)	90.260(2)	90	90

In order to assess the above described findings and confirm the proposed phase diagram, pure NVP powder was loaded in a 0.5 mm diameter glass capillary and thermalized using OXFORD 700 cryostream. To observe the transition temperature, which is different upon cooling or heating, the sample was first cooled down to -22°C (251 K), then reheated up to 77°C (350 K) with a 3 °C /min rate, while X-ray diffraction patterns were collected every 2 min. A last ramp to cool the sample to room temperature was performed at the same rate. The presence of the α -phase was detected by -111 peak (see figure V.2.b) and a tailored program was used to measure its intensity. Figure V.3 represents the integrated intensity of the characteristic peak of the α -phase with respect to the temperature. In this case, the intensity rises at 7°C upon cooling and disappears at 32°C upon reheating. The discrepancy between the data presented here and in literature^{76,139} might be a result of the different warming/cooling rate and technique used. Finding the transition temperature of a material using X-ray diffraction might lead to some ambiguity as there is no convention to define whether the temperature at which the peak appears or that at which the peak reaches full intensity should be used. In this study, to take diffraction patterns for pure α -NVP, the cells were cooled down in a freezer (~-10°C) before using the thermalization setup at 2°C, while some cells were cycled at 45°C to ensure only the β -NVP was present.

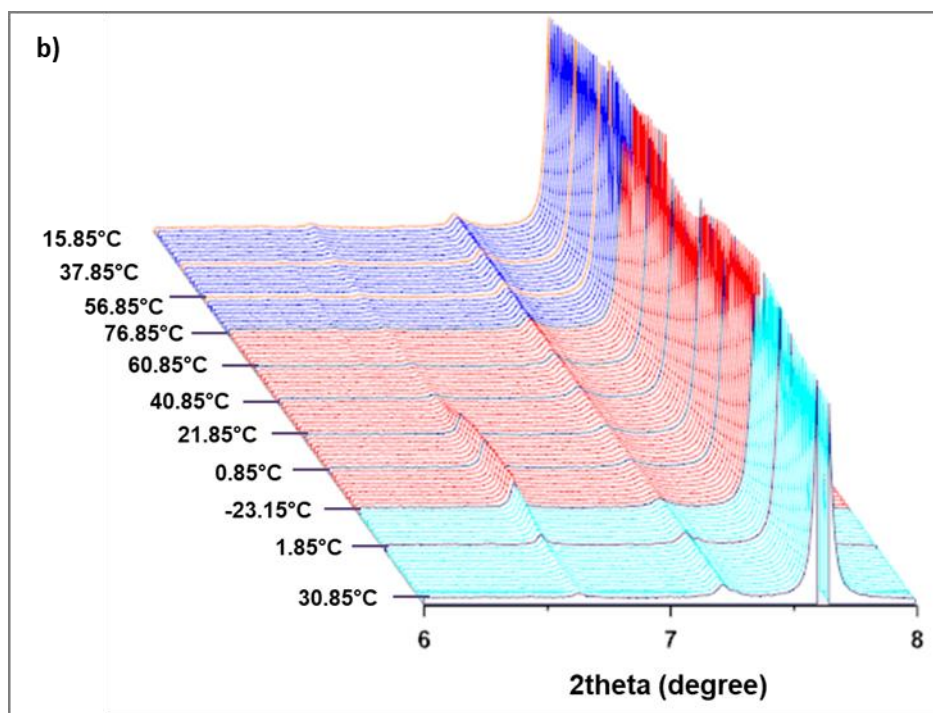
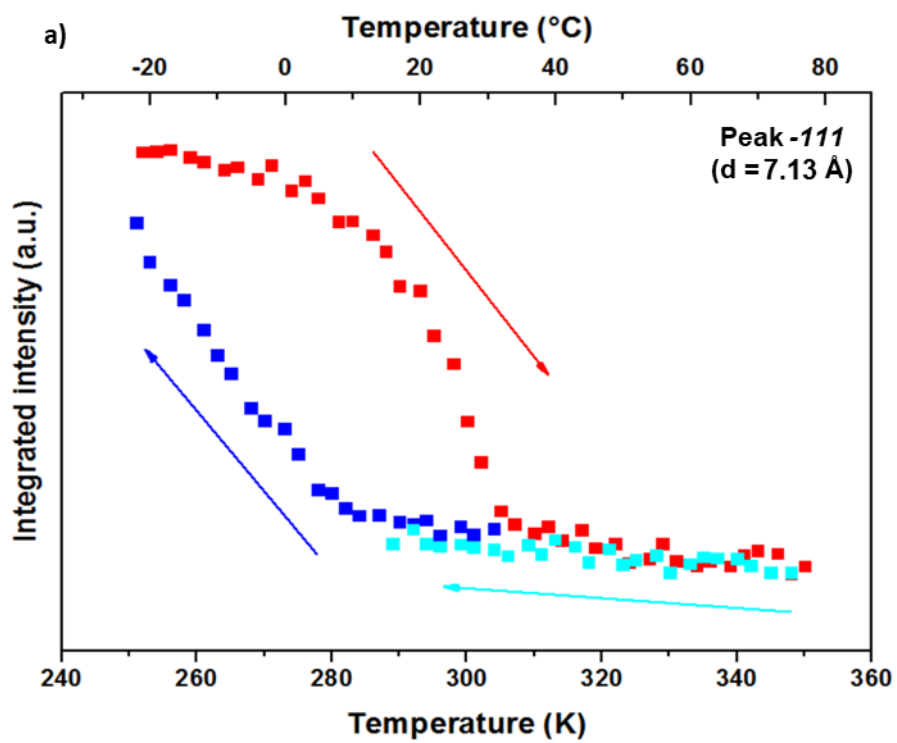


Figure V.3 – a) Evolution of the characteristic peak (-111) of the α -NVP phase as a function of temperature and b) evolution of the patterns as a function of temperature while cooling (blue) and heating (red)

V.2. Investigation of the redox mechanism for $\text{Na}_3\text{V}_2(\text{PO}_4)_3$ at room temperature

In order to get more information about the redox mechanism for NVP, and the presence of intermediate phases, *in situ operando* diffraction studies were carried out in collaboration with researchers at LRCS (Amiens, France). Indeed, contrary to Zhang et al. conclusion a two-phase mechanism is usually reported for the sodium (de-)intercalation process in NVP, that is from $\text{Na}_3\text{V}_2(\text{PO}_4)_3$ to $\text{Na}_1\text{V}_2(\text{PO}_4)_3$ ^{139,143} the latter being indexed within the $R\bar{3}c$ space group with $a, b = 8.426 \text{ \AA}$ and $c = 21.720 \text{ \AA}$. However, recent studies point at the existence of an intermediate compound with formula $\text{Na}_2\text{V}_2(\text{PO}_4)_3$ ^{77,146} observed while cycling a Na/NVP cell at C/5 *operando*. Studies were carried out at LRCS to better understand this phase and the optimal operating conditions to observe it; yet to the best of our knowledge, it was not observed *ex situ*. It is also important to note here that similar intermediate phases have been reported to form while oxidizing some substituted NASICON such as $\text{Na}_{3.2}\text{Mn}_{0.2}\text{V}_{1.8}(\text{PO}_4)_3$ or $\text{Na}_{3.4}\text{Mn}_{0.4}\text{V}_{1.6}(\text{PO}_4)_3$.⁷⁷

V.2.1. Preliminary *operando* experiments with synchrotron radiation

Preliminary experiments were carried out by Fan Chen in the framework of her PhD at LRCS in order to shed more light into the redox mechanism of NVP and the observation of the intermediate phase. For this, NVP was loaded in a Leriche cell with a metallic sodium negative CE and an electrolyte consisting of a 1M solution of NaPF_6 in EC:DMC:FEC (48:48:2) which will be referred later as NP30+FEC. FEC was here used as an additive to stabilize the SEI¹⁴⁷ on the sodium negative electrode.¹⁴⁷ Cells were cycled at C/10 (full oxidation and extraction of 2 moles of sodium ions in 20h) on MSPD powder diffraction beamline in ALBA at a $\lambda = 0.826 \text{ \AA}$ wavelength and a pattern was collected every 10 min. The electrochemical curve and patterns collected are presented in [figure V.4](#). Upon oxidation, the voltage profile exhibits a plateau at $\sim 3.4 \text{ V}$ while two phase transitions take place, first from $\text{Na}_3\text{V}_2(\text{PO}_4)_3$ to $\text{Na}_2\text{V}_2(\text{PO}_4)_3$ and secondly from $\text{Na}_2\text{V}_2(\text{PO}_4)_3$ to $\text{Na}_1\text{V}_2(\text{PO}_4)_3$, which contrasts with the solid solution mechanism proposed by Zhang.¹³⁹ Upon reduction, the plateau is observed at a lower potential, around $\sim 3.35 \text{ V}$, with a potential jump of 0.07 V at $x = 2.15$ in $\text{Na}_x\text{V}_2(\text{PO}_4)_3$, and the reverse process takes place, as can be inferred from the diffraction patterns. Upon reaching the potential threshold (2.5 V ; $x = 2.80$), there was still some peaks from the intermediary phase $\text{Na}_2\text{V}_2(\text{PO}_4)_3$ and the cell started to reoxidize. The intensity was manually switched upon reduction several times to ensure the process was fully reversible and the $\text{Na}_3\text{V}_2(\text{PO}_4)_3$ phase could be retrieved. The $\text{Na}_3\text{V}_2(\text{PO}_4)_3$ phase was observed after the second reduction (pattern 142, $x = 2.85$) but the following reductions were forced to collect more patterns of the $\text{Na}_3\text{V}_2(\text{PO}_4)_3$ phase.

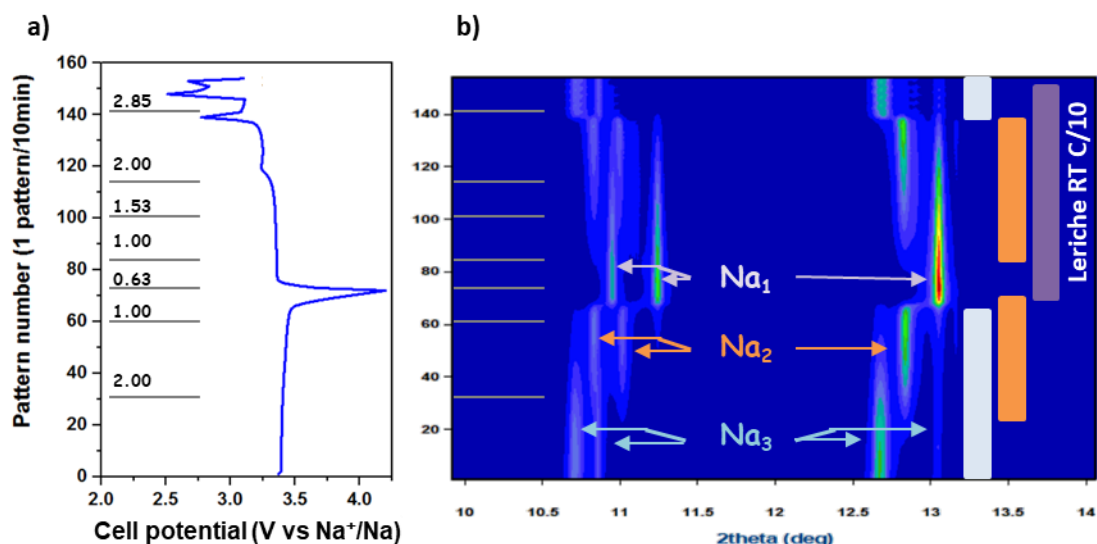


Figure V.4 - a) Pattern number (10min increment in time) vs cell potential and b) associated X-ray surface plots ($\lambda = 0.826 \text{ \AA}$) of a Leriche cell cycled with NVP using NP30+FEC electrolyte at C/10 at room temperature at MSPD. Grey ticks represent the calculated x values in $\text{Na}_x\text{V}_2(\text{PO}_4)_3$. White, orange and purple bands represent the patterns on which the Na_3 , Na_2 and Na_1 phases are visible, respectively.

Some patterns were selected to perform Rietveld refinement (or LeBail fittings in the case of $\text{Na}_2\text{V}_2(\text{PO}_4)_3$) and to extract the lattice parameters of the three different phases. The refinement of the intermediate $\text{Na}_2\text{V}_2(\text{PO}_4)_3$ phase was more complex due to the fact that no single phase patterns were available as it always coexists with another phase. A pattern containing $\text{Na}_2\text{V}_2(\text{PO}_4)_3$ as major phase but also $\text{Na}_1\text{V}_2(\text{PO}_4)_3$ was selected for the refinement. For the sake of clarity, the peaks related to the metallic Na CE and Be windows were excluded from the refinements (figure V.5). $\text{Na}_1\text{V}_2(\text{PO}_4)_3$ was refined within the $R\bar{3}c$ space group while $\text{Na}_2\text{V}_2(\text{PO}_4)_3$ was refined within the $P2/m$ space group. The parameters of the $\text{Na}_1\text{V}_2(\text{PO}_4)_3$ phase were refined first and later fixed to ease a preliminary refinement of the $\text{Na}_2\text{V}_2(\text{PO}_4)_3$ cell parameters. Once a decent fitting was found, both phases were refined at the same time to obtain the final values. These are summarized in table V.2, and are in good agreement with data reported previously.^{76,148}

It appears there is some discrepancy between the x measured through electrochemistry upon oxidation and reduction and phase composition observed for the electrodes. Indeed, the $\text{Na}_2\text{V}_2(\text{PO}_4)_3$ phase was observable between pattern 26 and 65 in oxidation ($x = 2.14$ and 0.83 respectively) and between pattern 92 and 141 in reduction ($x = 1.26$ and 2.85 respectively). It is also important to note that the $\text{Na}_1\text{V}_2(\text{PO}_4)_3$ phase appeared at $x = 1.10$, just before the switch to reduction, yet only disappeared at $x = 2.80$ upon reduction. This is consistent with results described in the literature^{77,139,143} as the detection of $\text{Na}_2\text{V}_2(\text{PO}_4)_3$ phase is elusive. Thus, *operando* data collection is crucial to get further insights on this matter.

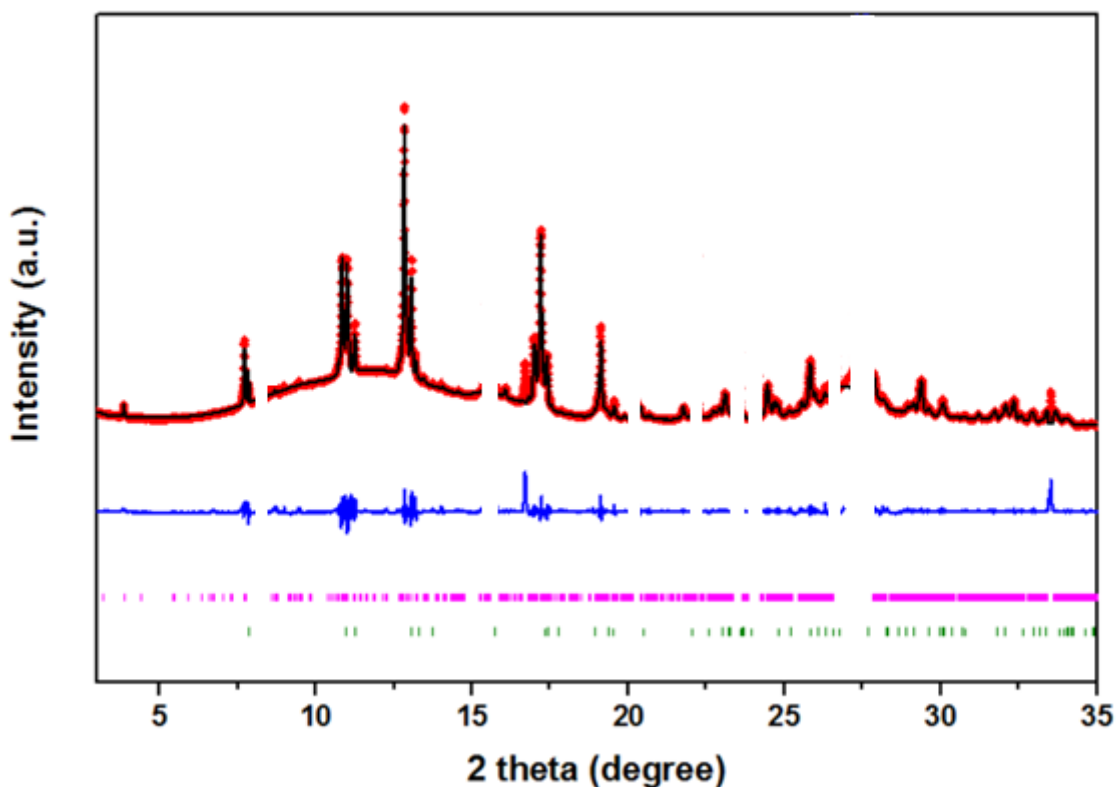


Figure V.5 – LeBail refinement of pattern N° 132 containing two phases: $\text{Na}_1\text{V}_2(\text{PO}_4)_3$ and $\text{Na}_2\text{V}_2(\text{PO}_4)_3$, the red dots correspond to the measured pattern, the black line the calculated pattern, the blue line the difference between the calculated and measured pattern. The pink ticks correspond to the $\text{Na}_2\text{V}_2(\text{PO}_4)_3$ phase while the green ones corresponds to the $\text{Na}_1\text{V}_2(\text{PO}_4)_3$ phase

Table V.2 – Lattice parameters and main peaks corresponding to the different phases observed

	$\text{Na}_3\text{V}_2(\text{PO}_4)_3$		$\text{Na}_2\text{V}_2(\text{PO}_4)_3$	$\text{Na}_1\text{V}_2(\text{PO}_4)_3$		
	Low temperature (α -phase)	High temperature (β -phase)				
Space group	<i>C2/c</i>	<i>C121</i>	<i>P2/m</i>	<i>R3c</i>		
a (Å)	15.086(9)	15.109(9)	14.847(2)	8.429(4)		
b (Å)	8.714(6)	8.718(1)	8.617(7)	8.429(5)		
c (Å)	8.810(5)	21.790(3)	21.554(2)	21.400(5)		
β (°)	124.550(3)	90.260(6)	90.435(1)	90.000		
Index	List of main peaks, 2θ at $\lambda = 0.826 \text{ \AA}$ / d-spacing in Å					
<i>202 + 112</i>	7.62°	6.22 Å	7.72°	6.12 Å		
<i>-204</i>	10.72°	4.42 Å	10.85°	4.37 Å	10.93°	4.33 Å
<i>020</i>	10.87°	4.36 Å	11.03°	4.30 Å	11.13°	4.26 Å
<i>023</i>	12.70°	3.73 Å	12.85°	3.69 Å	12.92	3.67 Å
<i>006</i>	13.03°	3.64 Å				

V.2.2. Operando experiment using a laboratory X-ray diffractometer (secondment at LRCS)

In this experiment, the cell was positioned in the diffractometer thanks to a camera in an attempt to place the sample tested as close as the center of the diffractometer as possible. While in synchrotron experiments, the comparison between the patterns collected in the cell and a preliminary measured capillary (see [section III.3](#)) is enabled by the fast data acquisition, repeating the procedure with a laboratory diffractometer would be too long and tedious; hence the patterns may be distorted due to the displacement of the sample with respect to the center. To properly process the powder patterns, displacement corrections have to be included in the refinement of the data. The determination of the so called displacement parameters is done by fixing the known unit cell of the pristine NVP (ideally obtained by *ex situ* data collection). During cycling, the refined displacement parameters are then fixed since the probed electrode material is not expected to move. Due to the higher divergence of the incoming beam on lab X-ray apparatus, the data are more sensitive to off centering compared to synchrotron.

Given the issues related to the electrochemical behavior of the *in situ* cells detected during the preliminary work discussed above, additional precautions were taken for cell assembly during this study. Normally, the negative material would be put directly in contact with the plunger (or pressed onto it in the case of metallic Na or Li). Since it was suspected that while screwing the plunger into the cell, the separator could be folded which could induce some short-circuits, a spacer was inserted between the plunger and the negative electrode and kept during other studies using this cell to ensure physical separation between the electrodes. In addition to that, a Celgard polypropylene separator was placed in contact with the sodium and a casted NVP electrode was used on the positive side to enhance the homogeneity of the electrochemical reaction. Given their crystal structure, NASICON compounds are not as sensitive to preferred orientation as layered materials (*e.g.* TiS_2 , see [section III.1](#)), and hence does not involve similar disadvantages. A schematic view of the resulting setup is given in [figure V.6](#). Since other tests ran afterwards showed that all these precautions were not necessary, this configuration was only used in some of the experiments.

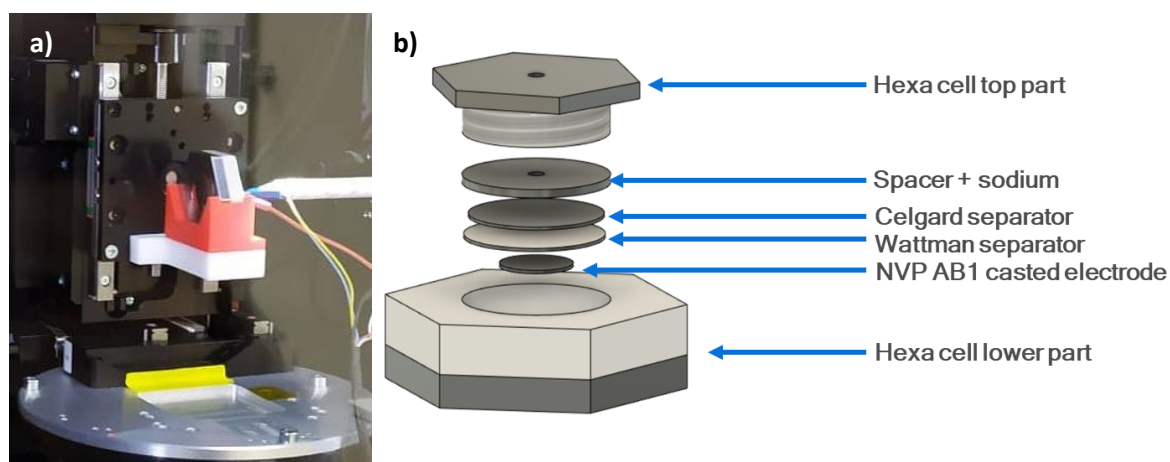


Figure V.6 – a) Hexagonal cell mounted on the D8 Discover diffractometer and b) exploded view of the cell configuration used in that study

The electrolyte used in all cases was NP30+FEC and the electrochemical tests were carried out at at C/10 (complete oxidation in 20h) between 2.5 V and 4.0 V. The cell was mounted on the D8 Discover, equipped with a molybdenum rotating anode ($\lambda = 0.709\text{\AA}$) and a pattern was collected every hour during 20 min (20 min data collection + 40 min break). Although the statistics are not as good as they would be for a synchrotron experiment, the collection rate is fast enough to see the material's evolution. An electrochemical curve and the corresponding surface plot are given in figure V.7. Since wavelength is different from the other experiments presented in this chapter, the X-ray diffraction patterns are presented in Q and a conversion to degrees at $\lambda = 0.826\text{\AA}$ is given to ease the comparison.

During oxidation, the voltage profile exhibits a plateau at $\sim 3.4\text{ V}$ while $\text{Na}_3\text{V}_2(\text{PO}_4)_3$ transforms into $\text{Na}_1\text{V}_2(\text{PO}_4)_3$. In a few patterns at the end of oxidation, faint traces of the intermediary $\text{Na}_2\text{V}_2(\text{PO}_4)_3$ are observed but the peaks were not intense enough to perform a refinement. During the reduction, the voltage plateau takes place at $\sim 3.3\text{ V}$ but no potential step is observed, despite the rate being the same as for the previous experiment. This difference could originate from a different cell polarization (Leriche vs hexagonal geometry), particle size (different synthesis batch) or electrochemical homogeneity (casted vs powder). It is interesting to see that the $\text{Na}_1\text{V}_2(\text{PO}_4)_3$ phase only appears when the potential rises at the end of the oxidation, and that the $\text{Na}_3\text{V}_2(\text{PO}_4)_3$ reappears just before the potential drops in reduction, in a similar way as observed previously. In the meantime, $\text{Na}_1\text{V}_2(\text{PO}_4)_3$ reversibly transforms back to $\text{Na}_3\text{V}_2(\text{PO}_4)_3$ without observation of intermediary phase Figure V.8 displays the 1st, 17th and 20th selected patterns from which the presence of the three phases can be inferred. Le Bail fitting of the diffraction pattern of $\text{Na}_3\text{V}_2(\text{PO}_4)_3$ taken *ex situ* considering monoclinic symmetry ($C121$) gives $a = 15.08(2)\text{\AA}$, $b = 8.70(1)\text{\AA}$, $c = 21.78(8)\text{\AA}$ and $\gamma = 90.27(2)^\circ$, in good accordance with the previous refinements (see Table V.1).^{53,77} Using those results, the displacement parameters were refined with Le Bail method on the first pattern collected *in situ* by fixing the phase's parameters.

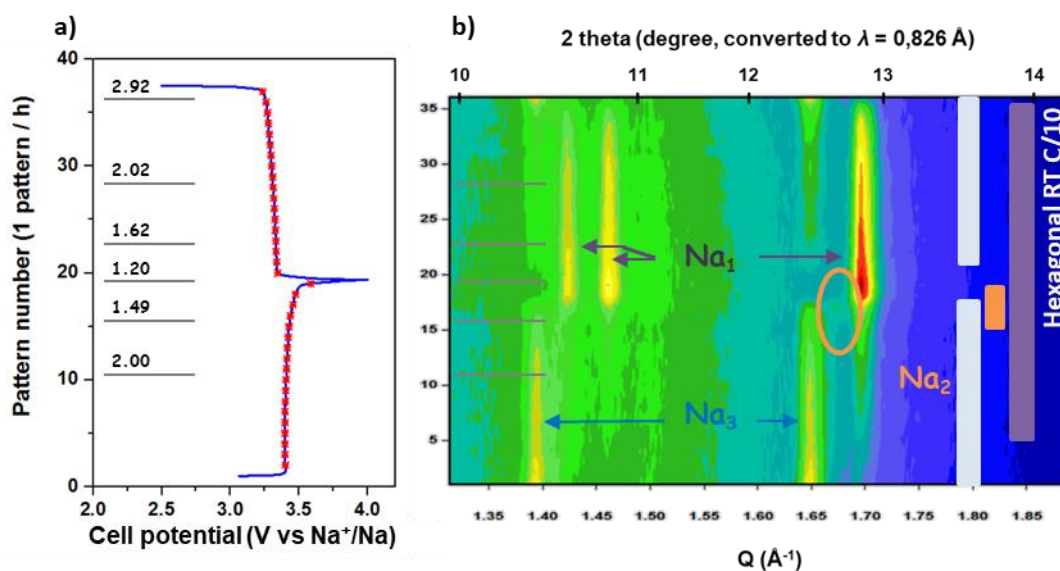


Figure V.7 — a) Pattern number (1h increment in time) vs cell potential, every red dot represents a pattern and b) associated X-ray surface plots ($\lambda = 0.709\text{\AA}$) taken while cycling a hexagonal cell loaded with NVP using NP30+FEC electrolyte at C/10 on a D8 discover diffractometer. Data is presented in Q (\AA^{-1}) and a conversion to degrees at $\lambda = 0.826\text{\AA}$ is provided on the upper axis. Grey ticks represent the calculated x values in $\text{Na}_x\text{V}_2(\text{PO}_4)_3$. White, orange and Purple bands represent the patterns on which the Na_3 , Na_2 and Na_1 phases are visible, respectively.

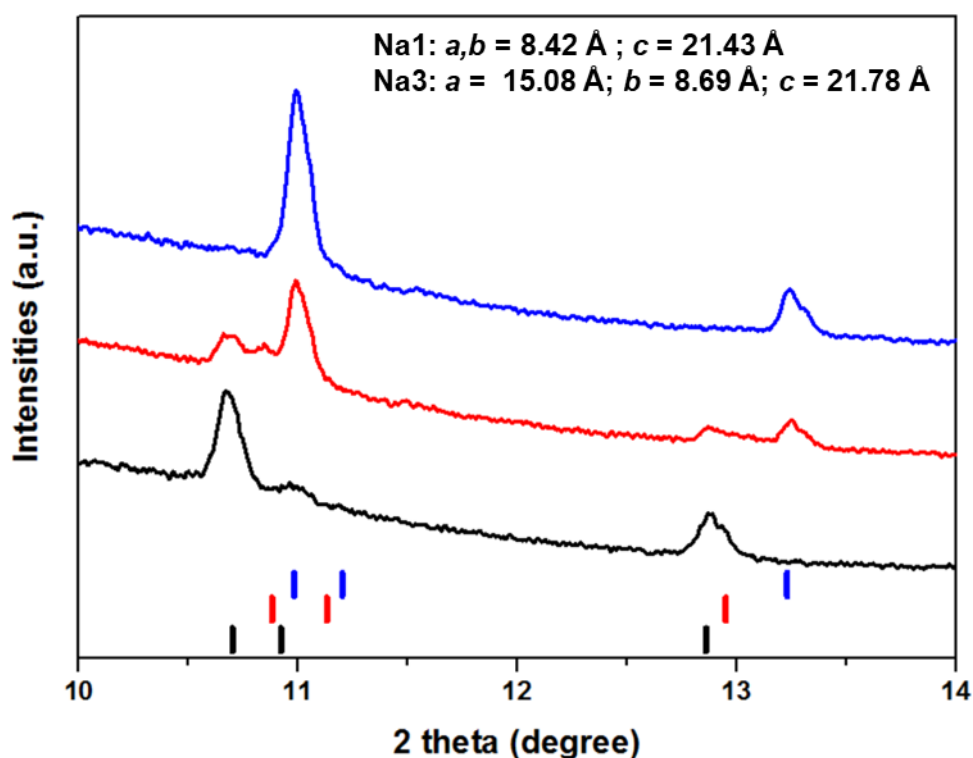


Figure V.8 - X-ray diffraction patterns n°1, 17 and 20 of the cycling presented above. Black, red and blue ticks represent the positions of peaks corresponding for $\text{Na}_3\text{V}_2(\text{PO}_4)_3$, $\text{Na}_2\text{V}_2(\text{PO}_4)_3$, and $\text{Na}_1\text{V}_2(\text{PO}_4)_3$ respectively.

In that experiment, the intermediate phase $\text{Na}_2\text{V}_2(\text{PO}_4)_3$ was only observed in a few patterns before the end of the oxidation. This is consistent with data published so far^{77,139,143} even if the preliminary synchrotron experiment presented in [section V.2.1](#) proved that the intermediary phase can be observed in earlier stages of oxidation, which may point at some sluggish kinetics of the process. The common aspect between the studies reported in such references and the experiment presented in this section is that the X-ray diffraction data were collected using a laboratory diffractometer, resulting in patterns with less statistics than those achieved with synchrotron experiment. Yet, it is very likely that the conditions of the experiments such as C-rate and cell polarization depending on the geometry used (Leriché⁷⁷ or tailored prototype¹³⁹) will also have an influence on the results achieved. Thus, new synchrotron experiments were carried out using the three prototypes of thermalized cell at our disposal, which enabled data collection at ambient and non-ambient temperature

V.3. Temperature dependent synchrotron experiments

The aim of the temperature dependent experiments was to test the α -NVP phase in order to determine if the electrochemical behavior of the material would be different and/or if the $\text{Na}_2\text{V}_2(\text{PO}_4)_3$ phase could be observed more easily at non-ambient temperature. Out of the three thermalized prototypes, only the modified Leriché was used in non-ambient temperature conditions

(see [chapter IV](#)) before the experiments reported in this section while the other ones were used for the first time on a synchrotron beamline during this project. Because of this, the thermalized setups (hexagonal cell + ring, thermalized coin cell oven and thermalized Leriche) were as well initially used without circulating fluid, to assess the prototypes.

V.3.1. Hexagonal cell

V.3.1.1. Test at room temperature

To first test the thermalized hexagonal cell prototype, a room temperature *operando* experiment using synchrotron radiation was performed in this cell placed into the copper ring. The cell was assembled using a glassy carbon window on the negative side and beryllium window on the positive side. An aluminum foil was placed in contact with the Be window to protect it, on top of which NVP electrode was added. In this case, as well as in all the synchrotron *operando* measurements described hereafter, loose powder (mixture of NVP with 10% carbon black) was used in the positive electrode to increase powder averaging and minimize preferred orientation, despite the risk of less homogeneous reaction described above. Sodium metal was used as the negative electrode and pressed onto a hollowed stainless steel spacer, the electrolyte being NP30+FEC. Patterns were collected on the powder diffraction station of MSPD at $\lambda = 0.826 \text{ \AA}$. The cell was cycled at C/5 (full oxidation with extraction of two sodium ions in 10h) between 2.5 V and 4.2 V. The electrochemical curve and the patterns collected are presented in [figure V.9](#). The potential seemed to stabilize around 3.46 V upon oxidation, which is a bit higher than the expected value (3.40 V), and could be attributed to cell polarization. After 3h oxidation the potential became noisy, yet the patterns collected showed an evolution of the phase composition and hence the cell was not stopped. The noise could be the result of small short circuits between the cell and the copper ring used for thermalization, despite the cell being protected by Kapton foil. Because of the noise, it was impossible to track the potential jump around $x = 2$. The peaks corresponding to $\text{Na}_3\text{V}_2(\text{PO}_4)_3$ (initially observed at $2\theta = 10.72^\circ, 10.87^\circ, 12.70^\circ$ and 13.03°) gradually disappeared in the course of oxidation to the expense of a new set of peaks ($2\theta = 10.85^\circ, 11.03^\circ$ and 12.85°), which are typical of the $\text{Na}_2\text{V}_2(\text{PO}_4)_3$ phase and disappear upon further oxidation to the expense of peaks at $2\theta = 10.93^\circ, 11.13^\circ$ and 12.92° consistent with the formation of $\text{Na}_1\text{V}_2(\text{PO}_4)_3$. It is important to highlight that since some peaks corresponding to different phases have very similar positions ($\text{Na}_2\text{V}_2(\text{PO}_4)_3$ phase's peak at 10.85° and $\text{Na}_1\text{V}_2(\text{PO}_4)_3$ phase's at 10.93°) results could have been misleadingly interpreted as a shifting peak, likely because the peak broadened during the cycling. However, considering looking the other peaks, it is clear that the three phases are observed during this oxidation. After 11h ($x = 0.89$ in $\text{Na}_x\text{V}_2(\text{PO}_4)_3$) the voltage did not reach the threshold at 4.2 V, hence the cell was switched to reduction manually to avoid any problems linked to electrolyte decomposition. The potential stabilized around 3.3 V upon reduction and then dropped after 15.5h of cycling ($x = 2.05$) without any changes visible in the X-ray diffraction patterns throughout the full reduction process. At such stage of reduction, the presence of the intermediary $\text{Na}_2\text{V}_2(\text{PO}_4)_3$ phase could be expected, especially since it appeared at earlier stages in the experiment presented in [section V.2.1](#). However in that case, the electrochemistry was smooth and the potential rose at the end of the oxidation, switching the cell in reduction. In the present case, the potential was noisy and the cell had to be forced into reduction, and maybe because of that the electrolyte and/or the material was damaged which prevented further relevant observations. Refinements were performed on pattern 1, 25 and 80 to extract the

parameters of the Na_3 , Na_2 and Na_1 phase, respectively. In pattern 25, contrary to section V.2.1, the Na_2 phase was refined alone, although some faint peaks from the $\text{Na}_3\text{V}_2(\text{PO}_4)_3$ were present but did not hinder the refinement. Table V.3 summarizes the results of the refinements performed.

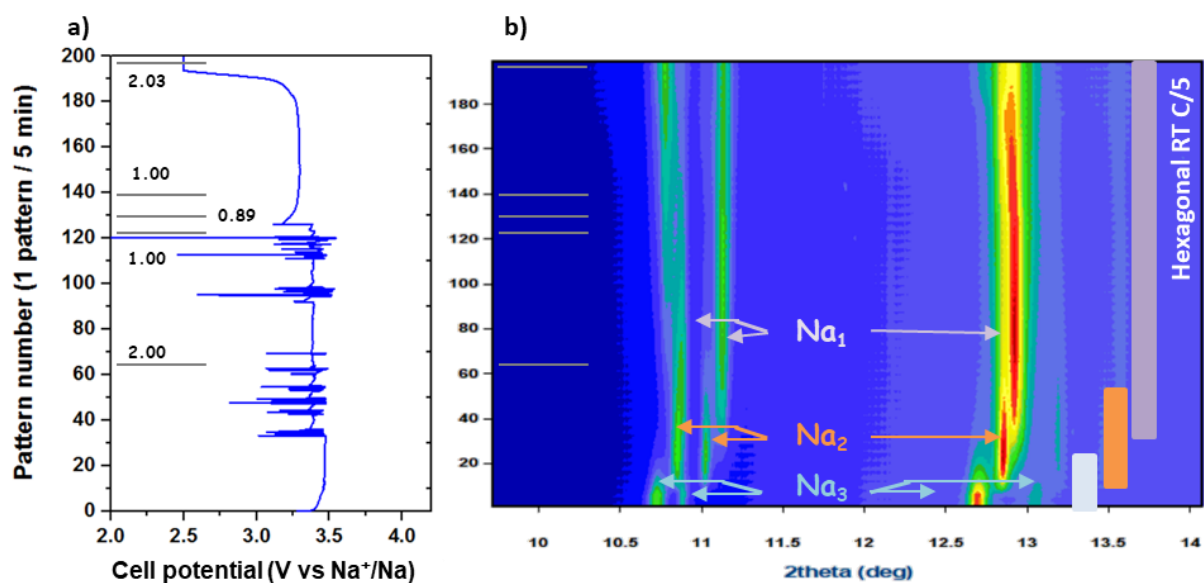


Figure V.9 — a) Pattern number (10min increment in time) vs cell potential and b) associated X-ray surface plots ($\lambda = 0.826 \text{ \AA}$) taken in a hexagonal cell cycled with NVP using NP30+FEC electrolyte at C/5 at room temperature at MSPD. Grey ticks represent the calculated x values in $\text{Na}_x\text{V}_2(\text{PO}_4)_3$. White, orange and purple bands represent the patterns on which the Na_3 , Na_2 and Na_1 phases are visible, respectively.

Table V.3 - Results of the refinements for the different phases found in the cycling of NVP observed during the experiment depicted in figure V.9

	$\text{Na}_3\text{V}_2(\text{PO}_4)_3$	$\text{Na}_2\text{V}_2(\text{PO}_4)_3$	$\text{Na}_1\text{V}_2(\text{PO}_4)_3$
Space group	<i>C121</i>	<i>P 2/m</i>	<i>R3c</i>
a	15.075(4)	14.876(3)	8.398(2)
b	8.702(6)	8.600(7)	8.398(2)
c	21.784(8)	21.543(3)	21.400(8)
γ	90.281(2)	90.290(7)	90.00

Despite the noisy cell potential, $\text{Na}_3\text{V}_2(\text{PO}_4)_3$ was oxidized to $\text{Na}_1\text{V}_2(\text{PO}_4)_3$ with the observation of the $\text{Na}_2\text{V}_2(\text{PO}_4)_3$ intermediate phase, which, as described above, is only reported in a couple of studies.^{77,146} This may be related to a metastable nature, as the C-rate seems to be a parameter influencing its formation. The geometry of the electrochemical cell (and more generally the setup) can induce polarization which may create overpotential and also have an impact on its observation. A comparison between patterns measured on powder and casted electrodes in synchrotron could help in further optimizing the protocol.

Further experiments would have been necessary to completely optimize the system, especially a comparison of different C-rates¹⁴⁶ would be informative. More time would have also been needed master the hexagonal cell setup and to identify the sources of possible current leakage to avoid any potential disruption.

Impact of thermal history of the sample

Since the transition between α - and β -NVP follows a temperature hysteresis (12.2°C when cooling and 25.8°C when heating) a sample measured at room temperature could contain either α -NVP or β -NVP depending on its thermal history. Thus, the thermalized setup was used and the liquid bath was set to 45°C to observe the β -NVP phase and to 2°C to observe the α -NVP phase.

To assess the thermal stability at room temperature of both the α - and β -NVP phase, an *in situ* cell was prepared and placed in the freezer (at $\sim -10^\circ\text{C}$) for 1 hour. A pattern was collected right after the cell was taken out of the freezer and after a few hours, at open circuit voltage, without connecting it to any potentiostat. While the characteristic peak of the alpha phase (-111 at $d = 7.13 \text{ \AA}$) was observable when the cell just came out of the freezer, it was absent from the pattern taken a while after, which means that, although the temperature in the experimental hutch was below the phase transition, thermalization was necessary to keep the α -NVP phase and prevent its evolution. An analogous experiment was done placing a cell at 60°C for 1h in a stove to ensure whether the β -NVP phase evolved when the temperature decreased. The peaks corresponding to the α -NVP phase were absent from the patterns collected right after the cell was taken out of the stove and also after waiting a few hours at ambient temperature, which points us to conclude that it is unlikely the transition to the α -phase would occur in normal operating condition and simply heating the material before preparing the cell would be sufficient to avoid the α -NVP phase peak. All the patterns measured are presented in [figure V.10](#).

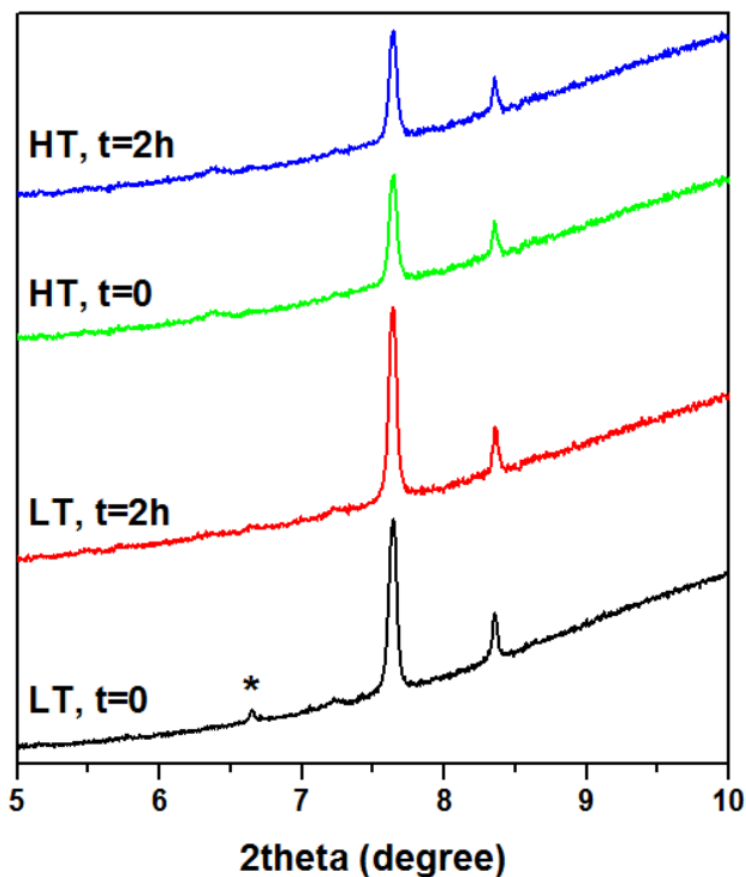


Figure V.5 - Patterns of NVP taken in cells stored at Low and High temperature, right out of the freezer/oven and after 2 hours, the asterisk represents the characteristic peak of the α -phase

V.3.1.2. The α -NVP phase (2°C)

In this part and the following sections, the intermediary and final phases found during oxidation at low temperature are denoted as $\text{Na}_2\text{V}_2(\text{PO}_4)_3'$ and $\text{Na}_1\text{V}_2(\text{PO}_4)_3'$ respectively as the experiments performed during the course of this thesis do not allow to ensure they are the same phases as those observed during testing at room temperature (starting from the β -phase).

A hexagonal cell was prepared as described above and launched upon oxidation at C/5 as well but this time at low temperature (bath temperature = 2°C). A stream of dry nitrogen was blown in front of the larger window to avoid water condensation. The electrochemical curve and X-ray patterns are presented in figure V.11. During this measurement, the beam was lost during a few patterns (75 to 78) and the corresponding region is marked by a blue band. The oxidation started with a pseudo-plateau around 3.4 V and potential continues to increase as the oxidation goes on. After 6h of cycling ($x = 1.86$ in $\text{Na}_x\text{V}_2(\text{PO}_4)_3$), the potential reached 3.45 V before dropping to 3.4 V. Although a potential jump is noticed around $x = 2$, its magnitude seems to be too high to be related to intrinsic electrochemical phenomena. Despite our efforts to isolate the cell, some water may have condensed on the body which may have some unexpected effects. Regarding the X-ray diffraction patterns, the $\text{Na}_2\text{V}_2(\text{PO}_4)_3'$ phase can be observed from pattern 19, where the peaks corresponding to $\text{Na}_3\text{V}_2(\text{PO}_4)_3$ decrease in intensity, while the $\text{Na}_1\text{V}_2(\text{PO}_4)_3$ phase appeared from pattern 124. At the end of the

oxidation, both $\text{Na}_2\text{V}_2(\text{PO}_4)_3$ and $\text{Na}_1\text{V}_2(\text{PO}_4)_3'$ phase are found to co-exist. It is important to note that the characteristic peak of the α -phase (-111) was lost during the cycling at $x = 2.45$. No reduction was performed as the beamtime ended.

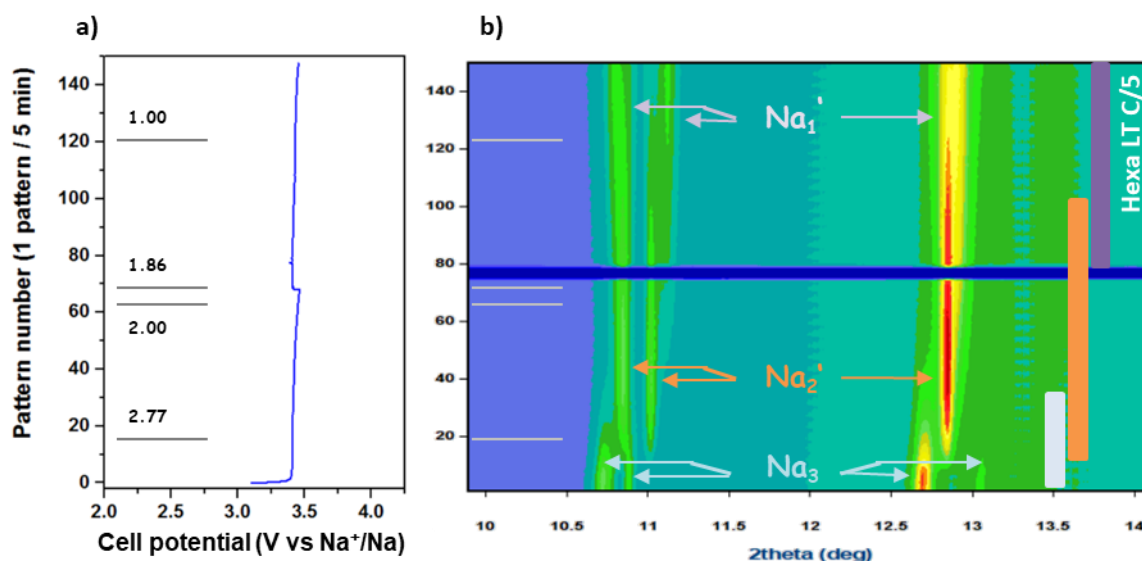


Figure V.11 – a) Pattern number (5 min increment in time) vs cell potential and b) associated X-ray surface plots ($\lambda = 0.826 \text{ \AA}$) of a hexagonal cell cycled with NVP using NP30+FEC electrolyte at C/5 at 2°C. Grey ticks represent the calculated x values in $\text{Na}_x\text{V}_2(\text{PO}_4)_3$. White, orange and purple bands represent the patterns on which the Na_3 , Na_2 and Na_1 phases are visible, respectively.

In that case, the distinction between the $\text{Na}_2\text{V}_2(\text{PO}_4)_3'$ and the $\text{Na}_3\text{V}_2(\text{PO}_4)_3'$ phase is not clear, and results are hence similar to those achieved by Zhang.¹³⁹ This may be due to sluggish kinetics related to the low temperature of the test, yet no conclusive results can be inferred from the data available to date and further studies would be required.

V.3.2. Experiments carried out using the coin cell oven

V.3.2.1. The β -NVP phase (45°C)

An *in situ* coin cell was loaded with a mixture of NVP and carbon black powder (10%), NP30+FEC electrolyte and sodium metal on the negative electrode. Since these cells have a non-conducting glass window, an aluminum foil was placed on the window on the positive electrode side to improve electronic conductivity. The cell was cycled at C/10 (20h to complete the oxidation) between 2.5 V and 4.2 V. The electrochemical curve and the patterns collected are presented in figure V.12. The beam was lost between pattern 358 and 421 which is represented by a blue band in the figure. During the oxidation, the voltage plateau at 3.4 V was observed in agreement with the data presented above. Since the potential did not increase, even after reaching $x = 0.75$ in $\text{Na}_x\text{V}_2(\text{PO}_4)_3$, the cell was manually switched upon reduction and a potential plateau around ~ 3.35 V was observed, after which the potential decreased to the threshold value at $x = 2.17$. Regarding the X-ray diffraction data, a similar behavior to the first cell described in section V.2.3 was observed (fig V.8). A rather smooth transition from $\text{Na}_2\text{V}_2(\text{PO}_4)_3$ to $\text{Na}_1\text{V}_2(\text{PO}_4)_3$ was observed, basing on the evolution of one peak (from 10.83° to 10.93°). However, since the cell was stopped at $x = 2.17$ upon reduction, the reverse process was not completed.

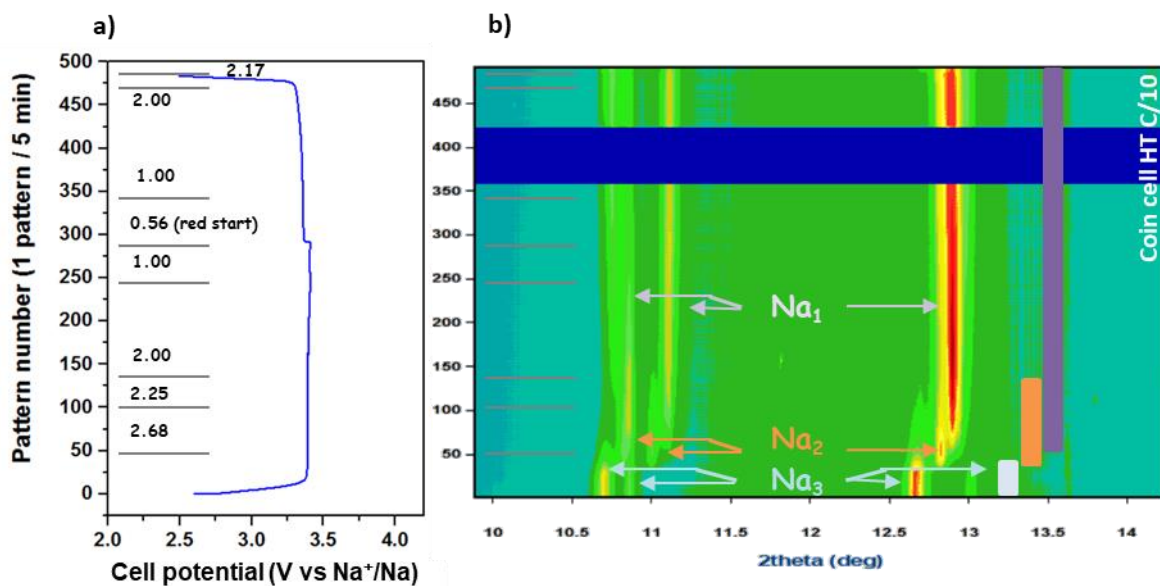


Figure V.12 – a) Pattern number (5 min increment in time) vs cell potential and b) associated X-ray surface plots ($\lambda = 0.826 \text{ \AA}$) of a coin cell cycled with NVP using NP30+FEC electrolyte at C/10 at 45°C . Grey ticks represent the calculated x values $\text{Na}_x\text{V}_2(\text{PO}_4)_3$. White, orange and purple bands represent the patterns on which the Na_3 , Na_2 and Na_1 phases are visible, respectively.

Although the coin cell is more compact and induces in general little to no polarization, there is still a large disruption between the x values calculated from the electrochemical capacity and the phase composition deduced from the X-ray diffraction patterns, with the $\text{Na}_1\text{V}_2(\text{PO}_4)_3$ appearing at $x = 2.25$. The $\text{Na}_2\text{V}_2(\text{PO}_4)_3$ phase's evolution upon oxidation is similar to the one presented in section V.2.2., as it fades away to form $\text{Na}_1\text{V}_2(\text{PO}_4)_3$, although the transformation takes place earlier in the present case, which may point at some metastable nature of this phase.

V.3.2.2. The α -NVP phase (2°C)

A second identical coin cell was oxidized at C/10 (complete oxidation in 20h) at 2°C . The electrochemical curve and patterns collected are presented in figure V.13. Between pattern 282 and 286, the beam was lost which is denoted by a blue band. A plateau at $\sim 3.4 \text{ V}$ is observed upon oxidation to $x = 0.97$ in $\text{Na}_x\text{V}_2(\text{PO}_4)_3$. During the process, the α -phase -111 peak is lost at $x = 2.56$. Interestingly, a new phase with peaks at 10.76° , 11.10° and 12.80° (respectively $d = 4.40$, 4.27 and 3.71 \AA) appears at $x = 1.63$. This phase was never reported to the best of our knowledge, and was not observed in other experiments. It is not sure whether it is a new intermediary phase with its presence being related to the low temperature and related to kinetics of the process, or if it originates from an inhomogeneity in the reaction. Still, its existence does not hinder the transformation to $\text{Na}_1\text{V}_2(\text{PO}_4)_3'$ at $x = 0.75$. Upon reduction $\text{Na}_2\text{V}_2(\text{PO}_4)_3'$ is formed but unfortunately the beam was lost before appearance of the $\text{Na}_3\text{V}_2(\text{PO}_4)_3$ phase could be observed.

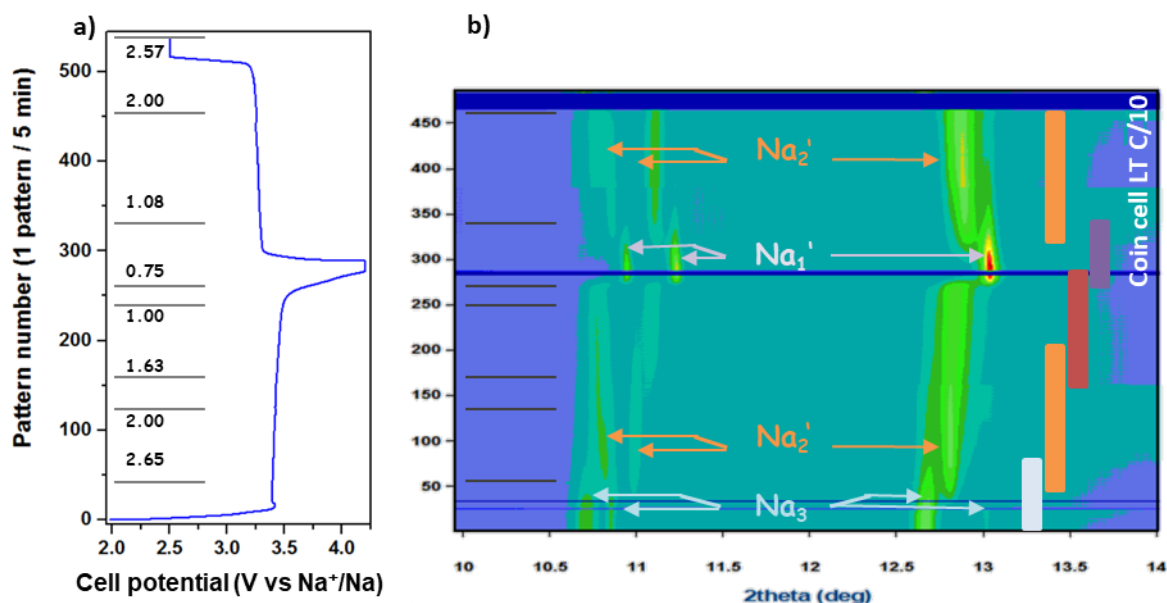


Figure V.13 – a) Pattern number (5 min increment in time) vs cell potential and b) associated X-ray surface plots ($\lambda = 0.826 \text{ \AA}$) of a coin-cell cycled with NVP using NP30+FEC electrolyte at C/10 at 2°C. Grey ticks represent the calculated x values in $\text{Na}_x\text{V}_2(\text{PO}_4)_3$. White, orange, purple and red bands represent the patterns on which the Na_3 , Na_2 , Na_1 and unknown phases are visible, respectively.

Overall, and aside from the observation of the new phase, which certainly deserves further investigation, the electrochemical signature and behavior is similar to what was expected and observed in previous experiments.

V.3.3. Experiments using the Leriche cell

Finally, the modified Leriche cells were also used to explore the electrochemical behavior of NVP.

V.3.3.1. Room temperature

The first experiment using the prototype of thermalized Leriche cell was carried out at room temperature. Be windows were used on both sides with the addition of a protective aluminum foil on the positive side. On the negative side, sodium metal was pressed directly onto the plunger and NP30+FEC was used as electrolyte. The cell was tested at C/7 with 15 minutes of OCV every hour. Since the thermalized cell is larger than the original cell and this was one of the first tests performed, this program was used to assess the cell polarization which was found to be 100 mV in average. The results are presented in figure V.14. Between pattern 27 and 34, the beam was lost and the missing patterns are represented by a blue band. Although the threshold voltages were set at 4.0 V in oxidation and 2.5 V in reduction, the cell never reached such potentials. The potential seemed to stabilize around 3.40 V, which is the expected value for the oxidation plateau, but after 8h ($x \approx 2$) a noisy behavior was observed before the potential ultimately dropped. In parallel, the intensity of the peaks corresponding to $\text{Na}_3\text{V}_2(\text{PO}_4)_3$ decrease to the expense of the peaks corresponding to $\text{Na}_2\text{V}_2(\text{PO}_4)_3$, despite both phases coexisting during the whole test. Interestingly, after 15h of

experiment (from pattern 95), the potential drops and the material reverts back to the pristine compound, while positive current is still applied to oxidize it. It is unsure why the potential became noisy and suddenly dropped: a possibility would be a current leakage through one current collector, or that the Kapton foil separating the cell body to the plunger was not placed properly, creating short circuits. However, it is surprising that in the experiment carried out at 45°C, although the potential dropped below 3.4 V, the $\text{Na}_1\text{V}_2(\text{PO}_4)_3$ phase remained stable while in this case (section V.2.4.1), the material transformed to $\text{Na}_3\text{V}_2(\text{PO}_4)_3$ as soon as the potential dropped below that equilibrium value. Although it is reasonable to conclude the cell stopped functioning normally, the formation of $\text{Na}_3\text{V}_2(\text{PO}_4)_3$ could again indicate that the $\text{Na}_2\text{V}_2(\text{PO}_4)_3$ phase is metastable. Still, it is remarkable that the intermediary phase was observed between the patterns 17 and 95, which corresponds to approximately 11 h of cycling. To fully assess this aspect, an *operando* oxidation could be carried out until the $\text{Na}_2\text{V}_2(\text{PO}_4)_3$ phase is visible, then the cell could be switched in OCV to see the potential evolution and whether the phase would transform or remain unchanged.

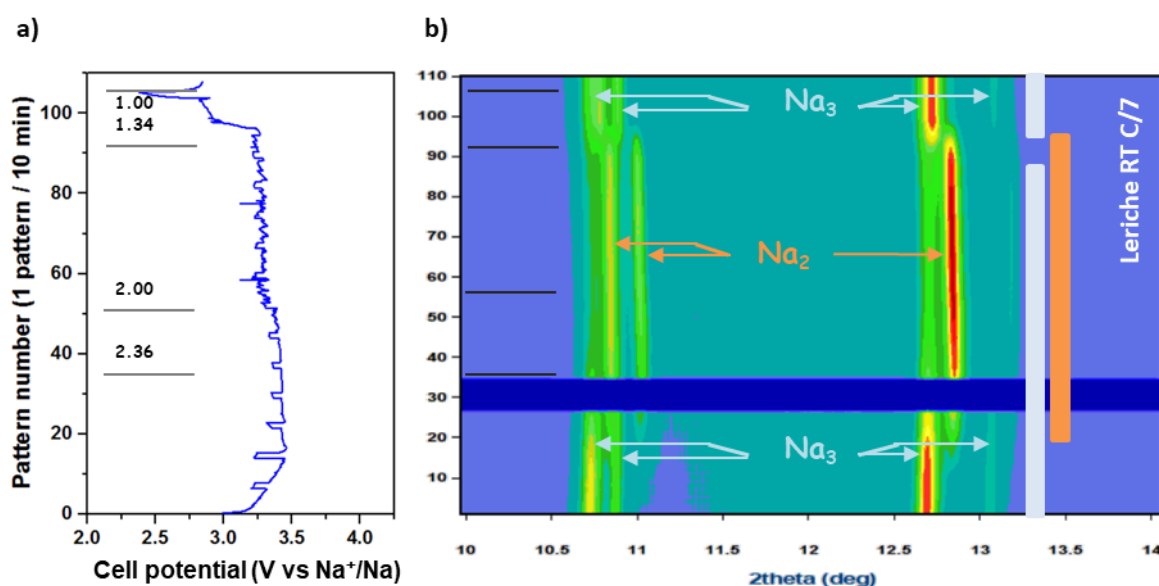


Figure V.14 — a) Pattern number (10min increment in time) vs cell potential and b) associated X-ray surface plots ($\lambda = 0.826 \text{ \AA}$) of a Leriche cell cycled with NVP using NP30+FEC electrolyte at C/7 at room temperature at MSPD. Grey ticks represent the calculated x values in $\text{Na}_x\text{V}_2(\text{PO}_4)_3$. White and orange bands represent the patterns on which the Na_3 and Na_2 phases are visible, respectively.

V.3.3.2. The α -NVP phase (2°C)

The following results were obtained by cooling down a thermalized Leriche cell analogous to the one described in the previous paragraph. The cell was tested at C/7 (full oxidation in 14 h) between 2.5 V and 4.2 V, and a 15 min OCV was applied every hour and an X-ray diffraction pattern was collected every 10 min. The corresponding results are shown in figure V.15. A voltage pseudo-plateau started at ~3.45 V and continued to increase, which could be due to a high cell polarization. The oxidation ended after 10 h after which the reduction started and a voltage pseudo-plateau started at 3.30 V lasting *ca.* 3 h. After that, a potential jump was observed from 3.23 V to another pseudo-plateau starting at 3.14V. Regarding the X-ray diffraction patterns, the characteristic peak of the α -phase was

lost at $x = 2.60$ and the oxidation of NVP follows the typical two-phases transformations behavior, with the appearance of the low temperature $\text{Na}_2\text{V}_2(\text{PO}_4)_3'$ first and later $\text{Na}_1\text{V}_2(\text{PO}_4)_3'$, without the intermediary phase seen in coin cell (section V.2.4.2.) being detected.

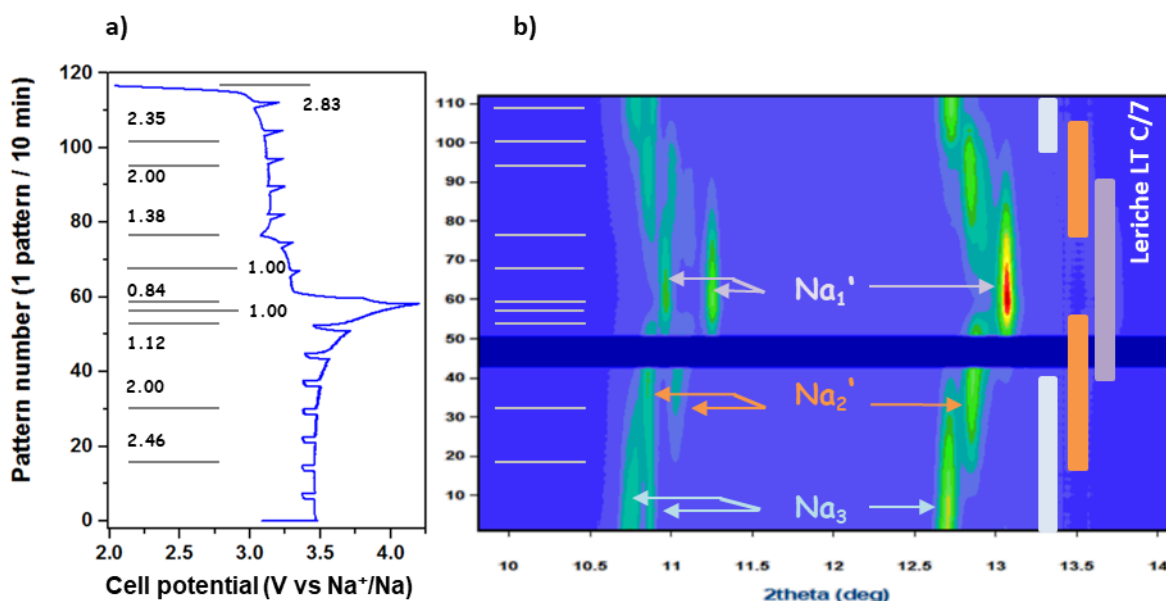


Figure V.15 – a) Pattern number (10 min increment in time) vs cell potential and b) associated X-ray surface plots ($\lambda = 0.826 \text{ \AA}$) of a Leriche cell cycled with NVP using NP30+FEC electrolyte at C/7 (15 min OCV every hour) at 2°C. Grey ticks represent the calculated x values in $\text{Na}_x\text{V}_2(\text{PO}_4)_3$. White, orange and purple bands represent the patterns on which the Na_3 , Na_2 and Na_1 phases are visible, respectively.

A relevant observation is that, although the cell is thermalized at low temperature to maintain the α -NVP phase, its characteristic peak disappears during the oxidation at similar x values (≈ 2.5) as shown in figure V.16. This behavior was observed in all cells tested at low temperature, independently of the cell type and the C-rate. Even if a doubt can remain regarding the coin cell oven, the other prototypes proved to thermalize properly (see section II.3.2.2) and thus the disappearance of the characteristic peak is likely due to the intrinsic electrochemical response of the material. The peak does not seem to be retrieved upon further reduction indicating that the electrochemical intercalation of sodium may induce some structuring towards the β -NVP phase, yet such speculations should be confirmed with further experiments.

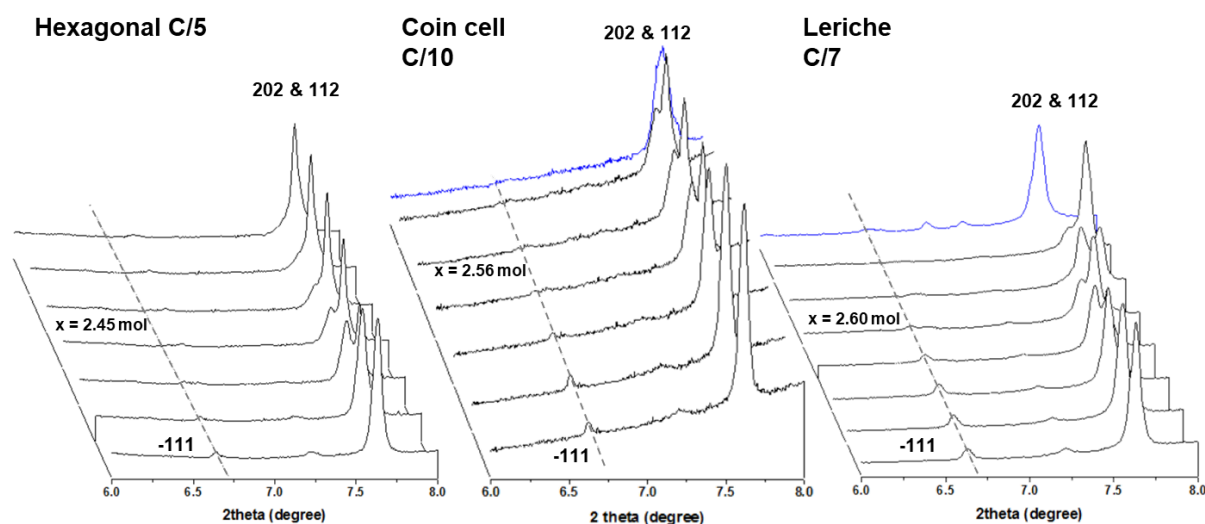


Figure V.16 - Patterns collected in oxidation of a hexagonal, coin and Leriche cell at 2°C, one pattern every hour and last pattern collected in reduction, if any, (blue)

V.4. Conclusion

In this chapter experiments describing sodium reversible (de-)intercalation from NVP were reported carried out at different temperatures and using different setups. Table V.3 summarizes the experimental conditions and the results achieved, figure V.17 the electrochemical curves and figure V.18 the corresponding surface plots. Some difficulties were encountered as the three electrochemical setups were used for the first time on our beamline, especially regarding the control of the potential (short circuits, lack of optimization). More *ex situ* work off beamline would have been required to master the cell performance and their thermalized setups, as well as to find the optimal electrochemical parameters (C-rate, type of electrode).

Table V.3 - Summary of all cells made during this chapter and of the observations made

Figure	Cell type	C-rate	Temperature (°C)	Electrochemical observations	X-ray diffraction observations
4	Leriche	C/10	Room temp.	Typical behavior	Typical behavior
6	Hexagonal	C/10	Room temp.	Typical behavior	Typical behavior
9	Hexagonal	C/5	Room temp.	Noisy oxidation, short reduction	Typical behavior in oxidation, no changes in reduction
11	Hexagonal	C/5	2°C	Red only	“sluggish” reaction
12	Coin cell	C/10	45°C	Forced to reduction, but normal behavior on the rest of the cycle	Typical behavior
13	Coin cell	C/10	2°C	Typical behavior	$\text{Na}_3\text{V}_2(\text{PO}_4)_3$, $\text{Na}_2\text{V}_2(\text{PO}_4)_3$, and an unknown phase are observed. Reversible
14	Leriche	C/7	Room temp.	Noisy oxidation & potential drop, no reduction	$\text{Na}_2\text{V}_2(\text{PO}_4)_3$ is observed but reverts to $\text{Na}_3\text{V}_2(\text{PO}_4)_3$
15	Leriche	C/7	2°C	Typical behavior	Typical behavior

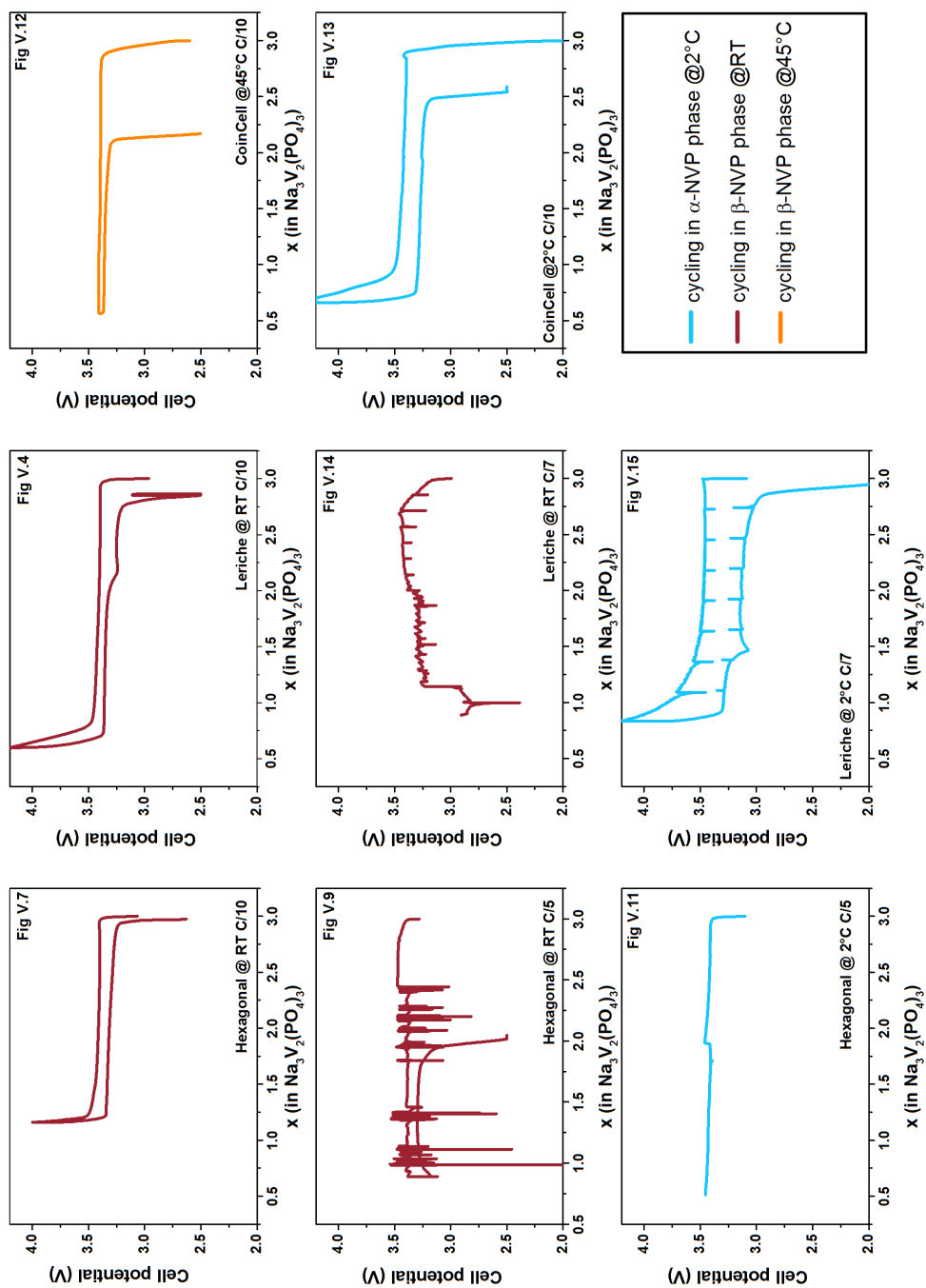


Figure V.17 - Summary of electrochemical behavior of all cells discussed in this chapter, cell potential vs the calculated x value in $\text{Na}_3\text{V}_2(\text{PO}_4)_3$

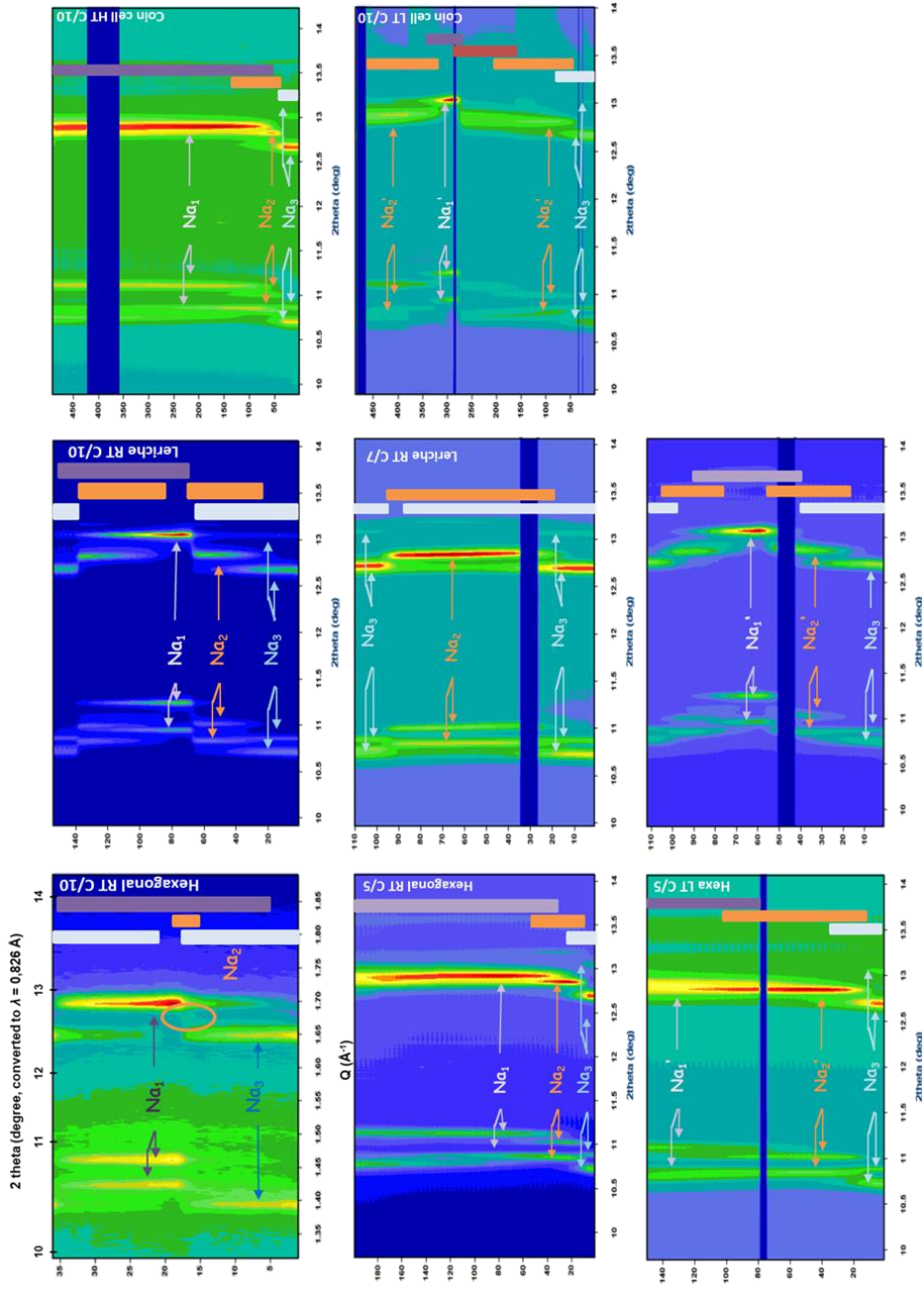


Figure V.14 - Summary of all surface plots presented in this chapter corresponding to the electrochemical curves presented before. Most pattern are measured at $\lambda = 0.826 \text{ \AA}$ except for the first one that was measured at $\lambda = 0.709 \text{ \AA}$. White, orange and purple stripes typically represent the domains of existence of the Na3, Na2 and Na1 phases respectively

Despite those issues, the same typical behavior of the material was observed in all cases, with an oxidation plateau (or pseudo-plateau) starting at ~ 3.4 V and a succession of biphasic transformations from $\text{Na}_3\text{V}_2(\text{PO}_4)_3$ to $\text{Na}_2\text{V}_2(\text{PO}_4)_3$, and from $\text{Na}_2\text{V}_2(\text{PO}_4)_3$ to $\text{Na}_1\text{V}_2(\text{PO}_4)_3$. Upon reduction, a (pseudo-) plateau starts at ~ 3.35 V and the reverse process takes place. In one case only, (figure V.14) $\text{Na}_2\text{V}_2(\text{PO}_4)_3$ was achieved which reverted to $\text{Na}_3\text{V}_2(\text{PO}_4)_3$ upon cell failure pointing at a possible metastable nature of this phase, which could explain its elusive behavior and the need of specific conditions to observe it, even *operando*.

Although thermalization is not mandatory to test the β -NVP phase, the characteristic peak of α -NVP disappears unless low temperature is kept in a tailored setup. Advantage was taken of the phase transition's hysteresis by placing the cells in the freezer prior to cycling to use a more moderate temperature during the experiment on the thermalized setup (2°C). The three cell prototypes (Leriche, coin cell and hexagonal cell) have proven their efficiency in terms of thermalization and of electrochemical cycling. To track the characteristic peak of α -NVP (-111), synchrotron radiation was crucial given the very low intensity of this peak. This reflection disappears upon oxidation at $x \approx 2.50$, even if the setup is thermalized, and does not reappear upon reduction, which seems to yield β - $\text{Na}_3\text{V}_2(\text{PO}_4)_3$, although additional data would be required for a reliable refinement.

In summary, *operando* experiments have proved to be a precious tool to observe the succession of the phases being formed during redox reactions taking place in sodium cells using NVP as positive electrode. The results achieved indicate that by optimizing the operating conditions (C-rate, powder or casted electrode, optionally temperature) and the setups (cell isolation), it could be possible to achieve electrodes containing $\text{Na}_2\text{V}_2(\text{PO}_4)_3$ as a single phase to get more information about its crystal structure.

General conclusion

During this thesis, three prototypes of thermalized *in situ* cells for *operando* X-ray diffraction were tested. Among them, the Leriche set up was modified in order to thermalize it with a fluid circulating in its body to ensure the probed material reaches the expected temperature. Despite exhibiting some polarization, this cell offers satisfying electrochemical performances. For the two other setups, namely the coin and hexagonal cells, the thermalization is enabled by an external device: an oven for the coin cell and a copper ring for the hexagonal cell. Both are working well in terms of thermalization and have their own advantages: the coin cells are closer to a commercial geometry and hence may be more representative of real performance and exhibit low polarization. However, they are expensive (12€/casing) and only one oven can be mounted at a time on the beamline. Moreover, they are not typically compatible with conventional laboratory X-ray diffractometers. On the other hand, the hexagonal cells are specifically designed to be used in laboratory equipment while being more compact than the modified Leriche set up. Yet, extra precautions are needed to ensure no unwanted contacts between the cell and the thermalized ring occur.

Different electrochemical systems were used to assess the performance of these cells while at the same time getting better comprehension of some processes taking place in the electrodes during the battery operation.

The first topic investigated dealt with the study of solvent cointercalation on a historical system: Li//TiS₂, which was also a preliminary test prior to undertaking research on calcium cells. A systematic study involving several electrolyte compositions (*i.e.* salts and solvents) was carried out to grasp its influence on the redox behavior of TiS₂. When the electrolyte contains propylene carbonate, a cointercalated phase forms at early stages of reduction, indexed within the *P3m1* space group with cell parameters $a, b = 3.514(3)$ Å and $c = 17.931(2)$ Å. The formation of this phase is independent of the salt and its amount related to the amount of propylene carbonate in the electrolyte. This process was found to be irreversible as this phase was not found to evolve upon oxidation and hence its formation induced a loss in capacity.

Similar studies were undertaken on calcium cells operating at 100°C to enable calcium plating and stripping at the counterelectrode, which were not successful, as only electrolyte decomposition was observed even at low intensities. In contrast, tests carried out at 65°C using activated carbon counterelectrode enabled to detect the reduction of TiS₂ (despite never complete probably due to slow kinetics) with the formation of two different phases, previously reported, the first containing co-intercalated solvent and the second presumably being a second-stage intercalate. Results achieved in a wide angular range enabled to propose the *P3m1* space group for both phases with c parameters close 18.41(5) Å and 19.23(5) Å respectively. The *operando* measurements were crucial to evidence shifts in the peaks corresponding to these reduced phases which can tentatively be ascribed to changes in composition (amount of intercalated calcium and/or solvent) upon reduction. The same process was evidenced at room temperature, yet with a smaller amount of phase formed. Given the slow kinetics of the system, experiments at much slower rates (and hence very beamtime consuming) would be needed to better grasp the full reduction mechanism, yet, the rates investigated (C/75 or C/50) were found to be a good compromise to get relevant information in a

reasonable period of time. An alternative perspective for the future could be to use laboratory X-ray diffractometers with a thermalized cell.

The hexagonal cell setup was specifically designed to fit laboratory diffractometers and was developed in LRCS. During this thesis, it was used to study the redox mechanism of $\text{Na}_3\text{V}_2(\text{PO}_4)_3$ in sodium batteries. This material was specifically chosen because it exhibits a phase transition near ambient temperature, with the α -phase appearing at low temperature and the β -phase being the phase usually observed at room temperature. Tests carried out without the thermalizing ring, in LRCS' laboratory diffractometer allowed the detection of the elusive intermediary phase $\text{Na}_2\text{V}_2(\text{PO}_4)_3$. Complementary *operando* synchrotron experiments enabled to index its diffraction pattern in the $P2/M$ space group with parameters: $a = 14.847(2) \text{ \AA}$, $b = 8.617(7) \text{ \AA}$, $c = 21.554(2) \text{ \AA}$ and $\beta = 90.435(1)^\circ$. Additional experiments were performed at -2°C and 45°C starting from the α - and β -NVP phases respectively. However, apart from the disappearance of the characteristic peak (-111) of the α -phase upon oxidation, no major changes were found as a result of the temperature modifications.

Developing thermalized cells is important to open a new possibility to study electrochemical systems that require a temperature control, by either heating up the cell to enhance the kinetics (calcium systems) or cooling down to observe a specific phase ($\text{Na}_3\text{V}_2(\text{PO}_4)_3$ or – as preliminary investigated in the course of this thesis (results not reported herein) - LiMn_2O_4 at low temperature). This setup could also be of interest for studies related to battery ageing, or to test batteries in real operating conditions. Indeed, in our electronic devices, batteries are exposed to changing temperatures depending on the season, but also to the Joule effect produced by the other components of the device (processor, graphic card); hence they barely ever operate at $20\text{-}25^\circ\text{C}$, the temperature at which they are usually tested in research laboratories.

Bibliography

1. Overshootday.org. Past Earth Overshoot Days. Accessed February 17, 2021. <http://www.overshootday.org/newsroom/past-earth-overshoot-days/>
2. Pearce F. Admit it: we can't measure our ecological footprint. *New Scientist*. <https://www.newscientist.com/article/mg22029445-000-admit-it-we-cant-measure-our-ecological-footprint/>. Published 2013.
3. Global Direct Primary Energy Consumption. Our World in Data. Published 2020. Accessed February 16, 2021. <https://ourworldindata.org/grapher/global-primary-energy?time=1990..latest>
4. Total greenhouse gas emissions. Our World in Data. Published 2020. Accessed February 16, 2021. [https://ourworldindata.org/explorers/co2?tab=chart&xScale=linear&yScale=linear&stackMode=absolute&endpointsOnly=0&time=earliest..latest&country=China~United States~India~United Kingdom~World®ion=World&Gas =All GHGs \(CO₂eq\)&Accounting =Production-based&](https://ourworldindata.org/explorers/co2?tab=chart&xScale=linear&yScale=linear&stackMode=absolute&endpointsOnly=0&time=earliest..latest&country=China~United States~India~United Kingdom~World®ion=World&Gas =All GHGs (CO₂eq)&Accounting =Production-based&)
5. IEA. *CO₂ Emissions by Sector, World 1990-2018.*; 2020. <https://www.iea.org/data-and-statistics/?country=WORLD&fuel=CO2 emissions&indicator=CO2BySector>
6. Fraunhofer ISE. Fraunhofer ISE: Photovoltaics Report. Published online 2020. Accessed February 17, 2021. <https://www.ise.fraunhofer.de/content/dam/ise/de/documents/publications/studies/Photovoltaics-Report.pdf>
7. Guezuraga B, Zauner R, Pölz W. Life cycle assessment of two different 2 MW class wind turbines. *Renew Energy*. 2012;37(1):37-44. doi:10.1016/j.renene.2011.05.008
8. The Nobel Prize. The Nobel Prize in Chemistry 2019 - Popular information. Published 2019. Accessed February 18, 2021. <https://www.nobelprize.org/prizes/chemistry/2019/popular-information/>
9. Markets and Markets. *Lithium-Ion Battery Market by Type (Li-NMC, LFP, LCO, LTO), Power Capacity (0-3,000 MAh, 3,000 MAh-10,000 MAh, 10,000 MAh-60,000 MAh, above 60,000 MAh), Industry (Consumer Electronics, Automotive, Industrial), Voltage, Region – Global Forecast to 2025.*; 2020. <https://www.marketsandmarkets.com/Market-Reports/lithium-ion-battery-market-49714593.html>
10. Root A. Why Lithium Could Be a New Risk for Tesla and Other Electric-Vehicle Makers. *Barron's*. <https://www.barrons.com/articles/new-risk-tesla-other-electric-vehicle-makers-lithium-supply-batteries-51601498472>. Published 2020.
11. U.S. Geological Survey. *Lithium Data Sheet - Mineral Commodity Summaries 2020.*; 2020. <https://pubs.usgs.gov/periodicals/mcs2020/mcs2020-lithium.pdf>
12. ACEA. Economic and Market Report: EU Automotive Industry Full-year 2019. *Eur Automob Manuf Assoc*. 2020;(May):1-25. Accessed April 26, 2021. https://www.acea.be/uploads/statistic_documents/Economic_and_Market_Report_full-year_2018.pdf

13. World Economic Forum. *World Economic Forum Annual Meeting 2016 Mastering the Fourth Industrial Revolution.*; 2016. http://www3.weforum.org/docs/WEF_AM16_Report.pdf
14. *CRC Handbook of Chemistry and Physics*. 97th ed.
15. Volta A. On the electricity excited by the mere contact of conducting substances of different kinds. *Philos Trans R Soc London*. 1800;90:403-431. doi:10.1098/rstl.1800.0018
16. Garche J. On the historical development of the lead/acid battery, especially in Europe. *J Power Sources*. 1990;31(1-4):401-406. doi:10.1016/0378-7753(90)80095-U
17. BAJ Website | Secondary battery sales statistics by volume Secondary battery sales statistics by volume. Published online 2009:2009-2009. Accessed March 1, 2021. <http://www.baj.or.jp/e/statistics/06.html>
18. McNaught AD, Wilkinson A. Standard Hydrogen Electrode. In: Blackwell Scientific Publications, ed. *The IUPAC Compendium of Chemical Terminology, 2nd Ed. (the "Gold Book")*. International Union of Pure and Applied Chemistry (IUPAC); 2008. doi:10.1351/GOLDBOOK.S05917
19. Lewis GN, Keyes FG. The potential of the lithium electrode. *J Am Chem Soc*. 1913;35(4):340-344. doi:10.1021/ja02193a004
20. Harris WS. Electrochemical studies in cyclic esters. Published online 1958. Accessed March 5, 2021. <https://www.osti.gov/servlets/purl/4305596/>
21. Scrosati B. History of lithium batteries. *J Solid State Electrochem*. 2011;15(7-8):1623-1630. doi:10.1007/s10008-011-1386-8
22. Crompton TR. Lithium — Iodine Batteries. In: *Small Batteries*. Macmillan Education UK; 1982:196-201. doi:10.1007/978-1-349-06319-2_9
23. Rüdorff W. Über die Einlagerung von unedlen Metallen in Graphit sowie in Metallchalkogenide von Typ MeX₂. *Chimia (Aarau)*. 1965;19:489.
24. Bichon J, Danot M, Rouxel J. Systématique structurale pour les séries d'intercalaires MxTiS₂ (M=Li, Na, K, Rb, Cs). *Comptes rendus Acad Sci, Ser C, Sci Chim*. 1973;276:1283-1286.
25. Whittingham MS. Electrical energy storage and intercalation chemistry. *Science (80-)*. 1976;192(4244):1126-1127. doi:10.1126/science.192.4244.1126
26. Whittingham MS. History, evolution, and future status of energy storage. In: *Proceedings of the IEEE*. Vol 100. Institute of Electrical and Electronics Engineers Inc.; 2012:1518-1534. doi:10.1109/JPROC.2012.2190170
27. Pereira N, Amatucci GG, Whittingham MS, Hamlen R. Lithium-titanium disulfide rechargeable cell performance after 35 years of storage. *J Power Sources*. 2015;280:18-22. doi:10.1016/j.jpowsour.2015.01.056
28. Goodenough JB, Mizushima K. Fast ion conductors. Published online 1980. Accessed March 5, 2021. <https://patents.google.com/patent/US4357215A/en?q=us+4%2C357%2C215>
29. Mizushima K, Jones PC, Wiseman PJ, Goodenough JB. Li_xCoO₂ (0 < x < 1): A new cathode material for batteries of high energy density. *Mater Res Bull*. 1980;15(6):783-789. doi:10.1016/0025-5408(80)90012-4
30. Armand M. The history of polymer electrolytes. *Solid State Ionics*. 1994;69(3-4):309-319.

doi:10.1016/0167-2738(94)90419-7

31. Rüdorff W, Hofmann U. Über Graphitsalze. *Zeitschrift für Anorg und Allg Chemie*. 1938;238(1):1-50. doi:10.1002/zaac.19382380102
32. Yoshino A, Sanechika K, Nakajima T. Secondary battery. Published online 1986. Accessed March 9, 2021. <https://patents.google.com/patent/US4668595A/en>
33. Yoshino A. The birth of the lithium-ion battery. *Angew Chemie - Int Ed*. 2012;51(24):5798-5800. doi:10.1002/anie.201105006
34. Fong R, von Sacken U, Dahn JR. Studies of Lithium Intercalation into Carbons Using Nonaqueous Electrochemical Cells. *J Electrochem Soc*. 1990;137(7):2009-2013. doi:10.1149/1.2086855
35. Naguara T, Tozawa K. Lithium ion rechargeable battery. In: *Progress in Batteries & Solar Cells*. ; 1990:209-217.
36. Thackeray MM, David WIF, Bruce PG, Goodenough JB. Lithium insertion into manganese spinels. *Mater Res Bull*. 1983;18(4):461-472. doi:10.1016/0025-5408(83)90138-1
37. Padhi AK, Nanjundaswamy KS, Goodenough JB. Phospho-olivines as Positive-Electrode Materials for Rechargeable Lithium Batteries. *J Electrochem Soc*. 1997;144(4):1188-1194. doi:10.1149/1.1837571
38. Dühnen S, Betz J, Kolek M, Schmuch R, Winter M, Placke T. Toward Green Battery Cells: Perspective on Materials and Technologies. *Small Methods*. 2020;4(7):2000039. doi:10.1002/smt.202000039
39. Blomgren GE. The Development and Future of Lithium Ion Batteries. *J Electrochem Soc*. 2017;164(1):A5019-A5025. doi:10.1149/2.0251701jes
40. Randau S, Weber DA, Kötz O, et al. Benchmarking the performance of all-solid-state lithium batteries. *Nat Energy*. 2020;5(3):259-270. doi:10.1038/s41560-020-0565-1
41. Janek J, Zeier WG. A solid future for battery development. *Nat Energy*. 2016;1(9):1-4. doi:10.1038/nenergy.2016.141
42. Bruce PG, Freunberger SA, Hardwick LJ, Tarascon JM. Li-O₂ and Li-S batteries with high energy storage. *Nat Mater*. 2012;11(1):19-29. doi:10.1038/nmat3191
43. Abraham KM, Jiang Z. A Polymer Electrolyte-Based Rechargeable Lithium/Oxygen Battery. *J Electrochem Soc*. 1996;143(1):1-5. doi:10.1149/1.1836378
44. Manthiram A, Fu Y, Chung SH, Zu C, Su YS. Rechargeable lithium-sulfur batteries. *Chem Rev*. 2014;114(23):11751-11787. doi:10.1021/cr500062v
45. Song MK, Cairns EJ, Zhang Y. Lithium/sulfur batteries with high specific energy: Old challenges and new opportunities. *Nanoscale*. 2013;5(6):2186-2204. doi:10.1039/c2nr33044j
46. Visco SJ, Nimon VY, Petrov A, et al. Aqueous and nonaqueous lithium-air batteries enabled by water-stable lithium metal electrodes. *J Solid State Electrochem*. 2014;18(5):1443-1456. doi:10.1007/s10008-014-2427-x
47. Ponrouch A, Bitenc J, Dominko R, Lindahl N, Johansson P, Palacin MR. Multivalent rechargeable batteries. *Energy Storage Mater*. 2019;20:253-262.

doi:10.1016/j.ensm.2019.04.012

48. Gopalakrishnan J, Kasthuri Rangan K. *Intercalation Chemistry*. Vol 4. Academic Press Accessed April 22, 2021. <https://pubs.acs.org/sharingguidelines>
49. Shacklette LW, Jow TR, Townsend L. Rechargeable Electrodes from Sodium Cobalt Bronzes. *J Electrochem Soc*. 1988;135(11):2669-2674. doi:10.1149/1.2095407
50. Hwang JY, Myung ST, Sun YK. Sodium-ion batteries: Present and future. *Chem Soc Rev*. 2017;46(12):3529-3614. doi:10.1039/c6cs00776g
51. Delmas C, Braconnier JJ, Fouassier C, Hagemuller P. Electrochemical intercalation of sodium in Na_xCoO_2 bronzes. *Solid State Ionics*. 1981;3-4(C):165-169. doi:10.1016/0167-2738(81)90076-X
52. Parant JP, Olazcuaga R, Devalette M, Fouassier C, Hagemuller P. Sur quelques nouvelles phases de formule Na_xMnO_2 ($x \leq 1$). *J Solid State Chem*. 1971;3(1):1-11. doi:10.1016/0022-4596(71)90001-6
53. Saravanan K, Mason CW, Rudola A, Wong KH, Balaya P. The first report on excellent cycling stability and superior rate capability of $\text{Na}_3\text{V}_2(\text{PO}_4)_3$ for sodium ion batteries. *Adv Energy Mater*. 2013;3(4):444-450. doi:10.1002/aenm.201200803
54. Ishado Y, Inoishi A, Okada S. Exploring Factors Limiting Three-Na + Extraction from $\text{Na}_3\text{V}_2(\text{PO}_4)_3$. doi:10.5796/electrochemistry.20-00080
55. Yan G, Mariyappan S, Rousse G, et al. Higher energy and safer sodium ion batteries via an electrochemically made disordered $\text{Na}_3\text{V}_2(\text{PO}_4)_2\text{F}_3$ material. *Nat Commun*. 2019;10(1):1-12. doi:10.1038/s41467-019-08359-y
56. Masquelier C, Croguennec L. Polyanionic (phosphates, silicates, sulfates) frameworks as electrode materials for rechargeable Li (or Na) batteries. *Chem Rev*. 2013;113(8):6552-6591. doi:10.1021/cr3001862
57. Ge P, Foulletier M. Electrochemical intercalation of sodium in graphite. *Solid State Ionics*. 1988;28-30(PART 2):1172-1175. doi:10.1016/0167-2738(88)90351-7
58. Doeff MM, Ma Y, Visco SJ, De Jonghe LC. Electrochemical Insertion of Sodium into Carbon. *J Electrochem Soc*. 1993;140(12):L169-L170. doi:10.1149/1.2221153
59. Jache B, Adelhelm P. Use of graphite as a highly reversible electrode with superior cycle life for sodium-ion batteries by making use of co-intercalation phenomena. *Angew Chemie - Int Ed*. 2014;53(38):10169-10173. doi:10.1002/anie.201403734
60. Irisarri E, Ponrouch A, Palacin MR. Review-Hard Carbon Negative Electrode Materials for Sodium-Ion Batteries. doi:10.1149/2.0091514jes
61. Ponrouch A, Dedryvère R, Monti D, et al. Towards high energy density sodium ion batteries through electrolyte optimization. *Energy Environ Sci*. 2013;6(8):2361-2369. doi:10.1039/c3ee41379a
62. Ponrouch A, Monti D, Boschini A, Steen B, Johansson P, Palacín MR. Non-aqueous electrolytes for sodium-ion batteries. *J Mater Chem A*. 2015;3(1):22-42. doi:10.1039/c4ta04428b
63. Tchitchekova DS, Monti D, Johansson P, et al. On the Reliability of Half-Cell Tests for Monovalent (Li^+ , Na^+) and Divalent (Mg^{2+} , Ca^{2+}) Cation Based Batteries. *J Electrochem*

- Soc.* 2017;164(7):A1384-A1392. doi:10.1149/2.0411707jes
64. Aurbach D, Skaletsky R, Gofer Y. The Electrochemical Behavior of Calcium Electrodes in a Few Organic Electrolytes. *J Electrochem Soc.* 1991;138(12):3536-3545. doi:10.1149/1.2085455
 65. Bervas M, Klein LC, Amatucci GG. Vanadium oxide-propylene carbonate composite as a host for the intercalation of polyvalent cations. *Solid State Ionics.* 2005;176(37-38):2735-2747. doi:10.1016/j.ssi.2005.09.009
 66. Ponrouch A, Frontera C, Bardé F, Palacín MR. Towards a calcium-based rechargeable battery. *Nat Mater.* 2016;15(2):169-172. doi:10.1038/nmat4462
 67. Wang D, Gao X, Chen Y, Jin L, Kuss C, Bruce PG. Plating and stripping calcium in an organic electrolyte. *Nat Mater.* 2018;17(1):16-20. doi:10.1038/NMAT5036
 68. Shyamsunder A, Blanc LE, Assoud A, Nazar LF. Reversible Calcium Plating and Stripping at Room Temperature Using a Borate Salt. *ACS Energy Lett.* 2019;4(9):2271-2276. doi:10.1021/acsenergylett.9b01550
 69. Li Z, Fuhr O, Fichtner M, Zhao-Karger Z. Towards stable and efficient electrolytes for room-temperature rechargeable calcium batteries. *Energy Environ Sci.* 2019;12(12):3496-3501. doi:10.1039/c9ee01699f
 70. Ponrouch A. Challenges and Opportunities in Interphased Ca Metal Anode Batteries. In: *International Battery Association (IBA) Meeting.* ; 2018.
 71. Tchitchekova DS, Ponrouch A, Verrelli R, et al. Electrochemical Intercalation of Calcium and Magnesium in TiS₂: Fundamental Studies Related to Multivalent Battery Applications. *Chem Mater.* 2018;30(3):847-856. doi:10.1021/acs.chemmater.7b04406
 72. Verrelli R, Black A, Dugas R, Tchitchekova D, Ponrouch A, Palacin MR. Steps Towards the Use of TiS₂ Electrodes in Ca Batteries. *J Electrochem Soc.* 2020;167(7):070532. doi:10.1149/1945-7111/ab7a82
 73. Chianelli RR, Scanlon JC, Rao BML. In situ studies of electrode reactions: The mechanism of lithium intercalation in TiS₂. *J Solid State Chem.* 1979;29(3):323-337. doi:10.1016/0022-4596(79)90189-0
 74. Leriche JB, Hamelet S, Shu J, et al. An Electrochemical Cell for Operando Study of Lithium Batteries Using Synchrotron Radiation. *J Electrochem Soc.* 2010;157(5):A606. doi:10.1149/1.3355977
 75. Lin F, Liu Y, Yu X, et al. Synchrotron X-ray Analytical Techniques for Studying Materials Electrochemistry in Rechargeable Batteries. *Chem Rev.* 2017;117(21):13123-13186. doi:10.1021/acs.chemrev.7b00007
 76. Chotard JN, Rouse G, David R, Mentré O, Courty M, Masquelier C. Discovery of a Sodium-Ordered Form of Na₃V₂(PO₄)₃ below Ambient Temperature. *Chem Mater.* 2015;27(17):5982-5987. doi:10.1021/acs.chemmater.5b02092
 77. Zakharkin M V., Drozhzhin OA, Ryazantsev S V., et al. Electrochemical properties and evolution of the phase transformation behavior in the NASICON-type Na_{3+x}Mn_xV_{2-x}(PO₄)₃ (0 ≤ x ≤ 1) cathodes for Na-ion batteries. *J Power Sources.* 2020;470:228231. doi:10.1016/j.jpowsour.2020.228231

78. Forero-Saboya JD, Lozinšek M, Ponrouch A. Towards dry and contaminant free Ca(BF₄)₂-based electrolytes for Ca plating. *J Power Sources Adv.* 2020;6:100032. doi:10.1016/j.powera.2020.100032
79. Fischer K. Neues Verfahren zur maßanalytischen Bestimmung des Wassergehaltes von Flüssigkeiten und festen Körpern. *Angew Chemie.* 1935;48(26):394-396. doi:10.1002/ange.19350482605
80. Verhoef JC, Barendrecht E. Mechanism and reaction rate of the karl-fischer titration reaction. Part I. Potentiometric measurements. *J Electroanal Chem.* 1976;71(3):305-315. doi:10.1016/S0022-0728(76)80017-4
81. Guyomard D, Tarascon JM. Li Metal-Free Rechargeable LiMn₂O₄ / Carbon Cells: Their Understanding and Optimization. *J Electrochem Soc.* 1992;139(4):937-948. doi:10.1149/1.2069372
82. Wang S, Kravchuk K V., Filippin AN, et al. Overcoming the High-Voltage Limitations of Li-Ion Batteries Using a Titanium Nitride Current Collector. *ACS Appl Energy Mater.* 2019;2(2):974-978. doi:10.1021/acsaem.8b01771
83. Myung ST, Hitoshi Y, Sun YK. Electrochemical behavior and passivation of current collectors in lithium-ion batteries. *J Mater Chem.* 2011;21(27):9891-9911. doi:10.1039/c0jm04353b
84. Morita M, Shibata T, Yoshimoto N, Ishikawa M. Anodic behavior of aluminum in organic solutions with different electrolytic salts for lithium ion batteries. *Electrochim Acta.* 2002;47(17):2787-2793. doi:10.1016/S0013-4686(02)00164-0
85. Kanevskii LS, Dubasova VS. Degradation of Lithium-Ion batteries and how to fight it: A review. *Russ J Electrochem* 2005 411. 2005;41(1):1-16. doi:10.1007/PL00022096
86. Dugas R, Forero-Saboya JD, Ponrouch A. Methods and Protocols for Reliable Electrochemical Testing in Post-Li Batteries (Na, K, Mg, and Ca). Published online 2019. doi:10.1021/acs.chemmater.9b02776
87. Armand MB. INTERCALATION ELECTRODES. In: *NATO Conference Series, (Series) 6: Materials Science.* Vol 2. Plenum Press; 1980:145-161. doi:10.1007/978-1-4684-3851-2_7
88. Rietveld HM. A profile refinement method for nuclear and magnetic structures. *J Appl Crystallogr.* 1969;2(2):65-71. doi:10.1107/S0021889869006558
89. Pecharsky VK, Zavalij PY. *Fundamentals of Powder Diffraction and Structural Characterization of Materials.* Springer US; 2005. doi:10.1007/b106242
90. Guinebretière R. *Méthodes et Techniques Expérimentales La Diffraction Des Rayons X Sur Des Échantillons Polycristallins Quels Instruments Pour Quelles Mesures ?*
91. Bianchini M, Fauth F, Brisset N, et al. Comprehensive investigation of the Na₃V₂(PO₄)₂F₃-NaV₂(PO₄)₂F₃ system by operando high resolution synchrotron X-ray diffraction. *Chem Mater.* 2015;27(8):3009-3020. doi:10.1021/acs.chemmater.5b00361
92. Johnson PD. Synchrotron Radiation. In: *Experimental Methods in the Physical Sciences.* Vol 29. ; 1997:23-43. doi:10.1016/S0076-695X(08)60611-0
93. Fauth F, Boer R, Gil-Ortiz F, et al. The crystallography stations at the Alba synchrotron. *Eur Phys J Plus.* 2015;130(8):160. doi:10.1140/epjp/i2015-15160-y

94. Fauth F, Peral I, Popescu C, Knapp M. The new material science powder diffraction beamline at ALBA synchrotron. In: *Powder Diffraction*. Vol 28. ; 2013:S360-S370. doi:10.1017/S0885715613000900
95. Bergamaschi A, Cervellino A, Dinapoli R, et al. The MYTHEN detector for X-ray powder diffraction experiments at the Swiss Light Source. *J Synchrotron Radiat*. 2010;17(5):653-668. doi:10.1107/S0909049510026051
96. DIRECT Detection - Dectris. Accessed April 13, 2021. <https://www.dectris.com/technology/hybrid-photon-counting/direct-detection/>
97. Mikulec B. Development of segmented semiconductor arrays for quantum imaging. In: *Nuclear Instruments and Methods in Physics Research, Section A: Accelerators, Spectrometers, Detectors and Associated Equipment*. Vol 510. Elsevier; 2003:1-23. doi:10.1016/S0168-9002(03)01672-3
98. Morcrette M, Chabre Y, Vaughan G, et al. In situ X-ray diffraction techniques as a powerful tool to study battery electrode materials. *Electrochim Acta*. 2002;47(19):3137-3149. doi:10.1016/S0013-4686(02)00233-5
99. Amatucci GG, Tarascon J-M. Apparatus for in situ x-ray study of electrochemical cells - Google Patents. Published online 1995. Accessed March 4, 2021. <https://patents.google.com/patent/US5635138A/en?q=US+5635138>
100. Tripathi AM, Su WN, Hwang BJ. In situ analytical techniques for battery interface analysis. *Chem Soc Rev*. 2018;47(3):736-751. doi:10.1039/c7cs00180k
101. Lebedev YA, Korolev YM, Polikarpov VM, Ignat'ev LN, Antipov EM. X-Ray powder diffraction study of polytetrafluoroethylene. *Crystallogr Reports*. 2010;55(4):609-614. doi:10.1134/S1063774510040127
102. Bianchini M, Brisset N, Fauth F, et al. Na₃V₂(PO₄)₂F₃ revisited: A high-resolution diffraction study. *Chem Mater*. 2014;26(14):4238-4247. doi:10.1021/cm501644g
103. Herklotz M, Weiß J, Ahrens E, et al. A novel high-throughput setup for in situ powder diffraction on coin cell batteries. *J Appl Crystallogr*. 2016;49(1):340-345. doi:10.1107/S1600576715022165
104. Dahn JR, Py MA, Haering RR. IN SITU X-RAY DIFFRACTION EXPERIMENTS ON LITHIUM INTERCALATION COMPOUNDS. *Can J Phys*. 1982;60(3):307-313. doi:10.1139/p82-040
105. Houdeville RG, Black AP, Ponrouch A, Palacín MR, Fauth F. Operando Synchrotron X-ray Diffraction Studies on TiS₂: The Effect of Propylene Carbonate on Reduction Mechanism. *J Electrochem Soc*. 2021;168(3):030514. doi:10.1149/1945-7111/abe983
106. Bear J, McTaggart FK. The sulphides, selenides, and tellurides of titanium, zirconium, hafnium, and thorium ii. chemical properties. *Aust J Chem*. 1958;11(4):458-470. doi:10.1071/CH9580458
107. Saurel D, Segalini J, Jauregui M, et al. A SAXS outlook on disordered carbonaceous materials for electrochemical energy storage. *Energy Storage Mater*. 2019;21:162-173. doi:10.1016/j.ensm.2019.05.007
108. Panitz JC, Wietelmann U, Wachtler M, Ströbele S, Wohlfahrt-Mehrens M. Film formation in LiBOB-containing electrolytes. *J Power Sources*. 2006;153(2):396-401.

doi:10.1016/j.jpowsour.2005.05.025

109. Rodríguez-Carvajal J. Recent advances in magnetic structure determination by neutron powder diffraction. *Phys B Phys Condens Matter*. 1993;192(1-2):55-69. doi:10.1016/0921-4526(93)90108-I
110. Whittingham MS. Chemistry of intercalation compounds: Metal guests in chalcogenide hosts. *Prog Solid State Chem*. 1978;12(1):41-99. doi:10.1016/0079-6786(78)90003-1
111. Thompson AH, Symon CR. Structural studies on Li_xTiS_2 . *Solid State Ionics*. 1981;3-4(C):175-179. doi:10.1016/0167-2738(81)90078-3
112. Dahn JR, McKinnon WR, Haering RR, Buyers WJL, Powell BM. STRUCTURE DETERMINATION OF Li_xTiS_2 BY NEUTRON DIFFRACTION. *Can J Phys*. 1980;58(2):207-213. doi:10.1139/p80-033
113. Radin MD, Van Der Ven A. Stability of Prismatic and Octahedral Coordination in Layered Oxides and Sulfides Intercalated with Alkali and Alkaline-Earth Metals. *Chem Mater*. 2016;28(21):7898-7904. doi:10.1021/acs.chemmater.6b03454
114. Emly A, Van Der Ven A. Mg intercalation in layered and spinel host crystal structures for mg batteries. *Inorg Chem*. 2015;54(9):4394-4402. doi:10.1021/acs.inorgchem.5b00188
115. Arroyo-De Dompablo ME, Ponrouch A, Johansson P, Palacín MR. Achievements, Challenges, and Prospects of Calcium Batteries. *Chem Rev*. 2020;120(14):6331-6357. doi:10.1021/acs.chemrev.9b00339
116. Dompablo MEA, Krich C, Nava-Avendaño J, Biškup N, Palacín MR, Bardé F. A Joint Computational and Experimental Evaluation of CaMn_2O_4 Polymorphs as Cathode Materials for Ca Ion Batteries. *Chem Mater*. 2016;28(19):6886-6893. doi:10.1021/ACS.CHEMMATER.6B02146
117. Dompablo MEA, Krich C, Nava-Avendaño J, Palacín MR, Bardé F. In quest of cathode materials for Ca ion batteries: the CaMO_3 perovskites (M = Mo, Cr, Mn, Fe, Co, and Ni). *Phys Chem Chem Phys*. 2016;18(29):19966-19972. doi:10.1039/C6CP03381D
118. Tchitchekova DS, Frontera C, Ponrouch A, Krich C, Bardé F, Palacín MR. Electrochemical calcium extraction from 1D- $\text{Ca}_3\text{Co}_2\text{O}_6$. *Dalt Trans*. 2018;47(33):11298-11302. doi:10.1039/c8dt01754a
119. Le Blanc-Sorreau A, Rouxel J. J. Facteurs physiques et structuraux dans les systemes d'intercalaires: systemes A^xTiS_2 , cas du calcium. *CR Acad Sc Paris*. 1974;279:C303.
120. Bian X, Gao Y, Fu Q, et al. A long cycle-life and high safety $\text{Na}^+/\text{Mg}^{2+}$ hybrid-ion battery built by using a TiS_2 derived titanium sulfide cathode. *J Mater Chem A*. 2017;5(2):600-608. doi:10.1039/c6ta08505a
121. Schöllhorn R, Zagefka HD, Butz T, Lerf A. Ionic bonding model of the pyridine intercalation compounds of layered transition metal dichalcogenides. *Mater Res Bull*. 1979;14(3):369-376. doi:10.1016/0025-5408(79)90102-8
122. Shannon RD. Revised effective ionic radii and systematic studies of interatomic distances in halides and chalcogenides. *Acta Crystallogr Sect A*. 1976;32(5):751-767. doi:10.1107/S0567739476001551
123. Black AP, Monti D, Frontera C, et al. *Operando* Synchrotron X-ray Diffraction in Calcium

- Batteries: Insights into the Redox Activity of $1D Ca_3 CoMO_6$ ($M = Co$ and Mn). *Energy & Fuels*. Published online June 16, 2021:acs.energyfuels.1c01343. doi:10.1021/acs.energyfuels.1c01343
124. Delmas C, Olazcuaga R, Cherkaoui F, Brochu R, Leflem G. New family of phosphates with formula $Na_3M_2(PO_4)_3$ ($M = Ti, V, Cr, Fe$). *C R Seances Acad Sci, Ser C*. 1978;287:169-171.
 125. Gopalakrishnan J, Rangan KK. $V_2(PO_4)_3$: A Novel NASICON-Type Vanadium Phosphate Synthesized by Oxidative Deintercalation of Sodium from $Na_3V_2(PO_4)_3$. *Chem Mater*. 1992;4(4):745-747. doi:10.1021/cm00022a001
 126. Cao X, Zhou J, Pan A, Liang S. Recent Advances in Phosphate Cathode Materials for Sodium-ion Batteries. *Acta Physico-Chimica Sin*. 2020;36(5). doi:10.3866/PKU.WHXB201905018
 127. Jian Z, Zhao L, Pan H, et al. Carbon coated $Na_3V_2(PO_4)_3$ as novel electrode material for sodium ion batteries Structure-Property Correlation for Amorphous Carbon View project Hydronium-ion batteries View project Author's personal copy Carbon coated $Na_3V_2(PO_4)_3$ as novel electrode material for sodium ion batteries. Published online 2011. doi:10.1016/j.elecom.2011.11.009
 128. Shen L, Li Y, Roy S, et al. A robust carbon coating of $Na_3V_2(PO_4)_3$ cathode material for high performance sodium-ion batteries. *Chinese Chem Lett*. Published online 2021. doi:10.1016/j.ccllet.2021.03.005
 129. Zhang B, Chen H, Tong H, et al. Synthesis and electrochemical performance of Ni doped $Na_3V_2(PO_4)_3/C$ cathode materials for sodium ion batteries. *J Alloys Compd*. 2017;728:976-983. doi:10.1016/j.jallcom.2017.09.020
 130. Zhou W, Xue L, Lü X, et al. $Na_3MV(PO_4)_3$ ($M = Mn, Fe, Ni$) Structure and Properties for Sodium Extraction. *Nano Lett*. 2016;16(12):7836-7841. doi:10.1021/acs.nanolett.6b04044
 131. Lalère F, Seznec V, Courty M, David R, Chotard JN, Masquelier C. Improving the energy density of $Na_3V_2(PO_4)_3$ -based positive electrodes through V/Al substitution. *J Mater Chem A*. 2015;3(31):16198-16205. doi:10.1039/c5ta03528g
 132. Aragón MJ, Lavela P, Alcántara R, Tirado JL. Effect of aluminum doping on carbon loaded $Na_3V_2(PO_4)_3$ as cathode material for sodium-ion batteries. *Electrochim Acta*. 2015;180:824-830. doi:10.1016/j.electacta.2015.09.044
 133. Chen F, Kovrugin VM, David R, et al. A NASICON-Type Positive Electrode for Na Batteries with High Energy Density: $Na_4MnV(PO_4)_3$. *Small Methods*. 2019;3(4):1800218. doi:10.1002/smtd.201800218
 134. Park S, Chotard JN, Carlier D, et al. Crystal Structures and Local Environments of NASICON-type $Na_3FeV(PO_4)_3$ and $Na_4FeV(PO_4)_3$ Positive Electrode Materials for Na-ion Batteries. *Chem Mater*.
 135. Delmas C, Cherkaoui F, Nadiri A, Hagenmuller P. A nasicon-type phase as intercalation electrode: $NaTi_2(PO_4)_3$. *Mater Res Bull*. 1987;22(5):631-639. doi:10.1016/0025-5408(87)90112-7
 136. Hong HYP. Crystal structures and crystal chemistry in the system $Na_{1+x}Zr_2Si_xP_3-xO_{12}$. *Mater Res Bull*. 1976;11(2):173-182. doi:10.1016/0025-5408(76)90073-8
 137. Lalère F, Leriche JB, Courty M, et al. An all-solid state NASICON sodium battery operating at

- 200°C. *J Power Sources*. 2014;247:975-980. doi:10.1016/j.jpowsour.2013.09.051
138. Gaubicher J, Wurm C, Goward G, Masquelier C, Nazar L. Rhombohedral form of $\text{Li}_3\text{V}_2(\text{PO}_4)_3$ as a cathode in Li-ion batteries. *Chem Mater*. 2000;12(11):3240-3242. doi:10.1021/cm000345g
139. Zhang G, Xiong T, Yan M, et al. In Operando Probing of Sodium-Incorporation in NASICON Nanomaterial: Asymmetric Reaction and Electrochemical Phase Diagram. *Chem Mater*. 2017;29(19):8057-8064.
140. Klinser G, Zettl R, Wilkening M, Krenn H, Hanzu I, Würschum R. Redox processes in sodium vanadium phosphate cathodes-insights from: Operando magnetometry. *Phys Chem Chem Phys*. 2019;21(36):20151-20155. doi:10.1039/c9cp04045e
141. Pivko M, Arcon I, Bele M, Dominko R, Gaberscek M. A $\text{Na}_3\text{V}_2(\text{PO}_4)_3$ (A = Na or Li) probed by in situ X-ray absorption spectroscopy. *J Power Sources*. 2012;216:145-151. doi:10.1016/j.jpowsour.2012.05.037
142. Broux T, Bamine T, Simonelli L, et al. VIV Disproportionation Upon Sodium Extraction from $\text{Na}_3\text{V}_2(\text{PO}_4)_2\text{F}_3$ Observed by Operando X-ray Absorption Spectroscopy and Solid-State NMR. *J Phys Chem C*. 2017;121(8):4103-4111. doi:10.1021/acs.jpcc.6b11413
143. Jian Z, Han W, Lu X, et al. Superior electrochemical performance and storage mechanism of $\text{Na}_3\text{V}_2(\text{PO}_4)_3$ cathode for room-temperature sodium-ion batteries. *Adv Energy Mater*. 2013;3(2):156-160.
144. Ding X, Huang X, Zhou S, et al. Synthesis of $\text{Na}_3\text{V}_2(\text{PO}_4)_3/\text{C}$ Composites as High-Performance Cathode Materials for Sodium Ion Batteries. *Int J Electrochem Sci*. 2019;14:2815-2821. doi:10.20964/2019.03.36
145. Zatovsky I V. NASICON-type $\text{Na}_3\text{V}_2(\text{PO}_4)_3$. *Acta Crystallogr Sect E Struct Reports Online*. 2010;66(2):i12-i12. doi:10.1107/S1600536810002801
146. Park S. (in preparation). Published online 2021.
147. Fondard J, Irisarri E, Courrèges C, Palacin MR, Ponrouch A, Dedryvère R. SEI Composition on Hard Carbon in Na-Ion Batteries After Long Cycling: Influence of Salts (NaPF_6 , NaTFSI) and Additives (FEC, DMCF). *J Electrochem Soc*. 2020;167(7):070526. doi:10.1149/1945-7111/ab75fd
148. Jian Z, Yuan C, Han W, et al. Atomic structure and kinetics of NASICON $\text{Na}_x\text{V}_2(\text{PO}_4)_3$ cathode for sodium-ion batteries. *Adv Funct Mater*. 2014;24(27):4265-4272. doi:10.1002/ADFM.201400173



*The greatest solace lies in
understanding this ancient
unseen stream... A shudder
before the beautiful.*

- Nightwish, Endless forms most
beautiful, 2015

